Cell Migration and Capillary Plexus Formation in Wounds and Retinae

Michael G. Watson

Submitted for the degree of Doctor of Philosophy
Heriot-Watt University
Institute of Petroleum Engineering

November 2012

Abstract

Cell migration is a fundamental biological phenomenon that is critical to the development and maintenance of tissues in multi-cellular organisms. This thesis presents a series of discrete mathematical models designed to study the migratory response of such cells when exposed to a variety of environmental stimuli. By applying these models to pertinent biological scenarios and benchmarking results against experimental data, novel insights are gained into the underlying cell behaviour.

The process of angiogenesis is investigated first and models are developed for simulating capillary plexus expansion during both wound healing and retinal vascular development. The simulated cell migration is coupled to a detailed model of blood perfusion that allows prediction of dynamic flow-induced evolution of the nascent vascular architectures – the network topologies generated in each case are found to successfully reproduce a number of longitudinal experimental metrics. Moreover, in the case of retinal development, the resultant distributions of haematocrit and oxygen are found to be essential in generating vasculatures that resemble those observed *in vivo*.

An alternative cell migration model is then derived that is capable of more accurately describing both individual and collective cell movement. The general model framework, which allows for biophysical cell-cell interactions and adaptive cell morphologies, is seen to have the potential for a range of applications. The value of the modelling approach is well demonstrated by benchmarking *in silico* cell movement against experimental data from an *in vitro* fibroblast scrape wound assay. The results subsequently reveal an unexplained discrepancy that provides an intriguing challenge for future studies.

Acknowledgements

Firstly, I would like to thank my supervisor Dr Steven McDougall for his endless support, patience and encouragement. I greatly appreciate all of the advice and guidance you have provided – even if, on occasion, I may have ignored it!

I would also like to thank the Engineering and Physical Sciences Research Council for funding my studies through a doctoral training account.

A special mention must go to my collaborators, whose contribution was critical to the completion of this work. Thanks to Professor Mark Chaplain, not only for convincing me that embarking on a PhD would be a good idea(!), but also for his continued support throughout the last four years. I also gratefully acknowledge Dr Maria Machado and Dr Andrea Devlin who, under the supervision of Dr Christopher Mitchell, performed the experiments that inform the angiogenesis models presented in this thesis. Thanks to you all for your efforts and the valuable discussions that pulled this work together.

Finally, I must thank the most important people in my life.

To Julie: I cannot thank you enough for your unconditional support – even when I put my PhD before everything – and also for being there to make me smile when I needed it most. You are amazing.

To my family: I am eternally grateful for your unwavering support and faith in me; not just over the last four years, but throughout my life. Without you this would never have been possible.

Contents

List of Publications

Machado M.J.C., Watson M.G., Devlin A.H., Chaplain M.A.J., McDougall S.R. & Mitchell C.A., 2011, Dynamics of angiogenesis during wound healing: a coupled *in vivo* and *in silico* study, *Microcirculation*, **18**, 183-197.

Watson M.G., McDougall S.R., Chaplain M.A.J., Devlin A.H. & Mitchell C.A., 2012, Dynamics of angiogenesis during murine retinal development: a coupled *in vivo* and *in silico* study, *J. R. Soc. Interface*, **9**, 2351-2364.

McDougall S.R., Watson M.G., Devlin A.H., Mitchell C.A. & Chaplain M.A.J, 2012, A hybrid discrete-continuum mathematical model of pattern prediction in the developing retinal vasculature, *Bull. Math. Biol.*, **74**, 2272-2314.

Chapter 1

Introduction

1.1. Background

The field of mathematical biology has grown immeasurably over recent decades and seen the development of theoretical models describing many diverse biological phenomena. The true potential of such models for providing novel insights into biological systems, however, has only recently been recognised on a broad scale. Indeed, there is a growing trend for biological and biomedical investigations to involve mathematical modellers working in close collaboration with those running pertinent experimental programmes. Such an approach is inherently advantageous to both parties: mathematical models can be informed and validated by the latest experimental data, whilst the corresponding *in silico* results can serve to reduce experimentation and focus future laboratory studies.

In this thesis, we utilise a range of *in vivo* data obtained from such an experimental collaboration, and set out to study the process of angiogenesis with particular focus on the role played by blood flow in the evolution of nascent vascular architectures. The cellular processes orchestrating the growth of these structures are also of great importance, however, and we follow this study by presenting a further model that incorporates these mechanisms in a more physically realistic manner. We begin, therefore, by firstly providing a brief introduction to the cell biology that is fundamental to our mathematical models.

1.2. Cellular Mechanisms of Development, Maintenance and Disease

The development of multi-cellular eukaryotic organisms from initial germ or somatic cells is a complex and fascinating biological phenomenon; a fully developed adult human body, for example, contains upwards of 200 different types of cells and approximately 10^{13} cells in total. In spite of the unavoidably intricate spatial and temporal interplay required between gene expressions, molecular interactions and cell movements, it is clear that the phenomenon of biological development is, in general, tightly controlled and, as a result, highly-reproducible. Although many of the molecular mechanisms driving such developmental cascades are yet to be fully elucidated, at a cellular level there exists a variety of well-known universal processes such as differentiation, migration, proliferation, adhesion and apoptosis. Notably, however, these features are not entirely unique to development; they also play a prominent role in tissue maintenance (e.g. wound healing) and in disease. For example, uncontrolled proliferation and invasive cell migration, which can ultimately lead to metastatic spread, are two of the hallmarks of cancer (Hanahan and Weinberg, 2000).

Although all five of these crucial cell behaviours will be considered at some stage in the mathematical models presented in this thesis; proliferation, migration and adhesion are the three of greatest relevance. Therefore, before proceeding to review pertinent mathematical modelling literature, we shall begin by summarising some of the basic biology characterising each of these processes. Note, however, that the following discussion is intentionally brief; the intention is not to explicitly detail the vast underlying molecular dynamics, but simply to provide a general survey of the key processes that drive the cellular responses in our models. Various biological scenarios are investigated in this thesis, and more problem-specific discussions will be embarked upon where necessary in succeeding chapters.

1.2.1. Cell Migration

The action of cell migration, or locomotion, can be loosely classified into two categories: cell *swimming* and cell *crawling*. In general, swimming refers to the movement of cells through a fluid, whilst crawling refers to movement across a solid substrate or through a fibrous matrix. The mechanical and molecular mechanisms of these two types of movement vary extensively and, for the purposes of this thesis, we shall choose to focus entirely on the latter phenomenon of cell crawling.

The crawling of cells has been typically studied *in vitro*, either on planar substrates or within deformable matrices. Much of the existing knowledge of this process has been collected by investigating the behaviour of, amongst other cell types, amoebae, leukocytes and fibroblasts. Such studies are of great importance because crawling is also known to be at the heart of a wide range of *in vivo* cell migration events. In late vertebrate embryonic development, for example, extensive cell migration is required to direct cells towards appropriate regions of the emerging body structure. Furthermore, tissue maintenance and the immune response in later life require the active migration and function of a menagerie of cell types, including fibroblasts, neutrophils and lymphocytes.

In the absence of external signals, cells have been shown to perform random walks; such a scenario, however, is not generally applicable for *in vivo* cell movements. Indeed, a variety of factors have been found to impose bias in the direction of migration of a cell within its microenvironment, including responses to gradients of adhesion (haptotaxis), diffusible chemicals (chemotaxis) and, perhaps more obscurely, light (phototaxis). As will be seen, the first two responses mentioned here are of great importance to the mathematical models of cell movement that will be presented in this thesis.

Whilst migrating randomly or in response to an external signal, it is important to understand the exact means by which a crawling cell propels itself forward in a chosen direction. The process that we shall therefore describe has been termed “fibroblast locomotion”, but the general framework, presented diagrammatically in Figure 1.1, is believed to depict the basis of active migration for any type of crawling cell. The forward propulsion first requires the extension of a protrusion from the front of the cell over the underlying substrate; such protrusions may take the form of blunt pseudopodia, flat lamellipodia or slender filopodia. Such cellular processes are believed to be formed by the rapid construction of a dense filamentous meshwork of polymerised actin in the cell cytoskeleton, thus forcing the plasma membrane to advance outwards. These protrusions subsequently attach to the substrate in front of the cell by forming points of adhesion, mediated primarily by a family of transmembrane proteins known as integrins. The absolute strength of these adhesions is known to vary from cell to cell, with the overall result seemingly that weakly-adhering cells are likely to migrate much more quickly. Finally, the cell utilises the newly formed anchorages at its front to support contraction of its body, and attachments at the rear of the cell are released to ultimately produce translocation of the cell and all of its intracellular components. The precise molecular mechanisms of this contraction remain a mystery, although it is widely believed that the actin cortex in the cytoskeleton again plays a prominent role.

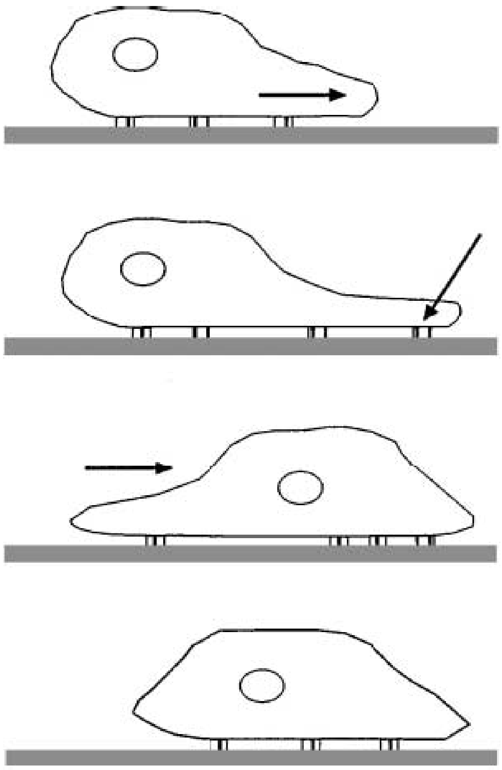

Figure 1.1: Schematic diagram illustrating the key features of cell crawling on a substratum. The temporal sequence of events entails (from top to bottom): extension of a protrusion from the front of the cell; attachment of the protrusion to the underlying surface; contraction of the cell body to pull the cellular contents forwards; release of surface adhesions at the back of the cell to produce an overall forward translocation. Image taken from Palsson (2001).

1.2.2. Cell Division

The division of cells is the fundamental process by which living organisms can develop and thrive. Tissue growth and organogenesis, in particular, rely on the repeated reproduction of particular cell types, whilst during adulthood proliferation is also required in order to replace cells that are damaged or have become obsolete. The sequence of events underpinning the division of all eukaryotic cells has been widely studied and, owing to its well-characterised recurring nature, has been termed the cell cycle. During this cycle the parent cell must duplicate all of its internal cytoplasmic organelles. More importantly, however, the DNA carried by the cell must also be accurately replicated in order that each of the two resulting daughter cells is genetically equivalent.

The standard cell cycle is conventionally split into a number of distinct phases, each of which demarcates a particular set of mechanical and molecular events during cell division; these phases, listed in order of occurrence, are known as G1, S, G2 and M. In addition, there also exists a state of quiescence, known as G0, which a cell may enter during passage through G1 if it withdraws from the natural progression of its cell cycle. A diagram of the typical progression of the cell cycle is presented in Figure 1.2. The various transitions between the respective states are regulated by a series of sophisticated molecular checks, known as the cell cycle control system. A cell may fail to pass a particular checkpoint if, for example, the necessary molecular machinery has failed to properly assemble or the local chemical environment is deemed unfavourable. Indeed, the composition of the local environment is believed to be of particular importance, since *in vitro* studies have predicted that cells will generally fail to proliferate in the absence of diffusible growth factors, whilst sufficient adhesion to an underlying substrate is also deemed to be a critical factor.

Most of the necessary cell cycle checks are made during the appropriately named gap phases, G1 and G2, where the cell may also be undergoing a small amount of growth. Once a cell has committed to S phase a great deal more activity is required, since this is the stage at which DNA is replicated in the nucleus. Furthermore, formation of the molecular machinery required during M phase is also initiated at this stage. Due to its inherently dynamic nature, M phase is by far the most complex and dramatic phase of the cell cycle. As such, we can further categorise this into two additional stages: mitosis, where the cell nucleus is divided, and cytokinesis, where two distinct daughter cells are formed by cleavage of the cytoplasm. The mechanical progression of mitosis requires the assembly of a microtubule-based structure known as the mitotic spindle. Following the breakdown of the nuclear envelope, this spindle captures the newly-replicated chromosomes of DNA and manoeuvres them towards opposite ends of the

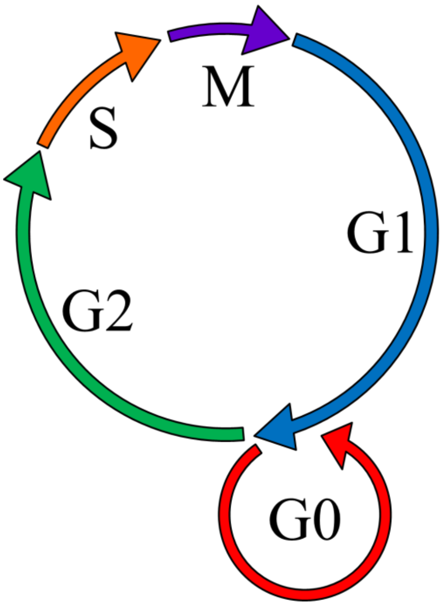

Figure 1.2: Schematic diagram showing the sequence of phases a cell will pass through during its division cycle; the cell splits into two daughter cells during the M phase. A cell may withdraw from its cycle and enter the quiescent G0 phase if it fails to satisfy the conditions of the cell cycle control system. Aside from G0, which may last an indeterminate amount of time, the lengths of the arrows give an indication of the relative time spent within each phase.

cell (i.e. towards the spindle poles). The mitosis stage is complete when two distinct nuclear envelopes begin to re-form, each containing identical sets of DNA. The final act, cytokinesis, requires the influence of a further cytoplasmic mechanical mechanism. As for cell migration above, this so-called contractile ring requires the assembly of actin filaments; however, a further protein known as myosin also plays an important role. The contractile ring initially forms close to the plasma membrane around the middle of the cell, and subsequent contraction pulls the membrane inwards to create a cleavage furrow that ultimately splits the cell in two. A diagram illustrating the key phases of both mitosis and cytokinesis is presented in Figure 1.3.

1.2.3. Cell-Cell Adhesion

In the discussion above, we remarked that adhesion to an underlying substrate is of great importance to the successful initiation or progression of both cell division and cell migration; however, it is also widely known that the formation of adhesion bonds from

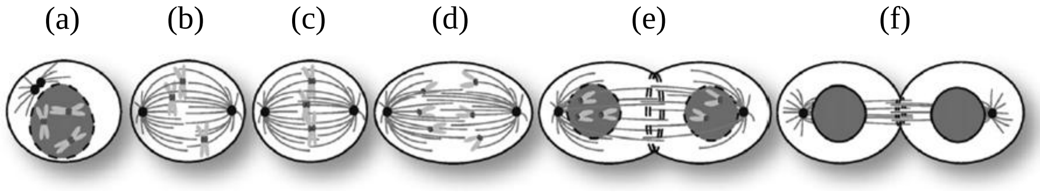

Figure 1.3: Schematic diagram showing the sequence of events undertaken by a cell during mitosis and cytokinesis: (a) DNA chromosomes have successfully replicated and the nuclear envelope begins to break down; (b) the bipolar mitotic spindle forms and captures the chromatid pairs; (c) chromatids are aligned at the cell equator; (d) sister chromatids are split and maneuvered towards opposite ends of the cell by the mitotic spindle; (e) two nuclear envelopes containing identical DNA begin to reform and a cytoplasmic contractile ring is formed in-between; (f) cell division is complete. Image taken from Vader et al. (2008).

one cell to another is a crucial factor in mediating both the initial assembly and long-term maintenance of tissues. During development, for example, selective adhesion between differing cell types allows migrating cells, upon reaching their terminal destination, to associate with appropriate neighbours and thus generate defined tissue structures. It is believed that the ultimate function of cell-cell adhesion is to hold two cell membranes sufficiently close together, in order that a range of complex structures known as cell junctions can subsequently be formed. Broadly speaking, three different types of cell junction are known to exist: occluding junctions (e.g. tight junctions), which allow neighbouring membranes to be tightly sealed together to create a largely impermeable cell layer; anchoring junctions (e.g. adherens junctions), which provide strong mechanical attachment between the cytoskeletal elements of two cells (or a cell and its substrate); and communicating junctions (e.g. gap junctions), which mediate the intercellular passage of either chemical or electrical signals.

From a molecular point of view, the basis of adhesion between two cells is a family of transmembrane proteins known as cadherins. In order for two cells to form adhesion bonds, cadherin molecules from each cell must undergo some form of extracellular association. It has been postulated that there are three distinct extracellular mechanisms by which this process may occur (Figure 1.4): homophilic binding, whereby two equivalent molecules from each cell combine; heterophilic binding, whereby two different molecules from each cell combine; and the rarely occurring phenomenon of extrinsic molecule-mediated binding. Cadherins are believed to associate via the extracellular homophilic mechanism, but a further set of intracellular proteins known as the catenins are required for successful completion of this process. Indeed, it has been shown that catenin-mediated anchorage within the actin cortex is crucial to cell-cell adhesion, since cells lacking such cytoplasmic binding domains cannot be held together. The above summaries provide a brief introduction to some of the cellular behaviour that is relevant to the mathematical modelling performed in this thesis; a great deal more information can be found in the excellent texts by Lackie (1986), Bray (2001) and Alberts et al. (2002).

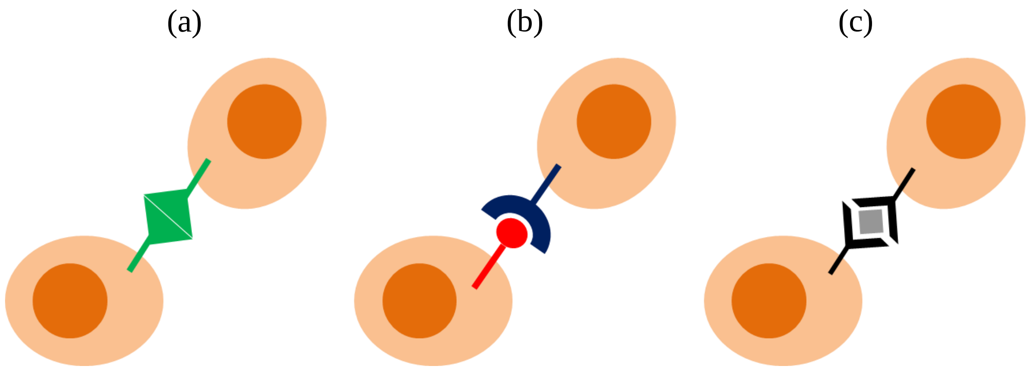

Figure 1.4: Schematic diagram illustrating the available mechanisms of cell-cell adhesion, namely: (a) homophilic binding, (b) heterophilic binding, and (c) binding through an extracellular molecule.

1.3. Angiogenesis

One pertinent biological scenario that we shall discuss here, however, is angiogenesis: the sprouting of new blood vessels from a pre-existing vasculature. Not only is this biological phenomenon of great relevance to three of the coming chapters; it is also a process largely co-ordinated by an interaction between the cell migration, adhesion and division mechanisms detailed above. The relevant cell type undergoing these events during angiogenesis is the endothelial cell (EC), which line the lumen of established blood vessels. There are a variety of developmental and reparative situations in which this process will occur, including during embryogenesis, organ growth and wound healing. In each of these cases angiogenesis will most likely occur for only a brief period; however, persistent uncontrolled angiogenesis may be exhibited in association with a variety of pathological scenarios such as arthritis, diabetic retinopathy and solid tumour growth (Folkman and Shing, 1992).

Angiogenesis is initiated when ECs are induced to sprout, proliferate and subsequently migrate away from the parent vasculature (Risau, 1997). A major contributing factor in the onset of vascular sprouting is the existence of tissue hypoxia (i.e. insufficient oxygen) – a problem encountered when a colony of cells lies too far from the nearest blood vessels. The hypoxic cells will secrete diffusible chemicals known as growth factors (a typical example being vascular endothelial growth factor, VEGF), and the increased growth factor concentration in the locality of the vessels will induce EC sprouts to form by breaking down the pre-existing vessel basement membrane (Carmeliet and Jain, 2000). In addition, the chemical gradient that is concurrently formed during growth factor secretion will act as a chemoattractant for the newly-formed endothelial tip cells, causing them to subsequently migrate towards the region of greatest hypoxia. It should be made clear, however, that this migration process, and the ultimate formation of new capillary tubes, is intrinsically coupled to a process of cell division. The tip cells sense local growth factor gradients by outwardly extending fine filopodia, and consequently respond by initiating their migratory machinery. ECs behind the tip cells, known as stalk cells, are then stretched through cell-cell adhesive contacts and subsequently divide to lengthen the nascent capillaries (Bentley et al., 2008). Migration of angiogenic ECs is also facilitated by matrix metalloproteinases (MMPs), also known as matrix degrading enzymes, which are produced by the endothelial tip cells themselves. These enzymes diffuse into the extracellular matrix (ECM) and degrade it to produce gradients which the ECs traverse in order to enhance ECM attachment (Davis et al., 2000; Yan et al., 2000; Hidalgo and Eckhardt, 2001; Sternlicht and Werb, 2001).

Through sustained angiogenesis, new capillary tubes and capillary loops, known as anastomoses, will form allowing functional blood flow to be established in the neo-vasculature. As required, significantly greater quantities of oxygen and nutrients can now be delivered to the previously hypoxic tissue. Particularly in non-pathological cases of angiogenesis, a direct consequence of increased oxygen delivery is the down-regulation of growth factor production. It is believed that VEGF, in particular, is a survival factor for ECs; hence, its oxygen-induced down-regulation below a critical level may make surplus neo-vessels vulnerable to apoptosis (Dor et al., 2001). In direct contrast to this, functional stability is lent to vascular networks by the recruitment of perivascular mesenchymal cells (pericytes) to endothelial tubes within the plexus (Gerhardt et al., 2003; Mitchell et al., 2006). Through the manifestation of these two competing events, the long-term plexus structure ultimately resembles a “mature” tree-like vasculature exhibiting a range of vessel sizes (Risau, 1997). An illustrative summary of many of the facets of angiogenic progression is presented in Figure 1.5.

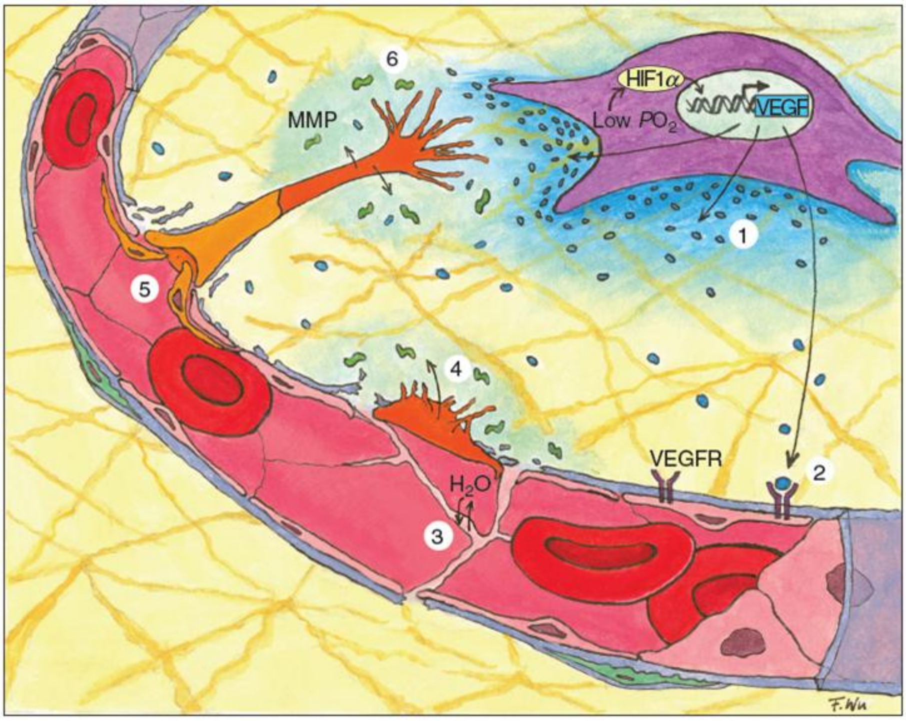

Figure 1.5: Schematic diagram illustrating the key processes in angiogenesis initiation and progression: (1) VEGF transcription and secretion by hypoxic cells; (2) VEGF binding on the surface of pre-existing vasculature; (3) increase in vessel permeability; (4) activated endothelial tip-cells break down the basement membrane; (5) sprouts extended by stalk cell proliferation; (6) tip-cells release MMPs to degrade the local ECM and enhance migration. Image taken from Qutub et al. (2009).

1.4. Review of Modelling Studies

Mathematical modelling of cellular behaviour has become widespread over the last 20-30 years, in line with various significant advancements in the biological and biomolecular sciences. A myriad of mathematical approaches have been proposed and developed in order to enhance understanding of the mechanisms underlying numerous developmental and pathological scenarios involving a wide range of cell types. The choice of a particular modelling style depends both on the biological scenario to which the model will be applied, and the desired aspects of this scenario that are to be investigated (e.g. microscopic or macroscopic features). Continuum models can be applied, for example, when the cell type of interest is sufficiently abundant, but if this is not the case a discrete cell model may be required.

In the interest of the work presented in this thesis we shall firstly focus our attention on providing a general overview of the vast field of discrete cell modelling, before proceeding to explore modelling work performed in the specific context of angiogenesis. It is worthwhile to note that a number of existing studies fall under the umbrella of both categories, but we shall approach the topics independently and endeavour to discuss a broad scope of adopted methodologies in each case.

1.4.1. Discrete Cell Modelling

Discrete models of cell behaviour can be classified into two general categories: lattice-based and lattice-free. As suggested by the nomenclature, lattice-based refers to a style of modelling whereby the *in silico* cells can only occupy, or migrate between, a finite set of discrete spatial positions. Such models, often known as cellular automata (CA), are driven by a set of appropriately defined “rules” and tend to be relatively simple to implement because concepts such as cell shape are generally neglected, whilst cell size is intrinsically encapsulated by the extent of the assumed lattice spacing.

A typical application of CA modelling is in the growth of multi-cellular colonies, such as tumours, where cells are assumed to undergo proliferation but do not migrate between lattice points. Interesting results can be generated from such models by imposing particular conditions on cell division such as the availability of nutrients (Gerlee and Anderson, 2007), spatial restrictions (Alarcon et al., 2005a) or level of micro-environment acidity (Patel et al., 2001). Powathil et al. (2011) have, for example, recently used such a model where cells compete for available oxygen in order to examine the implications of tumour therapies that target cells at particular stages in their cell cycle. Many CA models have, of course, also been proposed where cells undergo a combination of proliferation and migration. The assumed rules for transitions between grid points may allow for random stochastic motion, but continuum descriptions of macroscopic microenvironmental variables also provides the opportunity for biased random walks via chemotaxis (Beyer et al., 2002) or haptotaxis (Anderson et al., 2000). It is also possible for cell-cell interactions to be introduced; Anderson et al. (2005), for example, proposed an adhesion mechanism whereby a cell will cease migration when in the presence of a critical number of neighbouring cells. One perceived problem with representing the growth and movement of 2D cell populations on a lattice is the potential for numerical artefacts induced by the grid regularity. This issue was addressed by Block et al. (2007) who proposed a strategy in which an initial regular lattice is perturbed by randomly re-positioning each grid site within a square of side equal to the grid length and centred at the original site. Subsequently, constructing a Voronoi tessellation (i.e. delineating sets of spatial points that are closer to a particular site position than to any other site position) allows for a stronger representation of cell shape and cell-cell adhesion effects by defining polygonal surfaces that can share boundaries with more than the four possible nearest neighbours on the original regular lattice. A slight twist on traditional lattice-based discrete cell models are those that allow for the occupation of a single lattice site by multiple cells. Such an approach has been used, for example, to represent contact-inhibited fibroblast migration during healing of an *in vitro* scrape wound (Cai et al., 2006), and also in the context of tumour growth to mimic the experimental finding that tumour cells tend to follow each other along pathways of degraded host tissue (Mansury and Deisboeck, 2003). A further sub-set of models following this type of assumption are lattice-gas cellular automata (LGCA), wherein multiple occupancy of a node is allowable on the basis that each individual cell is associated with a particular distinct “channel”. Each channel could be assumed to represent, for example, a movement direction or a zero velocity resting state; see Tektonidis et al. (2011) for a recent example or the text by Deutsch and Dormann (2005) for a more general treatment of LGCA modelling.

Lattice-free modelling refers to methods where the position of a cell can be assigned to any point in continuous space, and is not restricted to discrete nodal grid values. In this regard, the type of lattice-free model that is most immediately comparable to general CA models are those in which each cell is represented by a discrete spatial point, maintaining the notion that cell shape and cell-cell interactions are not of great importance. This approach has typically been applied when studying *in vivo* movement of cell types residing within the relatively sparsely populated ECM; see, for example, a recent model of receptor-ligand driven neutrophil migration in competing chemoattractants (Wu and Lin, 2011). A model of this type that is of great importance to the work in this thesis, however, is a study of fibroblast migration during dermal wound healing, as developed in a series of papers (Dallon et al., 1999; Dallon et al., 2000; Dallon et al., 2001; McDougall et al., 2006a). This work, which investigated the mechanisms of scar formation by coupling the cell movement to production and re-orientation of fibres within the collagen matrix, has attracted much recent attention (Fomovsky et al., 2012). Indeed, modifications to the original framework include a revised stochastic differential equation for determining cell positions (Groh and Louis, 2010), an extension to 3D (Groh and Wagner, 2011), and the introduction of simple cell-cell interactions via assumed inelastic collisions when two cells come within a particular distance (Cumming et al., 2010).

A large number of models have been proposed that deal with cell behaviour and cell-cell interactions in a much more sophisticated manner, often through biophysical or mechanical assumptions that are strongly grounded in the underlying physics. Many models of this form typically assume that each cell occupies a spheroidal region of space about a central point. Moreover, each cell may also be capable of surface deformations in response to forces or stresses experienced through interaction with its environment, substrate or neighbouring cells. The physical balance between the adhesion and repulsion of cells in close proximity, for example, is often represented by a form of potential function that allows for both stretching and compression of the notional cell boundary. The multi-scale approach of Ramis-Conde et al. (2008a) expanded upon such a representation of cell-cell adhesion by explicitly including a molecular sub-model describing the cadherin-catenin kinetics discussed in Section 1.2.3. Mechanical and biophysical models of spheroidal cells have been used to investigate a wide range of biological phenomena including avascular tumour growth (Drasdo and Hoehme, 2003), *in vitro* aggregate formation (Galle et al., 2005; Byrne and Drasdo, 2009), cellular mechanisms of early development (Drasdo and Forgacs, 2000), cancer cell invasion of tissue (Ramis-Conde et al., 2008a; Ramis-Conde et al., 2008b; Ramis-Conde et al., 2009) and development of the breast cancer precursor known as ductal carcinoma *in situ* (DCIS) (Norton et al., 2010; Macklin et al., 2012). Mechanical models have also been proposed to describe the dynamics of cells that assume off-spheroidal, elongated morphologies. Palsson and Othmer (2000) modelled cells as ellipsoids that deform in a viscoelastic manner under “active” forces experienced during migration and “passive” forces applied by neighbouring cells. This work was used to examine how the features of collective cell behaviour, such as adhesion-driven sorting and *Dictyostelium discoideum* (Dd) slug translocation, can be explained entirely by the movements of, and interactions between, individual cells (Palsson, 2001; Dallon and Othmer, 2004). Models that incorporate a more detailed representation of cell shape have also been developed within a mechanical framework. The immersed boundary method, for example, assumes that each *in silico* cell is delineated by an elastic plasma membrane composed of a series of discrete points connected to each adjacent point by a linear spring (Rejniak et al., 2004). Cell-cell adhesion in this model can be introduced quite naturally by similarly linking points on neighbouring cells by further linear springs, while cell division can also be represented realistically by imposing contractile forces on points at opposing sides of the elastic membrane. Such models do not, however, tend to explicitly consider cell migration; typical applications involve scenarios of cell population growth and aggregation such as early tumour growth (Rejniak and Dillon, 2007; Rejniak, 2007) and *in vitro* epithelial acini formation (Rejniak and Anderson, 2008a; Rejniak and Anderson, 2008b). Other off-lattice mechanical models incorporating complex representations of cell shape include the approaches of Schaller and Meyer-Hermann (2005) and Brodland and Veldhuis (2002) where individual membrane boundaries are determined, and updated over time, by a Voronoi tessellation.

A further approach that is, in some sense, a hybrid of lattice-based and lattice-free modelling is the cellular Extended Potts model, where each individual uniquely-shaped cell is represented by several adjacent discrete points on an appropriately spaced grid. Also known as the Graner-Glazier-Hogeweg (GGH) model, the stochastic evolution of cell movements and configurations in this methodology is driven by the assumption that, in general, cells act to minimise their energy expense. This is described by a Hamiltonian expression that may consider the gain or loss of energy related to changes in, for example, cell volume or shared cell-cell surface contact (Graner and Glazier, 1992). Extensions to this original model have included proposed representations of cell proliferation (Stott et al., 1999), death (Hogeweg, 2000), differentiation (Savill and Sherratt, 2003), chemotaxis (Savill and Hogeweg, 1997) and haptotaxis (Turner and Sherratt, 2002) in order to study a range of pathological and developmental scenarios. A similar approach to the Extended Potts model is the "*hyphasma*" model developed by Meyer-Hermann and Maini (2005) to study lymphocyte motility. In this formulation each cell is still represented by a group of lattice points, but these are categorised into central immobile sub-units surrounded by bordering movable sub-units. The movement direction is pre-determined at each time step, and the cell translocates by stochastically adjusting its movable sub-units. The advantage of this approach is that cell volume can be completely conserved during migration, unlike for the Potts model where movement is necessarily associated with, at best, a transient volume increase.

The final sub-set of “discrete” cell modelling that we shall consider is a group of models that investigate, in a detailed manner, the processes driving the migration and conformational changes of single cells. The value of such models lies in the ability to study the poorly understood intracellular molecular dynamics that drive the typical cell behaviours that can be observed under a microscope *in vitro*. An example of this approach is the cytomechanical model proposed by Stephanou et al. (2004) to examine the role of actin polymerisation and depolymerisation in generating the spontaneous pulsatile membrane deformations seen in resting cultured fibroblasts. This model was later generalised to incorporate migration by assuming that, under certain conditions, the membrane protrusions adhere to the underlying substrate and provide sufficient traction for translocation of the cell body (Stephanou et al., 2008). This model is similar in concept, but mathematically very different to the work of Neilson et al. (2011) who modelled migration of a single cell that was represented by a temporally evolving finite element-based boundary. Cell movement in this model is directed towards pseudopod-like protrusions of the boundary, which are extended or retracted according to the solution of a reaction-diffusion system of activators and inhibitors on the notional cell surface. Further models of this type have also been developed; see, for example, Rubinstein et al. (2005) as an additional illustration of the range of adopted methodologies.

1.4.2. Angiogenesis Modelling

In the preceding section we discussed at length various modelling approaches whereby cells are treated as discrete entities; such a discussion is pertinent since the methodologies of the models adopted in this thesis are based on the same assumption. This is, of course, not to discount the importance of continuum approaches, which remain widely used due to their greater amenability to systematic mathematical analysis. Indeed, continuum models have been proposed to tackle a range of problems in both single cell and cell population dynamics; see the work of Gracheva and Othmer (2004), Painter and Sherratt (2003) and Armstrong et al. (2006) for some interesting examples. As will be seen in the forthcoming discussion, one particular application of continuum models that has been extensively explored is the migration and expansion of EC populations during angiogenic progression.

Over recent decades mathematical modelling of vascular network development has focussed pre-dominantly on the role played by ECs during tumour-induced angiogenesis. Typically, these models will consider the important mechanisms of EC proliferation, and EC migration in response to gradients of soluble growth factors and insoluble matrix macromolecules present in the tumour microenvironment. In early models, a popular choice for reproducing these interactions was by using systems of non-linear PDEs that describe the outward expansion of a capillary network from a parent vessel towards a solid tumour. One of the earliest models of this type was the continuum approach attributable to Balding and McElwain (1985), whose three species system incorporated a capillary density, a sprout tip density and a concentration of diffusible tumour angiogenic factor (TAF). In this model sprout tips are formed from existing capillaries and move in response to the TAF, with new capillaries assumed to form naturally in their wake. This type of assumption has been repeated in many other angiogenesis models (Byrne and Chaplain, 1995; Gaffney et al., 2002; Schugart et al., 2008; Xue et al., 2009; Aubert et al., 2011), and it has a number of inherent strengths: (i) it accounts for the experimental observation that EC proliferation pre-dominantly occurs immediately behind the migrating tip (c.f. Section 1.3); (ii) it facilitates a continuum representation of the discrete physical phenomena of tip branching and anastomosis; (iii) it allows differentiation between the unique responses of capillaries and tip-cells to their local chemical environment (e.g. growth factors bound by tip-cells only). In the absence of this formulation, a single equation is often used to simply represent the overall EC density (Chaplain and Stuart, 1993; Anderson and Chaplain, 1998a; Anderson and Chaplain, 1998b; Plank and Sleeman, 2004a). This approach was taken in the model of Orme and Chaplain (1996a) where tumour vascularisation and invasion was initiated by an assumed tactic response of tumour cells to EC gradients. Continuum models of varying complexity have also been derived to investigate the process of capillary sprouting from pre-existing vasculature; a necessary pre-requisite to angiogenic network formation (Orme and Chaplain, 1996b; Levine et al., 2000; Levine et al., 2001a; Levine et al., 2001b).

More recently, much attention has been focussed on developing extended forms of such continuum tumour angiogenesis models, by adopting a discrete approach that allows the progress of individual endothelial tip-cells and capillaries to be tracked in space and time. One of the first models of this type was developed by Stokes and Lauffenburger (1991) where 2D off-lattice vessel sprouts, under the influence of a chemoattractant, were spatio-temporally characterised by solving a stochastic differential equation for the velocity of the sprout tip. An alternative approach was later proposed in which the starting point was a continuum PDE model of EC migration incorporating the combined effects of diffusion, chemotaxis and haptotaxis. Discretisation of the equations in 2D provided a set of movement weightings informed by the chemical environment that were subsequently used to generate tip-cell transitions between points on an appropriately scaled lattice (Anderson and Chaplain, 1998b). Furthermore, aspects such as capillary branching and anastomoses, absent from the continuum description, were included in the discrete simulations by prescribing appropriate phenomenological rules. Importantly, this so-called hybrid discrete-continuum approach will provide the basis of the angiogenesis modelling to be presented in this thesis; it has also, however, been applied frequently by the wider modelling community (Wu et al., 2008; Owen et al., 2009; Pons-Salort et al., 2012). Indeed, this was the basis of the angiogenesis model applied by Zheng et al. (2005) in one of the first studies to explicitly couple tumour growth to tumour vascularisation. Other discrete tumour-induced angiogenesis models have also been proposed: Plank et al. (2004b) considered both lattice-based and lattice-free models, deriving their equations on the alternative basis of reinforced random walks (Othmer and Stevens, 1997); whilst Bauer et al. (2007) have proposed a Potts model of angiogenic sprout extension.

A major advancement in discrete tumour-induced angiogenesis modelling came with the implementation of blood flow simulation through *in silico* capillary structures (McDougall et al., 2002). In this study, vascular architectures generated by the Anderson and Chaplain (1998b) model were perfused under the assumption that each EC lattice element represents a rigid cylindrical vessel supporting a local Poiseuille flow regime. Including blood flow in this manner paved the way for novel investigations of the likely implications of network architecture, blood rheology and flow-induced structural adaptation of capillaries on the delivery of both nutrients and cancer therapies to the vascularised tumour (Stephanou et al., 2005; McDougall et al., 2006b; Stephanou et al., 2006; McDougall et al., 2010). A natural extension of this methodology is to couple a model of perfused tumour-induced angiogenesis to the growth of the tumour itself. Existing approaches of this type can be placed into two categories: those that assume vessel sprouting and growth towards a distal nutrient-starved tumour (Macklin et al., 2009; Cai et al., 2011; Pons-Salort et al., 2012), and those that assume localised sprouting for a tumour developing within *a priori* vascularised tissue (Welter et al., 2008; Owen et al., 2009; Shirinifard et al., 2009; Welter et al., 2009; Perfahl et al., 2011). Many dynamic feedbacks between the growth of the tumour and the evolution of the vasculature have been proposed, including mechanical considerations such as the intra-tumour, pressure-induced vessel occlusion reported by Macklin et al. (2009).

A second popular and important application of angiogenesis modelling concerns the healing of dermal wounds. As has been acknowledged (Chaplain and Byrne, 1996), many of the processes involved in tumour-induced angiogenesis are recapitulated in the much more physiologically desirable wound healing case. Accordingly, the many mathematical models reported to date tend to follow continuum PDE approaches comparable to those discussed above; for instance, Pettet et al. (1996a) derived a three species model incorporating endothelial tip-cells, blood vessels and a macrophage-derived chemoattractant source (c.f. Balding and McElwain, 1995). More extensive models were soon developed, however, variously including continuum representations of regenerating ECM, fibroblast migration and oxygen delivery (Pettet et al., 1996b; Olsen et al., 1997). Pettet and McElwain (2000) also proposed a somewhat different approach, representing the wound healing process as a Lotka-Volterra system where the capillary tips (i.e. predator) seek out the chemoattractant (i.e. prey). Analysis of this system allowed predictions to be made regarding necessary conditions for “healing” to be completed. After an apparent dip in interest, recent years have seen a raft of publications in this field; presumably due to the growing clinical need for effective therapeutic strategies to treat both chronic and diabetic wounds (Sen et al., 2009). Indeed, the potential benefits (and pitfalls) of clinically realistic oxygen supplementation therapies (Thackham et al., 2008) have been studied in a range of models of varying complexity (Schugart et al., 2008; Flegg et al., 2009; Flegg et al., 2010; Flegg et al., 2012). An eight species mechanochemical model of chronic wound healing, incorporating both angiogenesis and oxygen delivery, has also been developed where wound closure is measured by tracking the progression of a viscoelastic ECM (Xue et al., 2009; Friedman et al., 2010; Friedman et al., 2011). An omission with regard to the existing models in this field is that, in direct contrast to the case of tumour-induced angiogenesis, we are currently unaware of any models that take into account discrete aspects of the angiogenic response to injury.

In addition to studies of wound healing and cancer, there have also been a small number of models reported in the literature concerning vascular growth in the eye. Discrete approaches have been proposed for modelling angiogenic growth in the cornea (Tong and Yuan, 2001; Jackson and Zheng, 2010); the aim of the latter was to develop a multi-scale mechanical model capturing the key relationships between EC proliferation, sprout extension and capillary maturation. In terms of the retina, pathological angiogenesis has been explored by Maggelakis and Savakis (1996, 1999) via a simple continuum PDE model designed to investigate the interplay between VEGF, oxygen and nascent capillary density. Aubert et al. (2011) have recently reported 1D PDE simulations of cell migration in the murine retinal vascular plexus (RVP), and this appears to be the first attempt to model capillary plexus formation in the retina during normal physiological development. As highlighted above for the scenario of wound healing angiogenesis, it would appear that no models of discrete capillary growth in the retina have been reported to date.

The final modelling studies that we shall briefly consider focus on the small-scale dynamics at the advancing front of an angiogenic capillary plexus. Combining agent-based mathematical modelling with a complementary experimental programme, Bentley et al. (2008) investigated the mechanisms by which the Notch-Dll4 signalling pathway regulates retinal endothelial tip-cell selection, and filopodial extension, in response to VEGF. This model was later extended to include a mechanical EC representation in order to simulate the extension and adhesion properties exhibited during cell-cell anastomosis formation (Bentley et al., 2009). A study of the physiological properties of “blind-ended” vessels at the leading front of an expanding network has also been carried out by Guerreiro-Lucas et al. (2008), who applied lubrication theory to examine plasma flow patterning within closed, permeable axi-symmetric structures.

Finally, it should be noted that angiogenesis can also occur via an alternative mechanism to capillary sprouting: intussuceptive or splitting angiogenesis describes the poorly-understood rearrangement of ECs in existing vasculature to create additional capillaries. Some models of this process have been proposed (Szczerba and Szekely, 2005; Szczerba et al., 2009), including a study that compares the efficacy of oxygen delivery in both sprouting and splitting modes of angiogenesis (Ji et al., 2006). In this thesis, however, we shall be concerned exclusively with network expansion by sprouting and migration. For the interested reader, many more examples of the angiogenesis modelling approaches discussed above can be found in the review papers of Mantzaris et al. (2004), Peirce (2008) and Qutub et al. (2009).

1.5. Thesis Overview

As is apparent from the abundance of investigative mathematical modelling studies outlined above, the desire to obtain a deeper understanding of the individual and collective cell movements involved in development, maintenance and disease commands significant research interest. Strikingly, however, a great deal of effort remains focussed on understanding the mechanisms of solid tumour growth and invasion. The literature survey has revealed that, despite a variety of discrete modelling techniques being available, very few have been applied in contexts such as wound healing and retinal development. This is a situation that is remedied with the models developed in this thesis. The intention, however, is not simply to “fill a gap in the market” – by extending established models and tying our results to pertinent experimental data we gain novel insights into the systems that we study.

We begin in Chapter 2 by detailing a numerical technique for simulating the highly dynamic process of blood flow and structural adaptation in the microvasculature. Using some simple, idealised vascular architectures we proceed to demonstrate the vital importance of this methodology, which incorporates some of the latest advancements in vascular research. The perfusion model is subsequently fed directly into two experimentally-informed models of angiogenesis. In Chapter 3, we study the re-establishment of functional vasculature in a healing wound by adapting an existing hybrid PDE-discrete model of tumour-induced angiogenesis. Validation of this modelling approach is achieved by comparing the generated *in silico* vascular architectures with quantitative longitudinal data obtained from an *in vivo* murine burn wound assay. An extended form of the hybrid angiogenesis model is then used in Chapter 4 to model development of the murine retinal vasculature. This study is found to provide a significant test of all aspects of the modelling approach; the extended blood flow model, in particular, proves to be critical in generating nascent capillary structures that closely resemble those observed in the laboratory.

Although the studies of angiogenesis involve the simulation of discrete cell migration, the cells themselves are treated as essentially volumeless points. As a first step towards a more realistic representation of individual and collective cell movement, we revisit a discrete-point model originally derived to investigate fibroblast migration and scar formation during dermal wound healing. In Chapter 5, we begin to generalise this model with a view to developing a tool for studying 2D cell migration in a variety of contexts. Firstly, the discrete-point formulation is extended by incorporating a realistic representation of stochastic cell movement, before the model is further developed by the introduction of physically-sized spherical cells that undergo biophysical cell-cell interactions. The concept of physical cell morphology is addressed in a more detailed manner in Chapter 6: we allow our migrating cells to exhibit ellipsoidal forms that dynamically contract or elongate in response to local environmental stimuli. The potential of the complete model for studying both individual and collective cell behaviour is subsequently demonstrated by *in silico* benchmarking of real experimental data from an *in vitro* fibroblast scrape wound assay. Finally, in Chapter 7, we discuss our results and their implications before considering the future utility of our models, both individually and in combination.

Chapter 2

Simulating Blood Flow in the Microvasculature

2.1. Introduction

The fundamental purpose of the vasculature in any living organism is the delivery to cells of various crucial metabolites, such as oxygen and nutrients. This delivery takes place across the thin walls of the smallest blood vessels, known as capillaries, which thus play a critical role in the ability of the cardiovascular system to achieve its ultimate objective (Levick, 2000). The precise manner by which this metabolic delivery is achieved depends critically on the *architecture* of the capillary network, the *flow properties* of the blood contained in the capillaries and, furthermore, the flow-induced *adaptive response* of the capillaries. In this chapter we summarise some of the key biology of these inter-connected factors, introduce the method of blood flow simulation utilised in this thesis, and present a variety of simple results illustrating the key features of the modelling approach.

2.2. Biology of the Microvascular Circulation

Blood is a non-Newtonian biphasic fluid, consisting of a variety of cell types carried in plasma. Although white blood cells and platelets are present, from a mechanical and haemodynamic viewpoint their contribution is negligible compared to that of the oxygen-carrying red blood cells (RBCs). The volume fraction of RBCs in the blood is termed haematocrit, and typically takes the value 45% in human blood (Pries et al., 1996). A number of biophysical phenomena exist that govern the distribution of RBCs within individual vessels and, moreover, haematocrit across the wider network. These distributions strongly affect the flow properties of the blood and, hence, impact significantly on the efficacy of oxygen delivery.

It is well known that cell-cell and cell-vessel wall interactions have a significant impact on flow resistance and flow distribution within a vascular network (Pries et al., 1996). Cell-wall interactions tend to result in reduced RBC presence at the vessel wall with most cells congregating at the vessel centre – an effect termed "axial migration" (Bayliss, 1959; Goldsmith and Mason, 1961). Since the flow velocity of a fluid in a tube increases from zero at the tube wall to a maximum at the centre, axial migration results in an average RBC velocity that is larger than the corresponding average blood velocity. As a consequence of this the haematocrit contained *inside* the tube is reduced relative to the haematocrit *leaving* the tube (discharge haematocrit, H_D) – a phenomenon known as the Fahraeus effect (Fahraeus, 1929). Experimental investigations carried out with $H_D \approx 0.4$ have found the ratio of these values to reach a minimum of around 0.7 in tubes with radii of 5 – 10 μm (Fahraeus, 1929; Barbee and Cokelet, 1971; Albrecht et al., 1979).

A further phenomenon, the Fahraeus-Lindqvist effect, was first observed during the investigations of Martini et al. (1930) and Fahraeus and Lindqvist (1931). Experiments involving blood flow in glass tubes demonstrated a decrease in calculated blood viscosity with decreasing tube diameter, thought to be due to the "single file" cell motion that is encouraged by both RBC deformation and rouleaux formation at the tube centre. Later studies predict that the minimum viscosity occurs in tubes of radius 3.5 μm with an increase in smaller tubes (Pries et al., 1992). This clearly suggests that blood viscosity is influenced by interactions between the blood and the tube system through which it flows, and has thus been termed "apparent viscosity" (Pries et al., 1996). This name also gives rise to the term "relative apparent viscosity", defined as the apparent blood viscosity divided by the plasma viscosity. The Fahraeus-Lindqvist effect becomes more intriguing with the experimental measurements of Lipowsky et al. (1978, 1980) who reported that *in vivo* relative apparent viscosity is significantly larger than that reported *in vitro*. This was supported by a later study which predicted a minimum viscosity in vessels of radius 20 μm, and greater haematocrit dependence over a wide range of radii (Pries et al., 1994).

Various possibilities have been proposed to explain the discrepancy between *in vivo* and *in vitro* flow resistance in narrow tubes. These include the presence of white blood cells (generally removed during *in vitro* experiments), the irregularity of blood vessel cross-sections or the existence of a thin flow-retarding endothelial surface layer (Pries et al., 1990; Pries et al., 1994). One further possible explanation is the dissipation of energy due to enforced re-organisation of RBCs at vascular branch points. When the blood flow in a feeding vessel is split into two daughter vessels separated by a particular angle and with potentially very different diameters, the components of the blood may be distributed in different proportions – a process known as phase separation (Pries et al., 1996). Hence the haematocrit levels and viscosities in the daughter vessels may differ significantly relative to that in the parent vessel. Due to axial migration of RBCs, it is thus possible that a small side branch of a parent vessel may be perfused simply by plasma picked up from the cell-free layer at the parent vessel wall. This phenomenon is known as “plasma skimming”, as termed by Krogh (Pries et al., 1996).

Clearly, the occurrence of phase separation at each individual branch point of a vascular network will have consequences for the network-wide haematocrit distribution. RBCs will, in general, follow the higher flow pathway at a bifurcation thus resulting in a positive correlation between haematocrit and flow velocity. In analogy to the single vessel phenomenon, this result has been termed the “network Fahraeus effect” since average capillary discharge haematocrit is reduced with respect to the haematocrit in the feeding arteriole (Pries et al., 1986). A further consequence of phase separation and, in particular, plasma skimming is that consecutive small side branches from a main arteriole may take little or no RBCs from the flow. This results in a build-up of haematocrit as the flow makes its way along the arteriolar vessel tree towards the capillaries. Hence there is an increased likelihood of red blood cells undertaking long flow pathways through the network, and accordingly this is termed the “pathway effect” (Pries et al., 1989a; Pries et al., 1992).

The above description of a number of aspects of blood flow in the microcirculation make it clear that this biological system is extremely complex. The situation is further complicated, however, by the fact that these vascular networks are not inert, but are in fact subject to constant structural changes in order to maintain sufficient perfusion and meet the functional needs of surrounding tissues. At a cellular level, this angioadaptation is achieved through the contraction (vasoconstriction) or relaxation (vasodilatation) of vascular smooth muscle cells, which reside beyond the ECs in the vessel wall. Prominent vasodilatation can be elicited under a variety of circumstances such as during sustained exercise, pathological inflammation or reactive hyperaemia due to the release of a compressed artery (Levick, 2000). Under less extreme conditions, a number of factors have been reported to be capable of inducing changes in microvessel radii such as temperature, blood pressure, wall shear stress and metabolic conditions. Given that these factors are coupled variously with the blood flow and haematocrit in the network, it is therefore clear that the whole microvasculature is subject to a continuous dynamic feedback loop.

2.3. Network Modelling and Theoretical Studies of the Microvasculature

The technique of network modelling was first introduced over 50 years ago in the context of pore-scale fluid transport within the interstices of petroleum reservoirs (Fatt, 1956). The fully interconnected 2D lattice utilised in this early work was naturally extremely small (200-400 elements), but increased computational power has more recently led to the advent of 3D networks potentially containing hundreds of thousands of bonds (McDougall and Sorbie, 1997). Indeed, network modelling at the pore-scale has been widely studied; a comprehensive overview of relevant literature can be found in the text by Dullien (1992). The relevance of network modelling in the context of this thesis, however, pertains to its more recent application in the theoretical study of blood flow and related microvascular phenomena. Although the fields of petroleum engineering and microcirculatory investigation would seem entirely disparate, the cross-over lies in the assertion that modelling of the movement of oil through interconnected pores within solid rock structures is analogous to the simulation of blood flow through capillaries within a host tissue.

A widely employed strategy in the theoretical study of microvascular dynamics is to investigate the biomechanical properties of the constituent blood vessels and cells; see Schmid-Schoenbein (1999) for a review. Typical topics of investigation include analysis of the impact of RBC aggregation on blood viscosity (Sutton and Schmid-Schoenbein, 1994), viscoelastic modelling of vessel compliance (Price and Skalak, 1995) and prediction of the haemodynamic implications of RBC deformation during single-file flow through narrow capillaries (Secomb and Hsu, 1996; Secomb and Hsu, 2001). Two other methodologies that are of great relevance to the work contained in this thesis are analyses of the flow-induced phenomena of RBC dispersal and structural adaptation in microvascular networks. Theoretical studies of the former have been presented by, for example, Levin et al. (1986) and Alarcon et al. (2005b) in order to investigate the implications of non-uniform haematocrit distribution in capillary networks. An extremely detailed model has also been proposed recently, where blood rheological properties were examined in a flowing branched network where each RBC is represented as an individual entity (Pozrikidis, 2009; Davis and Pozrikidis, 2011). Structural adaptation has been considered by a number of groups (Honda and Yoshizato, 1997; Goedde and Kurz, 2001), but much attention has recently been drawn to the work of Pries and colleagues (Pries et al., 2010). The combined experimental and theoretical studies performed by this group have led to the proposal of a series of mathematical representations of haemodynamic and metabolic stimuli that contribute to the evolution of vessel diameter and wall thickness in established vascular networks (Pries et al., 1998; Pries et al., 2001; Pries et al., 2005). Various other aspects of this process have also been investigated, including long-term vessel adaptation dynamics in response to a reduction in blood supply (Gruionu et al., 2005), heterogeneity between the behaviour of normal and tumour vasculature (Pries et al., 2009), and the precise mechanisms of oxygen sensing in metabolic adaptation responses (Reglin et al., 2009). Interestingly, a recent stability analysis performed on some of these empirical adaptation equations for single vessels has predicted complex dynamics, with the potential existence of limit-cycle oscillations and multiple equilibria (Shafer et al., 2011). As will be seen in due course, much of the work performed by Pries and colleagues has proved to be invaluable in the development of our own model of angiogenesis and microvascular blood flow.

2.4. Modelling Foundations

The mathematical modelling of angiogenesis to be presented in this thesis takes its inspiration from the dynamic adaptive tumour-induced angiogenesis (DATIA) modelling of McDougall et al. (2006b). In this work, discrete capillary sprouting and growth from a parent vessel was coupled with simulation of blood flow and structural adaptation in order to assess the implications and efficacy of drug delivery to solid tumours. A typical quasi-steady state vascular network resulting from this study,

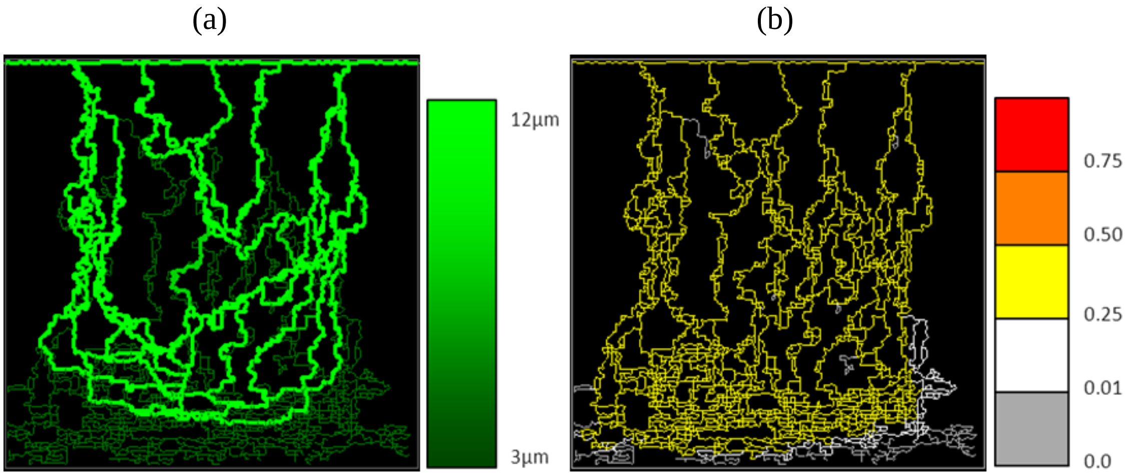

Figure 2.1: Typical example of a DATIA simulation from McDougall et al. (2006b), depicting a tortuous vasculature that has sprouted from a parent vessel (top of domain), grown towards a notional hypoxic solid tumour (bottom of domain), and remodelled structurally in response to a range of flow-related stimuli. Specifically, the images show distributions of (a) capillary radii and (b) haematocrit, where the lack of heterogeneity in each case is of particular note.

indicating the distributions of capillary radii and haematocrit, is presented in Figure 2.1. Inspection of these images reveals a number of limitations of the earlier modelling approach. Firstly, a homogeneous distribution of haematocrit is exhibited with all vessel segments mirroring the value at the network inlet. This is the consequence of an assumption that haematocrit is split in the same proportion as flow at bifurcations, at odds with the situation outlined in Section 2.2 where phase separation could be expected to produce significant heterogeneity. Secondly, the distribution of radii also lacks heterogeneity with vessels almost exclusively assuming either a fully constricted or fully dilated morphology. The dilated “backbone” was shown to carry a significant proportion of the flow and results in poor delivery of chemotherapeutic drugs or, conversely, nutrients. Although some recent publications have suggested that such angioarchitectures are realistic for tumour vasculature, non-cancerous vascular networks could be expected to exhibit a larger degree of structural heterogeneity (Maini et al., 2007; Pries et al., 2010). Hence, it is clear that a number of amendments to the blood flow simulation are required in order to more realistically reproduce the features of the real biological system.

The full blood flow model utilised in this thesis is now summarised, including details of the components introduced to address the issues outlined above.

2.5. Blood Flow Simulation Model

2.5.1. Basic Flow Calculation

The basis of the blood flow simulation model is the assumption of pseudo single-phase flow, where the blood in each capillary is treated as a homogeneous, non-Newtonian fluid with averaged bulk properties. Therefore, at the scale of a single capillary element of length L and radius R with respective pressures at each end denoted by P_1 and P_2, the approximate relationship between the capillary pressure gradient ΔP (i.e. $P_2 - P_1$) and flow Q takes the form of a Poiseuille-like expression:

$$Q = \frac{\pi R^4 \Delta P}{8\mu_{app} L}, \text{ with } \mu_{app}(R, H_D) = \mu_{rel}(R, H_D) \cdot \mu_{plasma}, \tag{2.1}$$

where μ_{app} is the apparent blood viscosity, which depends on the local blood haematocrit H_D, vessel radius and plasma viscosity μ_{plasma}. Varying as it does with both capillary radius and haematocrit, accurate experimental measurement of blood viscosity in living microvessels is non-trivial. We therefore apply the empirically-derived relationship (Pries et al., 1994):

$$\begin{gathered}\mu_{rel}(R, H_D) = \left[1 + (\mu_{0.45} - 1) \cdot \left(\frac{(1-H_D)^C - 1}{(1-0.45)^C - 1}\right) \cdot \left(\frac{2R}{2R-1.1}\right)^2\right] \cdot \left(\frac{2R}{2R-1.1}\right)^2, \\ \mu_{0.45} = 6e^{-0.085\cdot(2R)} + 3.2 - 2.44e^{-0.06\cdot(2R)^{0.645}}, \\ C = \left(0.8 + e^{-0.075\cdot(2R)}\right) \cdot \left(\frac{1}{1+10^{-11}\cdot(2R)^{12}} - 1\right) + \frac{1}{1+10^{-11}\cdot(2R)^{12}},\end{gathered} \tag{2.2}$$

where μ_{rel} is the relative apparent blood viscosity, $\mu_{0.45}$ is the value corresponding to a typical haematocrit of 0.45 and C describes the shape of the viscosity dependence on haematocrit. The relationship between *in vivo* relative apparent blood viscosity and vessel radius is illustrated graphically in Figure 2.2 for a range of haematocrit values. Having decided upon a local flow law, the next step of the modelling approach is to calculate the distribution of pressure and flow within an interconnected vascular bed. By fixing inlet and outlet pressures and assuming mass conservation (i.e. flow in equals flow out) at each node of the network, we arrive at a set of linear equations for the nodal pressures which can be solved numerically (by successive over-relaxation (SOR), for example). Calculating appropriate ΔP values from these solutions allows the flow in each capillary element to subsequently be determined from Equation 2.1 (note that additional details regarding the numerical implementation of this calculation can be found in Appendix A). This method of blood flow calculation has been utilised in a number of recent angiogenesis modelling publications (McDougall et al., 2002; Alarcon et al., 2003; Stephanou et al., 2005; Alarcon et al., 2006; Ji et al., 2006; McDougall et al., 2006b; Stephanou et al., 2006; Welter et al., 2008; Macklin et al., 2009; Owen et al., 2009; Welter et al., 2009; Perfahl et al., 2011). In the next section we introduce a further component that addresses one of the issues highlighted in Section 2.4.

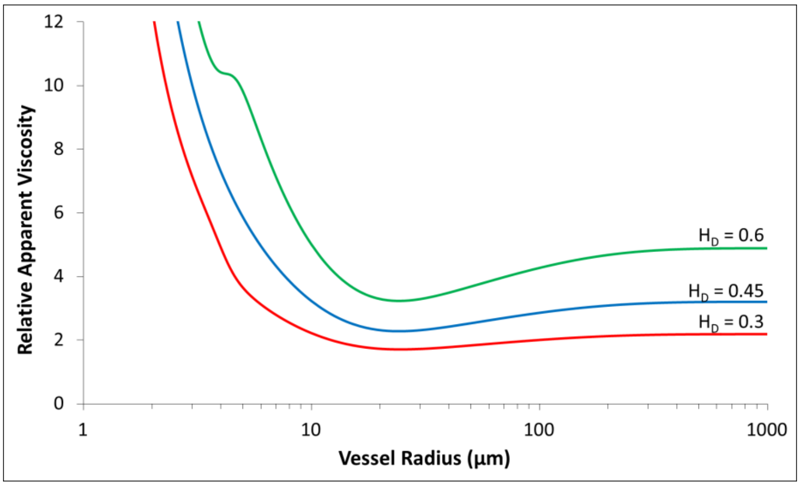

Figure 2.2: Plot of Equation 2.2 showing the empirically-derived relationship between *in vivo* relative apparent viscosity and vessel radius for different haematocrit (H_D) values (Pries et al., 1994).

2.5.2. Phase Separation

The Fahraeus effect, whereby the average RBC velocity through a tube is found to be larger than the corresponding average blood velocity, is known to be a direct manifestation of lateral variation in flow velocity and axial migration of RBCs. Since we elect to simulate blood as a pseudo single-phase fluid with averaged bulk properties, our perfusion model currently lacks the detail to explicitly reproduce such features.

However, much of the influence of the Fahraeus effect can be implicitly captured in the model by introducing the phenomenon of phase separation at vascular bifurcations.

Separation of plasma and red blood cells at bifurcations in the microvasculature has been widely studied both *in vivo* (Schmid-Schoenbein et al., 1980; Klitzman and Johnson, 1982) and *in vitro* (Yen and Fung, 1978; Fenton et al., 1985; Carr and Wickham, 1991; Enden and Popel, 1994). One such study conducted by Pries et al. (1989b) examined the behaviour at 65 simple branch points in the rat mesentery, yielding a parametric description of phase separation *in vivo*:

$$FQ_E = \frac{1}{1+exp\left[-\left\{A+B\ln\left(\frac{FQ_B-X_0}{1-(FQ_B+X_0)}\right)\right\}\right]}, \tag{2.3}$$

where FQ_B is the fraction of bulk blood flow received by a daughter vessel, FQ_E is the corresponding fraction of erythrocyte (RBC) flow, while the parameters A, B and X_0 determine the behaviour for a particular distribution of feeding and daughter vessel radii, and feeding vessel haematocrit. Note that pure plasma skimming (i.e. $FQ_E \equiv 0$) is assumed to occur whenever FQ_B is less than the threshold value X_0. By linear regression, Pries et al. (1989b) found the best fit for these parameters to be:

$$A_\alpha = \frac{-3.48\ln\left(\frac{R_\alpha}{R_\beta}\right)}{R_f},\ B = 1 + 3.49\left(\frac{1-H_D}{R_f}\right),\ X_0 = \frac{0.2}{R_f}, \tag{2.4}$$

where R_α, R_β, R_f are, respectively, the diameters of the two daughter branches and the feeding vessel, and H_D is the discharge haematocrit of the feeding vessel. Note the introduction of the subscript α in the first equation to denote that this is the form used to calculate FQ_E in daughter vessel α. The calculation for vessel β requires reciprocation of the R_α and R_β values, that is $A_\alpha = -A_\beta$.

The above equations adequately describe situations where a parent vessel splits into two daughter vessels, but angiogenic vascular plexuses, particularly prior to capillary pruning and maturation, may not be so hierarchical. Consequently, this phase separation formulation must be extended to include non-uniform combinations of vessel connectivity, flow direction, vessel radii, and feeding vessel haematocrit. A generalisation that is more widely applicable to heterogeneous vascular architectures, yet also maintains the key characteristics of the hierarchical model, is proposed here. Such a generalisation can be achieved through modification of the parameters in Equation 2.4, *viz*:

$$B = 1 + 3.49\left(\frac{1-\langle H_{D_{in}}\rangle}{\langle R_{in}\rangle}\right),\ X_0 = \frac{0.2}{\langle R_{in}\rangle}, \tag{2.5}$$

where $\langle H_{Din}\rangle$ is now the *average* discharge haematocrit over *all* feeding vessels (i.e. nodal supply), and $\langle R_{in}\rangle$ is the corresponding *average* feeding vessel diameter. Under the assumption of *n* daughter vessels we also have:

$$A_i = \frac{-3.48\ln\left(\frac{R_i}{\langle R_{out}\rangle_i}\right)}{\langle R_{in}\rangle}, \text{ with } \langle R_{out}\rangle_i = \frac{\left(\sum_{j=1}^{n} R_j\right)-R_i}{n-1}, \tag{2.6}$$

where A_i must be calculated for *each* daughter vessel downstream of the nodal supply. Using these new parameters along with the appropriate FQ_B values, Equation 2.3 can then be applied to determine FQ_E for each daughter vessel. It should be noted that, unlike the original parameterisation, the FQ_E values obtained are not guaranteed to sum to unity. Therefore, where necessary, these values must subsequently be normalised to determine the ultimate FQ_E values at each bifurcation. As will be seen, inclusion of this generalised phase separation mechanism in the blood flow simulation is found to have profound consequences for vascular development, haematocrit transport and oxygen delivery.

2.5.3. Structural Adaptation and Shunt Prevention

As discussed in Section 2.2, a consequence of phase separation in microvascular networks is the sizeable proportion of RBCs following major flow pathways (Pries et al., 1992). Depending upon the topology of the network, this may prove highly disadvantageous with respect to oxygen delivery to the tissue since small terminal vessels may receive little or no haematocrit. In healthy tissue, however, angioadaptation tends towards the prevention of large shear stresses, and so high flow shunts are relatively uncommon. Using data obtained from six rat mesenteric networks, Pries et al. (2001) have conjectured the existence of four main stimuli that contribute to the regulation of vessel radii in the microvasculature. Two of these, the so-called "conducted" and "convected" stimuli, contribute to the prevention of shunt formation by favouring the vasodilatation of segments that are part of long flow pathways. Many previous mathematical models (McDougall et al., 2002; Alarcon et al., 2006; Stephanou et al., 2005; Stephanou et al., 2006; McDougall et al., 2006b; Macklin et al., 2009; Owen et al., 2009; Alarcon et al., 2003; Perfahl et al., 2011) have neglected these stimuli and instead applied a stimulus relying solely on *local* flow conditions without reference to the position of a vessel within a connected vascular bed (Pries et al., 1998). As seen in Figure 2.1, in the absence of the conducted and convected stimuli, models predict the formation of dilated, inefficient shunt pathways. We firstly outline the rationale of the previous model, before describing the extended model incorporating the shunt-preventing stimuli.

The stimuli employed previously include the effects of wall shear stress S_{wss}, intravascular pressure S_p and a metabolic mechanism based on the local RBC volume flow rate S_{met} (Pries et al., 1998). The model assumes that the radial perturbation ΔR in a flowing vessel over a time step Δt is proportional to both the total stimulus acting on the vessel S_{tot} and to its radius prior to stimulation R, *viz*:

$$\begin{aligned}\Delta R &= S_{tot} R \Delta t,\\ &= \left[S_{wss} + k_p S_p + k_{met} S_{met} - k_s\right] R\Delta t,\\ &= \left[\log\left(\tau_w + \tau_{ref}\right) - k_p log \tau_e(P) + k_{met}\log\left(\left(\frac{Q_{met}}{Q \cdot H_D}\right) + 1\right) - k_s\right] R\Delta t.\end{aligned} \tag{2.7}$$

This equation shows that the vessel radius increases with increasing wall shear stress τ_w calculated from:

$$\tau_w = \frac{4\mu_{app}}{\pi R^3} \cdot |Q|, \tag{2.8}$$

while τ_{ref} is a small constant included to avoid singular behaviour at low shear rates. It is further assumed that vessel radii adapt in order to maintain a pre-set relationship between wall shear stress and intravascular pressure P (taken here to be the average of the nodal pressures at either end of each capillary segment). Therefore the pressure response is based on the expected level of wall shear stress τ_e, defined by:

$$\tau_e(P) = 100 - 86e^{-5000\cdot[\log(\log(P))]^{5.4}}. \tag{2.9}$$

In addition, Q_{met} defines a typical reference flow value, whilst k_p and k_{met} characterise the relative intensity of the pressure and metabolic stimuli, respectively. Finally, the parameter k_s represents the natural shrinking tendency of a vessel: proposed to reflect the requirement for positive growth stimuli in the maintenance of cell mass and vessel diameter (Pries et al., 1998).

As previously mentioned, the updated model introduces two shunt-preventing stimuli to replace the local metabolic stimulus in the above formulation (Pries et al., 2001). The first of these, the *convected* stimulus, is assumed to act by the addition of a metabolite to the blood at a rate that depends on the partial pressure of oxygen PO_2 in each segment. Thus, Pries et al. (2001) proposed that the convective flux of metabolite J_m increases as blood perfuses downstream and that the contribution from each vessel segment of length L_s can be calculated according to:

$$J_m^{down} = J_m^{up} + L_s\left(1 - \frac{PO_2}{PO_{2,ref}}\right), \tag{2.10}$$

whenever the intravascular PO_2 falls below the reference level $PO_{2,ref}$. Here, J_m^{down} refers to the flux of metabolite leaving a vessel segment and J_m^{up} corresponds to its upstream feeder flux. In our model, we approximate the intravascular PO_2 level by considering the volume flow of red blood cells QH_D in each segment. Hence, Equation 2.10 becomes:

$$J_m^{down} = J_m^{up} + L_s\left(1 - \frac{Q\cdot H_D}{(QH_D)_{ref}}\right), \tag{2.11}$$

where $(QH_D)_{ref}$ is a reference value for erythrocyte volume flow. Furthermore, we assume that the flowing metabolite splits in a flow-weighted fashion at diverging bifurcations.

This procedure can be used to determine a unique value for J_m in each flowing vessel segment. In general, this can be achieved by evaluating the convective flux at the segment mid-point by using the equation $J_m = (J_m^{down} + J_m^{up}) / 2$ (Pries et al., 2001); however, since the *in silico* vasculatures that we consider are comprised of many short capillary elements of broadly similar length, we simply choose $J_m = J_m^{down}$. Thus, the total convected metabolic stimulus S_m for local radial perturbation is calculated by the equation:

$$S_m = \log\left[1 + \frac{J_m}{(Q + Q_{ref})}\right], \tag{2.12}$$

where Q_{ref} is a small reference flow value included to prevent singular behaviour in segments with low flows.

Complementary to this we also include the *conducted* stimulus that is assumed to act via cell-cell communication by changes in electrical potential through gap junctions between smooth muscle and endothelial cells (Pries et al., 2001; Pries et al., 2010). Algorithmically, this response is assumed to arise in each vessel segment in proportion to the convection-derived S_m value in that segment. Specifically, the conducted response is passed upstream, against the flow, undergoing exponential decay, and the contribution from each vessel segment of length L_s is calculated according to:

$$J_c^{up} = (J_c^{down} + S_m) \cdot exp\left[-\frac{L_s}{L_c}\right], \tag{2.13}$$

where L_c is the decay length constant. Here, J_c^{up} and J_c^{down} refer, respectively, to the conducted signal strengths at the upstream and downstream ends of the vessel. In addition, the conducted signal is assumed to be split in equal proportions at diverging bifurcations.

Analogous to the case for the convected stimulus outlined above, we also determine a unique value J_c for each segment to represent the particular conducted signal strength in that vessel. Once again, rather than choosing to evaluate at the segment mid-point, we simply assume $J_c = J_c^{up}$. The total conducted metabolic stimulus S_c in each segment is then governed by the saturable response:

$$S_c = \frac{J_c}{J_c + J_0}, \tag{2.14}$$

where J_0 is the saturation constant.

Combining these shunt-preventing stimuli with the earlier wall shear stress and pressure responses, the final updated algorithm for the radius change ΔR of a vessel of radius R over a time-step Δt takes the form (Pries et al., 2001):

$$\begin{aligned} \Delta R &= S_{tot} R \Delta t, \\ &= \left[S_{wss} + k_p S_p + k_m [S_m + k_c S_c] - k_s\right] R \Delta t, \end{aligned} \tag{2.15}$$

where the parameters k_m and k_c are introduced to characterise the relative intensity of the shunt-preventing stimuli. It will be seen in due course that the inclusion of these conducted and convected stimuli in the perfusion model, as well as the introduction of phase separation, has a profound effect on the evolution of the various vasculatures that we consider.

2.6. Results

2.6.1. Phase Separation at Complex Vessel Junctions

In the summary of the blood flow simulation model, we noted that it was necessary to generalise the method of phase separation at bifurcations in order to be capable of handling non-uniform combinations of vessel connectivity and flow direction. In 2D modelling of tortuous angiogenic vasculatures prior to capillary pruning, for example, we may encounter scenarios where up to four vessel segments are associated with a single node. Consequently, the scenarios of particular interest are those where two vessels flow into the node and two vessels flow out or, alternatively, one vessel flows into the node and three vessels flow out.

In the former scenario, the situation is equivalent to the original model for simple bifurcations with the *average* feeding vessel radius and haematocrit now used to determine the downstream behaviour. An example of this scenario is presented in Figure 2.3a, where the fractional erythrocyte flow FQ_E is plotted against the fractional blood flow FQ_B in each daughter vessel for a particular combination of feeding vessel

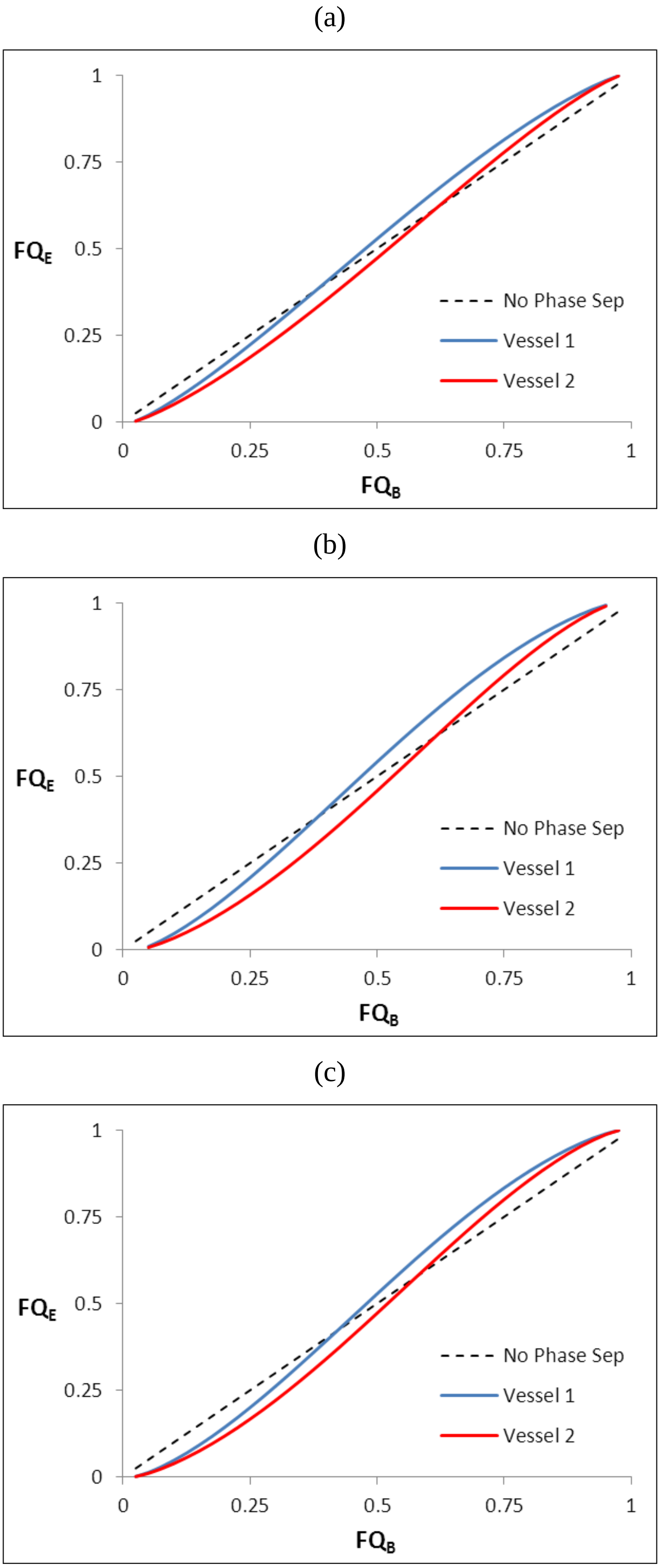

Figure 2.3: Caption overleaf.

Figure 2.3: Plots of the phase separation effect at a junction where two parent vessels feed two daughter vessels, showing the fractional erythrocyte flow (FQ_E) versus the fractional blood flow (FQ_B) in each daughter branch, as governed by Equations 2.3, 2.5 and 2.6. The daughter vessel radii are fixed at 5µm (blue line) and 7µm (red line). Plot (a) utilises parent vessels of radius 12µm and 9µm with haematocrits of 0.45, whilst plots (b) and (c) show the impact of reducing either the parent vessel radii (8µm and 6µm) or haematocrits (both 0.1), respectively. In the absence of phase separation, all data would lie on the line of identity (dashed black line).

radii, daughter vessel radii and inlet haematocrits (see the caption for specific details of values used). The linear dotted line indicates where both of these plots would lie in the absence of phase separation (i.e. $FQ_E \equiv FQ_B$). The additional graphs indicate that the phase separation effect is accentuated with decreasing size of the feeding vessels (Figure 2.3b vs. Figure 2.3a) and decreasing inlet haematocrit (Figure 2.3c vs. Figure 2.3a), as has been observed experimentally (Schmid-Schoenbein et al., 1980; Fenton et al., 1985; Pries et al., 1989; Carr and Wickham, 1991; Enden and Popel, 1994).

The case where one feeding vessel splits into three daughter vessels is much more complex, and also troublesome to represent graphically. In order to examine the phase separation dynamics predicted by the generalised model, we fix the value of FQ_B in one of the daughter branches (i.e. FQ_{B1}) and allow the other two (i.e. FQ_{B2} and FQ_{B3}) to vary over all other possible values, subject to the mass conservation constraint $FQ_{B1} + FQ_{B2} + FQ_{B3} = 1$ (i.e. for any $FQ_{B2} \in [0, 1 - FQ_{B1}]$ we have $FQ_{B3} = 1 - FQ_{B1} - FQ_{B2}$). For a particular combination of vessel radii and inlet haematocrit values (full details in the caption), Figures 2.4a and 2.4d plot FQ_E for each daughter vessel (i.e. FQ_{E1}, FQ_{E2} and FQ_{E3}, respectively) against FQ_{B2} with fixed values $FQ_{B1} = 0.3$ and $FQ_{B1} = 0.6$, respectively. Again, the linear dotted lines indicate where each plot would lie in the absence of phase separation (i.e. $FQ_{E1} \equiv FQ_{B1}$, $FQ_{E2} \equiv FQ_{B2}$ and $FQ_{E3} \equiv FQ_{B3}$). Due to the specific nature of the radii values used, it is difficult to provide a precise quantitative assessment of the results; however, it is interesting to note that, even though FQ_{B1} is fixed, the value of FQ_{E1} varies depending on the distribution of flow in the two other daughter branches. As in the above case, we also examine the impact of decreasing the feeding vessel radius (Figure 2.4b vs. Figure 2.4a and Figure 2.4e vs. Figure 2.4d) and

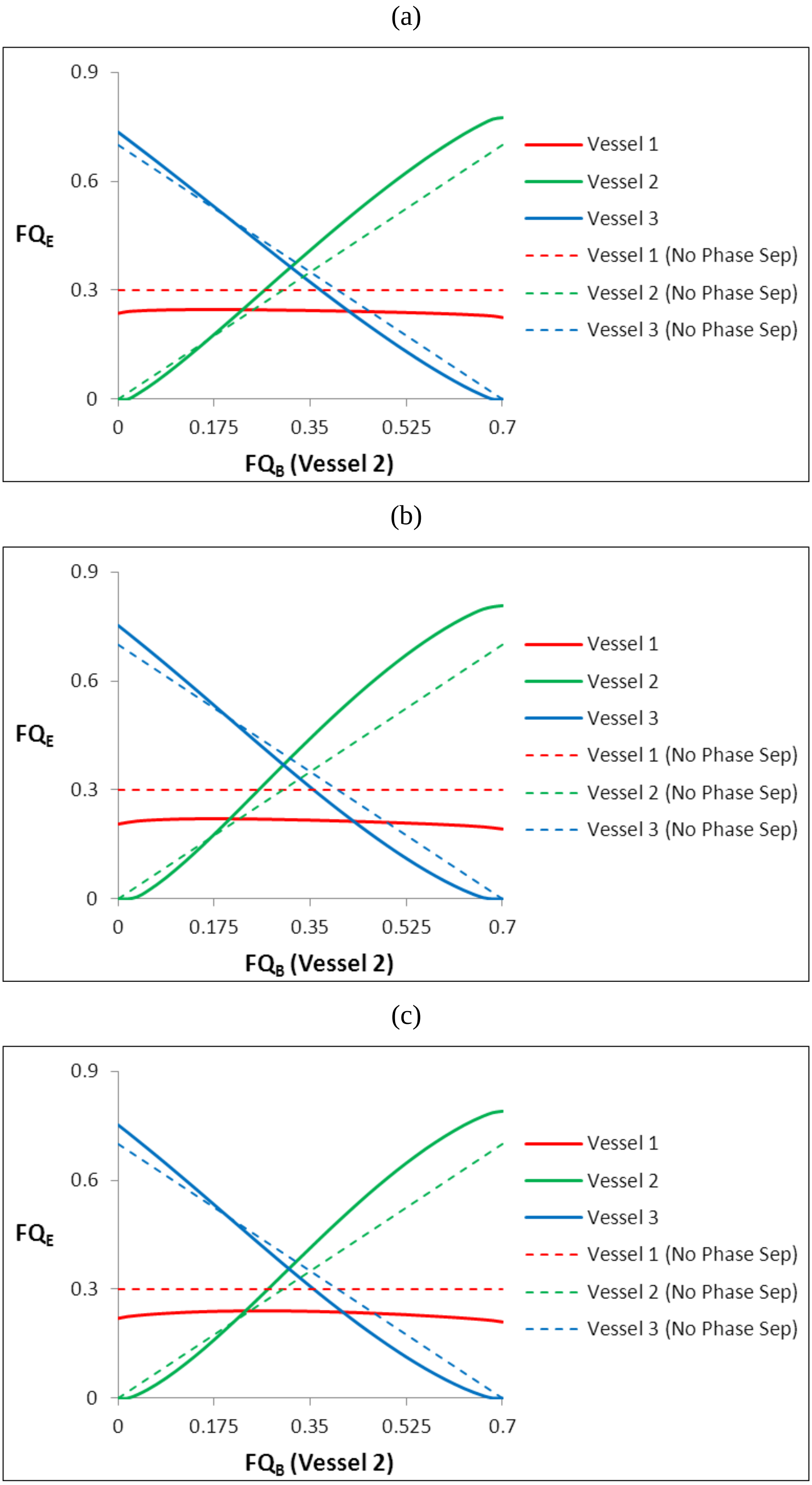

Figure 2.4: Caption overleaf.

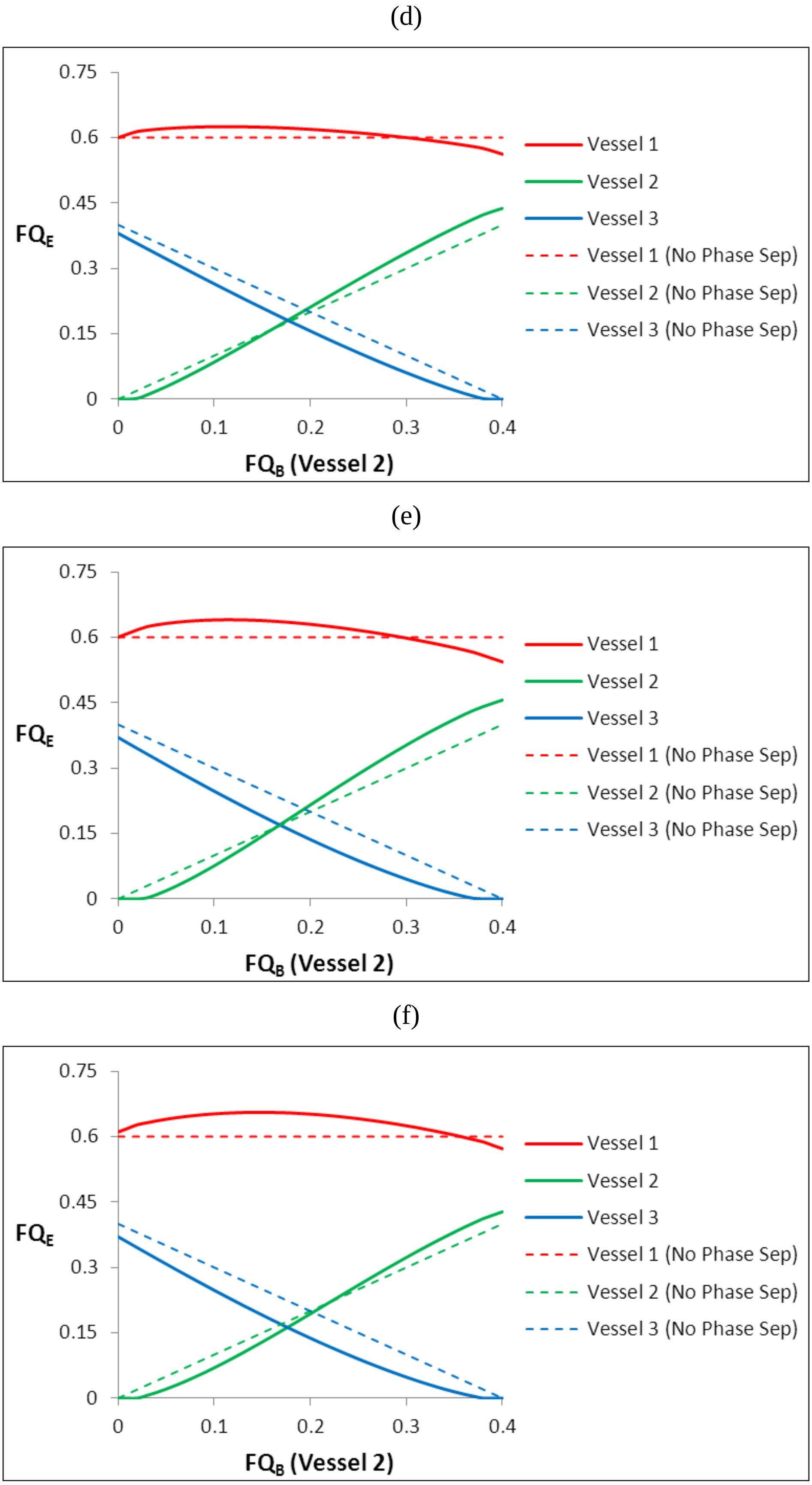

Figure 2.4: Caption overleaf.

Figure 2.4: Plots of the normalised phase separation effect at a junction where one parent vessel feeds three daughter vessels, as governed by Equations 2.3, 2.5 and 2.6. The fractional erythrocyte flow in each daughter branch (FQ_{E1}, FQ_{E2} and FQ_{E3}, respectively) is plotted against all possible values of the fractional blood flow in vessel 2 (FQ_{B2}), subject to the value of the fractional blood flow in vessel 1 (FQ_{B1}) being fixed at either (a-c) 0.3 or (d-f) 0.6. Note that these assumptions impose a condition on the fractional blood flow in vessel 3, i.e. $FQ_{B3} = 1 - FQ_{B2} - FQ_{B1}$. The daughter vessel radii are fixed throughout at 7.5μm (vessel 1, red line), 5μm (vessel 2, blue line) and 2.5μm (vessel 3, green line). Plots (a, d) have a parent vessel of radius 12μm with haematocrit of 0.45, whilst plots (c, e) and (d, f) show the impact of reducing the parent vessel radius (8μm) or haematocrit (0.1), respectively. In the absence of phase separation, all data would lie on the dashed lines.

the feeding haematocrit (Figure 2.4c vs. Figure 2.4a and Figure 2.4f vs. Figure 2.4d) – noting that each of these changes again accentuates the phase separation effect. Given the lack of experimental evidence on the phase separation behaviour at such complex vessel junctions, it is satisfactory to confirm that the generalised model conserves the key qualitative features that have been observed experimentally in simple bifurcations.

2.6.2. Phase Separation in a Simple Network

Having confirmed the behaviour of the phase separation model at various isolated vessel junctions, we now proceed to examine the impact of repeated occurrences within a vascular network. Pozrikidis (2009) recently developed a model to numerically simulate *separate* plasma and red blood cell dynamics in tree-like branching microvascular capillary networks. This study examined the implications of phase separation and the Fahraeus effect on cell residence times and the dispersion of haematocrit throughout the network. Although our continuum representation of flowing blood lacks this level of detail, using a similar branching network we can generate our own prediction of haematocrit distribution. The results are presented in Figure 2.5, where we employed a simple, sequentially branching, static (i.e. no angioadaptation) vessel network with a physically realistic input haematocrit of 0.45 (Figure 2.5a). The network features six “generations” of vessels, where the radius of each individual

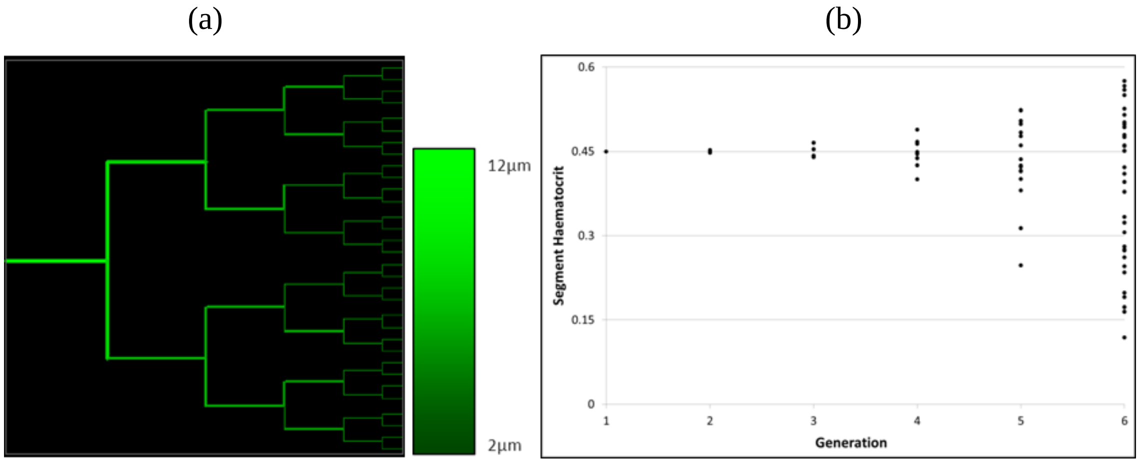

Figure 2.5: Numerical simulation showing the effect of phase separation on segment haematocrits in a flowing static vessel network with sequential bifurcations. The network employed, shown in (a), was generated by randomly selecting segment radii from pre-defined intervals. Defining segments from left to right by increasing "generation" (G), the following intervals were defined: G1 = 12.0-9.5μm; G2 = 10.5-8.0μm; G3 = 9.0-6.5μm; G4 = 7.5-5.0μm; G5 = 6.0-3.5μm; G6 = 4.5-2.0μm. Graph (b) plots the haematocrit in each segment against its generation; the input haematocrit was 0.45, and the range of segment haematocrits is seen to increase with increasing generation.

segment was chosen randomly from pre-defined intervals of equal size whose maximum value decreases with increasing generation (see the figure caption for specific values). From Figure 2.5b we observe that at steady-state the variation in segment haematocrit values increases with increasing generation, resulting in a wide distribution (~ 0.1 - 0.6) within the outlet segments. We can mainly attribute this behaviour to the radii distribution, with the flow, and therefore the haematocrit, favouring the least resistive pathways through the network.

Recall that our perfusion model is designed to represent blood as a continuum, without explicit separation into its constituent parts. Consequently, the results presented here are strongly encouraging; this simplifying assumption affords a huge computational saving, and the model still predicts significant heterogeneity in the distribution of haematocrit throughout the network.

2.6.3. Shunt-Prevention in a Simple Network

The other major advance made in the blood flow simulation model is the rigorous inclusion of the previously neglected conducted and convected stimuli in the angioadaptation algorithm. These two important stimuli are assumed to act in a manner that allows the transfer of metabolic information both upstream and downstream through vascular networks. As a result of this modification we could thereby expect our simulated vessel networks to evolve more realistic radii distributions with, in particular, an absence of dilated capillary shunts. This is confirmed by the comparison made in Figure 2.6, where we use a hypothetical looping network with topology reminiscent of an arterial-venous “petal” as found in the retinal vasculature. The network is initially uniform with all vessel segments of radius 4 µm, but is subsequently remodelled via flow-induced stimuli by either Equation 2.7 with a local metabolic response, or Equation 2.15 with the conducted and convected metabolic responses. Phase separation was also used in each of the simulations. The resultant steady-state network in Figure 2.6a was achieved using the same remodelling parameters as in Figure 2.1 (see figure caption for specific values) and we note the effective shunt that has been produced. The constricted vessels in the lower loop remain significantly smaller than all those above and, as such, will carry a significantly reduced flow. The haematocrit distribution in Figure 2.6c confirms this - the vessel segments are seen to be completely devoid of RBCs due to plasma skimming. Clearly, if this network were to appear *in vivo*, the distribution of radii would prove to be inefficient in the supply of oxygen and nutrient, with the lower tissue regions reliant on diffusion from the distal dilated vasculature. The corresponding radii and haematocrit distributions obtained by applying the shunt-preventing stimuli are shown in Figures 2.6b and 2.6d, respectively (see figure caption for parameter values). We now observe a significantly more robust response, with the network displaying a wide variety of vessel radii and, crucially, a conspicuous absence of shunting. Extensively dilated vessels are now far less numerous, and those that do exist are either supplying or draining a large number of other segments. The haematocrit distribution confirms that all flow pathways, including the lower loop, contain a significant haematocrit and therefore a significant flow. In contrast to the earlier situation, it seems that this scenario is much more physically realistic, with all surrounding tissue potentially having a proximal oxygen and nutrient filled source.

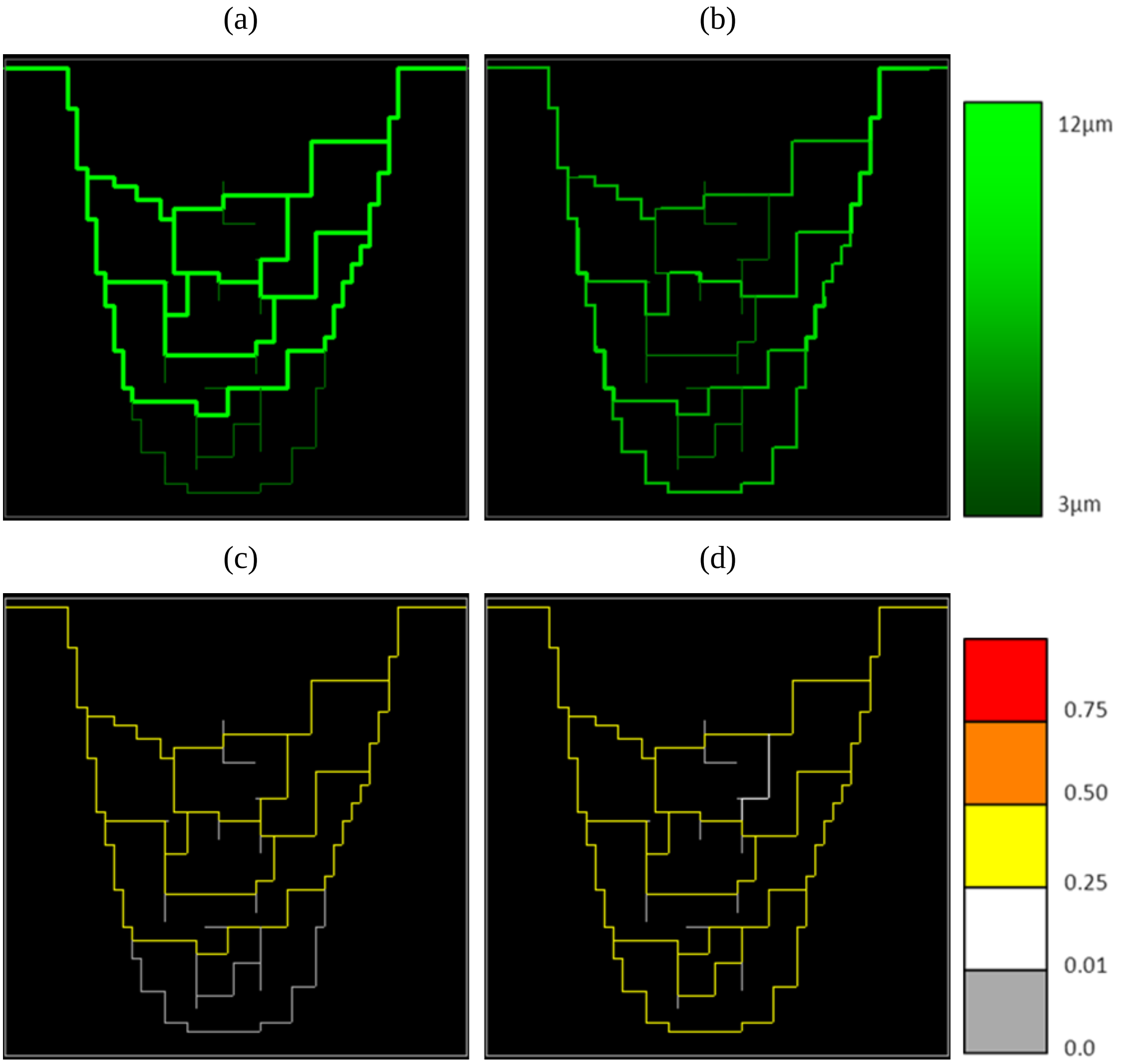

Figure 2.6: Comparison of the steady-state radii and haematocrit distributions produced by previous (Equation 2.7) and updated (Equation 2.15) radii adaptation algorithms upon flow simulation in an idealised vessel network. Snapshot (a) shows the radii distribution produced under the previous methodology (parameters: k_s = 0.35, k_p = 0.1, k_{met} = 0.07, τ_{ref} = 0.103 dyn · cm^{-2}, Q_{metab} = 1.9096 × 10^{-11} m^3 · s^{-1}), whilst (b) shows the equivalent result produced by the new methodology (parameters: k_s = 1.7, k_p = 0.8, k_m = 0.5, k_c = 2.8, J_0 = 250, τ_{ref} = 0.5 dyn · cm^{-2}, Q_{ref} = 1.0 × 10^{-18} m^3 · s^{-1}, $(QH_D)_{ref}$ = 6.75 × 10^{-14} m^3 · s^{-1}, L_c = 7.0 × 10^{-3} m). The corresponding haematocrit distributions are shown in (c) and (d), respectively. Phase separation was used in both simulations.

2.7. Discussion

A flowing vasculature is critical to living organisms since it provides an efficient means of oxygen and nutrient delivery throughout the body. In development, tissue repair and various pathological scenarios, such vasculatures are formed by the process of angiogenesis when ECs from existing vessels are induced to migrate in response to growth factors secreted by cells deprived of these crucial metabolites (Risau, 1997). The subsequent extent and distribution of oxygen delivery from the generated neo-vasculature depends on a variety of factors, including the ultimate architecture of the vessel network and the flow properties of the blood within it. The system is inherently complex, however, since these factors are determined by a variety of inter-connected biophysical phenomena such as angioadaptation, non-Newtonian effects and phase separation at microvascular bifurcations. Many previous perfusion models have neglected to consider some aspects of these phenomena that contribute to the evolution of vessel networks (c.f. Figure 2.1). In this chapter we have shown that the inclusion of both phase separation and shunt-preventing angioadaptation stimuli are vital to the *in silico* generation of non-pathological capillary architectures that exhibit realistic distributions of vessel radii and haematocrit.

In general, phase separation is the term used to describe the non-uniform distribution of plasma and erythrocytes at vascular bifurcations. The most extreme instance of this phenomenon is the occurrence of plasma skimming whereby small capillary side-branches may even be completely starved of RBCs. An empirical relationship describing these features at a solitary bifurcation was derived by Pries et al. (1989b), and a generalisation has been proposed here to handle the dynamics of phase separation at vessel junctions comprising irregular combinations of vessel connectivity and flow direction. At junctions comprising two feeder and two daughter vessels, or one feeder and three daughter vessels, the generalised model was, importantly, found to conserve the main features of the original model. A significant consequence of phase separation *in vivo* is that its repeated occurrence at a series of junctions can have important implications for the overall haematocrit distribution within a network. In order to investigate the ability of the model to reproduce such behaviour, we created an idealised branching network, where the radius of each vessel segment decreased with increasing generation. Although the blood is modelled as a continuum with averaged bulk properties, we found significant heterogeneity in the haematocrit distribution, with greatest variation in the terminal vessels.

Angioadaptation, the structural remodelling of blood vessels, is driven by the contraction or relaxation of vascular smooth muscle cells. Through investigation of rat mesenteric networks, Pries et al. (2001) have developed another empirical model in which vessel radii regulation is predicted to be governed by four distinct flow-induced responses – namely wall shear stress, intravascular pressure and two metabolic stimuli that act to prevent shunt formation. These so-called “conducted” and “convected” stimuli transfer information upstream and downstream, respectively, favouring the vasodilatation of vessels that feed and/or drain extensive networks. The conducted stimulus is assumed to act via cell-cell communication in the vessel walls, while the convected stimulus acts by metabolite addition to the blood (Pries et al., 2001; Pries et al., 2010). A number of previous mathematical models of blood flow and angioadaptation have neglected these two stimuli (McDougall et al., 2002; Alarcon et al., 2006; Stephanou et al., 2005; Stephanou et al., 2006; McDougall et al., 2006b; Macklin et al., 2009; Owen et al., 2009; Alarcon et al., 2003; Perfahl et al., 2011), applying instead a simple local metabolic response (Pries et al., 1998). Using a typical network of interconnected loops, the results presented here (c.f. Figure 2.6) clearly demonstrate the disparity in the steady-state vasculatures generated by replacing the local stimulus by the conducted and convected stimuli. The updated model results in a diversity of vessel radii, haematocrit perfusion within all segments and, most importantly, no dilated shunt pathways. From the standpoint of efficient oxygen delivery to surrounding tissues, these highly desirable features were in stark contrast to those seen using the simple local response.

From the biological details discussed throughout this chapter, accurate modelling of the various interactions between blood flow and angioadaptation *in vivo* could involve an almost arbitrary level of complexity. Indeed, when summarising one publication, Pries et al. (2005) state that “the model used... may seem overly complicated” but admit that “the complexity... seems to reflect the inherent complexity of the biological system it represents”. However, although the modifications made to the earlier perfusion model significantly increase computational complexity, the results obtained here – from a variety of simple scenarios – suggest that such changes are required for the model to reproduce the evolution of non-pathological vasculatures observed *in vivo*. This statement will be tested to the full in the coming chapters, as all of the features of the microvasculature discussed here will be combined to investigate selected scenarios of vessel network formation.

Chapter 3

Modelling Wound Healing Angiogenesis

3.1. Introduction

The first model of vessel network formation we present investigates the dynamics of wound healing angiogenesis in the specific context of a thermally-induced injury to the *panniculus carnosus* (*pc*) muscle of a mouse. Such an injury ablates the pre-existing vasculature within the wounded region. Throughout this study the model development was strongly coupled to an *in vivo* experimental programme investigating various aspects of the microvascular re-growth. The *pc*, a thin (30 – 50 μm wide) skeletal muscle layer on the dorsum of the mouse, is supplied by an isotropic and effectively 2D regular microvascular network. Wounds induced in this muscle layer heal in a centripetal fashion (Guerreiro-Lucas et al., 2008), and a gradual reorganisation of the microvascular architecture aims to ensure the re-establishment of the metabolic requirements of the regenerating tissue.

Numerous *in vivo* laboratory models of wound healing exist, measuring specific end points such as closure, vascular density and tensile strength (reviewed by Gurtner et al., (2008)). Laboratory models that collect longitudinal data from the same animal over time, however, are limited (Bluff et al., 2006; Ichioka et al., 1997). The model applied here involves the use of a dorsal skin-fold window chamber (DSWC; see Figure 3.1) such that the functional vasculature in the wounded region can be visualised in a single animal throughout the healing process. As such, various parameters can be quantified both temporally and spatially within a single lesion. The nature of this data (and the effective 2D vascular network structure) suggests that the *in vivo* experimental system is ideal for a mathematical bench-marking study.

Prior to describing the experimental system and the mathematical model in detail, we will first outline the basic structure of the skin and its underlying constituents, before providing some key biology of the healing process. In due course, a variety of results from the mathematical model will be presented for healing under normal conditions. Finally, by introducing an anti-angiogenic treatment into the experimental system, the robustness and predictive capability of the mathematical model is assessed.

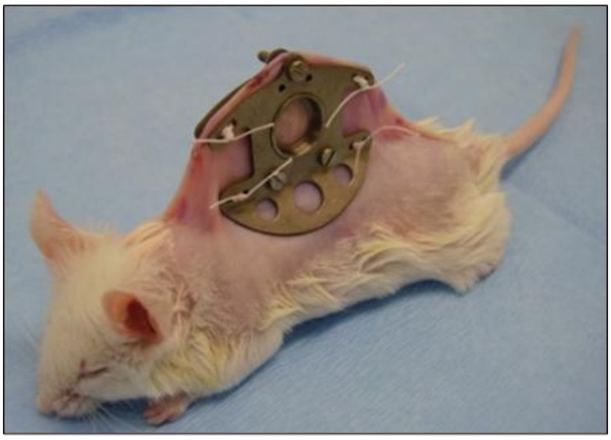

Figure 3.1: Image showing the rationale of the dorsal skinfold window chamber (DSWC) wound healing assay. The window chamber is implanted on the dorsum of the mouse, thus isolating a region of tissue for wounding and subsequent visualisation of the re-generating vasculature.

3.2. Anatomy of the Skin

Mammalian skin can loosely be described as comprising two distinct layers: the dermis and the epidermis. The thin outer epidermis, only a few cell layers thick, is avascular and dominated by continually renewing keratinocyte cells, which provide a first line of defence against pathogen invasion. The more acellular dermis, composed largely of connective tissue, is separated from the epidermis by a thin layer of fibres known as the basement membrane. Some cells do exist in the dermis, however, including fibroblasts and the endothelial cells that comprise the dermal vasculature. Diffusion of nutrient from these vessels serves the metabolic requirements of both the dermis and the epidermis. Beneath the dermis lies the hypodermis, or subcutaneous tissue, the role of which is to provide attachment to the underlying bone and, of particular pertinence here, muscle layers including the *pc*. A simple diagram depicting the layered structure of the skin is presented in Figure 3.2.

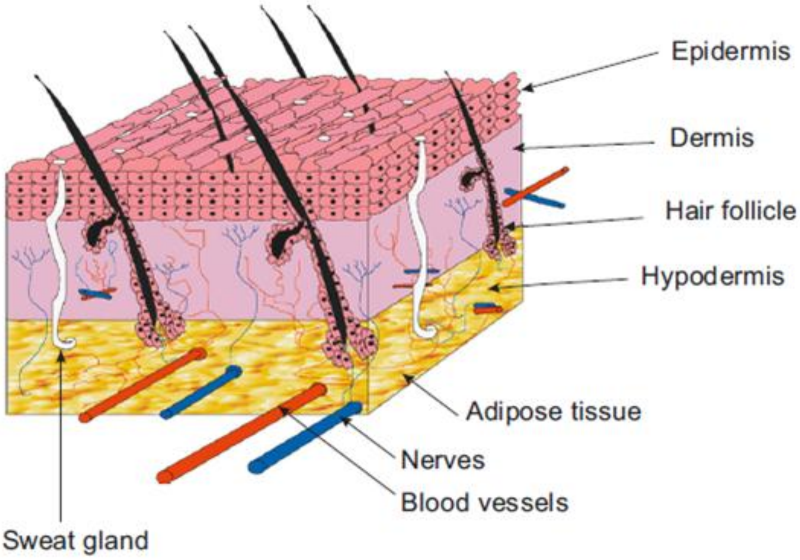

Figure 3.2: Schematic diagram illustrating the composition of mammalian skin. Image taken from Metcalfe et al. (2007).

3.3. Biology of Wound Healing

Wound healing is an essential and innate response to injury. Due to the inherent fineness of the epidermal layer, the majority of wounding events will cause some degree of damage to the underlying tissue. In such cases the healing process can be characterised by a sequence of overlapping events. Immediately post-wounding, bleeding from broken blood vessels results in the formation of a fibrin blood clot that temporarily closes the wounded region: a process known as haemostasis (Jennings and Hunt, 1991). This process is succeeded by three further phases which can loosely be termed inflammation, proliferation and repair (Clark, 1996). Figure 3.3 depicts a typical time course of dermal wound healing, summarising the key events in each phase and emphasising their overlapping nature.

The inflammatory stage sees the beginning of the influx of a number of cell types into the wound site, encouraged initially by the release of platelet-derived growth factor (PDGF) from platelets in the blood clot (Haugh, 2006). Dilation and increased

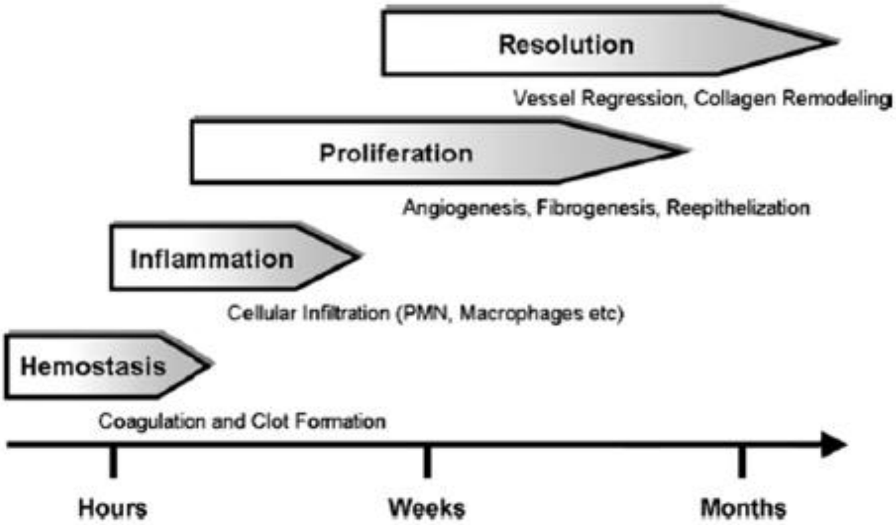

Figure 3.3: Schematic plot of the temporal sequence of events that characterise dermal wound healing. Image taken from Schwacha (2009).

permeability of the local vasculature allows monocytes (a type of white blood cell) to extravasate from vessels and, in response to the chemical stimulus, differentiate into macrophages (Singer and Clark, 1999; Sherratt and Dallon, 2002). Different types of macrophages, performing different roles, are known to be expressed during the healing process (Riches, 1996). Importantly, however, macrophages act to remove bacteria from the wound site and also secrete chemical stimuli such as transforming growth factor-beta (TGF-β) and additional PDGF (Singer and Clark, 1999; Robson et al., 2001).

These growth factors allow the commencement of the proliferative phase by attracting fibroblasts and triggering an angiogenic response to recruit ECs to the wound site (Pettet et al., 1995; Clark, 1996). Fibroblasts migrate towards the wound site from the surrounding tissue using the fibrin clot as a scaffold. Over a period of many months, during the final repair phase, this scaffold is gradually replaced by fibroblast-derived collagen fibres (Arnold and West, 1991). The new tissue is likely to differ in collagen composition and orientation from the pre-existing tissue and this is the basis of scar formation (Ehrlich and Krummel, 1996). Under the influence of chemical stimulus and mechanical stress, fibroblasts may also perform differentiation to become myofibroblasts (Wipf and Hinz, 2008; Wipf and Hinz, 2009). This fibroblast phenotype is primarily involved in wound closure by exerting a traction force around the wound edges (Grinnell, 1994). In conjunction with collagen fibre deposition and wound contraction in the dermis, the epidermal surface also undergoes a procedure of closure and regeneration. Although normal epidermal cells generally display an immotile, quiescent phenotype, it is known that this aspect of healing is driven by the migration and proliferation of epidermal cells in the periphery of the wounded region. The precise behaviour and mechanisms of these cellular processes are not fully understood but they are believed to be initiated by a combination of reduced contact inhibition and increased presence of growth factors near the wound edge (Clark, 1996).

Another key component of the tissue repair system is wound healing angiogenesis, which allows for the rapid re-establishment of a functional vasculature. This is critical since, not only is oxygen delivery inherently diminished by wounding, but oxygen demand is also increased beyond normal levels to drive the healing process. Extreme hypoxia can result in compromised healing or even tissue loss, and is thus a critical factor in the failure of healing in chronic or diabetic wounds (Sen, 2008). As discussed previously (c.f. Section 1.3), angiogenesis leads to a vascular network which is far more dense than would be observed in undamaged tissue. Thus, during the repair phase, portions of the initial wound area will experience a reduction in vessel density (Hashimoto and Prewitt, 1987).

3.4. Wound Healing Modelling Studies

In the literature review provided in Section 1.4 we made reference to a number of theoretical studies that have investigated the wound healing process. In keeping with the key themes of this thesis, however, we mentioned only those that have either taken a discrete approach to wound-induced cell migration, or investigated the angiogenic response to injury. As detailed in the above section, wound healing is characterised by a variety of inter-connected events and, accordingly, a much wider range of approaches have been adopted to model the many different aspects of this complex process. Therefore, before proceeding to discuss our hybrid modelling approach to wound healing angiogenesis, we shall first briefly review a selection of pertinent studies.

Some of the earliest mathematical modelling performed in this field considered healing of epidermal wounds, using a relatively simple approach with respect to the more complex interactions in the regenerating dermis (Sherratt and Murray, 1990; Sherratt and Murray, 1991; Sherratt and Murray, 1992). In these models the mathematical representation utilised two simple coupled PDEs to describe the evolution of epidermal cell density and a mitosis-regulating chemical factor. An extension to this model was later proposed to examine the molecular dynamics of the cross-talk between the dermis and epidermis during epidermal wound healing (Wearing and Sherratt, 2000). Models very similar to the original approach of Sherratt and Murray have also been developed to examine epidermal healing in the cornea (Dale et al., 1994; Gaffney et al., 1997; Gaffney et al., 1999), whilst mechanical models have been proposed to investigate the process of actin-driven epidermal healing in the developing embryo (Sherratt et al., 1992; Sherratt, 1993).

As mentioned in Section 3.3, dermal wound healing commences with a phase of inflammation in which macrophages infiltrate the wound site. In diabetic wound healing the inflammation phase is known to persist; potential mechanisms and therapeutic interventions for this problem were investigated by Waugh and Sherratt (2006, 2007) by assuming that there is a competition between two different wound macrophage phenotypes. A simple mathematical analysis suggested that persistence of inflammation may exist due to a self-reinforcing imbalance between reparative and inflammatory macrophages.

Following the inflammatory phase in normal wound healing, the proliferative phase proceeds via the simultaneous processes of angiogenesis and tissue regeneration. Fibroblasts are the key cell type in the latter and, as such, a number of mathematical models have been developed to investigate their interaction with the wound microenvironment. Haugh (2006), for example, developed a multi-scale continuum PDE model of fibroblast dermal wound invasion incorporating a representation of local PDGF gradient sensing through assumed quasi-steady cell surface receptor activation. More commonly studied, however, is the deposition of collagen by infiltrating fibroblasts as modelled by Dale et al. (1996, 1997), who investigated the possible mechanisms by which the scarring apparent in adult dermal healing is found to be entirely absent in the foetal analogue. Collagen production by fibroblasts in the ECM is known to be stimulated in the presence of nitric oxide (NO), a highly reactive molecule produced naturally by certain cell types but up-regulated extensively during the wound healing process. Therefore, the possible role of NO in the development of problematic hypertrophic or keloid scars has also been investigated in a seven species ODE model that incorporates representations of both blood vessel growth and oxygen delivery (Cobbold and Sherratt, 2000). Another important factor in the development of dermal scarring is the cell-flux and tissue-stress induced alignment of the ECM fibres within, and surrounding, the wounded region. This process has been modelled in a 2D continuum fashion by assuming the ECM density in the vicinity of a virtual wound to consist of a combination of two spatially orthogonal components (Olsen et al., 1999). Indeed, this macroscopic scale model provided the starting point for the discrete cell microscopic models of fibroblast migration and fibre alignment discussed earlier in Section 1.4.1 (c.f. Dallon et al., 1999; Dallon et al., 2000; Dallon et al., 2001; McDougall et al., 2006a).

A similar family of models to those discussed above are mechanochemical approaches, which have been used to investigate the mechanical and chemical events contributing to dermal tissue contraction and wound closure. One of the earliest approaches of this type was proposed by Olsen et al. (1995), whose model incorporated a novel spatio-temporal representation of myofibroblast density that contributed to the traction force in the assumed force balance equation for tissue displacement. This type of methodology has attracted interest again in recent years (Murphy et al., 2011; Murphy et al., 2012), where the mechanisms initiating the phenotype change from fibroblasts to myofibroblasts have been investigated in a model which also implements a moving boundary to demarcate the wounded and unwounded compartments of the healing lesion. Other models that represent wound closure by a spatially and temporally evolving interface include those proposed by Vermolen et al. (2006) and Javierre et al. (2009).

One final approach to the problem of wound healing that deserves mention concerns models that specifically focus on improving therapeutic interventions. For example, Jones et al. (2004) attempted to make a quantitative assessment of the level of tissue debridement required to enhance healing rates, whilst others have examined the biomechanical stresses associated with wound suturing in order to propose optimal surgical strategies (Chaudhry et al., 1998; Lott-Crumpler and Chaudhry, 2001). Comprehensive summaries of the modelling strategies outlined above, along with many more, can be found in the review papers of Sherratt and Dallon (2002), Fusi et al. (2009) and Geris et al. (2010).

3.5. *In vivo* Wound Healing Angiogenesis Assay

The unique aspect of the experimental wound healing angiogenesis system studied here is the ability to produce both spatial and temporal data from a single lesion. A brief outline of the experimental procedure is given below, followed by a summary of the experimental data detailing its key features. The experiments described below were performed by Maria Machado and Dr Andrea Devlin under the supervision of Dr Christopher Mitchell in the School of Biomedical Sciences at the University of Ulster.

3.5.1. Experimental Set-Up and Image Analysis

Initially the dorsal skinfold window chamber (DSWC) was implanted and, after 3 days, the mouse was anaesthetised before a single 100°C, 10 second contact wound was applied directly to the exposed *pc* taking care to avoid large blood vessels and neurovascular bundles. Visualisation of perfused vessels was achieved using a confocal microscope and intravenous injection of the plasma marker FITC-conjugated dextran. This was performed prior to wounding, immediately post-wounding, and 3, 6 and 9 days post-wounding.

Analysis of the captured images allowed the quantification of 3 important experimental parameters – wound area, vessel density (μm per 10^6 μm^2) and vessel junction density (number per 10^6 μm^2). Wound area was determined directly as the area devoid of FITC-dextran perfused vessels, whereas modified “Petri-metric” stereology techniques were used to determine both vessel density and vessel junction density (Howard and Reed, 2005). At each time point, measurements were obtained at the geometric centre of the wound and at 250 μm intervals directly north, south, east and west up to a distance of 750 μm. The analysis excluded areas of poor focus and those including large arterioles, large venules or crossed neurovascular bundles. The mean ± SEM values at each interval for each time point were determined.

3.5.2. Experimental Results

A summary of pertinent experimental results is presented in Figures 3.4 and 3.5. A more detailed analysis will be considered after the mathematical model has been introduced – here we simply draw attention to a number of important features of the *in vivo* system. Figure 3.4 shows a typical example of an imaged vessel network prior to wounding, and at days 3, 6 and 9 post-wounding. The regular parallel arrangement of the capillaries in the murine *pc* muscle is confirmed by Figure 3.4a, whilst Figures 3.4b-d confirm the centripetal healing progression. The quantitative results obtained from a number of experimental realisations (at least 6 mice in each case) are given in Figure

3.5 where each individual data point is plotted to emphasise the inherent noisiness of the data. Vessel densities (Figures 3.5a, c, e) and vessel junction densities (Figures 3.5b, d, f) are plotted at various distances from the wound centre on days 3, 6 and 9 post-wounding, respectively. The wound area data is presented in Figure 3.5g, where a notable feature from a mathematical modelling viewpoint is that the injury generates a wound with highly reproducible size (1.02 ± 0.1 mm^2 at day 0). However, it is important to note that the maximal wound area occurs by day 3 (1.25 ± 0.1 mm^2) - a phenomenon attributable to the contraction of muscle fibres within the surrounding *pc*.

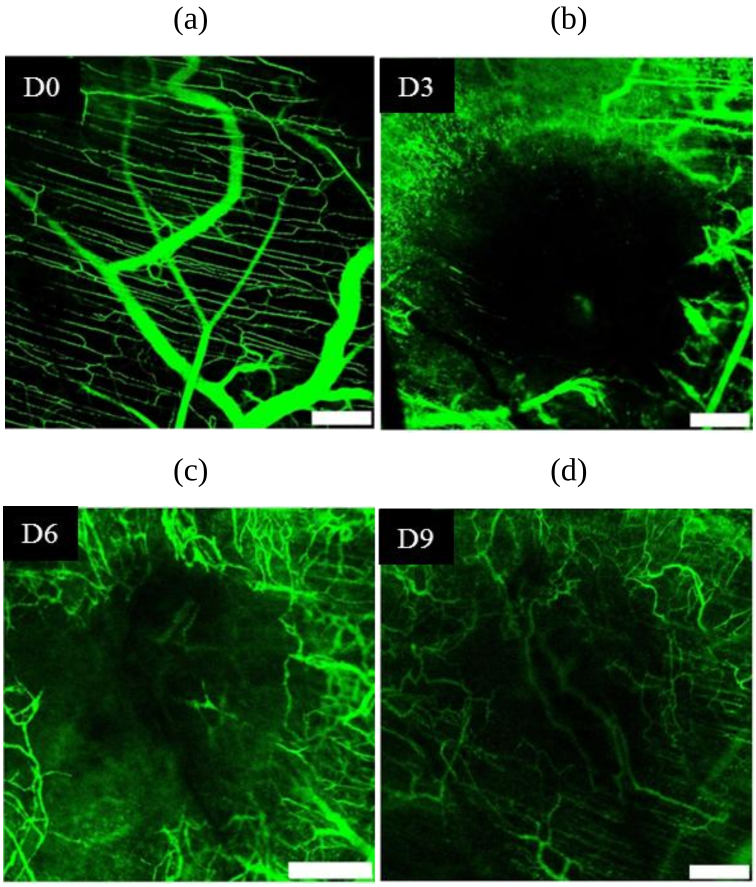

Figure 3.4: Confocal images of FITC-dextran perfused vessels in the *panniculus carnosus* muscle within the dorsal skin-fold window-chamber. Images were obtained from the same animal pre-wound (a) and at days (b) 3, (c) 6 and (d) 9 post-wounding. Scale bar = 250 μm.

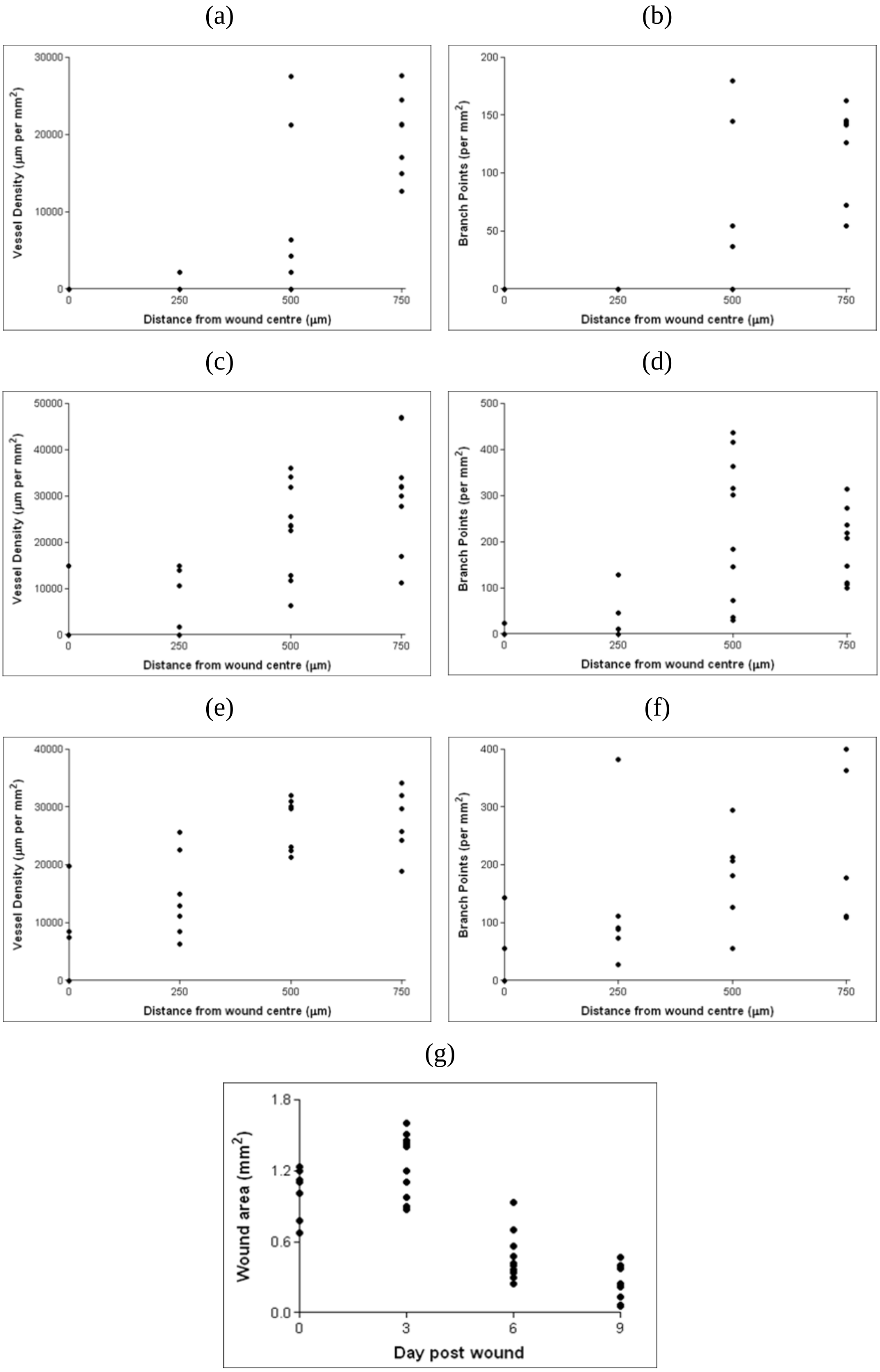

Figure 3.5: Caption overleaf.

Figure 3.5: Quantitative longitudinal data obtained from the dorsal skin-fold window-chamber assay. Plots show measurements of (a, c, e) vessel density and (b, d, f) vessel junction density on days 3, 6 and 9 post-wounding, respectively, at distances of 0, 250, 500 and 750 μm from the wound centre. Measurements of wound area on days 0, 3, 6 and 9 post-wounding are shown in plot (g). At least 7 data points are plotted in each case.

3.6. Mathematical Model of Wound Healing Angiogenesis

In recent years a number of mathematical models have been produced describing the healing of both epidermal and dermal wounds, most of which focus on a particular stage of the healing process. Here, we introduce the novel approach of explicitly growing a new vasculature via angiogenesis and intermittently passing blood through the regenerating network. Specifically, the mathematical model of angiogenesis that we employ utilises a hybrid PDE-discrete approach, first proposed by Anderson and Chaplain (1998b) but since supported by the work of various groups (McDougall et al., 2002; Anderson, 2005; Zheng et al., 2005; Wu et al., 2008; Owen et al., 2009; Pons-Salort et al., 2012). The model incorporates discrete capillary sprouting from the surviving vasculature, induced by a VEGF gradient (Gerhardt et al., 2003), and EC migration determined by random motility and sensing of local environmental cues. Sprout tip branching and fusion are included allowing the formation of anastomoses and, subsequently, simulation of blood flow in the nascent networks (McDougall et al., 2006b). The modelling assumptions are outlined below, followed by specific simulation details and a description of the *in silico* “image analysis” process. Note that additional details regarding the implementation of the angiogenesis modelling approach can be found in Appendix A.

3.6.1. Hybrid PDE-Discrete Model of Endothelial Cell Migration

Since the DSWC isolates a thin tissue region, a two-dimensional mathematical model provides an adequate representation of the *pc* microvascular network. The EC migration model assumes that the tip cells of new vessels have the ability to migrate through (i) random motility (diffusion), (ii) chemotaxis in response to VEGF released by macrophages, and (iii) haptotaxis in response to gradients in the ECM. The haptotactic response is manifested by EC production of matrix metalloproteinases

(MMPs), which diffuse and locally degrade the ECM. Although the full molecular details of this process *in vivo* are not well understood, we adopt an informed generalisation of a model previously used in the context of tumour-induced angiogenesis (Anderson et al., 2000; Levine et al., 2001b; McDougall et al., 2006b; Stephanou et al., 2006), whereby MMPs, produced by endothelial tip-cells, reduce the local concentration of matrix-bound proteins (Karagiannis and Popel, 2006; Yana et al., 2007). Denoting by n the EC density per unit area, the non-dimensional equation describing EC conservation is given by:

$$\frac{\partial n}{\partial t} = \underbrace{D\nabla^2 n}_{diffusion} - \underbrace{\nabla.\left(\frac{\chi}{1+\delta c}\cdot n\nabla c\right)}_{chemotaxis} - \underbrace{\rho\nabla.(n\nabla f)}_{haptotaxis}. \tag{3.1}$$

where the parameters D, χ and ρ quantify random motility, chemotactic sensitivity to VEGF (denoted c) and haptotactic response to gradients of ECM density (denoted f), respectively. Furthermore, the parameter δ reflects a decrease in chemotactic sensitivity with increasing VEGF concentration (Lapidus and Schiller, 1976).

The hybrid PDE-discrete system is completed by three further non-dimensional equations. Firstly, VEGF is bound by ECs at the plexus leading edge according to:

$$\frac{\partial c}{\partial t} = \underbrace{-\eta n_i c}_{\substack{tip\ cell\\ uptake}}, \tag{3.2}$$

where η represents the rate of uptake. The variable n_i is defined at each grid point on the discrete 2D lattice, and assumes a Boolean value in order to indicate the presence or absence of a tip cell at each spatial position. This is described by the equation:

$$n_i(l,m) = \begin{cases} 0, \text{ no tip cell present at } (l, m) \\ 1, \text{ tip cell present at } (l, m) \end{cases} \tag{3.3}$$

where l and m are positive parameters specifying particular nodal positions (i.e. $x = l\Delta x$ and $y = m\Delta y$). Therefore, more specifically, binding of VEGF is assumed to occur only at spatial locations where discrete endothelial tip cells are present.

Finally, we have two equations describing the interaction between tip-cell produced MMPs and the underlying ECM:

$$\frac{\partial f}{\partial t} = \underbrace{\beta n_i}_{\substack{tip\ cell \\ production}} - \underbrace{\gamma m f}_{\substack{MMP \\ degradation}} , \tag{3.4}$$

$$\frac{\partial m}{\partial t} = \underbrace{\alpha n_i}_{\substack{tip\ cell \\ production}} + \underbrace{\varepsilon \nabla^2 m}_{diffusion} - \underbrace{\nu m}_{decay} , \tag{3.5}$$

where *f* represents the ECM density and *m* the MMP concentration. The parameters α and β characterise, respectively, tip-cell production of MMPs and ECM. Meanwhile, MMP diffusion is quantified by ε, whilst MMPs degrade the ECM at a rate governed by γ and ν is the MMP decay constant.

Clearly, however, Equation 3.1 is a continuous PDE and cannot therefore be immediately used to track discrete ECs or capillary vessels. Such entities are of paramount importance here as, not only do we wish to compare our simulations with the *in vivo* experimental results, but also the extent of blood perfusion depends crucially upon the underlying architecture of the developing vascular plexus. Hence, we proceed to discretise Equation 3.1 and permit the migration of individual EC sprout tips.

Following the hybrid approach outlined in Anderson and Chaplain (1998b), we apply the Euler finite difference approximation (Mitchell and Griffiths, 1980) to Equation 3.1. The EC density at a particular spatial position can subsequently be expressed as a linear combination of the densities at positions within one grid length at the previous time-step, *viz*:

$$n_{l,m}^{q+1} = P_0 n_{l,m}^q + P_1 n_{l-1,m}^q + P_2 n_{l+1,m}^q + P_3 n_{l,m+1}^q + P_4 n_{l,m-1}^q, \tag{3.6}$$

where *l*, *m* and *q* are positive parameters specifying either the position of the cell on a 2D lattice (i.e. $x = l\Delta x$ and $y = m\Delta y$) or the current point in time (i.e. $t = q\Delta t$). The migration of an *individual* EC is then determined by the set of coefficients P_i: these coefficients are related to the likelihood of the cell remaining stationary (P_0), or moving to the left (P_1), right (P_2), up (P_3) or down (P_4). Naturally, these coefficients combine the effects of random movement and the local chemical environment (i.e. matrix-bound protein and growth factor concentration gradients). Any negatively-valued coefficients are set to zero, and the absolute value is added to the directly opposing coefficient. By then scaling such that the coefficients sum to unity, the particular migration direction of each sprout tip is determined stochastically from a set of normalised movement weightings.

3.6.2. Coupling Flow and EC Migration through Tip-Cell Branching and Anastomoses

The EC migration model outlined above is an appropriate starting point for the development of an *in silico* model of wound healing angiogenesis in the murine *pc*. However, in isolation, the inert capillary structures generated by the model are unlikely to be reliable indicators of healing efficacy. As discussed extensively in Chapter 2, oxygen delivery to the wound site depends critically upon the architecture of the developing neo-vasculature and the distribution of RBCs within it. Hence, we apply the method of blood flow simulation detailed in Section 2.5 (Equations 2.1 and 2.2), including the generalised phase separation algorithm (Equations 2.3, 2.5 and 2.6) and the structural adaptation model with shunt-preventing stimuli (Equation 2.15). By coupling EC migration and perfusion in this manner we can begin to simulate the wound healing response of ECs, at a vascular level, to migratory guidance cues and flowing network angioadaptation stimuli. In order to simulate blood flow, however, we require the migrating tip-cells to form closed capillary loops, known as anastomoses. Although these emerge naturally from the model when a tip-cell encounters another tip-cell or an existing capillary, the likelihood of this is occurring is enhanced by the inclusion of tip-cell branching whereby an additional tip-cell is added to the migrating capillary front. Biologically, the formation of new capillary loops at the leading edge of the endothelial plexus is controlled by VEGF-induced filopodial extension from tip cells via the complex intra-cellular Dll4/Notch1 signalling pathway (Bentley et al., 2008). To approximate this *in vivo* observation at a discrete level, the generation of new tip-cells from existing tip-cells is included phenomenologically, with branching dependent upon local VEGF concentration (see Table 3.1 for specific values). One further caveat to this methodology is that branching can only occur in tip-cells that have reached a certain level of maturation (i.e. new tip-cells cannot immediately undergo further

VEGF Concentration (c)	Branching Probability
$c \leq 0.3$	0.009
$0.3 < c \leq 0.8$	0.01
$0.8 < c \leq 0.98$	0.011
$c > 0.98$	0.012

Table 3.1: Sprout tip branching probabilities as a function of local VEGF concentration used in simulations of normal healing.

branching), which we define by the parameter t_{branch}. It should also be noted that side branching induced by wall shear stress in perfused vessels (McDougall et al., 2006b) is not considered here. Our simulations predict maximum wall shear stresses in the wound neo-vasculature of approximately 0.5 Pa – such small stresses would not be expected to produce additional branching in perfused vessels.

3.6.3. Model Parameterisation and Simulation Details

The domain is a square of length 2 mm with an initial circular wound of radius 0.68 mm positioned at its centre – this wound size takes account of the observed post-wound muscle fibre contraction. Large parent vessels are positioned at the upper and lower edges of the domain separated by 24 evenly spaced small parallel parent vessels that have been ablated within the wound area. The vascular network grows from the small parent vessels, with sprouts initiated at evenly spaced positions where the VEGF concentration exceeds the critical value c_{crit} (Figure 3.6). Initially, we assume the existence of a domain-spanning uniform ECM density (i.e. $f(x, y, 0) = 0.4$), and a radially symmetric VEGF concentration profile that decreases from the wound centre according to:

$$c(r) = e^{-\frac{r^2}{\omega}}, \tag{3.7}$$

where r is the normalised distance from the centre of the domain ($\omega = 0.85$). The *in vivo* study showed that, 3 days post-wounding, the wound site was flooded with macrophages (data not shown); hence, this assumed chemical profile effectively mimics

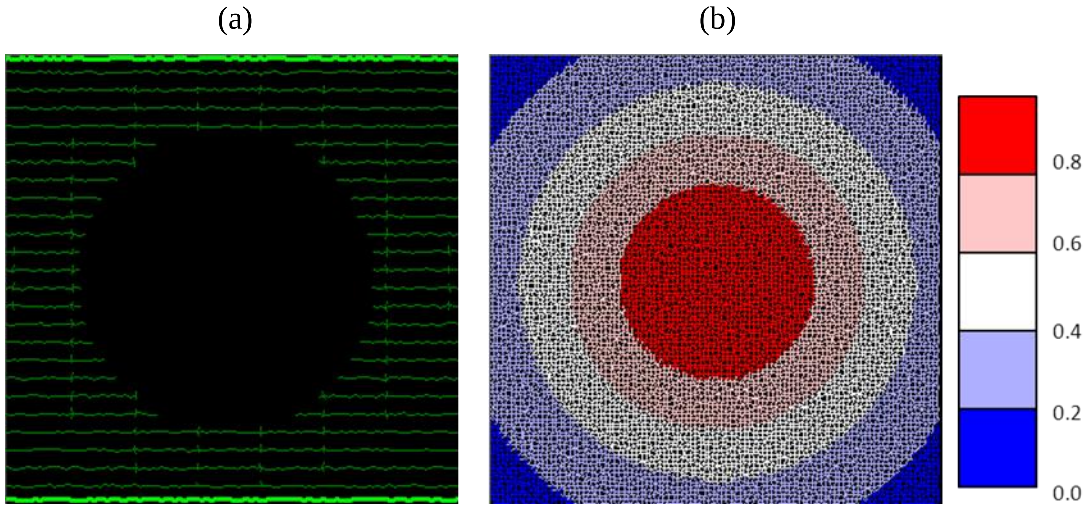

Figure 3.6: Initial conditions for the wound healing angiogenesis simulations showing (a) the intact post-wound vasculature with evenly-spaced initial sprouts and (b) the radially decreasing VEGF concentration profile given by Equation 3.7 (values correspond to the colour bar). Note that sprouts are only initiated in positions where the VEGF concentration exceeds the critical value c_{crit}.

the net result of VEGF-producing macrophage infiltration during the inflammatory phase of the healing response. No MMPs are present initially under the assumption that these are only produced once capillary sprouting has begun. Further to these initial conditions, zero-flux boundary conditions are imposed for all variables on all boundaries of the domain.

The experimental data (c.f. Figures 3.4 and 3.5) suggest a significant delay in the onset of angiogenesis after injury. Therefore, angiogenic sprouting is assumed to commence at day 2.0 post-wounding. Due to the difference in characteristic timescales, however, vascular network growth and blood flow cannot be simulated simultaneously. The nascent networks are therefore perfused to quasi-steady state at regular intervals of 24 hours – allowing the model to provide daily predictions of wound neo-vascular architecture throughout the healing process. Throughout perfusion, a fixed inlet haematocrit H_D^{in}, inlet pressure P_{in} and outlet pressure P_{out} are assumed in all parent vessels. Prior to wounding it is assumed that all parent vessels are capable of flow, and post-wounding the ablated vessels may regain flow due to reconnection via the angiogenic process. For all of the simulation results the radii of the 2 large parent vessels are held fixed at R_{max}, but the 24 smaller parent vessels and all neo-vessels are allowed to undergo angioadaptation. The radii of these vessels are permitted to remodel from a minimum of R_{min} up to a maximum of R_{max}. The vessel remodelling parameters were chosen such that, prior to wounding, the radii of the small parallel parent vessel segments would remodel to steady-state values in the range 3 – 4 μm, in line with experimental observations. All capillary sprouts emerging from the parent vessels are assigned an initial radius of R_{min} prior to perfusion. Unless otherwise indicated, the parameter values used in all simulations are summarised in Table 3.2.

3.6.4. *In silico* Image Analysis Protocol

For direct comparison with the *in vivo* data, spatial values for vessel density and vessel junction density were calculated throughout each simulation. Three annular regions were constructed with boundaries defined 80 μm either side of contours set at 250, 500 and 750 μm from the wound centre, respectively. Additionally, a circular region of radius 80 μm was constructed at the wound centre. The total length of all vessel segments and the number of vessel junctions within each of these four regions were calculated and the values appropriately normalised by the area of the region. In order to approximate the *in silico* wound area, the mathematical domain was split into 32 regions of equal angle about the wound centre and the distance from the wound centre to the nearest vessel was determined in each segment. These 32 values were then averaged to produce a surrogate "wound radius", and the area of a circle characterised by this radius is taken to represent the approximate wound area.

3.7. Numerical Simulation Results

3.7.1. Qualitative Comparison of *in vivo* and *in silico* Architectures

Combining all components of the mathematical model we can generate vascular architectures that closely resemble those observed *in vivo*. In Figure 3.7, simulated capillary networks are compared to vital imaging micrographs obtained experimentally at days 3, 6 and 9 post-wounding. Specifically, the images show *in vivo* wound neo-vasculatures (Figures 3.7a, d, g) and *in silico* distributions of both capillary radii (Figures 3.7b, e, h) and haematocrit (Figures 3.7c, f, i). On day 3, we note the strong angiogenic response both *in vivo* and *in silico* producing a dense mesh of vascular sprouts around the wound perimeter (Figure 3.7a, b). In the model a number of sprouts

Parameter	Definition	Value
D	EC random motility coefficient	3×10^{-5}
χ	EC chemotaxis coefficient	0.098
δ	EC chemotactic receptor saturation factor	0.6
ρ	EC haptotaxis coefficient	0.3
η	VEGF uptake rate by EC tips	0.1
β	ECM production rate by EC tips	0.05
γ	ECM degradation rate by MMPs	0.1
α	MMP production rate by EC tips	1×10^{-5}
ε	MMP diffusion coefficient	0.01
ν	MMP decay rate	0.3
L_c	Length constant for conducted stimulus decay	0.01 m
k_s	Relative intensity rate of vessel shrinkage	1.7
k_p	Relative intensity rate of the pressure stimulus	0.8
k_m	Relative intensity rate of the convected stimulus	0.38
k_c	Relative intensity rate of the conducted stimulus	3.68
J_0	Saturation constant for the conducted stimulus	250
τ_{ref}	Reference wall shear stress	0.5 dyn $\cdot$ cm^{-2}
$(QH_D)_{ref}$	Reference RBC flow rate	3.6×10^{-15} m$^3 \cdot$ s^{-1}
Q_{ref}	Reference flow rate	1×10^{-18} m$^3 \cdot$ s^{-1}
t_{branch}	Threshold age for EC tip branching	3.84 hours
P_{in}	Inlet blood pressure	3260 Pa
P_{out}	Outlet blood pressure	2060 Pa
R_{min}	Minimum permissible vessel radius	3.0×10^{-6} m
R_{max}	Maximum permissible vessel radius	1.2×10^{-5} m
μ_{plasma}	Bulk plasma viscosity	1.2×10^{-3} Pa $\cdot$ s
H_D^{in}	Inlet haematocrit value	0.45
c_{crit}	Critical VEGF concentration for initial sprouting	0.33

Table 3.2: Parameter values used in all simulations of normal healing.

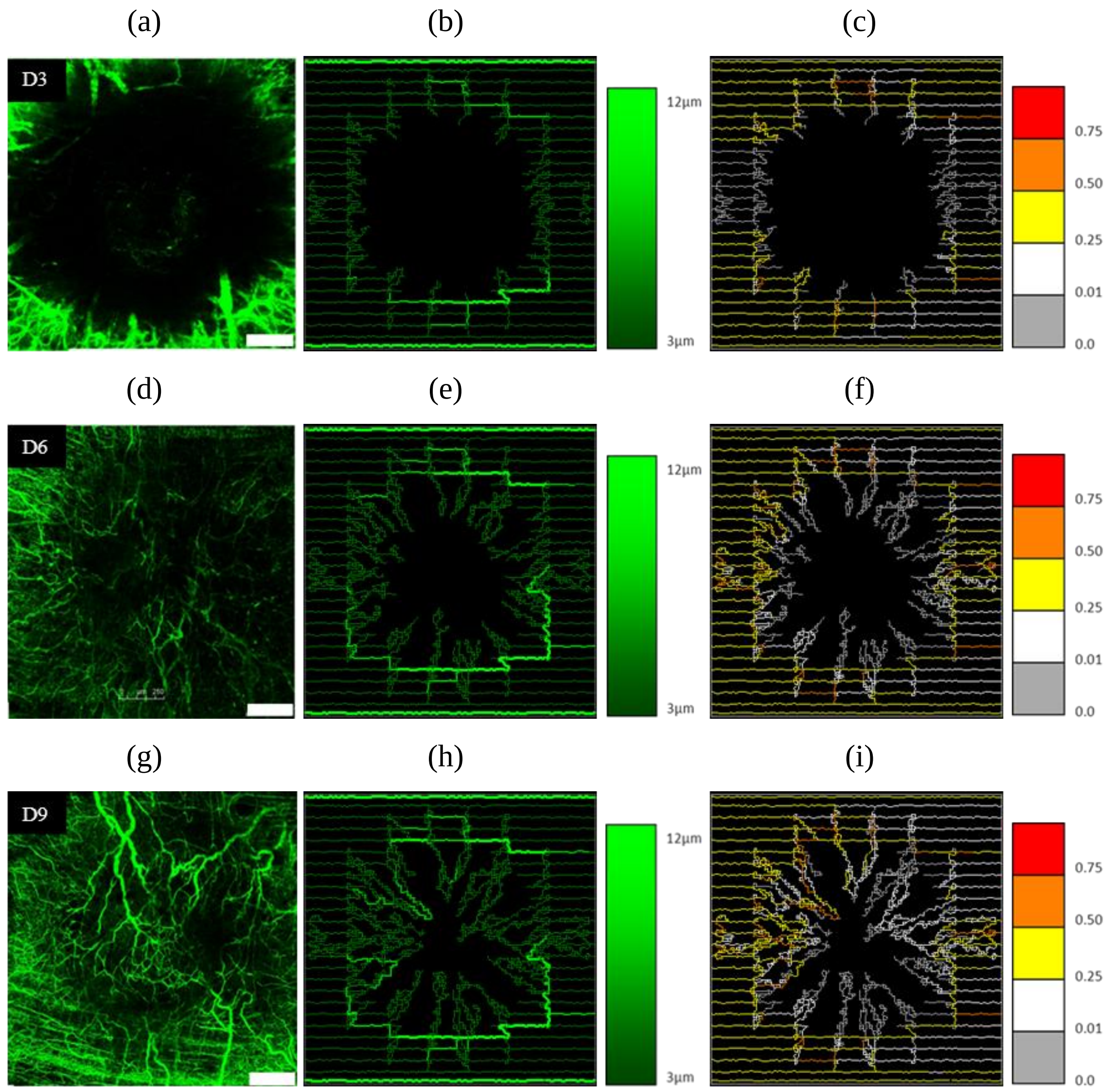

Figure 3.7: Qualitative comparison of experimental and numerical wound healing at days (a-c) 3, (d-f) 6 and (g-i) 9 post-wounding. Images show (a, d, g) FITC-dextran perfused *in vivo* capillary plexuses (scale bar = 250 µm) alongside *in silico* distributions of (b, e, h) capillary radii and (c, f, i) haematocrit.

have re-connected existing parent vessels and numerous occurrences of phase separation can already be seen, particularly on the right hand side of the domain (Figure 3.7c). A notable feature of the *in vivo* vasculature at day 3 is the conspicuous dilation of the vessels surrounding the wound (Figure 3.7a) – this is attributable to the initial inflammatory response and, as such, is not directly replicated by the modelling assumptions. The first signs of vascular remodelling are, however, observable in the simulation with dilated parent vessel segments emerging immediately above and below the wounded region (Figure 3.7b). This is a manifestation of the fact that these vessels are now part of lengthy flow pathways that drain and supply newly re-connected parent vessels. We would expect this dilation to increase the blood flow across the network and improve the delivery of oxygen to the hypoxic wound. By day 6, an angiogenic plexus proceeds towards the wound centre and many more vessels populate the wound area both *in vivo* and *in silico* (Figure 3.7d, e). Many fusions and anastomoses formations have now occurred, with the model displaying dilated pathways that traverse the wound boundary and carry a significant proportion of the haematocrit to the detriment of more distal parent vessels (Figure 3.7e, f). These pathways appear decidedly “shunt-like”, but for the available vessel architecture this is arguably the most effective means of delivering oxygen to the vessel-free zone. It seems likely that this effect would persist until the formation of wound-spanning vessels occurs, producing shorter flow pathways, reduced vessel dilation and less pronounced phase separation effects. Compared to pre-wound, uninjured tissue, the *in vivo* and *in silico* wound architectures at day 9 are highly disorganised and composed of several dilated capillary loops (Figure 3.7g, h; c.f. Figure 3.4a). Despite this, however, the model predicts that on average intra-wound haematocrit remains low with a number of smaller low-flow loops carrying little or no RBCs (Figure 3.7i).

3.7.2. Quantitative Comparison of *in vivo* and *in silico* Architectures

Although the simulated vascular architectures of Figure 3.7 compare favourably with the experimental images, a more quantitative comparison is required to provide a more rigorous test of their validity. In Figure 3.8 we present a series of graphs comparing the experimental values for vessel density (Figures 3.8a, c, e), vessel junction density (Figures 3.8b, d, f) and wound area (Figure 3.8g) with the simulated numerical values. The experimental results are plotted as the mean with standard error, whilst the lines displaying the *in silico* results represent the average behaviour from a series of 10 simulations. As can be seen, the model predictions compare very favourably both spatially and temporally with the *in vivo* data. The model predicts vessel junction densities slightly above or below the experimental values on each day at 500 µm from the wound centre but, otherwise, most data points are in excellent agreement over the course of the simulation. In particular, the quantitative rate of *in vivo* wound closure between days 3 to 9 is successfully reproduced (Figure 3.8g). Note that the day 9 experimental data suggests the wound is beginning to enter the repair phase of healing.

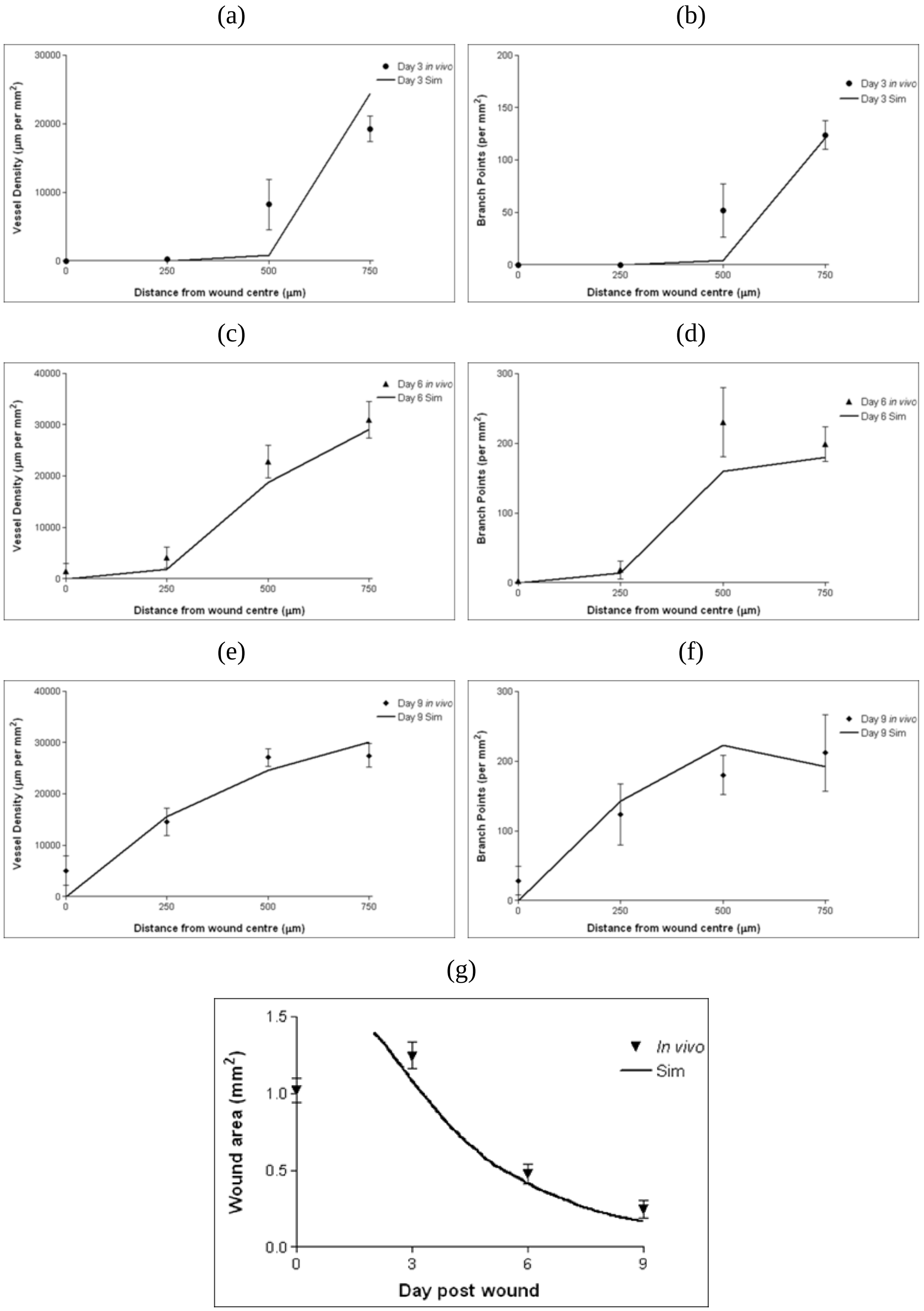

Figure 3.8: Caption overleaf.

Figure 3.8: Quantitative comparison of longitudinal wound healing data obtained by experiment (symbols with error bars) or simulation (solid lines). Plots show measurements of (a, c, e) vessel density and (b, d, f) vessel junction density on days 3, 6 and 9 post-wounding, respectively, at distances of 0, 250, 500 and 750 μm from the wound centre. Measurements of wound area on days 0, 3, 6 and 9 post-wounding are shown in plot (g). Experimental data are plotted as mean ± SEM of at least 6 measurements, whilst numerical data represent mean values from 10 independent simulations.

The mean vessel density at 750 μm from the wound centre (Figure 3.8e), and the mean vessel junction density at 500 μm (Figure 3.8f), both undergo a slight decrease suggesting that some vascular pruning may have occurred. Due to the lack of statistical significance in these variations, however, the evidence is somewhat inconclusive and therefore vascular pruning was not considered in the mathematical model.

3.8. Anti-angiogenic Wound Treatment

Under normal healing circumstances, the wound healing angiogenesis model has thus far been shown to be capable of generating a variety of qualitative predictions, whilst also quantitatively reproducing a number of experimental metrics. In order to confirm both the robustness and predictive capability of the model we now study the impact of introducing into the system an angiogenesis-perturbing treatment.

3.8.1. TNP-470

We consider the effect of the anti-angiogenic agent TNP-470 (also known as AGM-1470): a potent synthetic analogue of fumagillin (Ingber et al., 1990). TNP-470, previously shown to decrease the rate of murine cutaneous wound healing in a dose-dependent manner (Klein et al., 1999), is known to obstruct EC proliferation by inhibiting the action of the metalloproteinase methionine aminopeptidase (metAP-2) following protein synthesis in the cell (Griffith et al., 1997). The experimental procedures employed were identical to those outlined in Section 3.5.1, with the only exception that each animal was injected subcutaneously every other day with 30 mg/kg TNP-470 (Rutland et al., 2005) beginning on the day of wounding (i.e. day 0).

3.8.2. Mathematical Model Modifications

In order to predict the effect of TNP-470 application, only minor modifications to the model outlined in Section 3.6 are required. Since the anti-angiogenic agent is known to target EC proliferation, capillary tip branching probabilities are reduced by a constant factor with respect to their previous values (see Table 3.3 for details). This is not, however, the only representation of EC proliferation in the model: in order for the sprout tips to undergo migration, it is implicitly assumed that proliferation must have occurred in the trailing ECs. Therefore, since chemotaxis is the dominant migratory cue in the healing process, we further assume that the impact of TNP-470 is indirectly realised by a reduction in sprout tip chemotactic sensitivity to VEGF. As such, we adjust the appropriate parameter value to $\chi = 0.075$. All other parameter values and model assumptions remain unchanged.

VEGF Concentration (c)	Branching Probability
$c \leq 0.3$	0.0063
$0.3 < c \leq 0.8$	0.007
$0.8 < c \leq 0.98$	0.0077
$c > 0.98$	0.0084

Table 3.3: Sprout tip branching probabilities as a function of local VEGF concentration used in simulations considering the anti-angiogenic treatment, TNP-470.

3.8.3. Results

As for the untreated wound simulations, in Figure 3.9 we again compare the *in vivo* wound neo-vasculatures (Figures 3.9a, d, g) with the *in silico* distributions of capillary radii (Figures 3.9b, e, h) and haematocrit (Figures 3.9c, f, i) at days 3, 6 and 9 post-wounding. Fewer neo-vessels are observed around the wound periphery on day 3 compared to untreated animals (Figure 3.9a vs. Figure 3.7a), and this also holds for the simulation results (Figure 3.9b vs. Figure 3.7b). As expected, at day 6 the reduced angiogenic response in TNP-470 treated animals leads to an increase in the size of the vessel-free region both *in vivo* (Figure 3.9d vs. Figure 3.7d) and in the virtual wound (Figure 3.9e vs. Figure 3.7e). A number of parent vessels on the left hand side of the

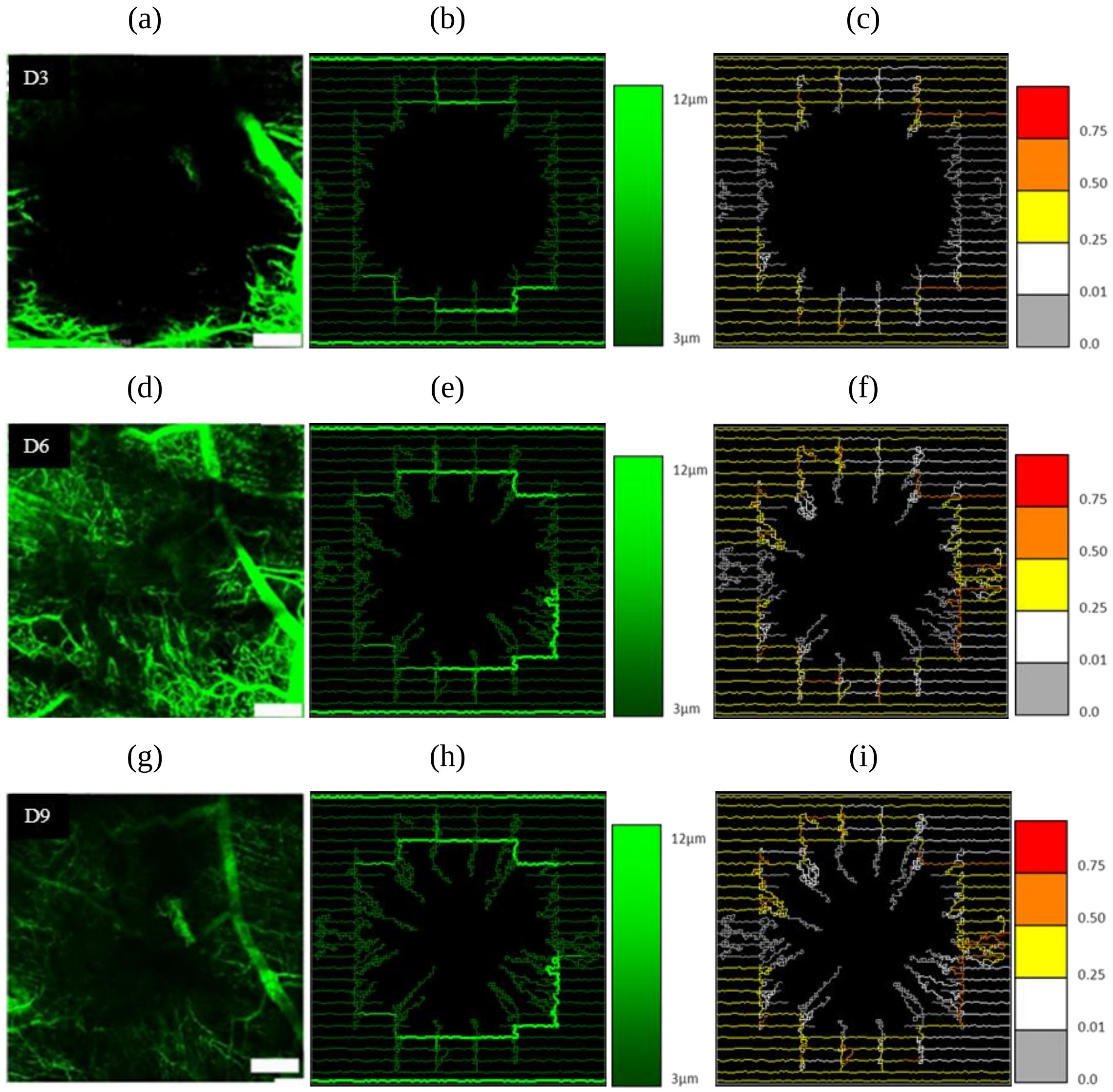

Figure 3.9: Qualitative comparison of experimental and numerical wound healing at days (a-c) 3, (d-f) 6 and (g-i) 9 post-wounding under the influence of an anti-angiogenic treatment. Images show (a, d, g) FITC-dextran perfused *in vivo* capillary plexuses (scale bar = 250 μm) alongside *in silico* distributions of (b, e, h) capillary radii and (c, f, i) haematocrit. The *in silico* results were obtained by reducing the chemotactic sensitivity to VEGF (c.f. χ = 0.075 vs. χ = 0.098) and reducing the capillary tip branching probabilities by a constant factor (c.f. Table 3.3 vs. Table 3.1).

wound have also failed to re-connect, reducing the capacity for flow across the network (Figure 3.9f). Notably, the continual suppression of capillary migration both *in vivo* and *in silico* leads to a disparity of anastomosed vessels within the wounded region (Figure 3.9g, h) – such connections were numerous in the untreated wounds (Figure 3.7g, h). The intra-wound haematocrit is also significantly reduced (Figure 3.9i vs. Figure 3.7i) and this is likely to have serious implications for oxygen delivery to the wound site, with diffusion continuing to be the dominant mechanism for transport.

A comparison of the *in vivo* quantitative data with corresponding data from the mathematical model is shown in Figure 3.10. Again we consider vessel density (Figure 3.10a, c, e), vessel junction density (Figure 3.10b, d, f) and wound area (Figure 3.10g), where each experimental data point represents the mean and standard error from 4 animals and the *in silico* results have been averaged from 10 independent simulations. The TNP-470 angiogenesis model captures the essential features of the experimental data. In particular, the model predicts the observed delay in advancement of the angiogenic plexus, with accurate reproduction of the vessel junction density (Figure 3.10d, f) and vessel density (Figure 3.10c, e) values at 250 μm and 500 μm from the wound centre on days 6 and 9. The experimental wound area value at day 3 is under-predicted by the model – possibly due to a TNP-470 treatment-induced delay in the onset of significant EC sprouting *in vivo* (Figure 3.10g vs. Figure 3.8g) – but the overall rate of *in silico* wound closure matches the experimental observation.

3.9. Discussion

The *pc* DSWC wound healing assay is particularly suitable for a parallel mathematical bench-marking study. Not only does the uninjured *pc* vessel network have a regular, essentially 2D arrangement, but the window chamber set-up allows the same regions of interest to be imaged in the same animal over time (Lehr et al., 1993; Guerreiro-Lucas et al., 2008). Additionally, focal heat-injury to the *pc* produces a non-perfused circular wound area with highly reproducible size, allowing quantification of angiogenesis in a spatially and temporally defined manner. These quantitative measures are critical for informing mathematical model development and, as such, the *in vivo* and *in silico* approaches described in this chapter were strongly coupled throughout our investigation.

The ultimate result of this combined study is a robust mathematical model with predictive capability and the potential to formulate hypotheses for *in vivo* testing. Although angiogenesis occurs in a wide range of natural and pathological settings, wound healing is one of the most straightforward to characterise biologically, lacking as it does the additional complexities associated with solid tumour growth, for example.

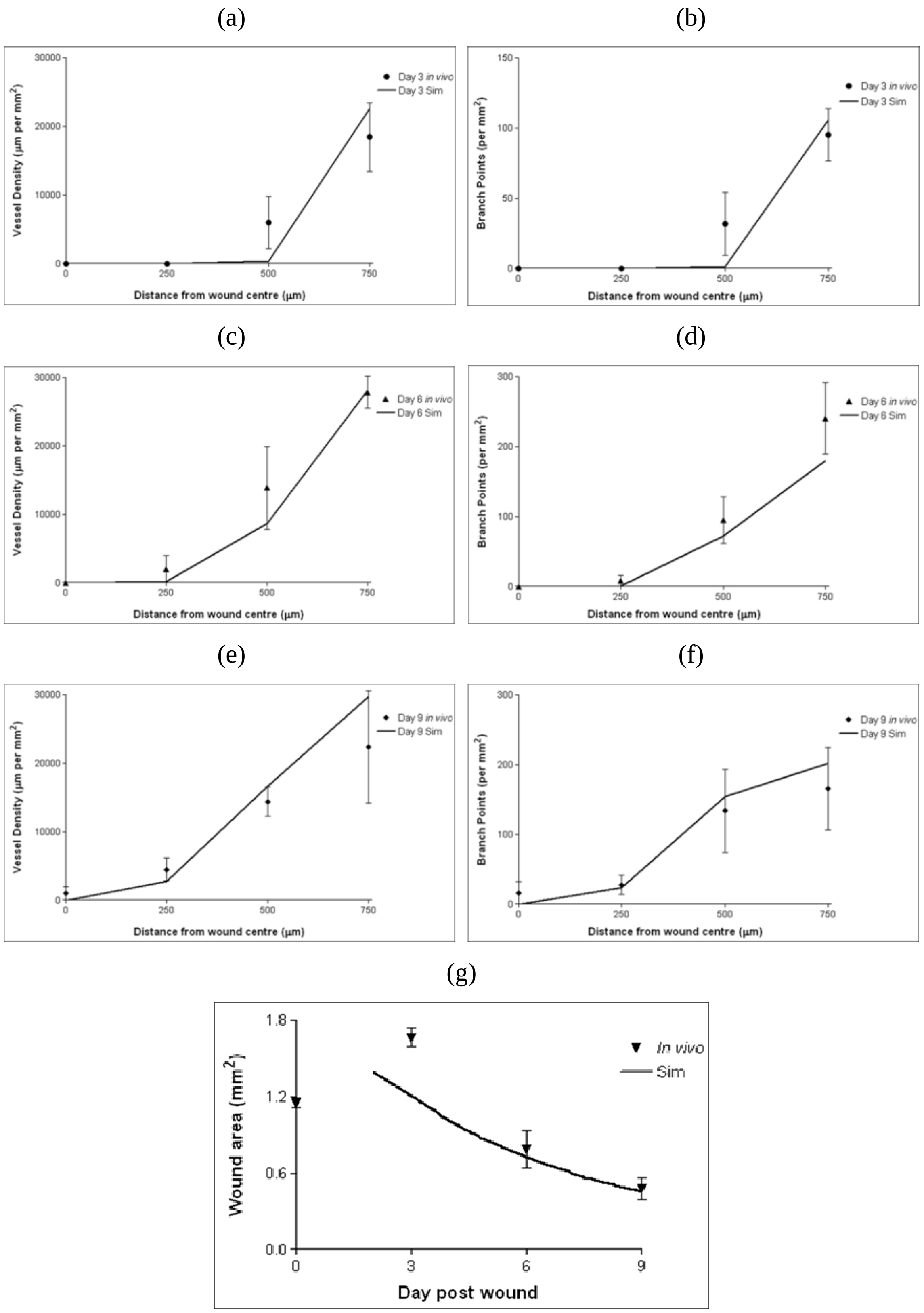

Figure 3.10: Caption overleaf.

Figure 3.10: Quantitative comparison of longitudinal wound healing data obtained by experiment (symbols with error bars) or simulation (solid lines) under the influence of an anti-angiogenic treatment. Plots show measurements of the vessel density (a, c, e) and vessel junction density (b, d, f) on days 3, 6 and 9 post-wounding, respectively, at distances of 0, 250, 500 and 750 μm from the wound centre. Measurements of wound area on days 0, 3, 6 and 9 post-wounding are shown in plot (g). Experimental data are plotted as mean ± SEM of 4 measurements, whilst numerical data represent mean values from 10 independent simulations.

Due to the wide variety of possible tumour types and associated micro-environments, most tumour angiogenesis models provide general qualitative predictions with little specific quantitative experimental validation (McDougall et al., 2006b; Owen et al., 2009; Welter et al., 2009; Cai et al., 2011). However, the *pc* wound data generated during this study is less variable and therefore provides a more rigorous test for the modelling approach. Once satisfactorily benchmarked against experiments, the model can then be extended and modified to explore more complex scenarios.

Various mathematical models of wound healing have been published over the last two decades, each focussing on a different aspect of the healing process. Only a handful of these have explicitly considered angiogenesis and a continuum PDE approach is typically adopted. In this work, however, we have proposed a multi-scale hybrid PDE-discrete model incorporating molecular cues, discrete capillary migration and flow-mediated vascular remodelling of nascent wound microvasculatures. The modelling results have been compared to qualitative and quantitative measures obtained from a standardised *in vivo* assay, and this, to our knowledge, represents the first attempt to compare *in silico* morphological data with longitudinal experiments of wound healing, aside from simple predictions of wound closure rates (Cardinal et al., 2008).

Under normal wound healing circumstances, the mathematical model qualitatively and quantitatively reproduces the sequential changes of the vasculature *in vivo*. Functional capillary density, an important microcirculatory parameter, increases over days 3 to 9 in the centre of the virtual and *in vivo* wounds (Figure 3.7), consistent with a centripetal progression of the vascular network leading edge. Comparison of model predicted values of vessel density, vessel junction density and wound area at days 3, 6 and 9 post-injury also correlate excellently with *in vivo* measurements (Figure 3.8). Successful bench-marking of the *in silico* EC migration and proliferation dynamics in this manner allows the true potential of the mathematical model to be realised. By simulating blood flow and structural adaptation in the nascent vasculatures, predictions beyond the scope of the experiment can be made regarding the evolution of capillary radii, haematocrit and, implicitly, wound oxygenation. Although generally termed shunt-preventing stimuli, the conducted and convected angioadaptation responses here contribute to the development of extensively dilated pathways throughout the first 9 days of healing. These vessels are seen to traverse the wounded region carrying a significant haematocrit and, in the absence of wound-spanning vessels, would most likely be beneficial for wound oxygenation. More direct delivery of oxygen to the wounded region would most likely be hampered, however, because intra-wound haematocrits and flows are predicted to be persistently low throughout the simulation.

The robustness of the mathematical model was subsequently tested by investigating its ability to reproduce the effect of systemic administration into the wound environment of TNP-470 – an anti-angiogenic agent. TNP-470 blocks the progression of ECs into the S-phase of the cell-cycle (Sin et al., 1997) and actively prevents their proliferation. This was incorporated into the mathematical model by reducing the likelihood of capillary branching and the capacity for chemotactic migration – mechanisms which implicitly require cell division to proceed. The *in silico* model largely reproduces the qualitative and quantitative outcomes of TNP-470 administration *in vivo*, with delayed vessel growth resulting in fewer anastomosed vessels and a large region devoid of vasculature at day 9. Further to this, the model predicts that intra-wound haematocrit is negligible even at day 9 post-wounding, while some ablated parent vessels have even failed to re-connect to the circulation.

The *in silico* results presented here are encouraging and suggest that we have developed a robust model of wound healing angiogenesis in the murine *pc*. Although it has not been incorporated here, an obvious extension to the mathematical model is the explicit simulation of oxygen transport from the vasculature to the wound. As the nascent vascular structures grow and remodel, the model has the potential to predict both the spatial and temporal evolution of oxygen concentration in and around the wound area. This is likely to form the basis of a future study: such results are of great interest since the extent of wound oxygenation is a key indicator of potential healing outcomes (Sen, 2008).

Although the model successfully reproduces the angiogenic response to injury, it is still lacking certain aspects of the wound healing process. For instance, the simulations are assumed to begin 2 days post-wounding and, as such, the inflammatory phase is largely neglected. Invading inflammatory cells such as macrophages are not explicitly incorporated – we simply mimic the release of pro-angiogenic factors from these cells by creating an initial VEGF gradient. As noted earlier, the model is unable to reproduce the extensive inflammatory vessel dilation observed at day 3 *in vivo*. However, it is likely that this dilation is caused by up-regulation of nitric oxide production by various cell types in the wound site (Witte and Barbul, 2002), and such a mechanism is not currently considered in the angioadaptation model. A further aspect neglected by the model is the deposition of ECM by infiltrating fibroblasts and the associated contact guidance effects on EC migration. These additional considerations are likely to form the basis for further future studies – the model presented here can be seen as a first stage towards the development of a more complete *in silico* virtual wound.

The mathematical model presented here has been shown to accurately simulate both the angiogenic response observed in healing wounds and the effect of anti-angiogenic therapeutic intervention. The novel approach described in this study, directly combining *in vivo* investigation and mathematical modelling, provides evidence for the benefits of a new experimental paradigm in which longitudinal *in vivo* data can be used to directly inform modelling and rigorously test the accuracy of *in silico* predictions.

Chapter 4

Modelling Development of the Murine Retinal Vascular Plexus

4.1. Introduction

In the previous chapter we presented a mathematical model of murine wound healing angiogenesis that was developed in close association with laboratory studies. We now modify and extend the earlier methodology to investigate development of the murine retinal vascular plexus (RVP). Having previously reasoned that the wound healing assay provides a significant test of the angiogenesis modelling approach, it will be seen that the well-ordered developmental process associated with the neo-natal retinal vasculature poses an even more demanding trial of the *in silico* study. This chapter will proceed by first detailing the structure of the adult retinal vasculature and describing the fundamental processes involved in its development. The key experimental results obtained from this investigation will then be summarised, followed by a presentation of the full mathematical model and a wide variety of relevant simulation results. The *in silico* RVP structures generated by the model are first compared with corresponding experimental sections at various stages of wild-type development, and we go on to report a range of predictions on retinal angiogenesis in transgenic animals. We will conclude by considering the future utility of the model and drawing appropriate conclusions.

4.2. Biology of the Retinal Vasculature

The retina is a thin (~ 0.5 – 1 mm) hemispherical tissue layer that lines the inner surface of the eye (Figure 4.1). At the centre of the retina lies the optic nerve, which contains the axons of retinal ganglion cells (RGCs) responsible for the passage of light-induced nerve impulses to the brain. The retina and the optic nerve emerge from the developing brain during embryogenesis and, as such, are considered to belong to the central nervous system.

A variety of neural cell types exist in the layered retinal structure, including the photo-receptive rods and cones, and in the adult retina these are nourished by a similarly layered vasculature. Moving from the front to the back of the eye, there exist three layers known as the primary (superficial), intermediate (inner plexiform) and deep (outer plexiform) vascular plexuses, respectively. The layers are inter-connected by vessels that project perpendicularly from each plexus, with the primary plexus considered to be predominantly arterial and the deep plexus predominantly venous (Paques et al., 2003; Fruttiger, 2007).

The origin of these layers had been unclear but it has recently been shown that their development is driven by a process of angiogenesis rather than vasculogenesis (*de novo* formation of vessels by endothelial precursor cells known as angioblasts) (Fruttiger, 2002). During early development the hyaloid vasculature, an arterial network in the vitreous, provides nutrient to the inner eye. Blood is supplied to this vasculature from the central hyaloid artery in the optic nerve and is subsequently drained through the choroidal net on the outside of the eye. Later in development, the primary vascular plexus emerges by endothelial sprouting from the optic nerve head and migration across the inner retinal surface. In parallel with this process, the pre-existing hyaloid vasculature is believed to regress (Figure 4.2). The intermediate and deep vascular plexuses are subsequently formed by downward sprouting from the veins, venules and capillaries of the primary plexus. This cascade begins proximally to the optic nerve and spreads outwards until perpendicular projections cover the entire retinal surface. It is believed that these sprouts are guided into the deeper layers of the retina by Mueller cell processes, with most sprouts migrating to form the deep vascular plexus while the intermediate layer is formed predominantly by branching. A schematic of the layered retinal structure is presented in Figure 4.3, alongside examples of the typical *in vivo*

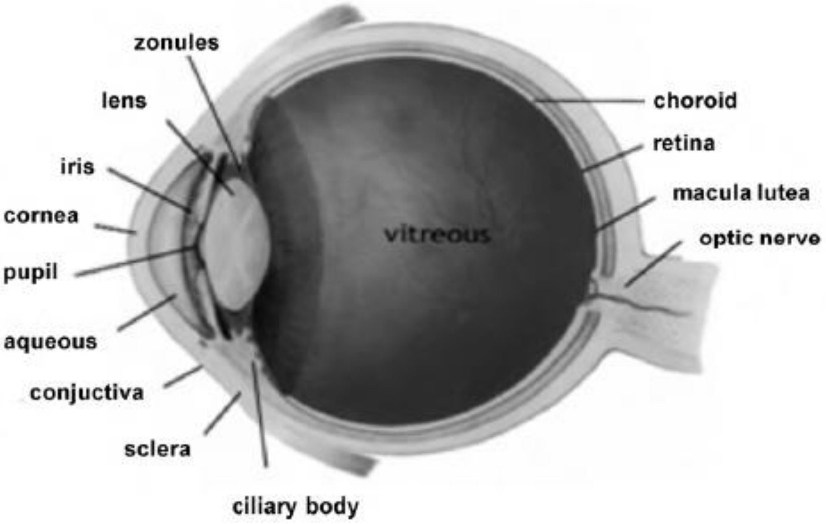

Figure 4.1: Schematic diagram showing the structure of the eye. Image taken from Bozukova et al. (2010).

capillary architectures displayed within each vascularised layer. The investigation we have carried out here focuses entirely on the development of the murine superficial RVP and, as such, the formation of the intermediate and deep vascular layers will be considered no further in this thesis. The application of the model to investigate the developmental dynamics of these additional layers will form the focus of future studies. A thorough review of the relevant literature concerning various aspects of retinal vascular development has been presented by Fruttiger (2007).

In the case of the postnatal murine eye, the factors regulating superficial RVP formation are relatively well understood (Fruttiger, 2002; Gariano, 2003). Aside from ECs, the other cell variety intimately involved in this developmental process is the astrocyte – another type of glial cell. EC migration outward from the optic nerve depends upon the formation of a dense astrocytic network across the inner retina: a process that begins 4 – 5 days prior to the emergence of the first angiogenic sprouts. Astrocytes in the optic nerve head express the PDGF-A receptor (PDGFR-α), and are induced to migrate over the inner retina in response to PDGF-A produced by RGCs (Mudhar et al., 1993; Fruttiger et al., 1996). Over-expression of PDGF-A in neonatal transgenic mice reduces the extent of the astrocytic network (Fruttiger et al., 1996; West et al., 2005) suggesting that astrocyte migration is dependent upon a gradient of PDGF-A. For the mice considered in this investigation, astrocyte migration from the optic

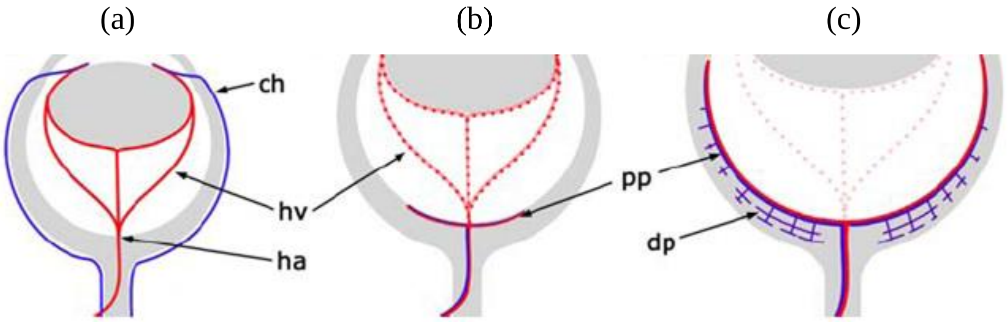

Figure 4.2: The retinal vasculature is remodelled significantly during development. (a) The hyaloid vasculature (hv) within the vitreous is initially supplied by the hyaloid artery (ha) and drained by the choroidal net (ch) on the outside of the eye. (b) As the arteries and veins of the primary plexus (pp) grow across the retinal surface, the hyaloid vasculature regresses. (c) Venous sprouting from the primary plexus subsequently results in growth of the intermediate and deep vascular plexuses (dp). Note that the eye also undergoes substantial growth throughout this process. Image taken from Fruttiger (2007).

nerve has previously been shown to begin between embryonic day (E) 15.5 and 18.5, and by postnatal day (P) 3 an astrocytic template covers the entire inner retinal surface (Aubert et al., 2011). Note that the murine gestation period lasts 21 days, such that E21 or P0 both refer to the day of birth.

The emergence of the astrocyte network, with associated chemotactic and haptotactic guidance cue production, provides a stable scaffold for subsequent EC migration (Dorrell et al., 2002). The importance of haptotaxis is demonstrated by the finding that EC migration is prevented by inhibiting the ability of ECs to bind fibronectin: an outcome achieved by intraocular injection of anti-integrin αβ1 antibodies (Uemura et al., 2006). Poorly-oxygenated astrocytes produce VEGF-A prior to vascularisation and this chemotactic factor is responsible for inducing EC migration to ultimately produce a nascent vascular network over the inner retinal surface. VEGF-A mRNA is expressed in a number of different splice-variants, each with a varying ability to bind heparin residues in the ECM or diffuse freely (Park et al., 1993; Shima et al., 1996; Ferrara et al., 2002; Keyt et al., 2006). VEGF-A_{165} is the most widely expressed human splice-variant, and its murine homolog, VEGF-A_{164}, can both bind to ECM and diffuse in the extracellular milieu. VEGF-A_{164} is widely expressed during development (Ng et al.,

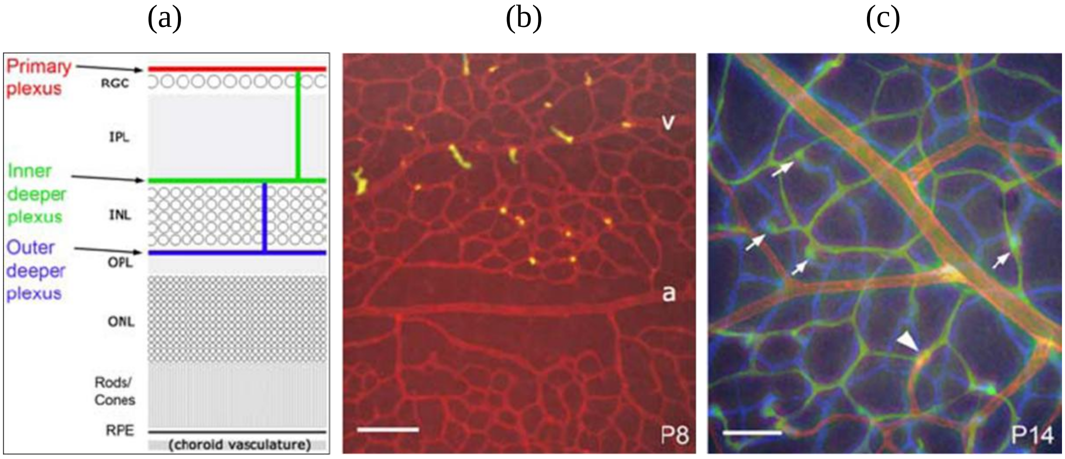

Figure 4.3: The fully developed retina is a layered, vascularised structure composed of various cell types; image (a) shows a schematic diagram in cross-section (RGC: retinal ganglion cells; IPL: inner plexiform layer; INL: inner nuclear layer; OPL: outer plexiform layer; ONL: outer nuclear layer; RPE: retinal pigment epithelium). Stained retinal whole mounts obtained during development show (b) the primary vascular plexus (red) at post-natal day (P) 8, and (c) the intermediate (green) and deep (blue) vascular plexuses at P14 (scale bars = 100 μm). In (a), downward projecting sprouts (green) are seen emerging from veins and capillaries but not from arteries. In (c), the arrows indicate established connections between the intermediate and deep plexuses, while the arrowhead indicates a connection between the primary and intermediate plexuses. Image adapted from Fruttiger (2007).

2001) and is the major isoform responsible for RVP formation (Stalmans et al., 2002; Gerhardt et al., 2003). Intra-ocular injection of VEGF-A sequestering antibodies has been found to inhibit endothelial migration and delay plexus formation (Uemura et al., 2006). Furthermore, removal of the VEGF gradient in the retina, via increased VEGF-A expression in transgenic mouse models, also reduces the extent of EC migration (Gerhardt et al., 2003; Mitchell et al., 2006). A broad summary of the mechanisms of RVP development is presented graphically in Figure 4.4, highlighting the key interactions between the various biological processes.

Under normal circumstances, EC sprouting from the ophthalmic vein begins around P0 and the subsequent dense vascular plexus reaches the retinal periphery by P8. Sequential formation of anastomoses allows perfusion of the expanding network and over time the plexus matures and remodels to reveal a hierarchical vascular tree with

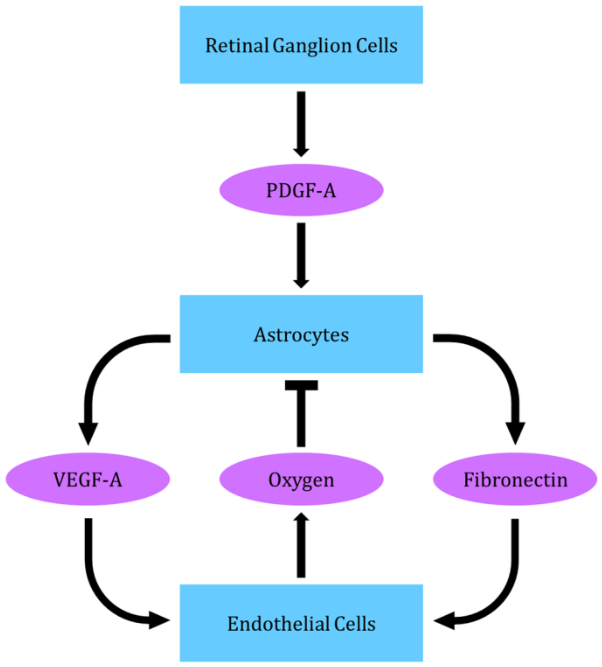

Figure 4.4: Flowchart showing the key interactions between the prominent cell types involved in RVP development. Prior to birth retinal ganglion cells secrete PDGF-A, which induces astrocytes to proliferate and migrate across the inner retina. Production of VEGF-A and fibronectin by astrocytes subsequently promotes neonatal angiogenesis by endothelial cell chemotactic and haptotactic responses, respectively. Finally, the formation of blood vessels and delivery of oxygen inhibits further astrocyte activity.

clearly defined arteries and veins (Fruttiger, 2007). Astrocytes respond to the onset of perfusion by gradually downregulating VEGF-A expression (West et al., 2005; Uemura et al., 2006), and this is followed by a reduction in EC numbers since, in addition to its role as a chemotactic agent, VEGF-A also impacts EC viability (Alon et al., 2005; West et al., 2005). An outward wave of vascular pruning therefore proceeds, resulting in the emergence of capillary-free zones around arteriolar segments where VEGF concentrations dip and oxygen concentrations peak (Fruttiger, 2007). The long-term maturation of the neo-vasculature, via recruitment of pericytes and smooth muscle cells, allows older animals to pose a stronger resistance to such hyperoxia (Fruttiger, 2007). Pericytes lend functional stability to vascular networks, prevent the leakage of circulatory components and, importantly, reduce the requirement for survival factors such as VEGF-A.

4.3. Theoretical Studies of the Retinal Vasculature

Before proceeding to describe the details of the current approach, we shall first briefly draw attention to other recent combined experimental and theoretical studies pertaining to the haemodynamics of the retinal circulation. Some of the earliest such studies combined data from microelectrode-facilitated measurement of intraretinal oxygen tensions with a 1D mathematical model of oxygen consumption that accounted for the various tissue layers throughout the depth of the retina (Yu and Cringle, 2001; Cringle et al., 2002; Cringle et al., 2006). By fitting the model to experimental data obtained from the retinae of rats, rabbits and guinea pigs, rates of oxygen consumption in the layers of highest demand were quantified. An analysis of oxygen distribution within the retinal vasculature has recently been performed by Liu et al. (2009), who simulated blood flow and oxygen transport in a reconstructed human arterial tree. Since human retinal arterial vessels are relatively large, the assumed convection-diffusion model for oxygen provided detailed predictions of not only the oxygen tension within particular segments, but also radial variations throughout their length. Most immediately comparable to the work in this thesis, however, are the investigations performed by Ganesan and colleagues, who have performed a detailed circulation analysis in a fully-developed three layer murine retinal network (Ganesan et al., 2010a; Ganesan et al., 2010b). Their network was constructed by an image-based approach, and using blood flow simulation techniques analogous to those presented in Chapter 2, albeit with a fixed distribution of vessel radii, provided a range of predictions regarding the distributions of haematocrit, pressure, viscosity and wall shear stress. More recently, their model has been extended to consider the impact upon these microcirculatory parameters when a pulsatile flow regime is introduced (Ganesan et al., 2011). As will be seen in Section 4.6, many of the results from these publications are found to accord with predictions made from our study of murine retinal development.

4.4. *In vivo* Investigation of Superficial Retinal Vascular Plexus Development

The relationship between the developing retinal vasculature, its constituent cell types, and the molecular cues that regulate this process can be readily visualised (Uemura et al., 2006). In this study, experimental measurements at various developmental stages, from E15.5 to P8, were used to inform the corresponding modelling approach. As in

Chapter 4, we provide a brief outline of the experimental procedure followed by a summary of the key experimental results. The *in vivo* experiments described below were performed by Dr Andrea Devlin under the supervision of Dr Christopher Mitchell in the School of Biomedical Sciences at the University of Ulster.

4.4.1. Experimental Set-Up

Mice were euthanised and, following removal and fixation of the globe, retinal whole mounts were prepared by making four radial cuts to produce a flat petal-like shape. Prior to euthanasia, some animals were trans-cardially perfused under terminal anaesthesia with the plasma marker FITC-dextran in order to image flowing segments at the RVP leading edge. ECs were identified using isolectin-B4 biotin-conjugate (Iso-B4) whilst astrocyte nuclei were detected with the pan-astrocytic antibody rabbit anti-Pax2 (Pax2). The astrocyte network itself was imaged using rabbit anti-fibronectin antibody. Appropriate images were captured at a range of objective magnifications.

4.4.2. Experimental Results

Retina whole mount images and data used to inform development of the mathematical model are presented in Figures 4.5 and 4.6. At E15.5, Pax2 immunoreactive astrocytes are located around the boundary of the optic nerve chiasm (Figure 4.5a), and by E18.5 a dense network is observed to have reached halfway across the retina (Figure 4.5b). Formation of the superficial RVP begins in the region bordering the optic nerve at P0, with the emergence of a dense network of Iso-B4 immunoreactive ECs (Figure 4.5c). At P3, astrocytes have reached the retinal periphery (Figure 4.5g) while the expanded EC plexus is now dense and highly branched (Figure 4.5d). Differentiated arterioles and venules are evident by P3, and by P5 a permanent pattern of five pairs of alternating arterioles and venules is established. Vascular pruning of the immature plexus begins near the optic nerve chiasm around P3, and capillary-free zones are evident along arterioles at P5 – venules are not extensively pruned (Figure 4.5e). By P8, pruning around primary arterioles is conspicuous across roughly 70% of the retinal radius, with clear vessel-free zones also surrounding secondary arterioles (Figure 4.5f). A quantitative summary is presented in Figure 4.5g, where it is clear that astrocyte and EC migration occur in conjunction with significant retinal growth. Retinal radius, measured

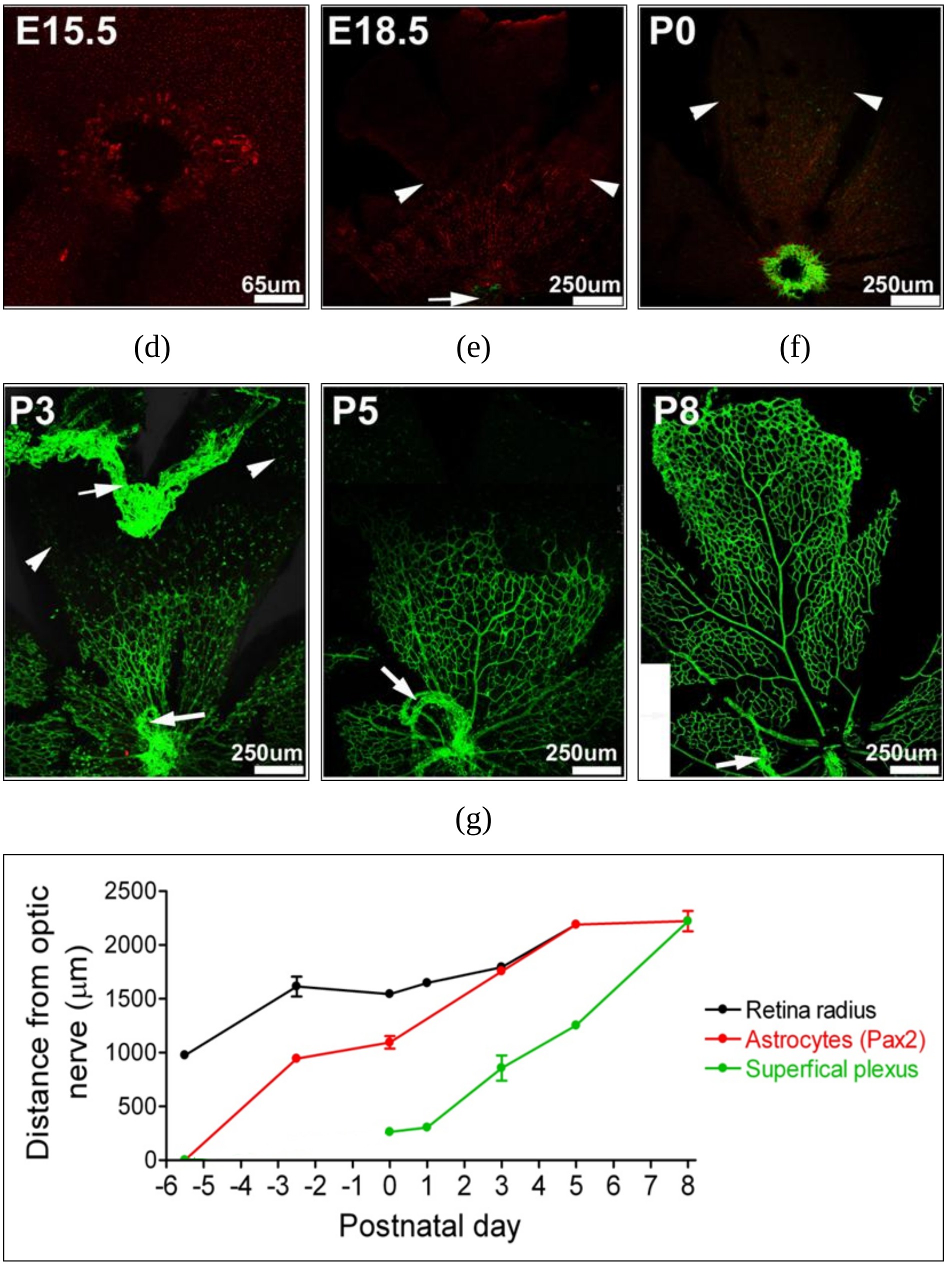

Figure 4.5: Caption overleaf.

as the distance from the centre of the optic nerve chiasm to the retinal edge, increases approximately 2-fold between E15.5 and P5. The endothelial plexus reaches approximately halfway across the fully-grown surface by P5 and approaches the periphery by P8.

Images taken at higher magnification reveal more details of the key processes controlling developmental progression. Prior to astrocyte migration, at E15.5,

Figure 4.5: Astrocyte and endothelial migration occur in parallel to retinal growth during formation of the superficial retinal vascular plexus. (a-f) Confocal images of immunohistochemically-stained murine retinal whole mounts showing the extent of astrocyte (Pax2, red) and endothelial cell (Iso-B4, green) migration at various embryonic (E) and postnatal (P) stages (note that the globe-shaped retina has been cut and flattened into a petal-like shape). Arrowheads in (b, c) indicate the extent of astrocyte migration; arrowheads in (d) indicate Iso-B4 positive microglial cells; arrows in (b, d-f) indicate remnants of the embryonic hyaloid architecture which supplies the growing lens. (g) Corresponding quantification of retinal radius (black), astrocyte (red) and endothelial (green) migration during formation of the superficial plexus in neonatal mice. Note that the endothelial network does not emerge from the optic nerve region until around the day of birth. Distances are measured from the centre of the optic nerve; data are plotted as mean ± SEM of at least 4 measurements.

fibronectin immunoreactivity is not detected on the retinal surface. However, the patterns of fibronectin and Pax2 immunoreactivity are closely matched at both E18.5 and P3 (data not shown). Moreover, endothelial tip-cells are subsequently seen to extend fine filopodial processes along the astrocyte-produced fibronectin scaffold (Figure 4.6a). Perfusion is detected up to the periphery of the expanding network at P3, indicating that the immature RVP leading edge contains flowing vessels (Figure 4.6b). This finding indicates that flow-mediated remodelling may play a significant role in capillary pruning of the plexus, even during the earliest stages of development.

4.5. Mathematical Model of Superficial Retinal Vascular Plexus Development

The growth and differentiation of the mammalian neural retina occurs postnatally in a highly reproducible and spatiotemporally distinct manner. Moreover, the discussion throughout Sections 4.2 and 4.4 reveals a dynamic and exquisitely-balanced process that provides an excellent target for a mathematical modelling study. As discussed previously in Section 1.4.2, modelling of *pathological* angiogenesis has been extensively explored by the mathematical modelling community over the past few decades but there have been relatively few attempts to model angiogenesis associated

(a)

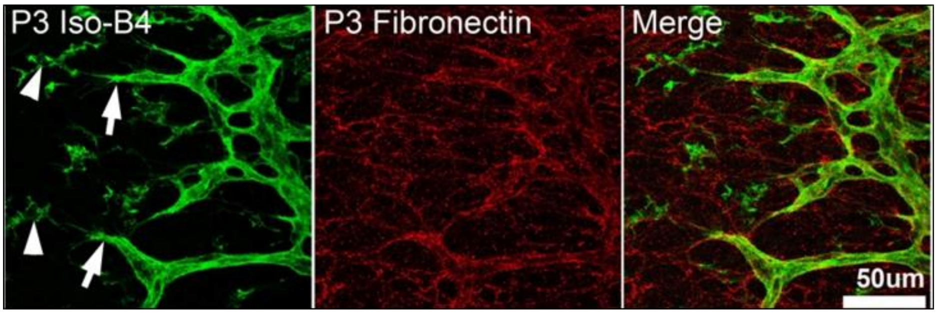

(b)

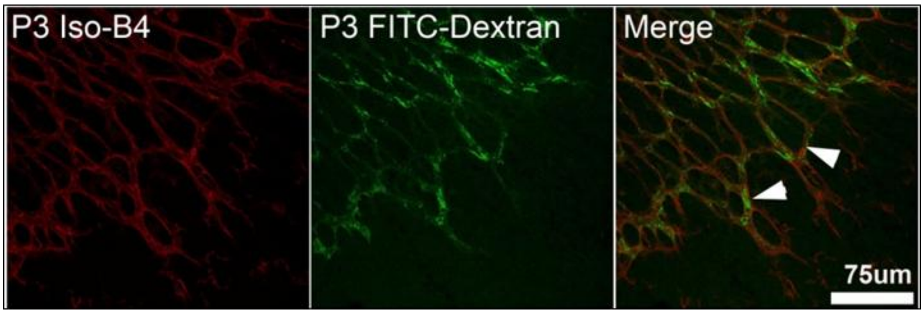

Figure 4.6: Immunohistochemically-stained confocal images of murine retinal whole mounts at postnatal day 3 (P3) reveal that astrocytes act as a template for endothelial sprouting and formation of the perfused vascular plexus. (a) The astrocyte network expresses fibronectin (rabbit anti-fibronectin antibody, red), which acts as a template for endothelial cell growth (Iso-B4, green). Endothelial tip-cells at the leading edge of the migrating vascular plexus (arrows) extend fine filopodial extensions over the fibronectin network. Iso-B4 positive microglia cells are also observed (arrowheads). (b) Co-visualisation of the plexus leading edge (Iso-B4, red) and intra-luminal plasma (FITC-dextran, green) indicates that perfused migrating retinal vascular plexus (arrowheads) is observed up to the region immediately behind endothelial tip-cells.

with normal development. A simple 1D continuum model of superficial RVP development *has* recently been reported, focusing on the evolution of astrocyte and EC profiles in response to appropriate growth factor concentrations (Aubert et al., 2011). In order to increase the prospect of meaningful predictions regarding RVP development in transgenic mice, however, a more complete modelling approach is required to firstly reproduce wild-type retinae. As in the wound healing angiogenesis study of the previous chapter, the approach we employ is inspired by the work of Anderson and Chaplain (1998b). The hybrid formulation allows for individual cell tracking, blood vessel topology visualisation, and reproduction of the dynamic remodelling phenomena associated with *in vivo* retinal development. The interactions between growth factors and relevant cell types – including VEGF-A production by astrocytes and the chemotactic response of astrocytes and ECs to PDGF-A and VEGF-A, respectively – are considered, and blood perfusion, with associated remodelling, is included throughout plexus development. The complete mathematical model, informed by a range of morphological and molecular *in vivo* data obtained between E15.5 and P8, is now detailed below. Note that additional details regarding various aspects of the modelling approach can be found in Appendix A.

4.5.1. Discrete Cell Migration and Growth Factor Evolution

The mathematical model begins with the emergence of astrocytes from the optic nerve region at E15 and subsequently describes their migration across the inner retinal surface. This migration is driven primarily by a chemotactic gradient of PDGF-A concentration (p), produced by the underlying plexus of RGCs (formed at an earlier stage of development). Astrocytes also exhibit some degree of random motility through the extension of numerous processes and are thought to respond haptotactically to gradients of extracellular RGC-bound protein density (e). Denoting by a the astrocyte density per unit area, the governing dimensionless equation describing astrocyte migration can consequently be summarised as:

$$\frac{\partial a}{\partial t} = \underbrace{D_a \nabla^2 a}_{diffusion} - \underbrace{\nabla.\left(\frac{\chi_p a}{(1+\xi_p p)} \nabla p\right)}_{chemotaxis} - \underbrace{\nabla.(\rho_e a \nabla e)}_{haptotaxis}. \tag{4.1}$$

The parameters D_a, χ_p and ρ_e characterise random motility, chemotactic response to VEGF-A and haptotactic response to RGC-bound protein, respectively. Note that the chemotaxis term also includes the parameter ξ_p, which reflects a decrease in chemotactic sensitivity at high PDGF-A concentrations (Lapidus and Schiller, 1976). Although Equation 4.1 describes the spatial and temporal evolution of astrocyte density, discretisation allows individual astrocyte tip cells to be tracked. This is achieved in an identical manner to that described for individual ECs in Equation 3.6.

During migration, astrocytes at the leading edge of the developing front bind PDGF-A, which is also free to diffuse and decay within the retinal tissue. Therefore, the dimensionless PDE characterising PDGF-A activity is:

$$\frac{\partial p}{\partial t} = \underbrace{D_p \nabla^2 p}_{diffusion} - \underbrace{\eta_p a_i p}_{uptake} - \underbrace{\sigma_p p}_{decay}, \tag{4.2}$$

where D_p is the normalised PDGF-A diffusion coefficient, η_p is the uptake rate of PDGF-A by discrete astrocytes at the leading edge (a_i), and σ_p is a decay constant. Biologically, η_p represents trans-membranic receptor binding of PDGF-A molecules such that they are no longer available to other cells (Mudhar et al., 1993; Fruttiger, 2002; Gerhardt et al., 2003; West et al., 2005; Uemura et al., 2006). Note that a_i is a Boolean value (1 or 0) that indicates the presence or absence of an astrocyte tip cell at a given position; this is defined in an identical manner to Equation 3.3 for endothelial tip cells in the earlier wound healing angiogenesis model.

Migrating astrocytes branch in response to PDGF-A and assume a stellate phenotype. This produces a dense astrocyte mesh that subsequently forms the foundation for capillary network expansion. During the formation of this astrocytic scaffold, hypoxic astrocytes secrete the growth factor VEGF-A, which acts as the primary chemoattractant for ECs. VEGF-A is capable of diffusing freely through the retinal tissue, whilst it is also bound by EC tip cells as they migrate. Therefore, the assumed dimensionless PDE characterising the evolution of VEGF-A concentration (c) can be written in the following form:

$$\frac{\partial c}{\partial t} = \underbrace{\alpha_c a_i^*}_{production} + \underbrace{D_c \nabla^2 c}_{diffusion} - \underbrace{\eta_c n_i c}_{uptake} - \underbrace{\sigma_c c}_{decay}, \tag{4.3}$$

where α_c is a measure of the production rate of VEGF-A by hypoxic astrocytes, D_c is the normalised VEGF-A diffusion coefficient, η_c is the uptake rate of VEGF-A by discrete endothelial tip-cells (n_i; a Boolean value defined as above for astrocytes), and σ_c is a decay constant. Similarly to both a_i and n_i, the variable a_i^* is defined only at grid points of the discrete lattice. This normalised value approximates the extent of local astrocyte hypoxia at each grid point according to the equation:

$$a_i{}^*(l,m) = \frac{2 - a_n(l,m)}{2}, \tag{4.4}$$

where l and m are positive parameters specifying a particular nodal position (i.e. $x = l\Delta x$ and $y = m\Delta y$), and a_n denotes the number of astrocytes identified with the node that are "covered" by ECs (i.e. on a 2D lattice this corresponds to a single value in the range 0 to 2).

As shown in Figure 4.5c, EC sprouts begin to appear at the optic nerve chiasm at P0 – some 6 days after the emergence of the first astrocytes. The production of VEGF-A by astrocytes therefore results in a pre-existing chemoattractant gradient on the retinal surface prior to endothelial migration. ECs, like their astrocyte companions, exhibit a degree of random motility, respond haptotactically to variations in density of matrix-bound proteins such as fibronectin (f), and migrate up gradients of chemoattractant (VEGF-A in this case). Correspondingly, the dimensionless equation describing the evolution of EC density takes a similar form to that describing astrocyte migration:

$$\frac{\partial n}{\partial t} = \underbrace{D_n \nabla^2 n}_{diffusion} - \underbrace{\nabla.\left(\frac{\chi_c n}{(1+\xi_c c)} \nabla c\right)}_{chemotaxis} - \underbrace{\nabla.\left(\rho_f n \nabla f\right)}_{haptotaxis}. \tag{4.5}$$

The parameters D_n, χ_c and ρ_f govern the random, chemotactic and haptotactic responses, respectively, while ξ_c once more quantifies reduced sensitivity to chemoattractant gradients at large concentrations. Notably, this equation is in an identical form to Equation 3.1 and, as such, we again refer back to Equation 3.6 to describe the methodology of generating discrete endothelial tip-cell migration.

4.5.2. Matrix Metalloproteinases and Extracellular Proteins

The remaining equations required to complete the model of retinal angiogenesis describe the key interactions between MMPs and extracellular proteins, leading to degradation of the host tissue and facilitating astrocyte and EC migration via haptotaxis. As in the wound healing model of the previous chapter, we assume that MMPs, now produced by both astrocyte and endothelial leading edge tip-cells, reduce the local concentration of matrix-bound proteins. The respective MMPs produced by astrocytes and ECs are free to diffuse and interact with their target matrix proteins and also exhibit a degree of natural decay. The matrix proteins themselves are produced locally by migrating astrocytes (Zhang et al., 2004; He et al., 2007) and are degraded by the appropriate enzyme. In line with these assumptions, the corresponding equations are:

$$\frac{\partial m_a}{\partial t} = \underbrace{\alpha_{m_a} a_i}_{production} + \underbrace{D_{m_a} \nabla^2 m_a}_{diffusion} - \underbrace{\sigma_{m_a} m_a}_{decay}, \tag{4.6}$$

$$\frac{\partial m_n}{\partial t} = \underbrace{\alpha_{m_n} n_i}_{production} + \underbrace{D_{m_n} \nabla^2 m_n}_{diffusion} - \underbrace{\sigma_{m_n} m_n}_{decay}, \tag{4.7}$$

$$\frac{\partial e}{\partial t} = \underbrace{\beta_e a_i}_{production} - \underbrace{\gamma_e m_a e}_{degradation}\ , \tag{4.8}$$

$$\frac{\partial f}{\partial t} = \underbrace{\beta_f a_i}_{production} - \underbrace{\gamma_f m_n f}_{degradation}\ , \tag{4.9}$$

where m_a and m_n are the concentrations of MMP produced by astrocyte and endothelial tip-cells, respectively. The α_i refer to the local production rates of each enzyme, D_i are the corresponding diffusion coefficients, and the σ_i are decay constants. The two distinct matrix-bound proteins (e.g. vitronectin, fibronectin) are produced by astrocyte tip-cells at rates β_e and β_f, and degraded by their corresponding enzyme at rates γ_e and γ_f. Before proceeding it should be clarified here that the normalised Equations 4.1 – 4.9 are obtained using a fully consistent time non-dimensionalisation. Therefore, cell densities, bound protein densities, concentrations of MMP and growth factor concentrations all evolve on an analogous timescale throughout RVP expansion.

4.5.3. Astrocyte and Endothelial Tip-Cell Branching

The final aspect of the cellular biology that needs to be addressed in the migration model is the process of astrocyte and EC branching. In Section 3.6.2, for the wound healing angiogenesis model, we approximated the outcome of complex VEGF-induced cell signalling pathways at the plexus edge by phenomenologically assuming that the likelihood of endothelial sprout tip branching is increased with increasing VEGF concentration. We make the same assumption for VEGF-A here, and the specific values are detailed in Table 4.1 where we note that a slight adjustment is required depending on the domain size. Further to this relationship, it is believed that migrating astrocytes branch in response to PDGF-A and exhibit a stellate phenotype that results in the formation of a dense astrocyte scaffold (Fruttiger et al., 1996). The experimentally observed astrocyte network expansion is therefore consistent with the assertion that the retinal surface is “flooded” with PDGF-A so in this case we assume instead a constant branching probability p_{branch}^{AC}. For both astrocytes and ECs we again further assume that branching can only occur in tip-cells that have reached a certain level of maturation, defined by t_{branch}^{AC} and t_{branch}^{EC}, respectively.

Normalised VEGF-A Concentration ($c_0 = c / c_{ref}$)	Branching Probability
$c_0 < 0.3$	0.04
$0.3 \leq c_0 < 0.5$	0.06
$0.5 \leq c_0 < 0.7$	0.16
$0.7 \leq c_0 < 0.8$	0.36
$c_0 > 0.8$	0.4

Table 4.1: EC sprout tip branching probabilities as a function of local normalised VEGF-A concentration. Note that the value of the normalising VEGF-A concentration c_{ref} varies with the domain size (i.e. 3 mm x 3 mm domain: $c_{ref} = 0.075$; 4.4 mm x 4.4 mm domain: $c_{ref} = 0.066$).

4.5.4. Oxygen Delivery

Once again, the inclusion of tip-cell branching at the advancing vascular front is a crucial component in the formation of capillary anastomoses and, subsequently, the simulation of blood flow in the nascent retinal networks. As in the wound healing angiogenesis model, unless otherwise stated, the networks are perfused in a manner that incorporates both phase separation at bifurcations and realistic structural adaptation by appropriately applying Equations 2.1, 2.2, 2.3, 2.5, 2.6 and 2.15. In addition, we now also introduce the concept of oxygen delivery from the vasculature to the surrounding tissue. As will be seen in due course, this turns out to be a fundamental model inclusion with respect to reproduction of the experimentally observed process of capillary pruning near arterioles.

Many previous mathematical models that have considered the transport of oxygen from a discrete vasculature to the local environment have been derived in the context of tumour-induced angiogenesis (Alarcon et al., 2003; Macklin et al., 2009; Welter et al., 2009). The general technique in these approaches is to assume that each individual capillary element provides a source of oxygen, the strength of which varies, for example, in proportion to the segment haematocrit. Since the dynamics of oxygen transport equilibrate on a timescale significantly shorter than that of cell proliferation, the advantage of such an approach is that a quasi-steady state assumption can be invoked when solving the reaction-diffusion equation for oxygen. Hence at each time step of capillary growth, a quasi-steady oxygen concentration profile can be calculated that allows continuous oxygen-related feedback to be considered in the EC migration model. The clear disadvantage of this approach, however, is the lack of explicit coupling to the underlying capillary flow regime; the inherent assumption being that the rate of oxygen transfer across capillary walls is negligible in comparison to the rate of oxygen supply (i.e. blood flow) to each segment. That is to suggest, in fact, that the only constraint on delivery of oxygen from the vasculature to surrounding tissues is the rate at which oxygen can diffuse (i.e. a diffusion-limited process). In the microvasculature, however, where vessel permeabilities to oxygen are high and many flow rates are relatively low, the ability to deliver oxygen depends crucially on the rate of oxygen supply and therefore the process is very much flow-limited (Levick, 2000). In the retina, in particular, where a hierarchical vascular structure is observed, we would expect a large degree of heterogeneity in the capability to deliver oxygen to the tissue as we move downstream from arterial to venous sub-regions of the plexus. In order to capture this feature in the model, we must explicitly incorporate the effect of perfusion on tissue oxygen delivery. This is achieved by simultaneously solving the following coupled equations (presented here in dimensional form for ease of interpretation):

$$\frac{\partial S_T}{\partial t} = D_{ST} \cdot \nabla^2 S_T + \frac{\pi K}{2} \cdot \sum_{\substack{vessel\\ sources}} \left[\frac{R_i \left(S_{V_i} - S_T \right)}{{L_i}^2} \right] - \sigma_{ST} S_T, \tag{4.10}$$

and:

$$\frac{\partial S_V}{\partial t} = \frac{F Q_E}{\pi R^2 L} \cdot \sum_{\substack{feeder\\ vessels}} \left[Q_j S_{V_j} \right] - \frac{Q S_V}{\pi R^2 L} - \frac{K}{2R} \cdot \sum_{\substack{tissue\\ sinks}} \left[S_V - S_{T_k} \right], \tag{4.11}$$

where S_T represents the tissue oxygen concentration and S_V is the concentration of oxygen in a particular vessel. We assume that the blood-borne erythrocytes are the sole source of oxygen, carrying it into the domain from the optic nerve inlets. At any given instant, the oxygen concentration in an individual vessel segment corresponds to the product of the volume fraction of RBCs in the vessel (i.e. haematocrit) and the amount of oxygen carried by those cells.

Equations 4.10 and 4.11 effectively combine three different modes of oxygen transport. Firstly, diffusion in the extracellular retinal tissue as characterised by the diffusion coefficient D_{ST} in Equation 4.10; secondly, downstream convection in the vasculature as described by the first two terms in Equation 4.11, where R, L and Q represent the radius, length and volume flow rate, respectively, of the segment in question; and, thirdly, transmural transfer between the tissue and the vessels at a rate governed by the surface area of the vessel wall and its permeability, K. Note the appearance of FQ_E in Equation 4.11, defined earlier in Section 2.5.2. This represents the fraction of RBCs at the feeding node that will enter the vessel, and is included to ensure that oxygen is distributed in the same proportion as RBCs at bifurcations. This first term in Equation 4.11 sums the contribution from each vessel flowing into the feeding node and from this the second term subtracts the concentration lost due to the outflow at the downstream end of the vessel.

These equations are solved in a framework where each 3D tissue element occupies the void between potential vessel positions, such that the dimensional length of each vertex is equal to the average vessel segment length. The transmural oxygen transfer component in Equation 4.10 is therefore made up from contributions from up to 12 separate perimeter vessels. Accordingly, each individual vessel also shares a boundary with up to 4 neighbouring tissue blocks such that each shares an equal surface area for oxygen transfer – this explains the final summation term in Equation 4.11. Throughout the period of retinal development that we consider (i.e. up to 8 days post-birth), oxygen-rich regions of the RVP contain a dense mesh of ECs and astrocytes. It therefore seems reasonable to assume that the background consumption of oxygen will experience no notable spatial or temporal variations. Thus, the final term in Equation 4.10 represents an assumed removal of oxygen from the tissue at rate σ_{ST}, describing not just the decay of oxygen, but also its uptake by the underlying host tissue and cellular plexuses.

4.5.5. Capillary Plexus Pruning

In Sections 4.2 and 4.5.1 we have alluded to the important role of local oxygen tension in determining the extent of VEGF-A production by astrocytes. Another highly oxygen-dependent process is the removal of poorly perfused vessels situated in areas of low VEGF-A concentration. In order to capture this important aspect of the developmental progression, oxygen transport between the vasculature and the host retinal tissue has been included in the model. The spatial distribution of oxygen throughout the RVP can be calculated at any given time, and these data can be used to inform capillary pruning. Specifically, we impose three conditions that must be simultaneously satisfied by a vessel segment in order for pruning to occur at that location:

1. The average oxygen concentration in the tissue surrounding the vessel must be above a critical value S_{Tcrit},
2. The age of the vessel must exceed a critical threshold A_{crit},
3. The vessel must be devoid of positive flow-related stimuli (c.f. Equation 2.15).

The first condition relates to the biological observation that oxygen downregulates production of VEGF, itself believed to be an EC survival factor (Dor et al., 2001; West et al., 2005; Scott et al., 2010; Weidemann et al., 2010). The critical age condition captures the experimentally observed lack of vascular pruning at the leading edge of the progressing endothelial plexus (c.f. Figures 4.5d-f) where capillary-free zones predominantly appear behind the leading edge during the first 8 days post-birth. The final condition captures the notion that each of the flow-related angioadaptation stimuli in Equation 2.15 plays a role in providing survival signals to the vessels. In essence, this is invoked when the radius of a vessel segment has dropped to its minimum permissible value R_{min}, implying that the positive growth stimuli have failed to overcome the natural shrinking tendency (parameterised by k_s).

4.5.6. Initial and Boundary Conditions

The largest domain considered for computational simulation corresponds to a 4.4 mm x 4.4 mm retinal surface, which equates to the maximum murine retinal diameter observed experimentally up to P20. The underlying capillary network template consists of 220 x 220 nodes, and amounts to approximately 50,000 individual capillary elements that are distorted to ameliorate topological flow bias (McDougall et al., 2002). The ophthalmic vein, from which the vascular network emerges, is located at the optic nerve head, which itself sits within the optic nerve chiasm of approximately 520 µm in diameter. This is represented in the model as an equivalent tissue-free void in the centre of the numerical domain. Zero-flux boundary conditions are imposed on the inner and outer domain boundaries such that the astrocytes, ECs, growth factors, MMPs and bound proteins remain confined to the retinal surface. The astrocyte and endothelial plexuses are initiated by the placement of 40 astrocyte and 10 endothelial sprouts that are evenly distributed around the perimeter of the optic nerve chiasm. The endothelial sprouts are phenotypically labelled *a priori* as being either arterial or venous, and these are distributed in an alternating pattern (Figure 4.7a); *in vivo*, it is thought that the fate of individual sprouts may already be determined at this early stage of development (Erber et al., 2006; Davies et al., 2010). All simulations begin at E15, with the initiation of the migratory response of astrocytes – the onset of EC migration is delayed by 6 days until birth in accordance with experimental observations.

We initially assume that RGC-produced PDGF-A has reached a steady-state concentration profile across the inner retinal surface prior to astrocyte emergence from the optic nerve. Zero concentration of PDGF-A is initialised in the region of the optic nerve head and, elsewhere, varies radially according to:

$$p(r) = p_{max} - \lambda e^{-\frac{r^2}{\omega}}, \tag{4.12}$$

where r is the normalised distance from the centre of the domain ($p_{max} = 1.0$, $\lambda = 0.45$, $\omega = 0.45$). Bound protein densities are initialised to unity, whilst VEGF-A and MMP concentrations are initialised to zero.

The final set of boundary conditions relate to the various aspects of the perfusion model. Prior to endothelial migration, there are no anastomoses on the retinal surface with only disconnected alternating arterial and venous sprout tips present; the former connected to a high pressure arterial circulation and the latter connected to a lower pressure venous system. In order to keep the two circulations separate until loop formation on the RVP, two additional planes are added below the main simulation domain (Figure 4.7b). The first of these contains only arterial parent vessels that connect each of the 5 arterial sprouts directly to the main *inlet* port of the system (located at the far left of the domain). The second additional plane contains only venous parent vessels that connect the venous sprouts directly to the main *outlet* of the system (located at the far right of the network). This orderly configuration allows inlet and outlet pressures (P_{in} and P_{out}, respectively) to be independently controlled and guarantees that flow on the retinal surface can only begin once endothelial anastomosis formation has occurred. The arterial and venous parent vessels are assigned radii R_{PV} that not only remain fixed throughout simulation, but are also larger than the maximum possible adapted vessel radius R_{max} on the developing plexus. This helps to ensure a uniform delivery of haematocrit to the developing capillary plexus by minimising the impact of any heterogeneity in the path lengths travelled, and bifurcations negotiated, by blood flowing through the parent vessels. Any asymmetry in the delivery of blood to the RVP was found to have a strongly detrimental effect on the evolution of physiologically realistic capillary structures. On the commencement of flow, blood with a fixed haematocrit H_D^{in} and oxygen load S_V^{in} is fed into the high pressure arterial inlet. Oxygen concentrations in both the tissue and vessels are initialised to zero and, finally, zero-flux tissue oxygen boundary conditions are imposed around the domain.

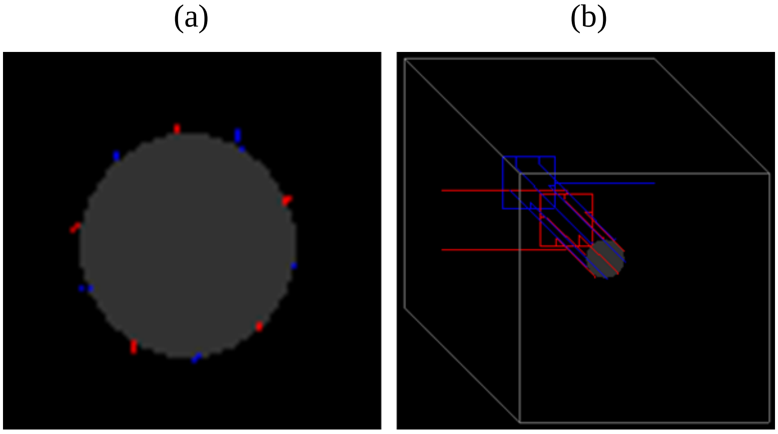

Figure 4.7: Initial vascular configuration for all simulations showing (a) 10 endothelial cell sprouts evenly spaced around the optic nerve, and (b) the underlying set-up of parent vessels. Segments connected to the high pressure arterial inlets (b, far left of domain) are identified in red, while segments connected to the venous outlet (b, far right of domain) are blue.

4.6. Numerical Simulation Results

A spectrum of simulation results is presented in this section, ranging from the straightforward simulation of astrocyte and EC migration, to more involved growth and perfusion-dominated remodelling of the developing RVP. Unless otherwise stated, all of the simulations take place on a domain of size 4.4 mm x 4.4 mm using the model equations described above, and apply the base case parameters listed in Table 4.2.

Parameter	Definition	Value
D_n	EC random motility coefficient	0.00018
χ_c	EC chemotaxis coefficient	0.4
ξ_c	EC chemotactic receptor saturation factor	0.6
ρ_f	EC haptotaxis coefficient	0.0125
D_a	Astrocyte random motility coefficient	0.00018
χ_p	Astrocyte chemotaxis coefficient	0.18
ξ_p	Astrocyte chemotactic receptor saturation factor	0.6
ρ_e	Astrocyte haptotaxis coefficient	0.0125
D_c	VEGF diffusion coefficent	0.005
η_c	VEGF uptake rate by EC tips	0.1
σ_c	VEGF decay rate	5.0
α_c	VEGF production rate by hypoxic ACs	3.5
D_p	PDGF diffusion coefficient	0.0025
η_p	PDGF uptake rate by ACs	0.1
σ_p	PDGF decay rate	3.0
D_{ma}	MDE diffusion coefficient	0.001
α_{ma}	MDE production rate by AC tips	0.00001
σ_{ma}	MDE decay rate	3.0
D_{mn}	MDE diffusion coefficient	0.001
α_{mn}	MDE production rate by AC tips	0.00001
σ_{mn}	MDE decay rate	3.0
β_f	ECM production rate by AC tips	0.5
γ_f	ECM degradation rate	0.1
β_e	ECM production rate by AC tips	0.5
γ_e	ECM degradation rate	0.1
μ_{plasma}	Bulk plasma viscosity	1.2×10^{-3} Pa · s
H_D^{in}	Inlet haematocrit value	0.45
S_V^{in}	Inlet vessel oxygen concentration	0.45

Table 4.2: Parameter values used in the base case simulations of wild-type RVP development.

Parameter	Definition	Value
D_{ST}	Oxygen diffusion coefficient	2.5×10^{-10} m$^2 \cdot$ s^{-1}
σ_{ST}	Oxygen consumption rate	0.02 s^{-1}
K	Vessel permeability to oxygen	2.5×10^{-4} m $\cdot$ s^{-1}
S_{Tcrit}	Critical tissue oxygen concentration for pruning	0.38
A_{crit}	Critical vessel age for pruning	1 day
P_{in}	Inlet arterial blood pressure	10660 Pa (4.4 mm) 9860 Pa (3 mm)
P_{out}	Outlet venous blood pressure	2060 Pa
R_{min}	Minimum permissible vessel radius	3.0×10^{-6} m
R_{max}	Maximum permissible vessel radius	1.2×10^{-5} m
R_{PV}	Radius of all arterial and venous parent vessels	1.4×10^{-6} m
k_s	Natural shrinking rate of vessels	1.7
k_p	Relative intensity rate of the pressure stimulus	0.8
k_m	Relative intensity rate of the convected stimulus	0.5
k_c	Relative intensity rate of the conducted stimulus	2.6
J_0	Saturation constant for the conducted stimulus	250
τ_{ref}	Reference wall shear stress	0.5 dyn $\cdot$ cm^{-2}
Q_{ref}	Reference flow rate	1.0×10^{-18} m$^3 \cdot$ s^{-1}
$(QH_D)_{ref}$	Reference RBC flow rate	6.75×10^{-14} m$^3 \cdot$ s^{-1}
L_c	Length constant for conducted stimulus decay	0.01 m
t_{branch}^{EC}	Threshold age for EC tip branching	1.85 hours
t_{branch}^{AC}	Threshold age for AC tip branching	1.85 hours
p_{branch}^{AC}	Astrocyte tip branching probability	0.28

Table 4.2 (cont'd): Parameter values used in the base case simulations of wild-type RVP development. (Note that P_{in} is the only parameter modified dimensionally when the domain size is rescaled – an increase in the pressure drop is required to maintain consistent inlet and outlet pressures on the retinal surface.)

4.6.1. Retinal Vascular Plexus Formation in the Absence of Blood Flow

As a first, simple benchmarking study we focus our attention on cellular migration across the RGC plexus, commencing with the appearance of initial astrocyte sprouts around the optic nerve at E15. We ignore any concept of blood flow in the model at this stage; the main concern here is reproduction of the evolving cellular fronts observed experimentally. As such, Figure 4.8 shows the progression of the astrocyte and EC networks as they respond to their various guidance cues. The corresponding concentration profiles of VEGF-A, produced by hypoxic astrocytes and bound by endothelial tip-cells, are shown in Figure 4.9. Astrocyte activity is observed in isolation on the retinal surface prior to birth, with a dense, highly connected scaffold emerging from the optic nerve chiasm (Figure 4.8a) and releasing VEGF-A into the surrounding milieu (Figure 4.9a). At P0, endothelial sprouts begin to migrate chemotactically in response to VEGF-A gradients laid down by the preceding astrocytes, producing nascent capillary structures that are highly disorganised and excessively branched (Figure 4.8b). The astrocyte front reaches the outer periphery of the RGC plexus at around P5, by which time the capillary plexus has extended approximately halfway across the domain (Figure 4.8c). Over this period, the VEGF-A concentration has evolved to produce a radial, wave-like profile travelling outwards into the domain from the optic nerve. Throughout plexus development, the peak of the concentration profile straddles the migrating front of the two cell types – lagging behind the leading edge of astrocytes, but guiding the EC progression behind (Figures 4.9b and c). A comparison between experimental and model data of the temporal development of the two cellular fronts is shown in Figure 4.10 – the *in silico* results are found to be in excellent quantitative agreement with the laboratory observations.

The down-regulation of VEGF-A production by astrocytes in proximity to functional vasculature is found to be crucial in the emergence of the travelling wave profile of growth factor, as can be seen by simulating the system in the absence of EC migration. In Figure 4.11 we present panels of the evolving VEGF-A gradients in this scenario, and it is clear that no travelling-wave peak is observed (note that each panel has its own legend to emphasise the regions of peak concentration at each time point). A peak concentration emerges initially at a small distance from the optic nerve where the astrocytic network first becomes very dense (Figure 4.11a), and this peak simply widens as time goes on (Figure 4.11b). Ultimately, VEGF production is balanced by decay, and the domain becomes flooded with the growth factor (Figure 4.11c).

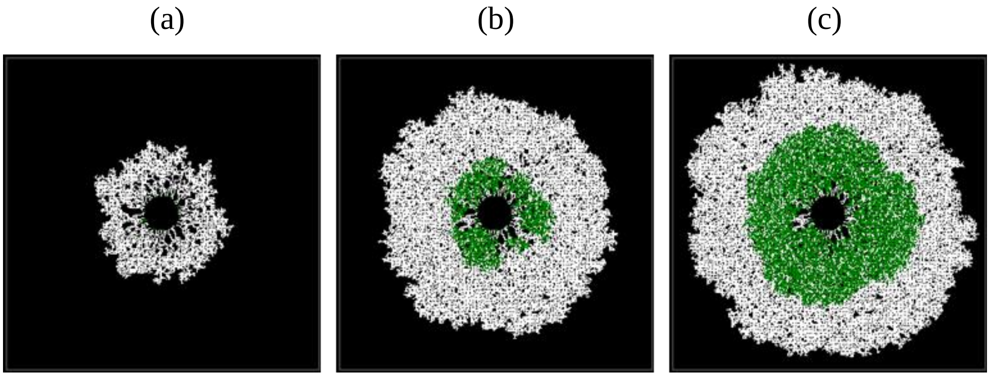

Figure 4.8: Growth of the retinal astrocyte network (white) and endothelial cell plexus (green) on a 4.4 mm x 4.4 mm domain. Migration of astrocytes begins at E15, while the endothelial cells follow at P0 – no flow is considered in this simulation. The snapshots shown here correspond to (a) E19.3, (b) P2.5 and (c) P4.7.

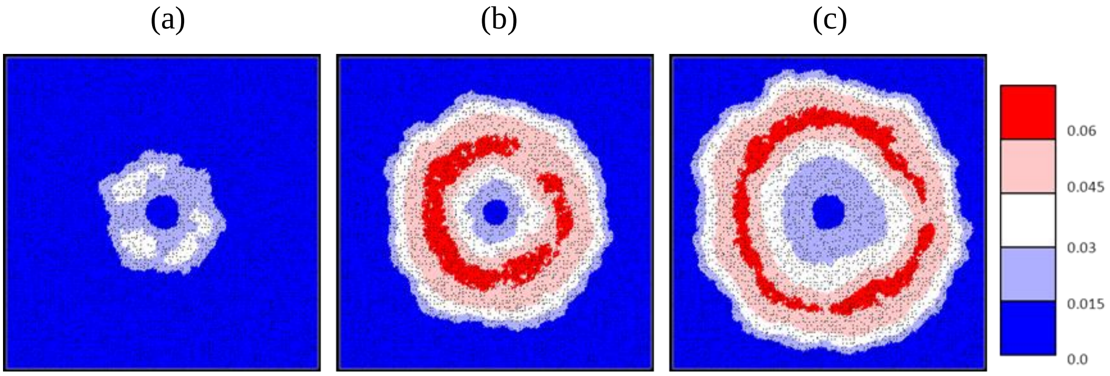

Figure 4.9: Evolution of the VEGF-A concentration profile corresponding to the snapshots of astrocyte and EC migration in Figure 4.8.

4.6.2. Retinal Vascular Plexus Formation in the Absence of Shunt Prevention

Whilst the cell migration results presented in the previous section are useful in establishing a quantitative link between experiment and simulation, they are only concerned with the temporal evolution of astrocyte and endothelial fronts as they migrate across the retinal surface. The lack of perfusion-related remodelling means that the only heterogeneity in evidence corresponds to the emergence of small acellular islands within the developing plexuses – a manifestation of the stochastic nature of the migration and branching processes. However, *in vivo* retinal vasculatures are highly

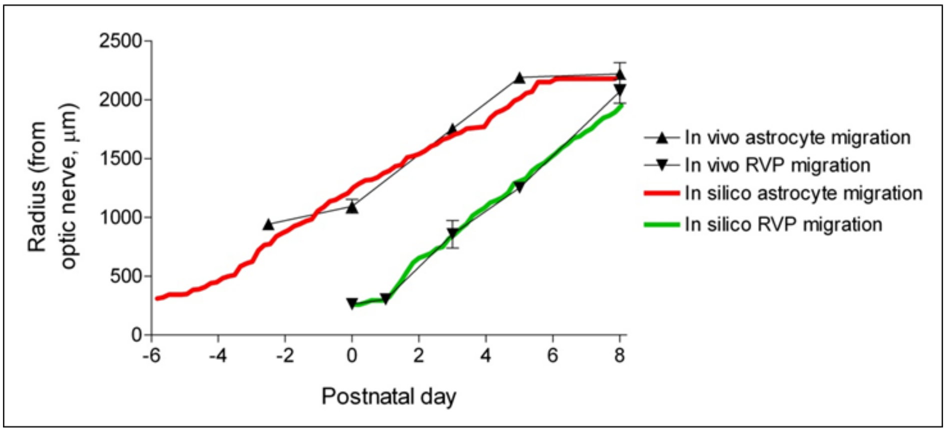

Figure 4.10: Plot comparing the rate of frontal advance of astrocytes and endothelial cells obtained experimentally with those obtained by simulation. Astrocyte migration is represented by triangles with error bars (*in vivo*) or a solid red line (*in silico*), while endothelial cell migration is represented by inverted triangles with error bars (*in vivo*) or a solid green line (*in silico*). Note that the experimental data corresponds to that presented in Figure 4.5.

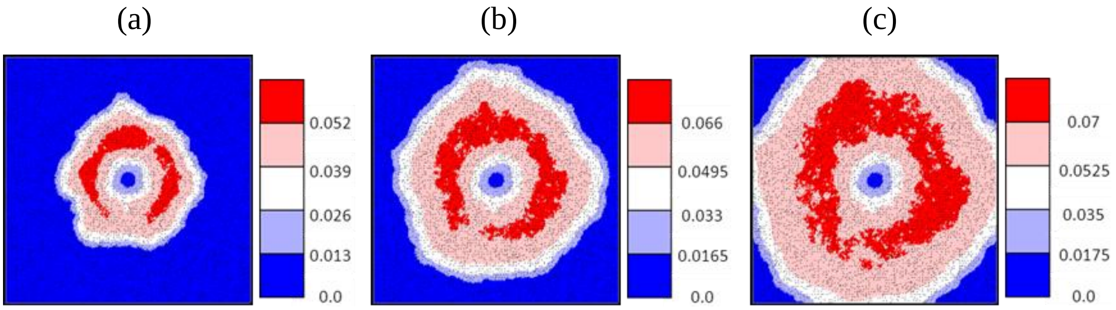

Figure 4.11: Evolution of the VEGF-A concentration profile in the absence of endothelial cell migration (note that the scale bar has been re-normalised for each image). The snapshots shown here correspond to (a) P0.4, (b) P4.0 and (c) P7.5.

structured, consisting of alternating arterial and venous vascular trees characterised by a hierarchy of capillary radii (c.f. Figure 4.5). In order to address this model deficiency, it is necessary to introduce perfusion, oxygen delivery and plexus remodelling as described in Sections 4.5.4 and 4.5.5. The simulation protocol adopted for all subsequent simulations incorporating blood flow is now briefly described.

As detailed in Section 4.5.6, each simulation begins at E15 with the initiation of astrocyte migration from the optic nerve chiasm, followed by the onset of EC migration at E21/P0. Ideally, flow and remodelling of the nascent capillary bed should be simulated whenever a new endothelial anastomosis occurs. The computational effort required to undertake such an assignment is necessarily prohibitive, however, so a compromise must be reached: a small sensitivity study determined that perfusion of the capillary bed to steady-state up to every 30 hours was adequate without compromising the final plexus architecture. The first period of flow is elected to begin around P2.5, when the EC network is fully connected and of an appreciable size. The volumetric flow-rate, blood rheological properties and capillary radius of each individual segment are then updated according to the appropriate equations described in Chapter 2, and re-iterated in Section 4.5.4. Once the structure of the vascular bed has converged to a steady state, Equations 4.10 and 4.11 for oxygen delivery are solved throughout the domain – resultant data are then used to prune the capillary network according to the algorithm detailed in Section 4.5.6. This newly pruned network subsequently provides the starting point for the next iteration of the angiogenesis model.

As a first attempt towards capturing the flow-induced development of hierarchical vascular structures in the retina, we neglect to consider the conducted and convected metabolic angioadaptation stimuli first discussed in Section 2.5.3. Instead we revert to the well-documented flow stimuli that have been applied previously in the context of tumour-induced angiogenesis (c.f. Section 2.4). Specifically, this requires the application of Equation 2.7 rather than Equation 2.15 for determining vessel dilation or constriction – all modifications to the base case parameters are given in Table 4.3. It should be noted, furthermore, that this simulation was performed on a reduced domain size of 3 mm x 3 mm (i.e. 150 x 150 nodes). Naturally, this restricts the time range of the simulation because the EC front now reaches the domain boundary at around P5; ultimately, however, this has no impact on the conclusions that we draw from the outcome of the simulation.

The resulting retinal vasculature is shown in Figure 4.12 – a self-reinforcing capillary shunt develops (Figure 4.12a), regardless of the extent of the outwardly-growing plexus. Consequently, due to phase separation, a non-zero haematocrit is restricted to a region proximal to the optic nerve (Figure 4.12b), and oxygen delivery to the retinal plexus is greatly restricted (Figure 4.12c). Such a dramatic dilation of both arterial and venous vessels proximal to the optic nerve head is not characteristic of wild-type retinae. In this tightly controlled developmental setting of neonatal RVP formation, this is a profound demonstration of the conclusion that was intimated by Figure 2.7 in Section

Parameter	Definition	Value
k_s	Relative intensity rate of vessel shrinkage	0.35
k_p	Relative intensity rate of the pressure stimulus	0.1
k_{met}	Relative intensity rate of the metabolic stimulus	0.07
τ_{ref}	Reference wall shear stress	$0.103\ \mathrm{dyn} \cdot \mathrm{cm}^{-2}$
Q_{met}	Reference flow rate	$1.9096 \times 10^{-11}\ \mathrm{m}^3 \cdot \mathrm{s}^{-1}$

Table 4.3: Parameter values used in the simulation of Figure 4.12, where the capillary radii evolve according to Equation 2.7 rather than Equation 2.15. All other relevant parameter values remain unchanged (c.f. Table 4.2).

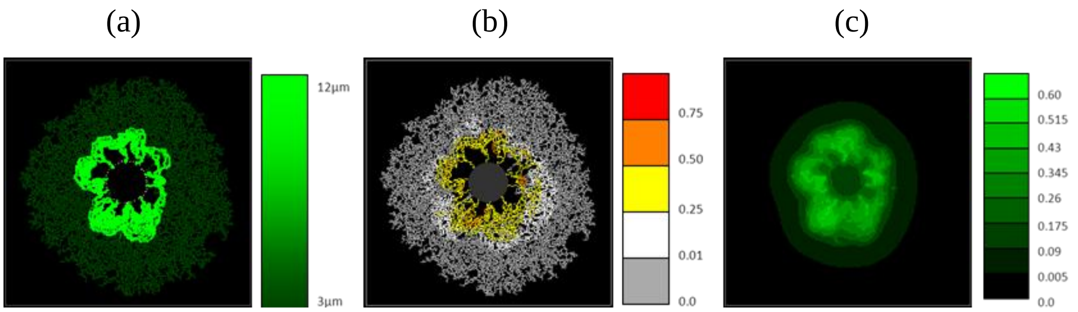

Figure 4.12: Snapshots at P4.7 from a vasculature which has undergone three cycles of growth, flow, oxygen delivery and pruning on a 3 mm x 3 mm domain. The structural adaptation algorithm applied here is described by Equation 2.7 – the particular parameters used can be found in Table 4.3. Specifically, the images show distributions of (a) capillary radii, (b) haematocrit and (c) tissue oxygen concentration.

2.6.3: mechanisms of shunt-prevention are critical in the generation of physiologically realistic capillary architectures. Therefore, the final phase of model development involves the inclusion of the latest flow-based angioadaptation stimuli as derived by Pries and co-workers (Pries et al., 2001; i.e. Equation 2.15).

4.6.3. Retinal Vascular Plexus Formation Incorporating Shunt Prevention

The base case simulation using the complete model is presented in Figure 4.13 where we again employ the full 4.4 mm x 4.4 mm domain. Each image highlights the behaviour of a particular model component throughout the development of the RVP:

from the commencement of blood flow at approximately P2.5 until the network approaches the domain boundaries at P8. Specifically, the panels show the post-flow, steady-state distribution of capillary architecture, network haematocrit, vessel oxygen concentration, tissue oxygen concentration, and areas of capillary pruning (i.e. a graphic highlighting the specific position of each pruned vessel segment, and the specific time point at which it was removed).

The progression of the underlying astrocyte network, and the associated VEGF-A gradients left in its wake (c.f. Figures 4.8 and 4.9), provides a crucial mechanistic link between the initial stages of retinal development and the later formation of a hierarchical capillary vessel network. It is apparent that the astrocyte front moves rapidly away from the optic nerve head and simultaneous VEGF-A production creates a travelling wavefront, with the peak concentration lying behind the migrating tip-cells. EC migration commences at P0, with network expansion driven largely by the chemotactic response to gradients of VEGF-A which trail an outward-moving maximum. The first period of flow takes place at P2.7, and angioadaptation, oxygen delivery and vascular pruning have already taken place throughout the nascent capillary network (Figures 4.13a, j, m). A striking feature of the haematocrit distribution at this early stage of development is its large degree of spatial heterogeneity within the network (Figure 4.13d), fashioned largely by the process of phase separation at vascular bifurcations. Almost every capillary element carries some level of haematocrit, suggesting that the extreme phenomenon of pure plasma skimming is largely absent within the dense mesh of vessels. Moreover, we note the presence of a number of vessel segments characterised by haematocrits exceeding 0.75, occurring mainly in two small pockets near the leading edge of the plexus. Recall that the input haematocrit value $H_D^{in} = 0.45$, indicating the occurrence of a concentrating effect in RBCs as blood flows to more distal areas of the retina. This result correlates well with the work of Ganesan et al. (2010), who observed equatorial vessel haematocrit values approaching 0.8 when simulating flow through an image-based network model of the fully developed adult murine retinal vasculature. In Figures 4.13g and 4.13j we show the distributions of vessel oxygen and tissue oxygen tension, respectively, where both are seen to map closely onto the distribution of haematocrit. As a consequence of blood flow and structural adaptation, a co-ordinated vasculature begins to emerge from the originally-homogeneous capillary bed (Figure 4.13a); with a number of the arteries tentatively

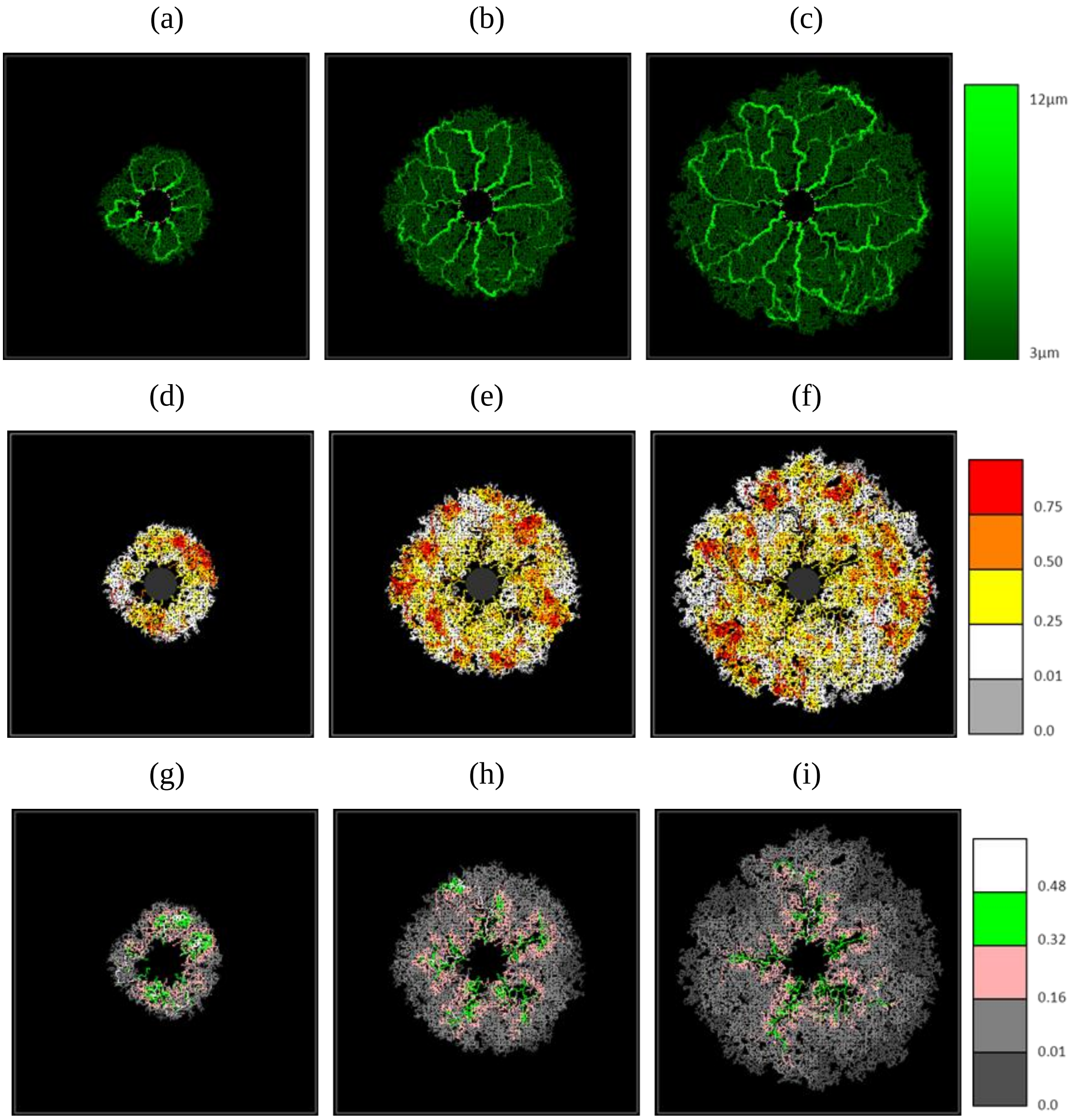

Figure 4.13: Snapshots of a developing retinal vascular plexus on a 4.4 mm x 4.4 mm domain showing (a-c) vessel radii, (d-f) haematocrit, (g-i) vessel oxygen concentration, (j-l) tissue oxygen concentration and (m-o) pruned capillary segments. Each column corresponds to a particular time point, namely (from left to right) P2.7, P5.2 and P7.7. Images from intermediate days have been omitted.

forming dilated anastomoses with each of their neighbouring veins. Even at such an early stage of development, this realistic looking network clearly constitutes a significant improvement on that presented in Figure 4.12a, further emphasising the importance of introducing shunt-preventing stimuli into the angioadaptation algorithm. It is also possible to observe the onset of oxygen-induced vascular pruning at this stage,

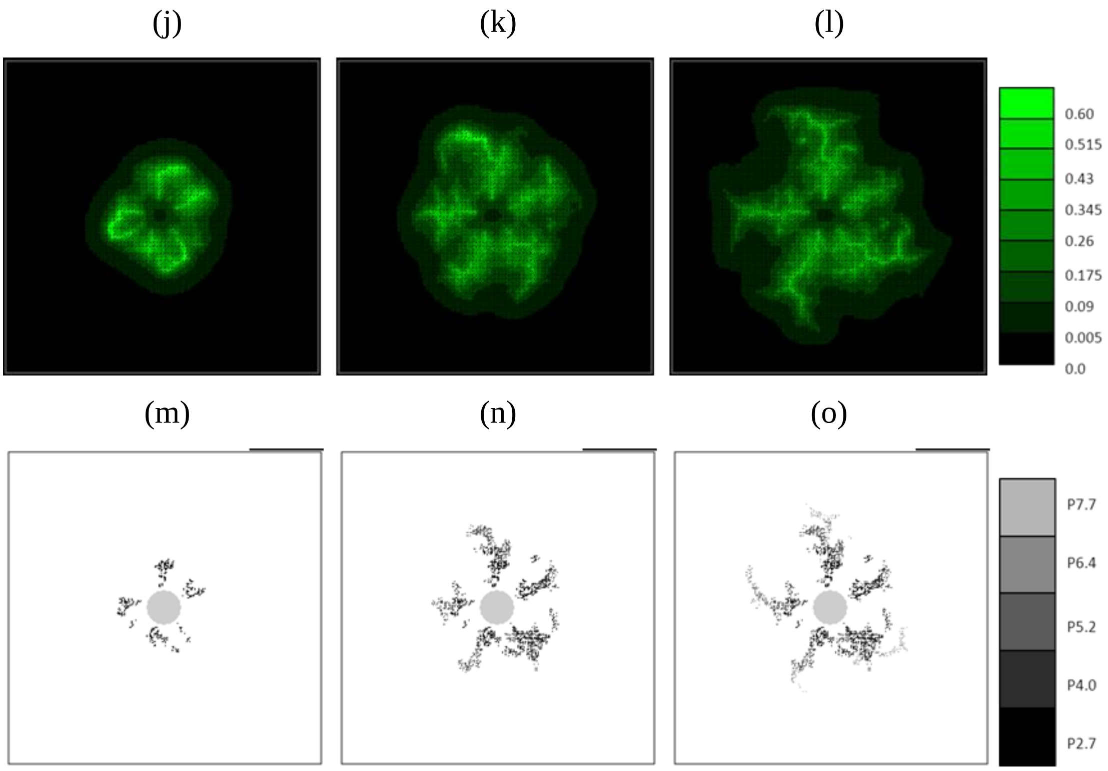

Figure 4.13 (cont'd): Snapshots of a developing retinal vascular plexus on a 4.4 mm x 4.4 mm domain showing (a-c) vessel radii, (d-f) haematocrit, (g-i) vessel oxygen concentration, (j-l) tissue oxygen concentration and (m-o) pruned capillary segments. Each column corresponds to a particular time point, namely (from left to right) P2.7, P5.2 and P7.7. Images from intermediate days have been omitted.

particularly around the uppermost artery, where a small capillary-free zone develops. For clarity, each pruned capillary segment is shown in Figure 4.13m. At this early time, only a small amount of pruning is seen, accentuating the presence of the small dilated arterio-venous loops.

After each 30 hours of growth, the simulated vasculature undergoes a cycle of flow, oxygen transport and capillary pruning. For brevity, we exclude simulation images from intermediate days and proceed immediately to consider the RVP at P5.2 – after the third cycle of perfusion and remodelling. The dynamic nature of capillary plexus development can be immediately inferred from a comparison between Figures 4.13a and 4.13b. As the vascular bed grows, changes in the network architecture are detected by the sensitive shunt-preventing stimuli and small dilated loops, prevalent near the optic nerve head at earlier times, are remodelled to produce larger arterio-venous loops capable of efficiently transporting blood towards peripheral regions of the domain. An interesting natural consequence of the angioadaptation algorithm is that the radii of arterial inlet segments evolve to be consistently smaller than their venous outlet counterparts (Figure 4.13b). Again, this corresponds to results obtained by Ganesan et al. (2010) who used a combination of measurements from confocal scanning microscopic images and the optimisation principle of Murray's law to quantify the diameter of each vessel segment of the murine superficial RVP. The haematocrit distribution throughout the plexus is again seen to be highly heterogeneous at P5.2 (Figure 4.13e). Although a large percentage of capillaries carry a proportion of RBCs that is lower than the input haematocrit value, localised regions towards the retinal equator again exceed 0.75. In contrast to P2.7, however, the haematocrit distribution no longer shares a strong correlation with the vessel oxygen profile (Figure 4.13h) and many of the high haematocrit regions of the capillary bed now display diminished vessel oxygen concentrations. This phenomenon is attributable to the increased plexus size, since narrow low-flow capillaries have a limited capacity to deliver oxygen to equatorial regions and, moreover, much of the oxygen transported transmurally from vessel to tissue occurs proximal to the arterial sources. This is also clear by inspection of the tissue oxygen profile (Figure 4.13k), as the majority of oxygen is seen to be supplied by the dilated anastomoses and oxygen tensions dip significantly as the venous sinks are approached. Vascular remodelling up to P5.2 is presented in Figure 4.13n: capillary-free zones are now conspicuous around each of the five inlet arteries and the most prominent region of vessel loss exists around the uppermost artery. Here, pruning is seen to extend along the length of the arterial section, before abating as the more hypoxic venous section is traversed.

The final period of blood perfusion covered by the base case simulation takes place at P7.7, and the corresponding results demonstrate the significant role played by flow and vascular remodelling in determining the final form of the retinal vasculature (Figure 4.13c). The removal of many small capillaries on either side of the main arterial vessels increases their prominence as major flow pathways, ensuring that they are retained as the network continues to expand towards the edge of the retinal surface. The emergence of the well-defined network architecture has a large impact on the distribution of retinal haematocrit (Figure 4.13f). Due to repeated occurrences of phase separation, the regions of greatest haematocrit are seen to be situated in the vicinity of the dilated arterio-venous loops, whilst lower haematocrit values characterise regions lying between the main vessels. The haematocrit increases downstream of each bifurcation on the arterial side, peaking at the retinal equator before gradually decreasing again towards the outlet veins. Referring back to Section 2.2, we note that this phenomenon is a well-known occurrence in the microvasculature and has been termed the "pathway effect" (Pries et al., 1989a; Pries et al., 1992). Notably, we again see a similarity to the work of Ganesan et al. (2010) who observed the same behaviour, albeit in a sparser, three-layer fully developed retinal vascular network. Under the assumption that RBCs are the primary source of oxygen in the system, this phenomenon also has interesting implications for the delivery of oxygen from the vasculature to the tissue. Oxygen is fed into the network at a constant concentration and leaves the vessels transmurally as it flows downstream. Therefore, in the absence of phase separation we would see a decreasing gradient of vessel oxygen concentration as we move downstream through bifurcating arterial trees – starving the outer regions of the retina of oxygen. However, phase separation actually leads to an *increasing* gradient of haematocrit away from the optic nerve, with the result that peak tissue and vessel oxygen tensions can occur far from the network inlets (Figures 4.13i and 4.13l). Such a result was not observed in the work of Liu et al. (2009) who examined the distribution of oxygen partial pressure in a human arterial retinal network. This is due, however, to the absence of phase separation in their model, which they attribute to the lack of research in this field for human vasculatures. It seems likely, due to the larger diameter of the vessels involved, that the effects of phase separation would be less prominent than found here in the murine case. We note in this case that a further consequence of the oxygen distribution is the degree of vascular pruning of small capillaries, which is re-inforced around a number of the dilated arterioles and now extends more than halfway towards the retinal periphery (Figure 4.13o).

This plethora of results not only correlate well with experimentally observed outcomes, but also provide a number of valuable insights into the developmental process that would be difficult to obtain in the laboratory. For example, the mathematical model provides important predictions of: the dynamics of RVP growth, with particular regard to the spatial and temporal evolution of VEGF-A concentration; the importance of hypothesised upstream convected and downstream conducted angioadaptation stimuli; the role played by phase separation in vascular pruning and the subsequent impact on overall plexus architecture; the temporal variation in haematocrit, vessel oxygen concentration and tissue oxygen concentration distributions throughout RVP growth. The latter of these is deemed to be particularly significant: obtaining physiological measures from neonatal mice is challenging because they do not open their eyes until around P16. Further to these predictions, in Figure 4.14, we also observe a qualitative similarity between *in vivo* and *in silico* network architectures at specific time points. It should be highlighted that no effort was made to explicitly reproduce the experimental whole-mount data quantitatively: the *in silico* capillary architectures emerged naturally from the adopted modelling approach. Specifically, Figure 4.14 shows images in the vicinity of the uppermost arteriole of the wild-type base case simulation at P2.7, P5.2 and P7.7, against typical arteriolar regions observed experimentally at P3, P5 and P8. We note, in particular, the similarities in the distribution and extent of oxygen-induced capillary pruning.

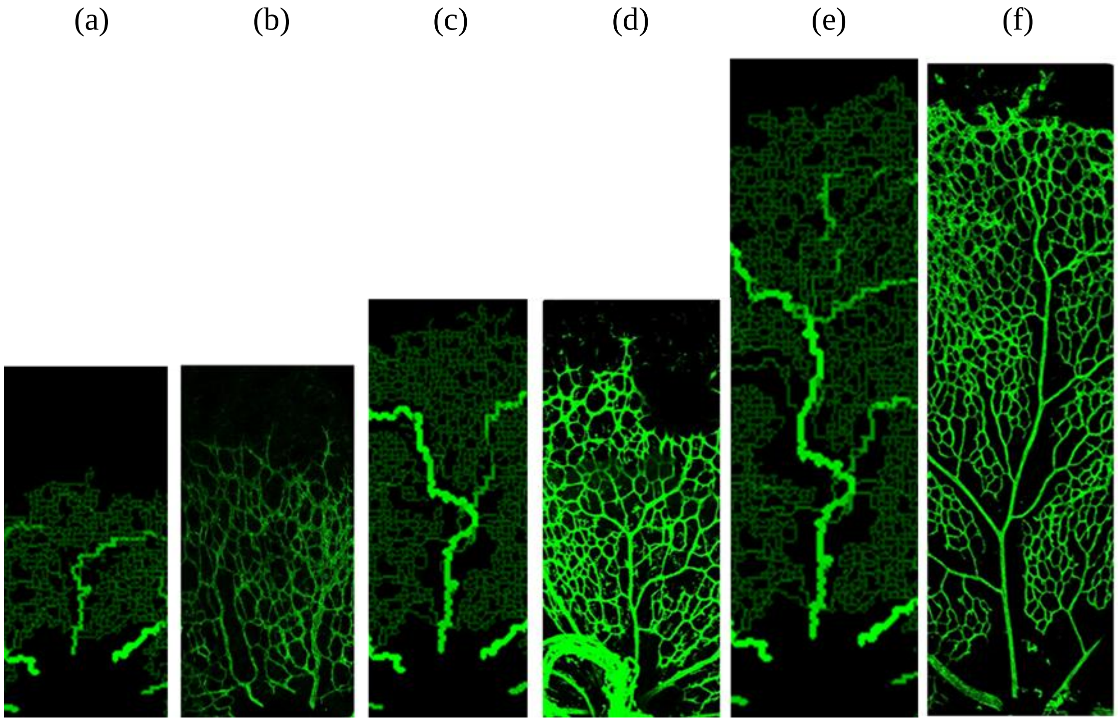

Figure 4.14: Detailed comparisons between *in vivo* and *in silico* capillary migration and remodelling in the developing retina. Specifically, the snapshots show (a) *in silico* P2.7, (b) *in vivo* P3, (c) *in silico* P5.2, (d) *in vivo* P5, (e) *in silico* P7.7 and (f) *in vivo* P8. The colours of the *in silico* vessel segments correspond to the colour bar in Figure 4.13a-c.

One final prediction we can obtain from the model, which has not yet been discussed, is the underlying distribution of capillary pressures in the network. Indeed, calculation of the pressure field for such a complex and evolving topology is found to be one of the most intricate aspects of the modelling process. Recall that two additional planes were added below the main simulation domain (Figure 4.7b). The first of these contains only arterial parent vessels and a looped manifold that connects each arterial sprout directly to the main inlet ports of the system. The second additional plane contains only venous parent vessels and a further looped manifold connecting the venous sprouts directly to the main outlet of the system. The pressure field corresponding to the superficial retinal vasculature at P7.7 in the base case simulation is shown in Figure 4.15a: high pressure arterial regions, seen to fan out from the optic nerve head towards the retinal equator, are interspersed with radiating low pressure areas. The figure gives a useful insight into the global dispersal of perfusing nutrients during retinal development and could also inform the application of future therapeutic interventions. A more quantitative analysis of the pressure distribution is presented in Figure 4.15b. The periodic nature of the arterio-venous pressures measured azimuthally at distances of 0.5 mm, 1.0 mm, and 1.5 mm from the centre of the domain is self-evident, with the amplitude of the pressure variations highest close to the optic nerve and progressively damped towards the edge of the domain.

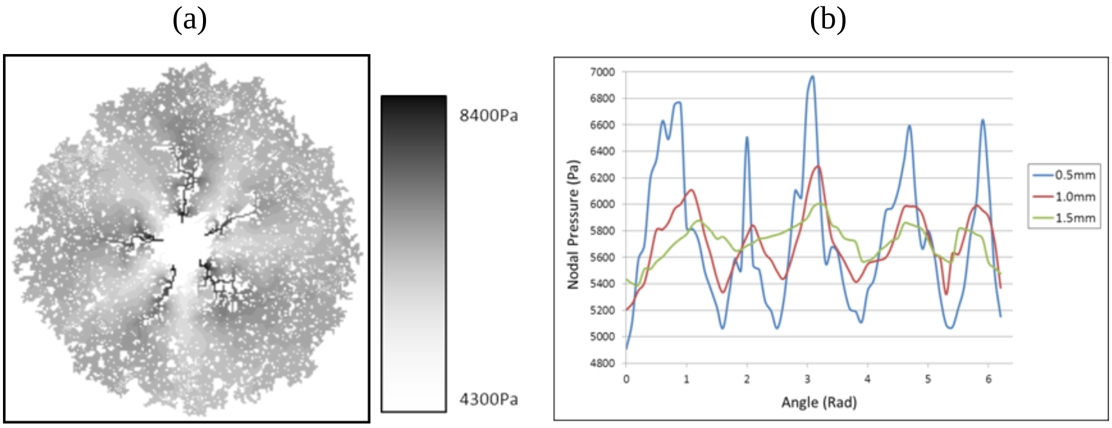

Figure 4.15: Quantification of the pressure distribution underlying the vasculature of Figure 4.13c. Specifically, the images show (a) contour plot of the nodal pressures on the superficial retinal vascular plexus, and (b) azimuthal pressure variations at the distances 0.5 mm (blue), 1.0 mm (red) and 1.5 mm (green) from the optic nerve centre.

4.7. Aberrant Plexus Formation

Having successfully anchored the mathematical model to the available experimental data from wild-type mice, a number of sensitivity analyses were next carried out to investigate the impact of a number of potential pathological or “mutant” cases which may impede normal development. In the interests of computational efficiency, most sensitivities were performed on a reduced domain size of 3 mm x 3 mm – as mentioned earlier in Section 4.6.2, this restricts the time range of the simulation to a maximum of around 5 days post-birth. Naturally, in these cases, a new base case simulation is required with which to make appropriate comparisons. For the relevant sensitivities shown, the vasculature presented represents the end point of 3 cycles of growth, flow, angioadaptation, oxygen delivery and capillary pruning. This is, however, sufficient time to appreciate the impact of the various parameter perturbations. We return to the full 4.4 mm x 4.4 mm domain for the final sensitivity, since the impact of this model alteration is not wholly appreciable until the later developmental stages.

4.7.1. Astrocyte Chemotaxis

The first sensitivity carried out using the model examines the impact of the underlying astrocyte plexus upon the subsequent migration of ECs during angiogenesis. The chemotactic response of astrocytes to PDGF-A, secreted by the RGCs at an earlier stage of development, was varied through the parameter χ_p in Equation 4.1. We investigated both a tenfold decrease and increase in the chemotactic parameter, and the resulting astrocyte networks at E17.7 (i.e. prior to the onset of angiogenesis) are shown in Figure 4.16. As the astrocyte chemotactic response is varied, the plexus architecture changes markedly: suppressed chemotaxis produces a slow-growing, dense astrocyte scaffold, whilst enhanced chemotaxis results in a rapidly-growing network that is a good deal sparser across half of the domain. The temporal evolution of the respective astrocyte fronts from E15 through to P3, compared with that of the base case simulation, is plotted graphically in Figure 4.17.

Perhaps the most interesting aspect of the sensitivity, however, is the effect that perturbed astrocyte chemotaxis has on the evolution of retinal VEGF-A concentrations and subsequent progression of angiogenesis. Capillary networks and contours of VEGF-A concentration at P4.7 are shown in Figure 4.18. VEGF-A is produced by hypoxic astrocytes, and so the onset of angiogenesis begins to down-regulate production in areas of the domain that are perfused with oxygen-rich blood. The model predicts that RVP development would be most damaged if the underlying astrocyte scaffold was produced too rapidly, namely under conditions of increased chemotactic sensitivity to PDGF-A. In this case, VEGF-A is primarily produced close to the retinal periphery

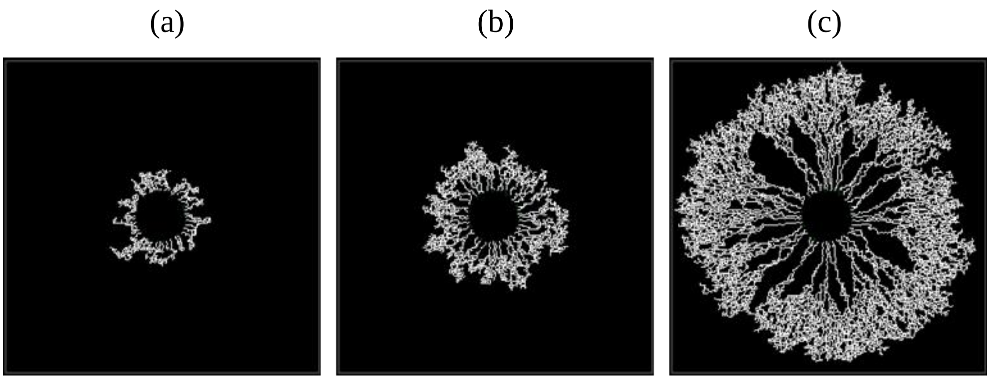

Figure 4.16: Snapshots at E17.7 displaying the astrocyte network on a 3 mm x 3 mm domain for a range of astrocyte chemotaxis coefficient (χ_p) values. The particular values considered were (a) 0.018, (b) 0.18 (base case) and (c) 1.8.

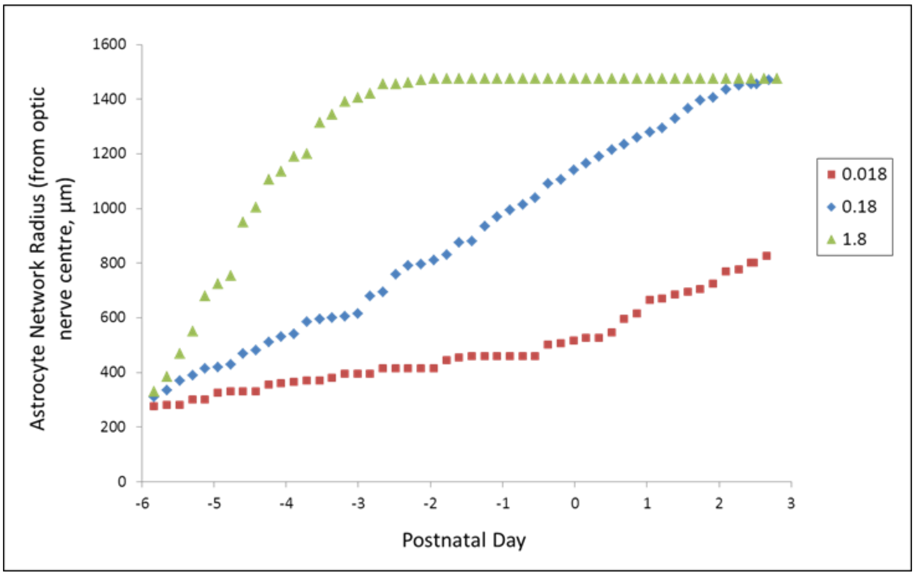

Figure 4.17: Plot comparing the rate of astrocyte frontal advance for each simulation in Figure 4.16. The series correspond to the astrocyte chemotaxis coefficient (χ_p) values 0.018 (blue diamonds), 0.18 (red squares) and 1.8 (green triangles). The plot is terminated around P3, when the base case astrocyte network (χ_p = 0.18) reaches the domain boundary.

where the density of hypoxic astrocytes is substantial (Figure 4.18c). The relative paucity of astrocytes proximal to the optic nerve means that VEGF-A gradients are woefully inadequate in providing chemotactic support for the emerging ECs and, consequently, the resulting vascular plexus is substantially compromised (Figure 4.18f).

Although no direct *in vivo* studies of astrocyte chemotaxis appear to have been reported to date, pathologically the sensitivity can be related to observations in transgenic mouse models where PDGF-A is overexpressed by RGCs or astrocytes (Fruttiger et al., 1996; West et al., 2005). In these experimental systems, astrocyte numbers are found to increase with increased concentration of PDGF-A, yet migration is suppressed. This suggests that a domain rich in PDGF-A could act as a promoter of astrocyte mitosis, whilst simultaneously saturating any chemotactic response.

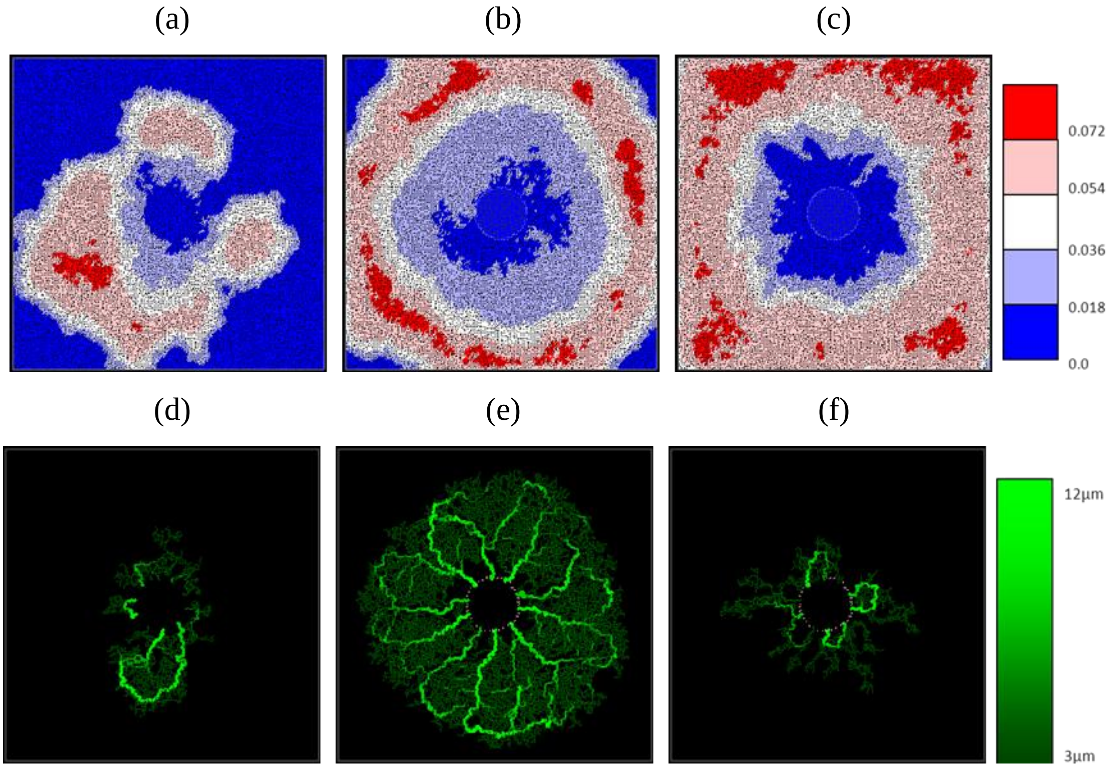

Figure 4.18: Snapshots at P4.7 displaying the (a-c) VEGF-A concentration profiles and (d-f) vessel radii distributions corresponding to the astrocyte scaffolds previewed in Figure 4.16. As above these were generated on a 3 mm x 3 mm domain using the astrocyte chemotaxis coefficient (χ_p) values (a, d) 0.018, (b, e) 0.18 (base case) and (c, f) 1.8.

4.7.2. VEGF-A Isoform

The second sensitivity we consider examines the impact of varying the specific isoform of VEGF-A produced by the astrocytes. Variations in the diffusive properties of different VEGF-A isoforms are well documented, and a number of murine transgenic mouse models specifically expressing, or over-expressing, a single isoform have been reported (Ash et al., 2000; Stalmans et al., 2002; Mitchell et al., 2006; Rutland et al., 2007). It has been shown that high molecular weight compounds are closely associated with reduced intra-matrix diffusion and increased binding tendency.

In order to investigate the repercussions for capillary migration on account of this aspect of VEGF-A isoform mis-expression, the *in silico* model is simulated using a VEGF-A diffusion coefficient (D_c) that is an order of magnitude greater than that characterising the wild-type case (a numerical analogue of isoform VEGF-A$_{120}$, for example). The resulting network at P4.7 is shown in Figure 4.19f, where we observe retarded capillary migration in comparison with that seen in the base case (Figure 4.19e). Increased diffusion produces both a shallower overall VEGF-A profile and reduced concentrations at the leading edge (Figure 4.19c vs. 4.19b). This result compares favourably with data from studies describing the RVP structure in transgenic mice (Gerhardt et al., 2003; Mitchell et al., 2006), where removal of the VEGF-A gradient, by increased VEGF-A expression, reduces the extent of endothelial migration. In the *in silico* setting here, both chemotaxis and capillary branching are necessarily impaired, resulting in a vascular network of irregular shape with numerous unperfused islands of retinal tissue. Although we omit the results here, the irregular mutant network is also found to produce an aberrant distribution of pressure, where the extent of the high and low pressure regions varies erratically. This causes some of the inlet arterioles to become compromised and constricted with inevitable implications for oxygen delivery to the retinal tissue.

Decreasing the VEGF-A diffusion coefficient in the model, again by an order of magnitude, allows us to predict the gross morphology of the RVP in mutant mice that over-express VEGF-A isoforms having greater binding affinity to the ECM (VEGF-A$_{188}$, for example). The resulting network, again at P4.7, is shown in Figure 4.19d, where reduced diffusion results in more localised pooling of VEGF-A and shallower concentration gradients (Figure 4.19a vs. 4.19b). Consequently, we again see a weakened angiogenic response, which in this case is partly attributable to the reduced chemotactic sensitivity at high VEGF-A concentrations (c.f. Equation 4.5).

Overall, the results from this sensitivity support the notion that the base case VEGF-A diffusion coefficient is optimum in producing a rate of capillary plexus expansion that is both perfectly consistent with wild-type retinal angiogenesis, and highly favourable for efficient delivery of oxygen and nutrients. It has been clearly demonstrated that the

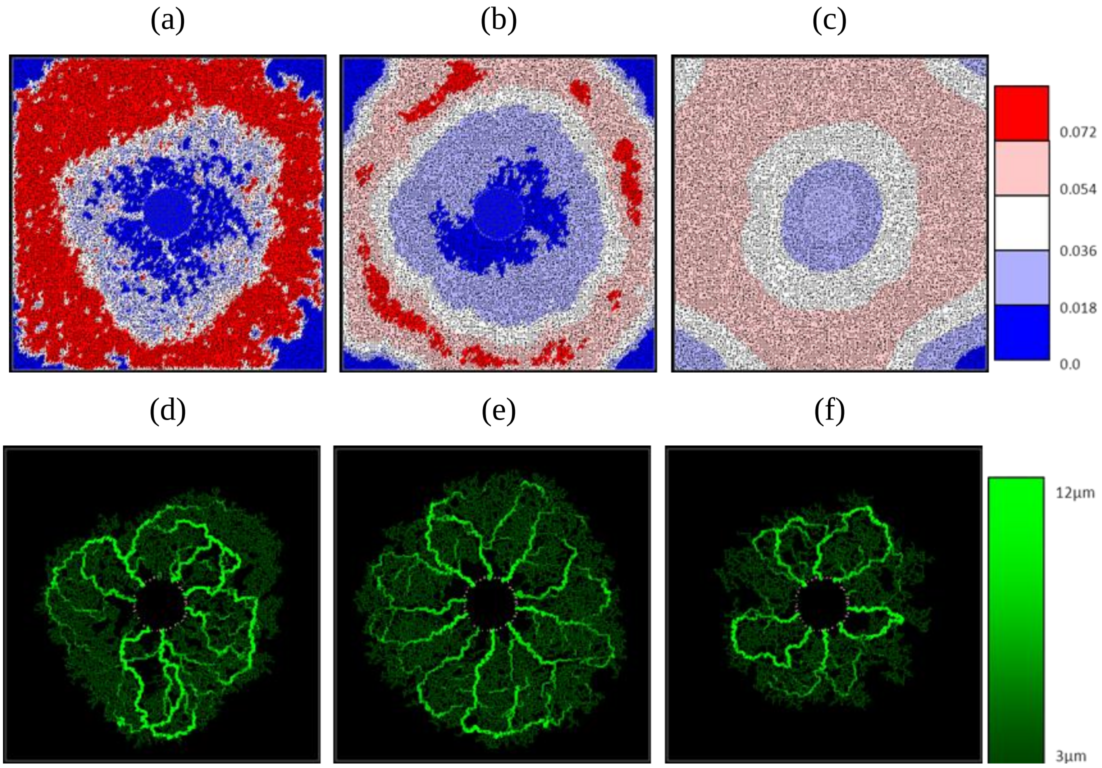

Figure 4.19: Snapshots at P4.7 displaying the (a-c) VEGF-A concentration profiles and (d-f) vessel radii distributions on a 3 mm x 3 mm domain for a range of VEGF-A diffusion coefficient (D_c) values. The particular values considered were (a, d) 0.0005, (b, e) 0.005 (base case) and (c, f) 0.05.

dominant VEGF-A isoform has a profound effect upon retinal development through its interaction with migrating ECs during angiogenesis. The model predicts that isoforms such as VEGF-A$_{120}$ could be expected to result in the formation of numerous poorly branched large diameter vessels, similar to the *in vivo* observations of Mitchell et al. (2006), whilst higher molecular weight isoforms would lead to the formation of large dilated vascular sacs, which have previously been reported in VEGF$_{188}$ mice by Rutland et al. (2007).

4.7.3. Inlet Haematocrit and Oxygen Consumption

The final series of sensitivity simulations performed on a 3 mm x 3 mm domain examines the importance of oxygen supply to the retina during superficial plexus development. Two parameters have been varied in the model: tissue oxygen consumption rate σ_{ST}, and input arterial haematocrit H_D^{in}, with the concomitant relative variation in input arterial vessel oxygen concentration S_V^{in}. An increased haematocrit is often symptomatic of hyperoxic conditions, whilst a reduced rate of oxygen consumption is indicative of reduced metabolism. Simulation results at P4.7 for increased input haematocrit ($H_D^{in} = 0.6$) and decreased oxygen uptake ($\sigma_{ST} = 0.002\text{s}^{-1}$) are shown in Figure 4.20 – base case panels are also presented for visual comparison. An increased haematocrit leads to the persistence of high RBC concentrations throughout dilated arterio-venous loops; the impact of phase separation at capillary junctions is less pronounced (Figure 4.20e vs. 4.20a). Consequently, large tissue oxygen tensions are maintained in the vicinity of all major vessels and extensive capillary remodelling occurs (Figures 4.20f and 4.20g). This ultimately causes substantial capillary-free zones to appear within the plexus (Figure 4.20h) and a state of hyperoxia is found to persist throughout retinal development; a situation that is replicated in the clinically significant condition of retinopathy of prematurity (Stout and Stout, 2003). This phenomenon is further amplified under conditions of reduced oxygen consumption (Figures 4.20i-l). Here, the entire retinal domain becomes flooded with oxygen and capillary-free zones are pervasive. These observations are similar to those witnessed in laboratory mouse models of oxygen-induced retinopathy. In this experimental model, neonatal mice are placed in a high oxygen environment, which leads to an increase in arteriolar oxygen concentration. The region of the retina within the oxygen diffusion limit of larger arterioles then becomes hyperoxic, and the subsequent cascade of events includes VEGF-A down-regulation, inhibition of endothelial plexus formation and vaso-obliteration of immature capillaries (West et al., 2005; Weidemann et al., 2010).

4.7.4. Capillary Pruning

The final model perturbation that we consider further illustrates the benefits of constructing a mathematical model that can be used to conduct simple numerical experiments, and potentially help to focus future *in vivo* experimentation. In this case we simulate the development of the RVP in a “numerical mutant” that has no capacity for capillary pruning – such an evaluation provides useful insight into the importance of pruning in the natural progression of wild-type plexus development *in vivo*. We return to the full 4.4 mm x 4.4 mm domain for this study, since stronger conclusions can be drawn from comparisons made in the latter stages of superficial RVP formation. Moreover, for ease of comparison, we perform this simulation on a vascular network

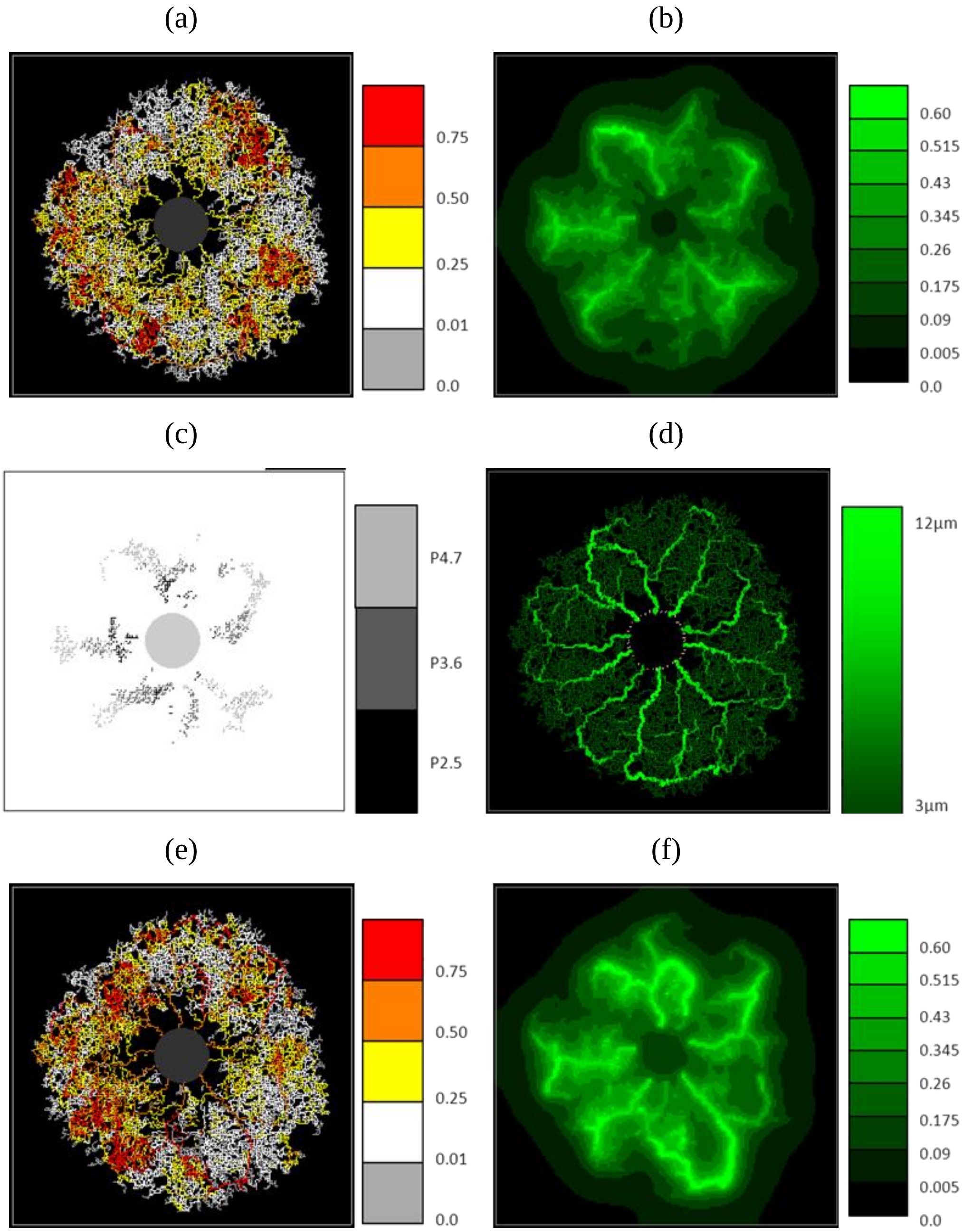

Figure 4.20: Snapshots at P4.7 of three different scenarios simulated on a 3 mm x 3 mm domain. Images (a-d) show the base case (parameter values $H_D^{in} = 0.45$ and $\sigma_{ST} = 0.02$), while (e-h) demonstrate the outcome of increasing inlet haematocrit ($H_D^{in} = 0.6$) and (i-l) display the result of reducing oxygen consumption ($\sigma_{ST} = 0.002$). In each case the images display (a, e, i) haematocrit, (b, f, j) tissue oxygen concentration, (c, g, k) pruned capillary segments and (d, h, l) vessel radii.

that evolves in an identical fashion to the wild-type case (c.f. Figure 4.13) – that is, at each flow period the vasculatures are exactly the same except for the absence of any

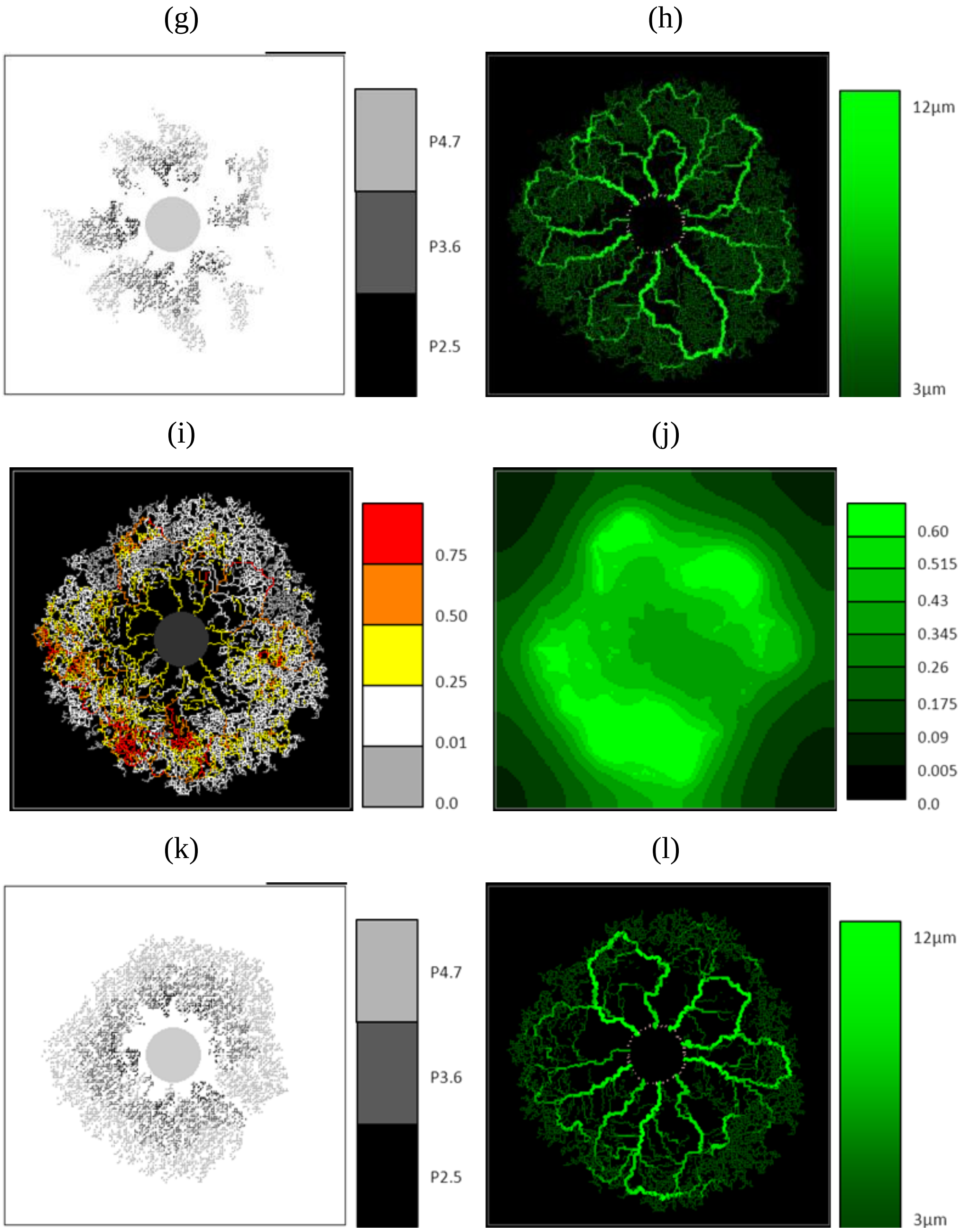

Figure 4.20 (cont'd): Snapshots at P4.7 of three different scenarios simulated on a 3 mm x 3 mm domain. Images (a-d) show the base case (parameter values ${H_D}^{in}$ = 0.45 and σ_{ST} = 0.02), while (e-h) demonstrate the outcome of increasing inlet haematocrit (${H_D}^{in}$ = 0.6) and (i-l) display the result of reducing oxygen consumption (σ_{ST} = 0.002). In each case the images display (a, e, i) haematocrit, (b, f, j) tissue oxygen concentration, (c, g, k) pruned capillary segments and (d, h, l) vessel radii.

previously pruned segments in the wild-type network.

The two end-point vasculatures at P7.7, corresponding to the presence or absence of capillary pruning, are presented in Figures 4.21a and 4.21d, respectively. Comparing these images it is apparent that, despite the extensive pruning in the wild-type case (c.f. Figure 4.13o), the spatial distribution of dilated vessels between the two final structures is broadly similar. In the absence of pruning, the angioadaptation algorithm still produces dilated arteriolar-venular loops, although there are slightly fewer dilated secondary arterioles (Figure 4.21d). The key aspect of the sensitivity is highlighted when examining the underlying blood rheology and flow properties of the capillary structures. Comparing the distributions of haematocrit (Figure 4.21b vs. 4.21e), it is clear that, in the absence of pruning, RBCs are distributed far more heterogeneously in the retinal plane, with a large fraction remaining within dilated vessels throughout their journey. This is attributable to the increased potential for plasma skimming at capillary junctions, as RBCs in the main feeder vessels bypass numerous slow-flowing side branches such that these vessels receive predominantly plasma. This is particularly evident in the arteriole at the “4 o’clock” position in Figure 4.21e, where pure plasma skimming (i.e. side branches receiving *only* plasma) is encountered – something that is not observable in the wild-type simulation. As a consequence of increased skimming, the distribution of vessel oxygen is also highly concentrated around the dilated arteriolar segments (Figure 4.21f).

Combining this series of results, we can conclude that vascular pruning reduces the extent of phase separation in the developing RVP, thereby preventing the build-up of large arteriolar haematocrits and high vessel oxygen concentrations. Rather than distributing flow from the main arterioles amongst many neighbouring capillaries, pruning of some segments induces an increased share of blood flow to those that are poorly supplied. These segments are then more likely to dilate and carry RBCs and oxygen to more distal regions of the superficial plexus. This hypothesis is confirmed by the contour plot of Figure 4.22, where we present the distribution of the *differences* in tissue oxygen concentration between the two simulations at P7.7. Areas of light colour indicate superior oxygenation in the wild-type simulation, whilst dark colours indicate areas that were better oxygenated in the mutant. The plot implies that the pruned network delivers oxygen to the tissue in a more efficient manner, with lower oxygen tensions around the main arterioles and increased tensions in venous regions. It should be remarked that, although the end-point vasculatures did not evolve to be completely identical, the evidence presented would seem to discount this as the sole reason for the observed differences in tissue oxygen concentration. In summary, the model predicts

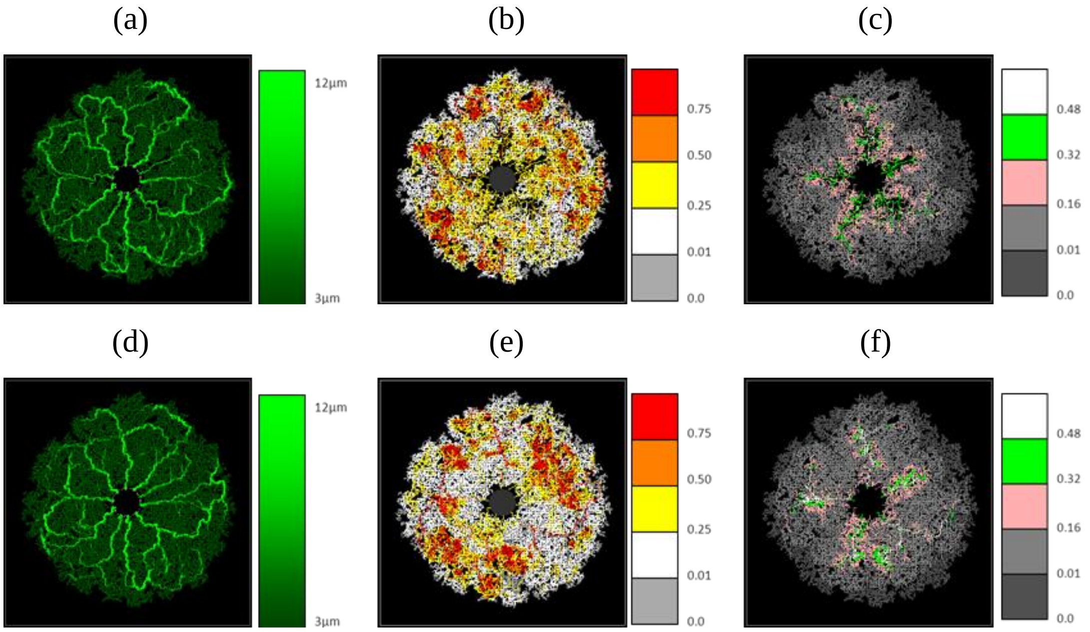

Figure 4.21: Snapshots at P7.7 on a 4.4 mm x 4.4mm domain displaying the simulated (a, d) vessel radii, (b, e) haematocrit and (c, f) vessel oxygen distributions in the (a-c) presence and (d-f) absence of capillary pruning. Images (a-c) correspond to the wild-type images of Figure 4.13c, f, i; the vascular architecture in (d-f) evolves identically, with the exception of any occurrences of pruning in the wild-type simulation.

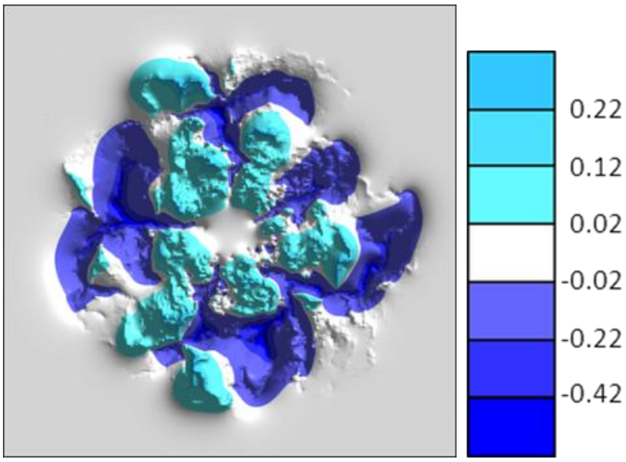

Figure 4.22: Contour plot displaying the differences in tissue oxygen concentration between the two simulations presented in Figure 4.21. Light-coloured regions indicate a greater concentration in the wild-type simulation (Figure 4.21a-c), while dark-coloured regions indicate a greater concentration in the "mutant" simulation (Figure 4.21d-f).

that, under the influence of phase separation of plasma and RBCs at vascular bifurcations, capillary pruning in the developing murine retinal vasculature is a major factor in promoting the efficient delivery of oxygen to distal regions of the plexus.

4.8. Discussion

The spatial and temporal development of nascent capillary networks plays a major role in determining tissue patterning and function. It is therefore important to understand how various cellular and molecular cues interact with migrating cells throughout angiogenic cascades. The growth and differentiation of the mammalian neural retina is dependent upon the formation of a multi-layered, interlinked vascular supply. The very nature of this RVP formation demarcates the system as ideal for *in vivo* angiogenesis investigation, and also represents an exquisitely-balanced objective for an *in silico* modelling study.

A previously reported 1D study of retinal angiogenesis has successfully reproduced rates of astrocyte and EC migration across the retinal plane during plexus development (Aubert et al., 2011). The inherent weakness of such a model, however, is the lack of scope for generating spatial information across the entire retinal surface. Therefore, in this study, a more realistic 2D hybrid PDE-discrete model has been derived in order to track the migration of individual astrocyte and endothelial tip-cells towards the outer retinal boundary. The *in silico* RVP structures generated by the model have been compared with corresponding experimental data at various stages of development and excellent agreement has been demonstrated.

It is important to recognise that the developing RVP is not an inert structure; the vascular bed adapts and remodels in response to a wide variety of metabolic and chemical stimuli. Hence, the complex capillary architectures observed *in vivo* in the retina can never be reproduced using simple migration equations alone. Indeed, it has been demonstrated that the retina poses a considerable test of angiogenesis modelling, and perfusion-related phenomena – based on the latest developments in vascular research – must be included to fully capture the intricacies of the *in vivo* observations. Specifically, the impact of incorporating phase separation of plasma and RBCs at capillary junctions (Pries et al., 1989a), and hypothesised conducted and convected angioadaptation stimuli (Pries et al., 2001; Pries et al., 2010), has been shown to be substantial (see also Secomb et al. (2007) for a similar approach to this study that deals with the interaction between angiogenesis, remodelling and capillary pruning - although not in the specific context of the murine retinal vasculature). The inclusion of these metabolic mechanisms in many earlier treatments of angiogenesis modelling has been somewhat lacking: in a tortuous *in silico* vasculature, the required concentration tracking algorithms are non-trivial to implement and, as such, become computationally prohibitive in extensive networks.

Throughout the modelling work, our approach has been firmly coupled to the experimental biology and we have attempted to honour the underlying cellular and vascular processes as closely as possible. The main focus of the investigation has been to understand how the various cellular, molecular, and metabolic cues regulate RVP growth and form in both wild-type and “mutant” situations. In the wild-type case, a broad spectrum of simulation results has been presented; ranging from straight-forward application of the astrocyte and endothelial migration equations, to more involved perfusion-dominated remodelling of the developing vascular plexus. The main outcomes of the retinal study have been the following:

- Initial cell migration results predicted that the evolution of VEGF-A concentration constitutes an outwardly moving radial profile, with a peak that lags behind the astrocyte leading edge and guides the EC progression behind. Concurrent data concerning the temporal development of the two cellular fronts were subsequently found to be in excellent quantitative agreement with laboratory observations. In the absence of capillary network formation, an ensuing failure to down-regulate astrocyte production of VEGF-A resulted in a flooding of the domain, with no wave-like growth factor profile observed.
- Small dilated loops prevalent near the optic nerve head at early times were remodelled as the vascular bed grew, replaced by more extensive arteriolar-venular loops that served to transport blood more efficiently towards equatorial regions of the domain.
- A large degree of spatial heterogeneity in haematocrit within the capillary plexus was noted. At all time-points considered, distal areas of the retina contained haematocrits exceeding 0.75 – a considerable increase on the input value, and caused predominantly by phase separation at capillary junctions.
- Phase separation leads to an *increasing* gradient of haematocrit away from the optic nerve, with the beneficial result that peak tissue and vessel oxygen tensions can manifest themselves far away from the arteriolar inlets.

The wild-type *in silico* RVP structures at various time points were compared with data from *in vivo* experiments and there was a high degree of both qualitative and quantitative agreement. Clearly, however, only a limited number of metrics have been applied in making such *in vivo* and *in silico* comparisons. Comprehensive model validation would require significantly more quantitative experimental measures to be produced, such as temporal data relating to the distributions of vessel density and capillary radii. We note that there are some minor differences between the simulated and observed architectures: *viz,* the mathematical model predicts large calibre arteries all the way up to the growing front, whilst *in vivo* vessels tend to taper off towards the periphery. This is principally due to a slight underestimation of decay in the upstream convected angioadaptation stimulus coupled with a likely underestimation of the maturity level required for nascent vessels to remodel. The model also predicts vascular plexuses that are slightly more dense than the observed retinal vasculatures (cf. Figure 4.14), and this is mainly attributable to the fact that they are grown discretely on an underlying distorted lattice – a slightly increased nodal spacing may have helped to optimise the comparison.

Having benchmarked the model against wild-type data, a range of “mutant” sensitivities was then reported with the aim of giving some insight into both the implications of, and mechanisms associated with, ocular conditions characterised by aberrant angiogenesis. The key outcomes of this aspect of the study can be summarised as follows:

- Suppression of astrocyte chemotaxis was found to produce a slow-growing, dense astrocyte scaffold and, conversely, enhanced chemotaxis resulted in a rapidly-growing, sparse network. The model predicted that development of the retinal vasculature would be most damaged if the underlying astrocyte scaffold was produced too rapidly. Experimentally, overexpression of PDGF-A in transgenic mice has been shown to reduce the extent of astrocyte migration in neonatal mice (Fruttiger et al., 1996; West et al., 2005), suggesting astrocyte migration is dependent on a gradient of PDGF-A; the modelling results presented here are highly consistent with this observation.
- Different isoforms of VEGF-A have different molecular weights and a varying ability to bind heparin residues in the ECM and diffuse freely (Park et al., 1993; Shima et al., 1996; Ferrara et al., 2002; Keyt et al., 2006). Reduced VEGF-A diffusion resulted in extensive localised pooling of VEGF-

A close to the optic nerve, leading to a weaker global angiogenic response. Interestingly, however, an increase in VEGF-A diffusion also led to a lower rate of capillary growth. Our results clearly demonstrate that the dominant VEGF-A isoform has a profound effect upon retinal development through its interaction with migrating ECs during angiogenesis.

- An increased input haematocrit was found to cause persistence of high RBC concentrations throughout dilated arterio-venous loops. Consequently, these loops maintained high local oxygen tensions and capillary pruning was seen to be extensive. This state of hyperoxia, which persisted throughout development, was further amplified under conditions of reduced oxygen consumption. These results parallel the vascular pathology observed in both human retinopathy of prematurity (Stout and Stout, 2003) and murine models of the same disease (Stone et al., 1996; Claxton and Fruttiger, 2003; Dorrell et al., 2010; Scott et al., 2010).
- In a numerical "mutant" with diminished potential for capillary pruning, RBCs were distributed in a highly heterogeneous manner with large concentrations around the main dilated loops and low concentrations in all other regions. Comparing the resultant tissue oxygen distribution with that from a wild-type scenario led to the hypothesis that the removal of vessel segments around primary and secondary arterioles actually increases the efficiency of oxygen delivery to distal regions of the developing superficial plexus. This result predicts that the extensive vascular pruning occurring throughout RVP development optimises the network for nutrient delivery.

A major advantage in studying the retinal vasculature is that it provides a capillary system that can be observed with relative clarity both *in vivo* and post mortem. Although a complete understanding of the developing retinal circulation is still lacking, it certainly provides an excellent target for theoretical studies. The hierarchical structure of the RVP poses a rigorous test of any angiogenesis model – such patterning is generally absent in the context of tumour-induced angiogenesis, for example – and it would appear that complex perfusion-related stimuli hold the key to understanding how these structures develop *in vivo*. It should be re-iterated that the retina is not simply a 2D structure and, in addition to the superficial RVP considered here, two deeper plexuses form through subsequent vertical sprouting as the retina expands. The application of the model to investigate the development of these additional layers has not been considered here. Nonetheless, it is hoped that the model could serve as a useful starting point for future research in this area, particularly with a view towards a better understanding of pathological ocular conditions.

Chapter 5

A New Generalised Model of Cell Migration I: Cell-Cell and Cell-Matrix Interactions

5.1. Introduction

In Chapters 3 and 4, the models of cell migration that have been presented were developed alongside a strongly coupled experimental programme. The architectures of the capillary (and astrocytic) networks generated by the wound healing and retinal cell migration models (c.f. Equations 3.1 – 3.5 and 4.1 – 4.9) have been shown to produce excellent agreement with various *in vivo* metrics (c.f. Figures 3.6, 3.8 and 4.10). Arguably, however, it is the inclusion of blood perfusion through the capillary networks that provides the most interesting and informative results. The concept of cell migration in these approaches is inherently simplistic, represented by a series of discrete events whereby tip-cells move from one grid point to another on an underlying lattice. Although the direction of this movement is intrinsically linked to various experimentally observed migratory cues from the local environment, other important features, such as contact inhibition and cell proliferation, are approximated rather broadly. By moving towards a lattice-free model, and considering cells with a stronger concept of physical size and shape, it becomes possible to study the spatial dynamics of cell migration events in much greater detail. The work presented in this chapter describes just such a lattice-free model that could provide the first step towards a more general angiogenesis model.

The model that we present in this chapter takes its inspiration from the agent-based approach of McDougall et al. (2006a), who performed 2D simulations of fibroblast migration and tissue regeneration during *in vivo* dermal wound repair. We propose a series of model extensions informed by a collection of theoretical and laboratory studies from the literature. The intention is to design a framework that is relatively general, such that the model has the potential to be applied in a variety of *in vitro* and *in vivo* settings for a range of different crawling cell types.

After briefly reviewing the modelling study upon which this work is based, we introduce the full set of equations governing discrete-point cell migration in the spatial domain. A few generalisations of this methodology are proposed, before the model is more extensively modified to incorporate cells that are physically-sized and capable of interacting with others in their locality. Initially our cells exhibit a loosely spherical morphology, but this constraint will be relaxed later in Chapter 6. For both the discrete-point and spherical cell formulations we shall also present a series of pertinent simulation results in order to demonstrate the range of behaviours that can be generated by modifying key parameters. The significance of these results will be discussed in the final section, before appropriate conclusions are drawn.

5.2. Modelling Foundations

As mentioned above, the overall model framework derives from the discrete-point cell migration model of McDougall et al. (2006a), which had previously been developed throughout a series of publications (Olsen et al., 1999; Dallon et al., 1999; Dallon et al., 2000; Dallon et al., 2001). This work considered the wound-induced recruitment of discrete-point fibroblast cells from healthy tissue (consisting of discrete collagen fibres) into a wounded region (consisting of discrete fibrin fibres), where the instantaneous migration direction was determined by three competing mechanisms: chemotaxis, persistence (i.e. the tendency to maintain the current migration direction) and contact guidance (i.e. alignment along the local fibre orientation). The migrating cells were also assumed to produce collagen and degrade fibrin in order that the fibrin clot would eventually be replaced by healthy collagenous tissue. Importantly, however, a further crucial feedback was included whereby the migrating cells re-oriented the fibrous collagen matrix in their locality. Consequently, this study provided numerous

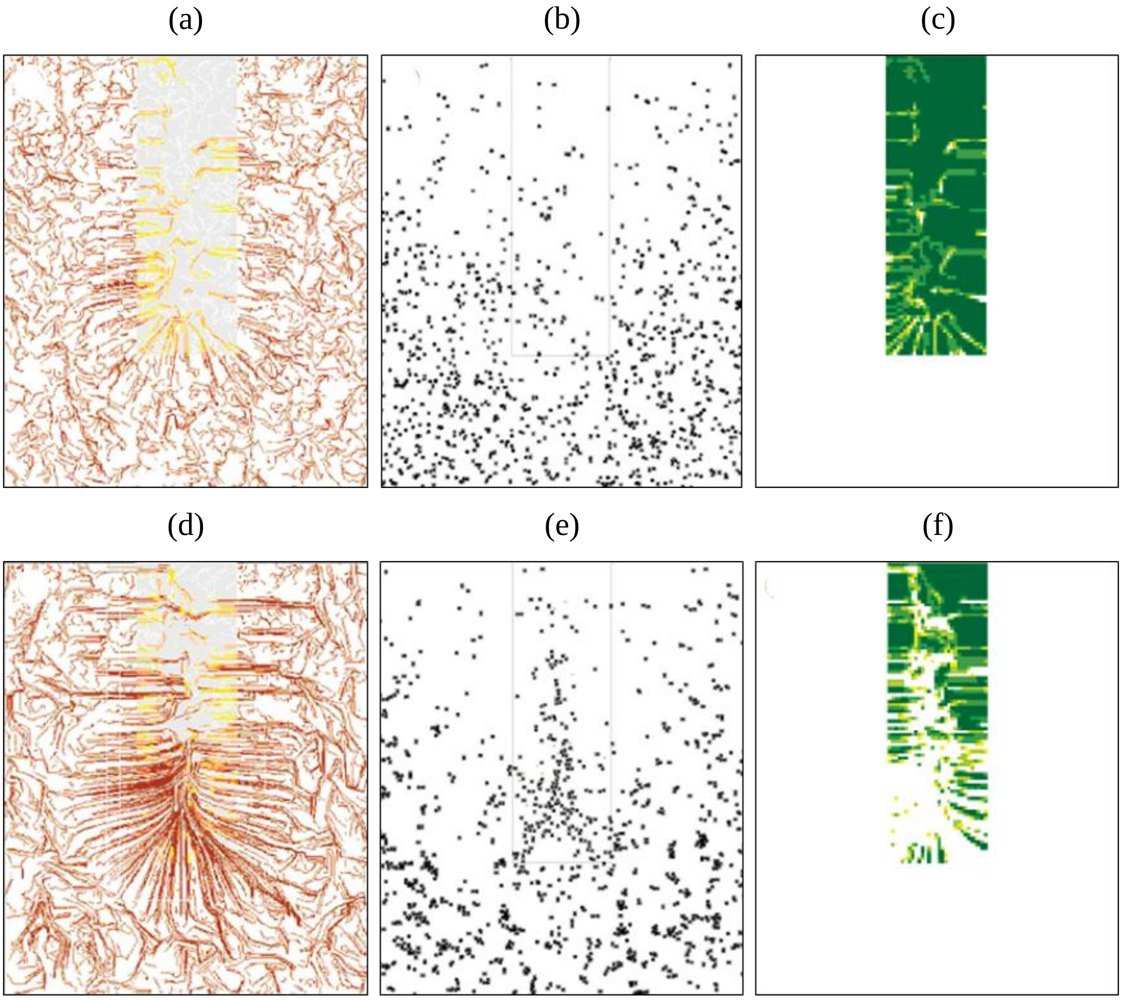

Figure 5.1: Snapshots taken from McDougall et al. (2006a) showing a typical simulation of wound-induced tissue regeneration after (a-c) 25 hours and (d-f) 100 hours. Specifically, the images show spatial distributions of (a, d) collagen fibre orientation and density, (b, e) fibroblast centroid positions and (c, f) fibrin density. Initially, the wounded region is filled with fibrin and devoid of both fibroblasts and collagen. Fibroblasts are subsequently recruited from the intact perimeter of randomly-oriented collagen towards the wound site in response to a chemoattractant gradient. The migrating cells lay down new collagen and degrade fibrin within the wound; however, the collagen fibres are simultaneously re-oriented towards the direction of cell movement, resulting in conspicuous collagen alignment (i.e. scar formation) in the vicinity of the wounded region.

predictions regarding the mechanisms of scar formation during the healing process, by investigating the emergence of conspicuous collagen fibre alignment in the vicinity of the wounded region. A series of images depicting the progression of a typical model simulation is presented in Figure 5.1.

As stated earlier, we wish to develop a generalised, adaptable cell migration framework that is applicable in a wide range of scenarios. The above discussion (and simulation images), however, indicate that the model of McDougall et al. (2006b) is limited to the behaviour of a particular cell type (fibroblasts) within a very specific environment (dermal wound healing). If we wish to consider other scenarios characterised by cell movement in the absence of chemoattractants or an underlying fibrous substrate, however, the existing model would simply predict continuous migration in a straight line (i.e. persistence only). This would appear to be rather unrealistic; as such, the inclusion of a new stochastic directional cue is just one of the generalisations that we choose make in the improved model discussed in the next section.

5.3. Discrete-Point Cell Model

As noted above, the original model of McDougall et al. (2006a) considers the migration of discrete-point cells on a lattice-free 2D domain. Although discrete-point migration models are inappropriate for studying systems in which cell-cell interactions are prominent, they provide an excellent methodology with which to examine the movement trajectories of cells existing in (relative) isolation. The model assumes that the movement of each cell is characterised by a direction $\boldsymbol{u}^i(t)$ in the plane and a speed $s^i(t)$, both of which vary in response to a range of local environmental factors. Note that throughout this chapter, the superscript *i* will be used to denote any variable that is defined for an individual cell. The motion of each cell is therefore governed by the equation:

$$\frac{d\boldsymbol{f}^i(t)}{dt} \equiv \dot{\boldsymbol{f}}^i(t) = s^i(t) \cdot \frac{\boldsymbol{u}^i(t)}{\|\boldsymbol{u}^i(t)\|}, \tag{5.1}$$

where $\boldsymbol{f}^i$ denotes the spatial position of the cell. Biologically, the calculation of $\boldsymbol{u}^i$ at a particular time is assumed to represent the direction in which a dominant pseudopod is established by attachment to the underlying substrate (c.f. Section 1.2.1). Therefore, the time between calculations of this vector should reflect the average frequency of pseudopod establishments for the particular cell type being modelled. This is the basis of our first proposed generalisation of the original model: rather than allowing each cell to calculate a new migration direction at *every* time step, we instead assume that $\boldsymbol{u}^i$ is calculated every τ_u time units, where τ_u approximates the time between pseudopod extensions (N.B. in order that $\boldsymbol{u}^i$ is not generally calculated in all cells at once, each cell is initially assigned a random point in its “pseudopod cycle”). Note that this imposes an upper bound (but no lower bound) on the time step size Δt when solving Equation 5.1 numerically. In the context of the model, the precise form of the vector $\boldsymbol{u}^i$ is determined by weighting the respective contributions of a range of migratory cues. We now proceed to explain the modelling rationale of each of these cues in detail.

5.3.1. Persistent Random Walk

In Section 5.2 we highlighted a deficiency in the model of McDougall et al. (2006a): in the absence of migratory cues such as a chemotactic gradient or contact guidance (e.g. *in vitro*), persistence becomes the only migratory cue and the model predicts that cells will migrate continuously in a straight line. We wish to modify the model in order that it is capable of predicting realistic migratory behaviour of cells in the absence of external environmental stimuli.

The characteristic motion of migrating cells in the absence of external cues has long been described as a so-called persistent random walk (Patlak, 1953), and a number of detailed mathematical models have been derived with which to analyse such behaviour (Othmer et al., 1988). In keeping with our agent-based approach, we propose a relatively simple method for incorporating this stochastic movement into our model – the inspiration for which was taken from recent research into the behaviour displayed by isolated *Dictyostelium discoideum* and *Polysphondylium* amoebae cells devoid of external signals (Li et al., 2008; Bosgraaf and Van Haastert, 2009). The approaches adopted in these studies are fundamentally different from one another: the former analyses cell trajectories, while the latter analyses pseudopod extension patterns. The overall conclusions regarding the general migratory behaviour, however, are much the same. The cells are found to perform a series of long, relatively straight zig-zagging “runs” interspersed by random “turns” – it is believed that this motion enhances the opportunity of finding a target or external signal. Furthermore, due to the highly conserved migratory machinery of eukaryotic cells, this type of behaviour is most likely characteristic of an array of different cell types (Li et al., 2008).

In order to reproduce such behaviour in the model, we require two separate components to describe the cell motion: persistence, which we retain from the original model, and a newly-formulated stochastic stimulus. Persistence, the tendency of cells to maintain their previous migration direction, is defined by the equation:

$$\boldsymbol{v}_a^i(t) = \dot{\boldsymbol{f}}^i(t - \tau_u), \tag{5.2}$$

which stipulates that at all times the persistence vector $\boldsymbol{v}_a{}^i$ is parallel to the previous direction of pseudopod attachment. In order to incorporate the stochastic element, we further define a random migration direction $\boldsymbol{v}_r{}^i$ given by:

$$\boldsymbol{v}_r^i(t) = \left(\cos\left(\theta_r^i(t)\right), \sin\left(\theta_r^i(t)\right)\right), \tag{5.3}$$

where $\theta_r{}^i(t) \in U(0,\ 2\pi)$. In a manner that is consistent with the original modelling approach, a persistent random walk is constructed by weighting the contributions of these two vectors in a temporally-defined manner, *viz*:

$$\boldsymbol{v}_{a,r}^i(t) = \left(1 - \rho_{a,r}^i(t)\right) \cdot \frac{\boldsymbol{v}_a^i(t)}{\|\boldsymbol{v}_a^i(t)\|} + \rho_{a,r}^i(t) \cdot \frac{\boldsymbol{v}_r^i(t)}{\|\boldsymbol{v}_r^i(t)\|}, \tag{5.4}$$

where $\rho^i{}_{a,r}(t) \in [0,1]$ determines the relative strength of the respective migratory cues. In order to understand the time-dependence of this process, we must first define a further parameter, which we define as the cell persistence time, $\tau_r{}^*$. We choose the value of $\tau_r{}^*$ to quantify the mean waiting time between random turns, and allow each cell to generate a series of independent delays between successive turns $\tau_r{}^i(t)$ from an exponential probability distribution (i.e. $\tau_r{}^i \sim Exp(\tau_r{}^*)$). The cells contain an internal clock that decrements the delay at each time step until the random turn occurs – a new delay is then calculated. Hence, in Equation 5.4, the variable $\rho^i{}_{a,r}(t)$ is selected at each time step from two fixed values:

$$\rho_{a,r}^i(t) = \begin{cases} \gamma_a, & \tau_r^i(t) > 0, \\ \gamma_r, & \tau_r^i(t) = 0, \end{cases} \tag{5.5}$$

where, in general, $\gamma_a < \gamma_r$. In this way, the long-term cell motion can be constructed from a sequence of directed zig-zag movements, characterised by γ_a, and occasional random turns, characterised by γ_r. It should be noted that although very short delays can be selected from the exponential distribution, the shortest possible time between two random turns is limited by the pseudopod establishment time, τ_u.

If required by the scenario of interest, the persistent random walk paths generated by the model can be supplemented by responses to further migratory stimuli. When a random turn occurs in the above formulation, this effectively represents the erasing of the cell "memory" to some degree (i.e. some/all cell directionality is lost). In the presence of other external signals (e.g. chemical gradient, fibrous substrate), however, we would not generally expect such significant loss of directionality. Therefore, a key assumption we require is that the component of random and persistent migration must be calculated prior to that of any other external stimuli. In essence, this stipulates that within a generalised environment, the random migratory cue will generate some background "noise" to the motion.

5.3.2. Contact Guidance

The term "contact guidance" refers to the phenomenon whereby the directionality of cell movement is influenced by the orientation of the underlying substrate, or surrounding matrix (Guido and Tranquillo, 1993). In the model of McDougall et al. (2006a), fibroblasts infiltrating the dermal wound were assumed to be guided by a fibrous matrix composed of both collagen and fibrin. Throughout the discussion that follows, we shall continue to refer to the matrix components as collagen and fibrin, but acknowledge that, in general, these could be replaced by other pertinent proteins (e.g. fibronectin) if required. Furthermore, it should be noted that any number of matrix components could be incorporated to inform cell movement in the model, but we continue to consider just two competing proteins as this provides an optimal means of explaining the methodology.

Each fibrous component is represented by a vector field that indicates the predominant matrix orientation at each spatial location. The collagen matrix orientation is denoted by $\boldsymbol{c}(\boldsymbol{x},t)$ and the fibrin matrix by $\boldsymbol{b}(\boldsymbol{x},t)$, where $\boldsymbol{x}$ represents the Cartesian co-ordinates of a point in the plane. Further to this, each protein is also assigned a density, denoted by $c^*(\boldsymbol{x},t)$ and $b^*(\boldsymbol{x},t)$, respectively. Cells are assumed to align their migration direction to the local fibre orientation such that the respective collagen and fibrin directional cues on cell *i* at position $\boldsymbol{f}^{i}(t)$ are given by:

$$\boldsymbol{v}_c^i(t) = \boldsymbol{c}\big(\boldsymbol{f}^i(t), t\big), \tag{5.6}$$

and:

$$\boldsymbol{v}_b^i(t) = \boldsymbol{b}\big(\boldsymbol{f}^i(t), t\big). \tag{5.7}$$

As for the random and persistent migratory cues outlined above, these two vectors can be combined to produce an overall matrix-associated directional stimulus, which we denote by $\boldsymbol{v}^{i}_{c,b}(t)$. This vector is calculated as follows:

$$\boldsymbol{v}_{c,b}^i(t) = \left(1 - \rho_{c,b}^i(c^*, b^*)\right) \cdot \frac{\boldsymbol{v}_c^i(t)}{\|\boldsymbol{v}_c^i(t)\|} + \rho_{c,b}^i(c^*, b^*) \cdot \frac{\boldsymbol{v}_b^i(t)}{\|\boldsymbol{v}_b^i(t)\|}\,, \tag{5.8}$$

where the weighting, which depends crucially on the respective local collagen and fibrin densities, takes the form (Figure 5.2):

$$\rho_{c,b}^i\left(c^*\big(\boldsymbol{f}^i, t\big), b^*\big(\boldsymbol{f}^i, t\big)\right) = \frac{b^*\big(\boldsymbol{f}^i, t\big)^{\alpha_{c,b}}}{b^*\big(\boldsymbol{f}^i, t\big)^{\alpha_{c,b}} + \Gamma \cdot c^*\big(\boldsymbol{f}^i, t\big)^{\alpha_{c,b}}}\,, \tag{5.9}$$

such that:

$$\rho_{c,b}^i(c^*, 0) = 0, \;\; \rho_{c,b}^i(0, b^*) = 1, \;\; \rho_{c,b}^i(b^*, b^*) = \frac{1}{1+\Gamma}\,. \tag{5.10}$$

Here, the exponent $\alpha_{c,b}$ describes the shape of this relationship between the protein densities, while Γ is used to quantify their respective importance in modifying the direction of cell migration.

It should be noted here that the form of this weighting has been modified from the original model of McDougall et al. (2006a), although the overall rationale is maintained. Previously, the lengths of the fibrous matrix orientation vectors at a

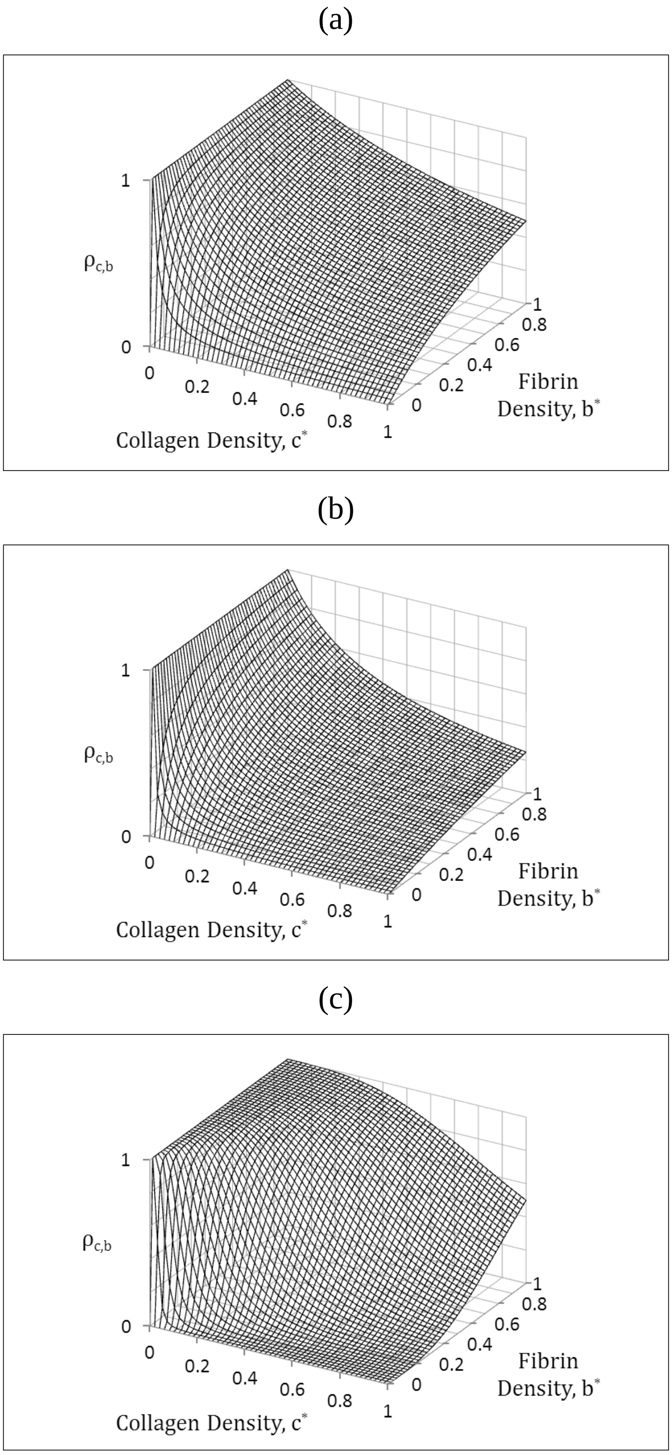

Figure 5.2: Series of examples of the functional form $\rho_{c,b}(c^*,b^*)$ defined in Equation 5.9, which describes the relative importance of collagen density c^* and fibrin density b^* in determining the overall matrix-associated directional cue for cell migration. The specific parameter values used were (a) $\alpha_{c,b} = 1$, $\Gamma = 1$, (b) $\alpha_{c,b} = 1$, $\Gamma = 3$, and (c) $\alpha_{c,b} = 3$, $\Gamma = 1$. Note that we have arbitrarily assumed both c^* and b^* have a maximum value of 1.

particular point in space (i.e. ||$\boldsymbol{c}(\boldsymbol{x},t)$|| or ||$\boldsymbol{b}(\boldsymbol{x},t)$||) were assumed to define the respective fibrous matrix densities at that point. In Equation 5.8, $\rho^i_{c,b}$ was assumed *fixed* and unit vectors were *not* calculated, such that the resultant weighting was dependent upon the relative fibrous densities of the two matrix components. Clearly, our new formulation maintains this assumption, but the introduction of the exponent $\alpha_{c,b}$ allows for a slightly more general relationship in determining the directional migratory response of a cell in the presence of both matrix components.

Having formulated equations to describe persistent random walks and contact guidance in the presence of distinct matrix proteins, we can now combine these two sub-models to simulate cell migration in response to a combination of these directional cues. Therefore, we define the vector:

$$\boldsymbol{v}^i_{(a,r),(c,b)}(t) = \left(1 - \rho^i_{(a,r),(c,b)}(c^*, b^*)\right) \cdot \frac{\boldsymbol{v}^i_{a,r}(t)}{\|\boldsymbol{v}^i_{a,r}(t)\|} + \rho^i_{(a,r),(c,b)}(c^*, b^*) \cdot \frac{\boldsymbol{v}^i_{c,b}(t)}{\|\boldsymbol{v}^i_{c,b}(t)\|}. \qquad (5.11)$$

In this case, we note that the weighting $\rho^i_{(a,r),(c,b)}$ between the two directions is again a function of the local collagen and fibrin densities. This assumption is intended to ensure that the extent of randomness in the cell movement is suppressed with increasing fibrous matrix density. Specifically, this weighting takes a general Hill function form with exponent $\alpha_{(a,r),(c,b)}$:

$$\rho^i_{(a,r),(c,b)}\big(y(c^*, b^*)\big) = \frac{y^{\alpha_{(a,r),(c,b)}} \cdot \left({y_{max}}^{\alpha_{(a,r),(c,b)}} - {y_{crit}}^{\alpha_{(a,r),(c,b)}}\right)}{y^{\alpha_{(a,r),(c,b)}} \cdot \left({y_{max}}^{\alpha_{(a,r),(c,b)}} - 2{y_{crit}}^{\alpha_{(a,r),(c,b)}}\right) + {y_{max}}^{\alpha_{(a,r),(c,b)}} \cdot {y_{crit}}^{\alpha_{(a,r),(c,b)}}}, \qquad (5.12)$$

where:

$$y = c^*\left(\boldsymbol{f}^i, t\right) + b^*\left(\boldsymbol{f}^i, t\right), \quad y_{max} = {c^*}_{max} + {b^*}_{max}, \quad y_{crit} = (c^* + b^*)_{crit}\ , \qquad (5.13)$$

where c^*_{max} and b^*_{max} are defined as the maximum allowable respective collagen and fibrin densities, and $(c^*+b^*)_{crit}$ is the combined protein density at which the directional cues will have equal weighting. Some typical examples of the function $\rho^i_{(a,r),(c,b)}$ are presented in Figure 5.3.

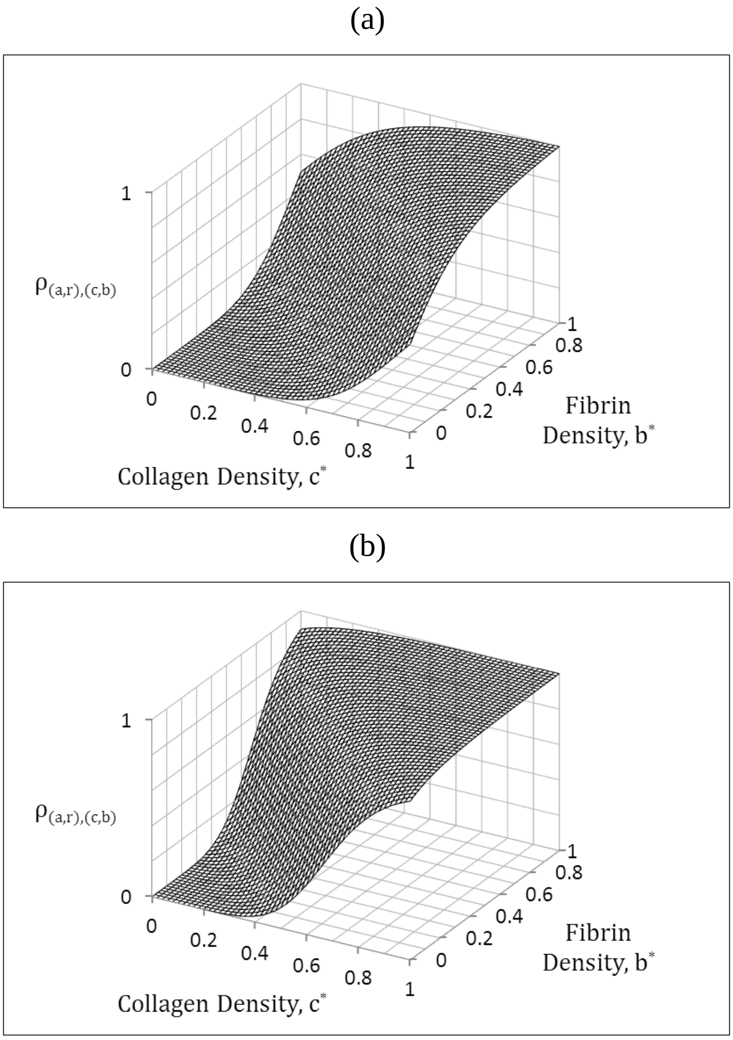

Figure 5.3: Typical examples of the functional form $\rho_{(a,r),(c,b)}(c^*,b^*)$ defined in Equations 5.12 and 5.13, which describes the importance of the collagen density c^* and fibrin density b^* in determining the overall migration direction of a cell experiencing matrix-associated contact guidance. In both cases we have the parameter values $c^*_{max} = b^*_{max} = 1$ and $\alpha_{(a,r),(c,b)} = 6$; however, in (a) $(c^* + b^*)_{crit} = 1$, and in (b) $(c^* + b^*)_{crit} = 0.7$. Note that $\rho_{(a,r),(c,b)}$ remains fixed for fixed values of $c^* + b^*$.

5.3.3. Chemotaxis

In theory, any number of distinct migratory cues could be combined to inform the *in silico* cell migration direction, but the final one we shall consider at this stage is chemotaxis. Although the model could be generalised to deal with cell migration induced by temporally evolving chemoattractant gradients, for the purposes of this thesis we shall only consider situations involving time-independent chemoattractant profiles. We define a fixed generic growth factor concentration, $K(\mathbf{x})$, throughout the simulation domain and assume that each cell will respond by migrating in the direction of the maximum local chemical gradient, such the final directional cue $\boldsymbol{v}_K{}^i$ is given by:

$$\boldsymbol{v}_K^i(t) = \nabla K(\boldsymbol{f}^i(t)). \tag{5.14}$$

Finally, we must consider how to approach combining chemotaxis with the other stimuli discussed above. Maintaining the now familiar notation, we define the overall vector incorporating all directional cues:

$$\boldsymbol{v}^i_{((a,r),(c,b)),K}(t) = \left(1 - \rho^i_{((a,r),(c,b)),K}\right) \cdot \frac{\boldsymbol{v}^i_{(a,r),(c,b)}(t)}{\left\|\boldsymbol{v}^i_{(a,r),(c,b)}(t)\right\|} + \rho^i_{((a,r),(c,b)),K} \cdot \frac{\boldsymbol{v}^i_K(t)}{\|\boldsymbol{v}^i_K(t)\|}. \tag{5.15}$$

In accordance with McDougall et al. (2006a), the weighting parameter takes a general Hill function formulation, which assumes a variation with the magnitude of the chemical gradient $\|\nabla K\|$, *viz*:

$$\begin{aligned}\rho^i_{((a,r),(c,b)),K}(\|\nabla K\|, c^*, b^*) = \\ \left[\frac{\|\nabla K\|^{\alpha_K} \cdot \left(\|\nabla K\|_{max}{}^{\alpha_K} - \|\nabla K\|_{crit}{}^{\alpha_K}\right)}{\|\nabla K\|^{\alpha_K} \cdot \left(\|\nabla K\|_{max}{}^{\alpha_K} - 2\|\nabla K\|_{crit}{}^{\alpha_K}\right) + \|\nabla K\|_{max}{}^{\alpha_K} \cdot \|\nabla K\|_{crit}{}^{\alpha_K}}\right] \\ \cdot \left[1 + \left(\nu_\rho - 1\right) \cdot \left(\frac{c^* + b^*}{c^*{}_{max} + b^*{}_{max}}\right)^{\beta_\rho}\right],\end{aligned} \tag{5.16}$$

where α_K is the Hill exponent and $\|\nabla K\|_{max}$ is the maximum magnitude of the chemical gradient across the domain. As an extension to the original model, however, we have also included an additional term that accounts for the impact of the matrix composition by modulating the maximal chemotactic weighting. In the absence of such a term, the Hill function alone would mean that chemotaxis is always the dominant directional stimulus in the presence of moderate chemical gradients, regardless of the fibrous matrix density. Therefore, $\nu_\rho \in [0, 1]$ defines the maximal chemotactic weighting (i.e. $\rho^i_{((a,r),(c,b)),K}$) at maximal matrix density, and β_ρ defines the manner in which this chemotactic weighting is modulated as the matrix density varies. Furthermore, with convention, the parameter $\|\nabla K\|_{crit}$ still represents the magnitude of chemical gradient at which the half-maximal chemotactic weighting occurs; however, we note that the precise value of this half-maximal weighting is now assumed to vary with the magnitude of the local matrix density.

We must remain aware, however, that Equation 5.15, and all of those presented so far, determines only the *directionality* of cell movement. The local matrix density, amongst other factors, can also strongly affect the overall migratory behaviour by modifying the instantaneous cell *speed*. This is the aspect of the model that we shall now proceed to consider in greater detail.

5.3.4. Cell Speed

The beauty of the approach outlined thus far is that the cell migration model is adaptable to a number of scenarios: the dynamics of each directional cue can be considered in isolation, or in combination with others, by simply selecting the appropriate $\boldsymbol{v}^i$ vector (e.g. Equation 5.4, 5.8, 5.14 or 5.15) and equating it to the vector $\boldsymbol{u}^i$ in Equation 5.1. In order to solve Equation 5.1 fully, however, we require to consider how the local environment of a cell impacts upon its instantaneous speed, $s^i(t)$.

We begin by assuming that in the absence of any external signals each cell will maintain a fixed speed s_0. This base-line value may subsequently be modulated by a series of factors attributable to each additional signal subsequently experienced, as described by the equation:

$$s^i(t) = s_0 \cdot {\psi_c}^i\left(c^*(\boldsymbol{f}^i, t)\right) \cdot {\psi_b}^i\left(b^*(\boldsymbol{f}^i, t)\right) \cdot {\psi_K}^i\left(\left\|\nabla K(\boldsymbol{f}^i)\right\|\right). \tag{5.17}$$

where ${\psi_c}^i$, ${\psi_b}^i$ and ${\psi_K}^i$ are functions that describe the respective effects of local collagen density, fibrin density and chemical gradient on the speed of each cell. These functions could be assumed to take a variety of forms; cell speeds could, for example, be increased by particular fibrous substrate densities, due to increased traction, but decreased within a densely-packed matrix (Bray, 2002). For simplicity, however, we shall assume throughout this thesis that each of these functions has an identical, monotonic form given by:

$${\psi_c}^i(c^*) = 1 + (\nu_c - 1) \cdot \left[\frac{c^*}{{c^*}_{max}}\right]^{\beta_{s,c}}, \tag{5.18}$$

$$\psi_b{}^i(b^*) = 1 + (\nu_b - 1) \cdot \left[\frac{b^*}{b^*{}_{max}}\right]^{\beta_{s,b}}, \tag{5.19}$$

$$\psi_K{}^i(\|\nabla K\|) = 1 + (\nu_K - 1) \cdot \left[\frac{\|\nabla K\|}{\|\nabla K\|_{max}}\right]^{\beta_{s,K}}, \tag{5.20}$$

where the ν terms determine the maximal extent of speed increase or decrease, and the β terms define the shape of each relationship. Specifically, we shall assume that cell speeds are increased in the presence of increasing chemoattractant gradient (i.e. $\nu_K > 1$), and decreased in the presence of increasing matrix density (i.e. $\nu_c < 1$, $\nu_b < 1$).

5.3.5. Modification of the Fibrous Matrix

The equations discussed up to this stage have been kept intentionally general, so that they have the potential to describe the migratory behaviour of a range of cell types. The final aspect of the original model framework that we have thus far neglected to consider, however, concerns the feedback loop whereby discrete cells remodel the underlying fibrous matrix as they migrate. Although we acknowledge that this process may be more relevant to particular cell-types (i.e. fibroblasts or other dermal cells), we present the full set of model equations for completeness.

We begin by defining a vector field $\boldsymbol{g}(\boldsymbol{x},t)$ that captures the effect, on the collagen fibres, of the overall cell "flux" within the domain:

$$\boldsymbol{g}(\boldsymbol{x},t) = \sum_{i=1}^{N} w^i(\boldsymbol{x},t) \cdot \frac{\dot{\boldsymbol{f}}^i(t-\tau_w)}{\|\dot{\boldsymbol{f}}^i(t-\tau_w)\|}, \tag{5.21}$$

where $w^i(\boldsymbol{x},t) \in [0,1]$ is a weight function that ensures each cell re-orients only *local* fibres, and N is the total number of cells in the domain. The time lag τ_w is included to represent the time taken for a cell to modify its direction of migration upon receiving directional cues from its environment (Dallon et al., 1999). In the case of an elongated fibroblast, for example, the head and tail of the cell may be transiently travelling in different directions. Since there is currently no explicit concept of cell shape in the model, however, the weight function applied by McDougall et al. (2006a) is used:

$$w^{\boldsymbol{i}}(\boldsymbol{x},t) = \max\left[1 - \frac{|f_1^i(t) - x_1|}{L}, 0\right] \cdot \max\left[1 - \frac{|f_2^i(t) - x_2|}{L}, 0\right], \tag{5.22}$$

where $\boldsymbol{x} = (x_1, x_2)$ and $\boldsymbol{f}^i = (f_1^i, f_2^i)$. The support of this function is, rather unrealistically, a square of side $2L$, but the concept of cell shape will be considered in greater depth at a later stage. We define the angles of the vector fields $\boldsymbol{c}(\boldsymbol{x},t)$ (collagen) and $\boldsymbol{g}(\boldsymbol{x},t)$ (cell flux), with respect to the horizontal, by $\theta_c(\boldsymbol{x},t)$ and $\theta_g(\boldsymbol{x},t)$, respectively, and the orientation of the collagen fibres is then updated via the equation:

$$\frac{d\theta_c(\boldsymbol{x},t)}{dt} = \kappa \|\boldsymbol{g}(\boldsymbol{x},t)\| \cdot \sin\left(\theta_g(\boldsymbol{x},t) - \theta_c(\boldsymbol{x},t)\right), \tag{5.23}$$

where κ is a positive parameter that quantifies the ability of the cells to reorder their underlying matrix.

Finally, the discrete-point cell migration model is completed by one further feedback loop. Within the same locality as the re-orientation of collagen fibres occurs, each cell also modifies the underlying matrix density. Specifically, fibrin is degraded by the cells as they migrate, whilst collagen is both produced and degraded. This process is described by the equations:

$$\frac{dc^*(\boldsymbol{x},t)}{dt} = [\delta_c - \sigma_c c^*(\boldsymbol{x},t)] \cdot \sum_{i=1}^{N} w^i(\boldsymbol{x},t), \tag{5.24}$$

$$\frac{db^*(\boldsymbol{x},t)}{dt} = -\sigma_b b^*(\boldsymbol{x},t) \cdot \sum_{i=1}^{N} w^i(\boldsymbol{x},t), \tag{5.25}$$

where δ_c is the rate of collagen production, while σ_c and σ_b are, respectively, the rates of collagen and fibrin degradation.

This completes the model formulation for discrete volumeless cells and we now go on to examine some simple sensitivities using the model. Note that additional details regarding the numerical implementation of the model can be found in Appendix B.

5.4. Discrete-Point Cell Simulation Results

Up to this point, the only significant extensions we have made to the original model framework are the introduction of a stochastic migratory cue, and the inclusion of some generalised functional forms to describe the weightings between the various stimuli that ultimately determine the overall migration direction. Therefore, in this section, we shall perform only some simple sensitivity studies to examine the typical cell trajectories now predicted by the model. For each scenario considered, we present 20 individual cell paths covering a period of 6 hours; each cell begins its journey at the centre of the domain with a randomly generated initial orientation. Unless otherwise stated, the base case parameters used across all simulations in this section are given in Table 5.1. Furthermore, for each sensitivity study, the specific values of the modified parameters can be found in the relevant figure caption.

Parameter	Definition	Value
s_0	External cue-free cell speed	60 μm · hr^{-1}
τ_u	Pseudopod establishment time	0.03 hr
τ_r^*	Cell persistence time	0.25 hr
γ_p	Random migration weighting	0.05
γ_r	Cell "memory" weighting	1
$\|\| \nabla K\|\|_{crit}$	Chemical gradient for half-maximal chemotactic weighting	$0.5\|\| \nabla K\|\|_{max}$
α_K	Chemotactic weighting Hill exponent	6
ν_K	Cell speed-modulation factor (chemotaxis)	5/3
$\beta_{s,K}$	Cell speed-modulation shape parameter (chemotaxis)	1
$\alpha_{(a,r),(c,b)}$	Contact guidance weighting Hill exponent	6
c^*_{max}	Maximal collagen density	1
b^*_{max}	Maximal fibrin density	0
$(c^*+b^*)_{crit}$	Matrix density for half-maximal contact guidance weighting	0.5
ν_c	Cell speed-modulation factor (collagen)	2/3
$\beta_{s,c}$	Cell speed-modulation shape parameter (collagen)	1
ν_ρ	Maximal chemotactic weighting at maximal matrix density	0.5
β_ρ	Chemotactic weighting suppression shape parameter	1

Table 5.1: Base case parameters used for all simulations in Section 5.4.

5.4.1. Persistent Random Walk

We begin by considering the simplest case of random cell movement in the absence of any external signals. As discussed in Section 5.3.1, the migration patterns generated by this component of the model are constructed as a series of directed, persistent "runs" (characterised by τ_r^* and γ_p), interspersed by random "turns" (characterised by γ_r). We proceed, therefore, to investigate the impact of modifying each of these three persistent random walk parameters. Note that, following Equation 5.17, cell speeds remain fixed at s_0 throughout these simulations.

Figure 5.4 presents the cell trajectories generated upon decreasing (Figure 5.4b) or increasing (Figure 5.4c) the base case value (Figure 5.4a) of the average cell persistence time τ_r^*. As expected, we observe that an increase in this value leads to cell trajectories exhibiting some very long, straight periods of movement, and a generally wider dispersal than the base case scenario. Conversely, a decrease leads to trajectories that largely remain confined to a small region about the domain centre due to the large frequency of randomly oriented turns. Note that, in this latter case, the value of τ_r^* was set equal to the value of τ_u (i.e. the pseudopod establishment time) such that a large portion of the calculated persistence times would have been *a posteriori* increased to this minimum value. Therefore, the extent of cell dispersal depicted by this simulation is approaching the minimal level for cells with these assumed properties.

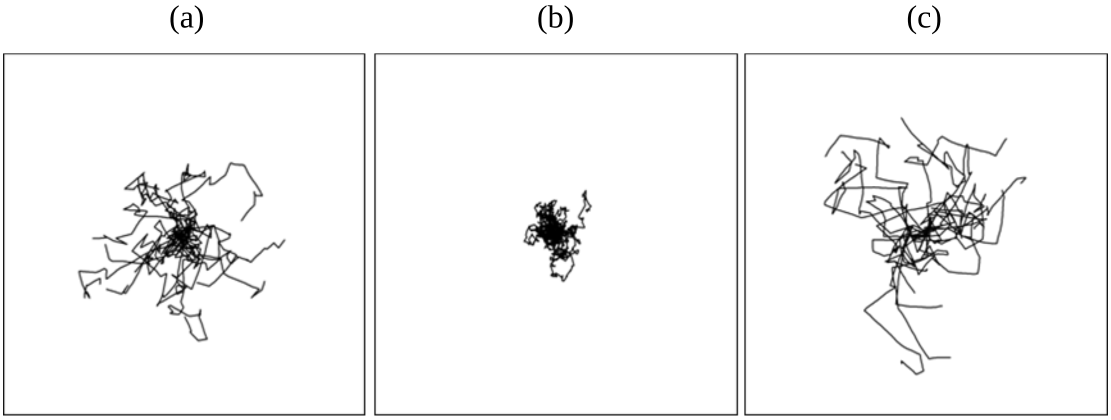

Figure 5.4: Typical cell trajectories over a 6 hour period obtained from the discrete-point cell migration model for a range of cell persistence time τ_r^* values (scale of images = 450 μm x 450 μm). Only the persistence and random directional cues were applied; images correspond to the parameter values (a) 0.25 (base case), (b) 0.03 and (c) 0.45.

In our base case parameter set, we have assumed that during “runs” there is only a very small level of noise (i.e. $\gamma_p = 0.05$) such that the simulated cell pathways exhibit many long, straight segments (Figure 5.5a). In Figures 5.5b and 5.5c we present the results obtained upon increasing this value five- or ten-fold, respectively. The first increase produces trajectories that largely resemble those from the base case, albeit with slightly reduced dispersal due to greater fluctuation in the cell paths during periods of persistence. The result of a further increase is more dramatic, however, with the cells unable to disperse at all because the calculated extension direction of every single pseudopod has a large stochastic element.

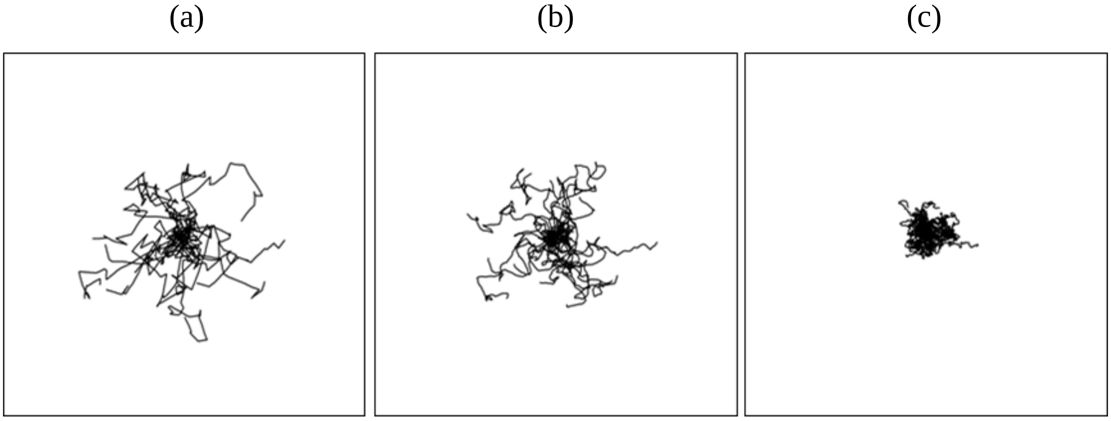

Figure 5.5: Typical cell trajectories over a 6 hour period obtained from the discrete-point cell migration model for a range of random component weighting γ_a values (scale of images = 450 μm x 450 μm). Only the persistence and random directional cues were applied; images correspond to the parameter values (a) 0.05 (base case), (b) 0.25 and (c) 0.5.

Finally, we consider the impact of varying γ_r, which essentially quantifies the level to which the cell "memory" is erased after each period of persistence. In the base case simulation (Figure 5.6a) we proposed that each "turn" was entirely random (i.e. $\gamma_r = 1$); we now present two further scenarios where this assumption is relaxed. The impact of the first reduction (Figure 5.6b) is relatively minimal with cell trajectories closely resembling the base case, albeit with a slightly reduced tendency to turn through large angles. A further decrease (Figure 5.6c) gives results far removed from the base case, however, and the cells now widely disperse by persisting in particular directions for long periods of time.

In summary, it is clear that the extent of dispersal displayed by the cells can be critically influenced by all three parameters characterising the persistent random walk. An increase in the cell persistence time, a decrease in the randomness of "turns" and an increase in the straightness of "runs" were all found to result in cells that, in general, migrated further from their initial position. In future, the model could be used to parameterise the behaviour of *in vitro* cells migrating in the absence of external signals. Experimental data concerning the distributions of run lengths and turn angles would be ideal for such an approach. We will discuss a similar benchmarking exercise in the next chapter.

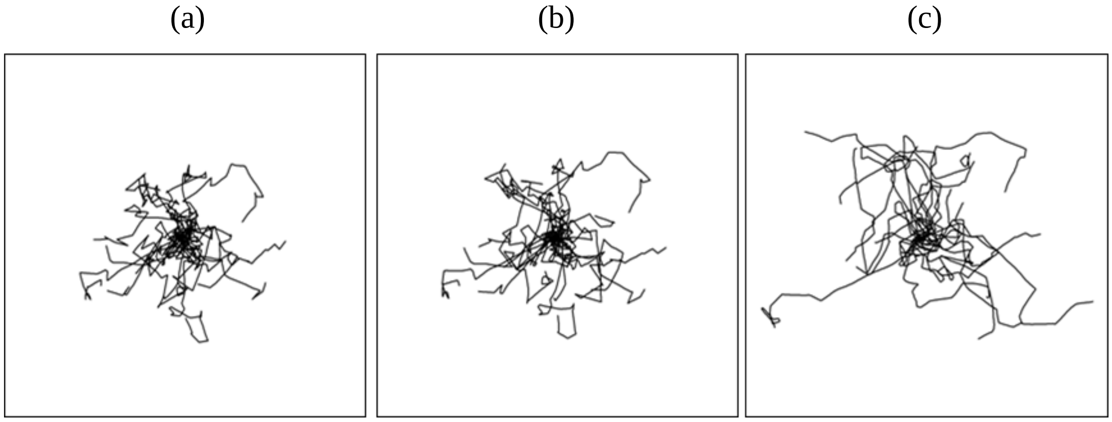

Figure 5.6: Typical cell trajectories over a 6 hour period obtained from the discrete-point cell migration model for a range of "cell memory" weighting γ_r values (scale of images = 450 μm x 450 μm). Only the persistence and random directional cues were applied; images correspond to the parameter values (a) 1 (base case), (b) 0.75 and (c) 0.5.

5.4.2. Chemotaxis

Although the results presented in the previous section are interesting, it is fair to say that, given the definitions made, they prove to be as expected. In the following sections, we increase the range of behaviours displayed by the model by including further directional cues in the generation of our cell trajectories. Firstly, we investigate the cell behaviour in response to a fixed chemoattractant profile. Within the simulation domain we assume an outwardly increasing concentric profile according to:

$$K(r) = 1 - e^{-\frac{r^2}{0.14}}, \tag{5.26}$$

where r is the normalised distance from the domain centre (Figure 5.7). Note that the full domain size is 1500 μm x 1500 μm, and $\|\nabla K\|_{max}$ is taken to be the maximum chemical gradient value across the whole domain.

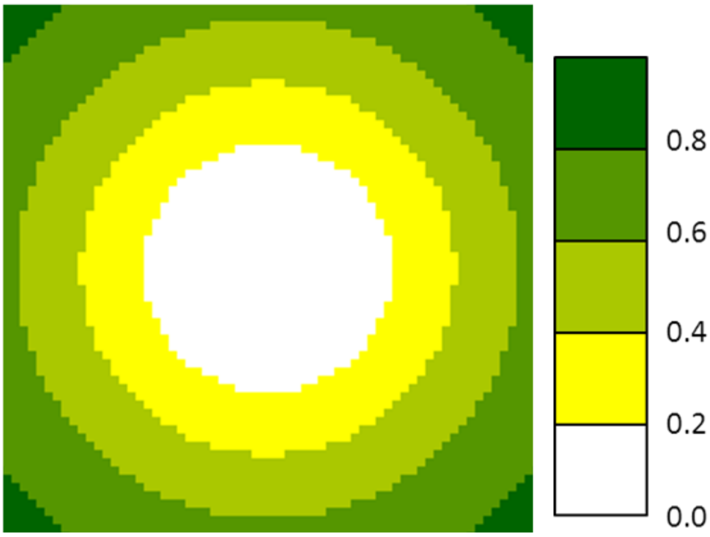

Figure 5.7: Profile of chemoattractant concentration, defined in Equation 5.26, that was used to generate the discrete-point cell trajectories presented in Figures 5.8, 5.11 and 5.12 (scale of image = 960 µm x 960 µm).

The sensitivity that we consider is to the parameter $\|\nabla K\|_{crit}$, defining the absolute chemical gradient at which the value of the chemotactic directional cue is half-maximal (i.e. $\rho^{i}_{((a,r),(c,b)),K} = 0.5$ in Equation 5.16, with $c^{*} = b^{*} = 0$). In the base case simulation (Figure 5.8a) we note that the cells initially perform random walks, due to the weak chemotactic response at the domain centre, before eventually embarking on largely straight pathways up the chemical gradient. Reducing the critical chemical gradient value (Figure 5.8b) increases the cells' receptiveness to shallow gradients; accordingly, they perform very short random walks before shooting directly outwards. Finally, Figure 5.8c shows the behaviour of cells that are less receptive to the chemical; in this case, some cells appear not to sense the chemoattractant at all over the entire course of the simulation. Furthermore, it can be seen that those who do seek out the chemical gradient begin to lose their way as they migrate beyond its peak.

5.4.3. Contact Guidance

We now remove the chemoattractant profile from the domain, and seek to investigate the simulated cell movement under the influence of contact guidance. We shall assume that the domain is filled with collagen only (i.e. $b^{*} = 0$) and, in order not to impose any particular directional bias, generate a randomly oriented collagen vector field $\mathbf{c}(\mathbf{x},t)$.

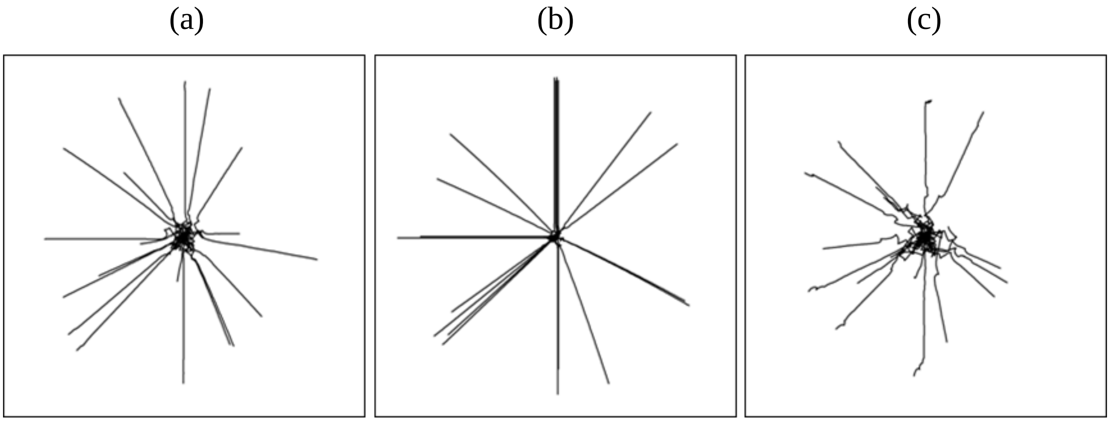

Figure 5.8: Typical cell trajectories over a 6 hour period obtained from the discrete-point cell migration model in the presence of an outwardly increasing chemoattractant profile for a range of $\|\nabla K\|_{crit}$ values (scale of images = 840 μm x 840 μm). The chemotaxis, persistence and random directional cues were applied; images correspond to the parameter values (a) $0.5\|\nabla K\|_{max}$ (base case), (b) $0.2\|\nabla K\|_{max}$ and (c) $0.8\|\nabla K\|_{max}$, where $\|\nabla K\|_{max}$ corresponds to the domain-wide chemical gradient maximum.

Furthermore, in order to mimic physically-realistic *in vivo* ECM, we generate a heterogeneous distribution of collagen density $c^*(\mathbf{x},t)$ (Figure 5.9). Note that this ensures a variation in the random walk-contact guidance weighting $\rho^i_{(a,r),(c,b)}$ for each cell over the course of a simulation. We define the minimum and maximum values of this profile to be c^*_{inf} and c^*_{sup}, respectively, such that we can consider the three distinct scenarios of low ($c^*_{inf} = 0.1$, $c^*_{sup} = 0.3$), medium ($c^*_{inf} = 0.4$, $c^*_{sup} = 0.6$) and high ($c^*_{inf} = 0.7$, $c^*_{sup} = 0.9$) collagen density. There are two additional points to note for each of the following simulations: we have arbitrarily set $c^*_{max} = 1$, and we do not consider any cell-induced modification to the density or orientation of this underlying matrix.

We perform a sensitivity study on $(c^*+b^*)_{crit}$ (c.f. Equation 5.13), which we shall refer to as simply c^*_{crit} since $b^* = 0$; this parameter therefore defines the critical collagen density at which the random walk and contact guidance directional cues are equally weighted. We choose a base case value $c^*_{crit} = 0.5$, and perform two sensitivities on this parameter at each of our three assumed collagen densities.

At low collagen density, we find that both the base case value and an increased c^*_{crit} value (Figures 5.10b and 5.10c, respectively) predict trajectories that are largely independent of the underlying matrix (i.e. closely resembling the base case simulation

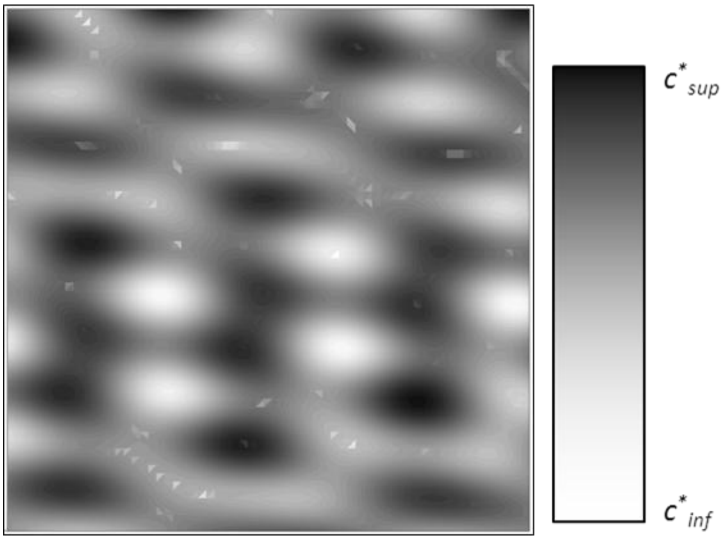

Figure 5.9: Profile of collagen density used to generate the discrete-point cell trajectories presented in Figures 5.10, 5.11 and 5.12 (scale of image = 960 μm x 960 μm). In each case, trajectories were obtained at low ($c^*_{inf} = 0.1$, $c^*_{sup} = 0.3$), medium ($c^*_{inf} = 0.4$, $c^*_{sup} = 0.6$) and high ($c^*_{inf} = 0.7$, $c^*_{sup} = 0.9$) collagen density. The reference value for maximal collagen density c^*_{max} was set to unity throughout.

in Section 5.4.1). Reducing c^*_{crit} produces greater competition between the two directional cues; the cells largely follow the collagen fibres but many break away in response to random directional perturbations, which are enhanced in the regions of lowest collagen density (Figure 5.10a). The base case simulation at medium collagen density (Figure 5.10e) follows an analogous pattern to Figure 5.10a since simultaneous increases in both c^*_{crit} and the matrix density results in comparable weighting values for the two directional cues. We note, however, that the level of dispersal is suppressed due to the concurrent reduction in cell speeds. At medium collagen density we once again find the trajectories to be relatively insensitive to increased c^*_{crit} (Figure 5.10f), but the result of a decrease is more drastic – the cells now follow the collagen fibres very closely and the stochastic nature of the trajectories is largely concealed. Almost identical behaviour to this is observed at high collagen densities for both the base case and reduced parameter value simulations (Figures 5.10g and 5.10h) and, although some randomness is still observed for increased c^*_{crit} (Figure 5.10i), cell dispersal remains relatively low due to a further cell speed reduction.

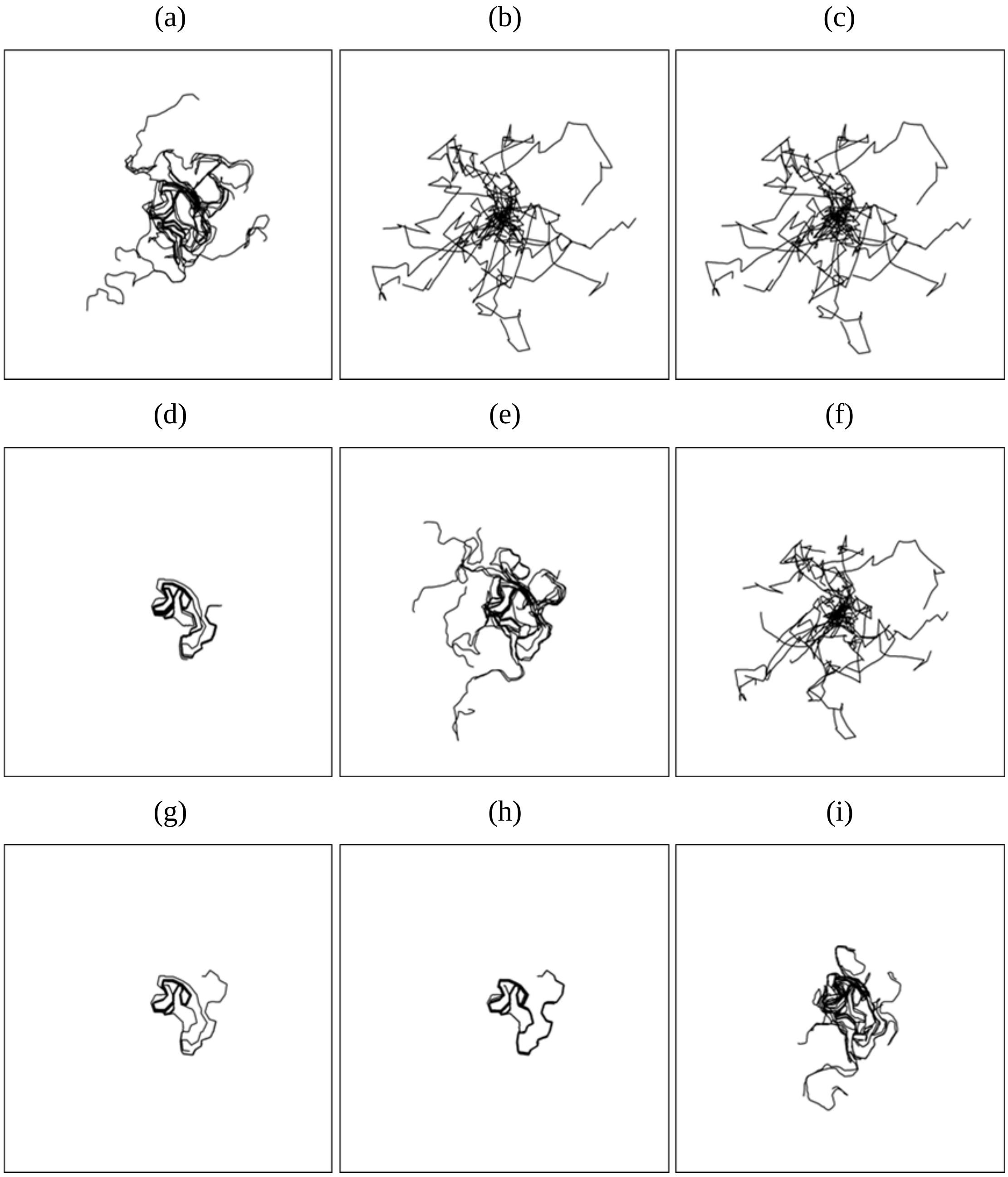

Figure 5.10: Typical cell trajectories over a 6 hour period obtained from the discrete-point cell migration model in the presence of a randomly-oriented collagen profile. The images show results at (a-c) low, (d-f) medium and (g-i) high collagen density for a range of c^{*}_{crit} values (scale of images = 510 μm x 510 μm). The contact guidance, persistence and random directional cues were applied; images correspond to the c^{*}_{crit} values (a, d, g) 0.2, (b, e, h) 0.5 (base case) and (c, f, i) 0.8.

5.4.4. Full Model

By combining all of the facets of the previous two sections, we can now apply the model in its entirety; that is, we investigate the migration patterns produced by cells responding to a chemotactic signal within fibrous matrices of variable density. In this case we shall perform sensitivity studies on the parameters $\|\nabla K\|_{crit}$ and v_ρ, which inform the calculation of the chemotactic weighting $\rho^i_{((a,r),(c,b)),K}$ in Equation 5.15. Recall that v_ρ defines the maximal chemotactic weighting at maximal matrix density c^*_{max}, while $\|\nabla K\|_{crit}$ represents the magnitude of chemical gradient at which the collagen density-dependent half-maximal chemotactic weighting occurs. Once again we select base case values ($\|\nabla K\|_{crit} = 0.5$, $v_\rho = 0.5$) and examine the impact of an increase or decrease in each individual parameter at low, medium and high collagen densities.

In order to aid understanding, in Table 5.2 we summarise the range of possible chemotactic weightings $\rho^i_{((a,r),(c,b)),K}$ for each of our simulations examining the sensitivity to $\|\nabla K\|_{crit}$. As expected, the results at low collagen density (Figure 5.11a-c) are qualitatively very similar to those presented previously in Figure 5.8; this is due to the fact that any contact guidance effects quickly become negligible as the chemical gradient increases. We note, however, that initial contact guidance in the shallow chemical gradient at the domain centre has accelerated the search for the chemotactic signal (c.f. scale of Figure 5.11 vs. scale of Figure 5.8). Increasing the collagen density to medium levels has an overall effect of increasing the strength of contact guidance; however, chemotaxis does remain the dominant cue in the presence of reasonable chemical gradients. The base case simulation of Figure 5.11e reflects this assertion, whereby cells follow the matrix fibres initially and then respond strongly to the chemoattractant. One consequence of the initial regime of contact guidance is shown by the reduced stochasticity in cell paths when $\|\nabla K\|_{crit}$ is decreased (Figure 5.11d). Groups of cells are forced to traverse similar fibre pathways in the first instance; the subsequent strongly biased chemotactic response reinforces this effect, and the cells share the same path over the whole course of the simulation. This result is not reflected in the case where cells are less receptive to shallow chemical gradients (i.e. $\|\nabla K\|_{crit}$ increased); the cells experience strong contact guidance for a longer period of time, making the paths much more tortuous and widely dispersed (Figure 5.11f). At high

	$\|\nabla K\|_{crit} = 0.2$	$\|\nabla K\|_{crit} = 0.5$	$\|\nabla K\|_{crit} = 0.8$
$c^* \in (0.1, 0.3)$	[0, 0.95]	[0, 0.95]	[0. 0.95]
$c^* \in (0.4, 0.6)$	[0, 0.8]	[0, 0.8]	[0, 0.8]
$c^* \in (0.7, 0.9)$	[0, 0.65]	[0, 0.65]	[0, 0.65]

Table 5.2: Range of possible chemotactic weighting $\rho^i_{((a,r),(c,b)),K}$ values (c.f. Equation 5.16) for each combination of collagen density c^* and critical chemoattractant gradient $\|\nabla K\|_{crit}$ value considered in the simulations of Figure 5.11.

collagen density, simulations with small $\|\nabla K\|_{crit}$ and the base case value now produce only three distinct outward trajectories (Figures 5.11g and 5.11h), while the cells with reduced chemotactic receptiveness now appear "trapped" by the matrix and struggle to orient towards the chemical gradient peak (Figure 5.11i).

Table 5.2 showed that, in the simulations of Figure 5.11, the assumed minimum value of the chemotactic weighting at high collagen matrix density was 0.65. We now consider two cases showing a general weakening or strengthening of chemotaxis suppression as a result of the local fibrous matrix density (i.e. v_ρ is either increased or reduced, respectively). In order to again aid understanding, Table 5.3 summarises the range of possible chemotactic weightings for each of the following simulations. Note that Figures 5.12b, 5.12e and 5.12h are identical to the base case results presented above (i.e. Figures 5.11b, 5.11e and 5.11h, respectively).

Our results show that, at low collagen density, the cells are entirely insensitive to changes in this parameter because the resultant modifications to the chemotactic weighting are essentially negligible (Figures 5.12a-c). At medium levels of collagen density the qualitative results are largely conserved in each case, but we note that the tortuosity of the trajectories is either enhanced for small v_ρ (Figure 5.12d) or reduced for large v_ρ (Figure 5.12f). We see a wider range of behaviours at high collagen densities: where the chemotactic response is only weakly suppressed, the cells slalom through the collagen fibres initially before responding to the increase in chemical gradient very directly; conversely, at strong chemotactic suppression, very few cells manage to migrate outwards in response to the chemical and these trajectories appear to remain strongly influenced by the underlying fibrous orientation over the full course of the simulation (Figure 5.12g-i).

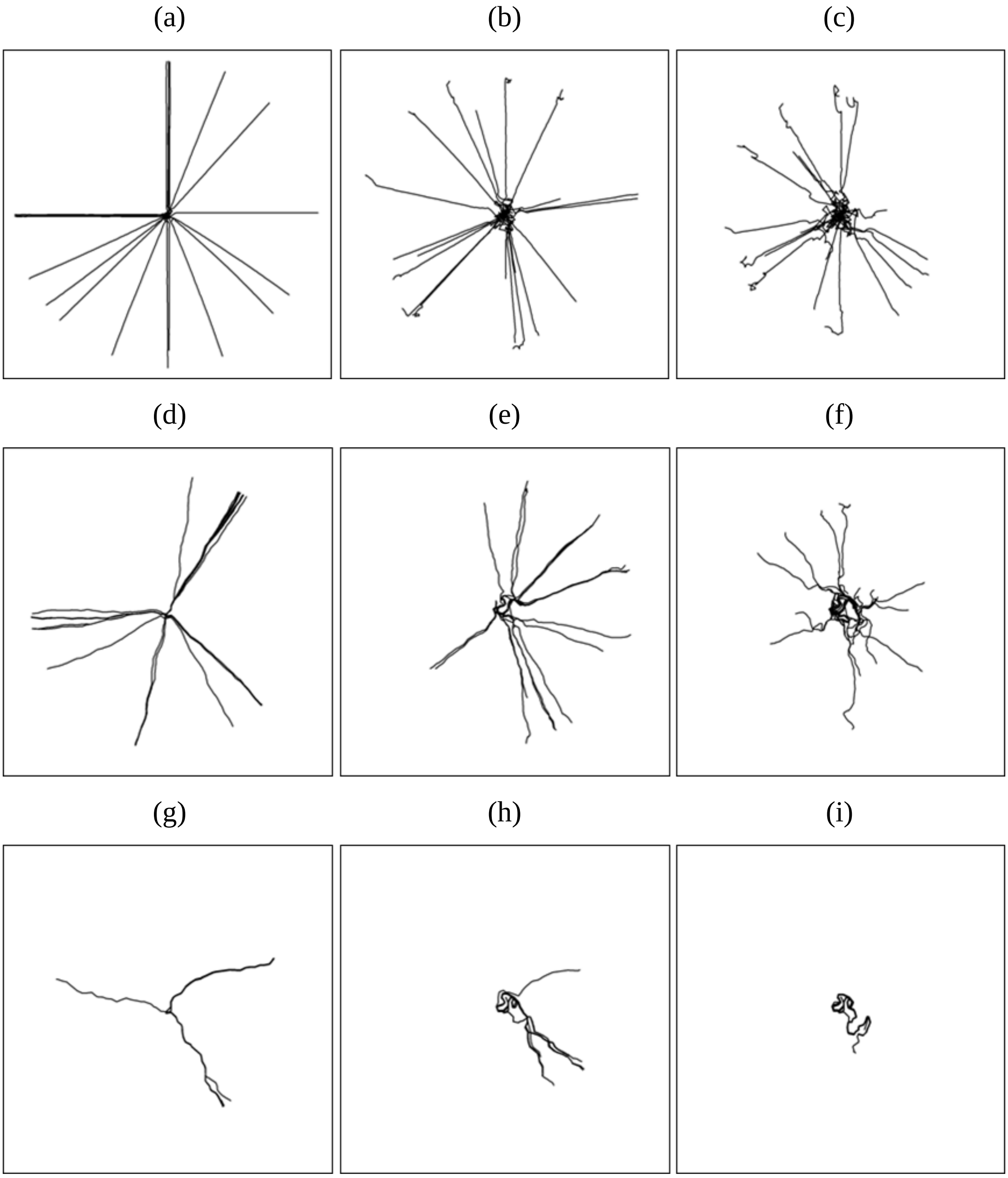

Figure 5.11: Typical cell trajectories over a 6 hour period obtained from the discrete-point cell migration model in the presence of a randomly-oriented collagen profile and an outwardly increasing chemoattractant profile. The images show results at (a-c) low, (d-f) medium and (g-i) high collagen density for a range of $\|\nabla K\|_{crit}$ values (scale of images = 960 μm x 960 μm). The contact guidance, chemotaxis, persistence and random directional cues were applied; images correspond to the $\|\nabla K\|_{crit}$ values (a, d, g) $0.2\|\nabla K\|_{max}$, (b, e, h) $0.5\|\nabla K\|_{max}$ (base case) and (c, f, i) $0.8\|\nabla K\|_{max}$, where $\|\nabla K\|_{max}$ corresponds to the domain-wide chemical gradient maximum.

Our simulations of the full cell migration model – combining stochastic movement with chemotaxis and contact guidance – predict a wide range of possible cell behaviours. We have considered how variations in both cell receptiveness to the chemical and matrix suppression of the chemotactic response impact on the overall cell pathways. At low collagen density, all of the resultant trajectories very much resemble the earlier simulations performed in the absence of any underlying matrix (c.f. Section 5.4.2). As the collagen density is further increased, however, the impact of contact guidance generally increases the tortuosity of the trajectories as the ability to undergo directed motion up the chemical gradient is reduced. These simulations indicate a key strength of the modelling approach: by manipulating the relative strengths of various directional stimuli, the model could potentially be used to reduce parameter searches in experimental programmes. Benchmarking the model against data from *in vitro* experiments where cells crawl on fibrous substrates, for example, could prove to be valuable, since the results may provide insights into the mechanisms of cell movement *in vivo*.

	$v_\rho = 0.1$	$v_\rho = 0.5$	$v_\rho = 0.9$
$c^* \in (0.1, 0.3)$	[0, 0.91]	[0, 0.95]	[0. 0.99]
$c^* \in (0.4, 0.6)$	[0, 0.64]	[0, 0.8]	[0, 0.96]
$c^* \in (0.7, 0.9)$	[0, 0.37]	[0, 0.65]	[0, 0.93]

Table 5.3: Range of possible chemotactic weighting $\rho^{i}_{((a,r),(c,b)),K}$ values (c.f. Equation 5.16) for each combination of collagen density c^* and matrix-associated chemotactic suppression v_ρ value considered in the simulations of Figure 5.12.

5.5. Spherical Cell Model

Whilst the discrete-point cell model can provide valuable predictions regarding the migration of cells in isolation, the lack of information regarding physical cell size inhibits the application of the model to scenarios where cell-cell interactions are known to be prominent. Furthermore, when considering only discrete cells, aspects such as cell proliferation can only be considered in a purely phenomenological sense. Therefore, in this section we seek to relax this approximation and move towards a more physically

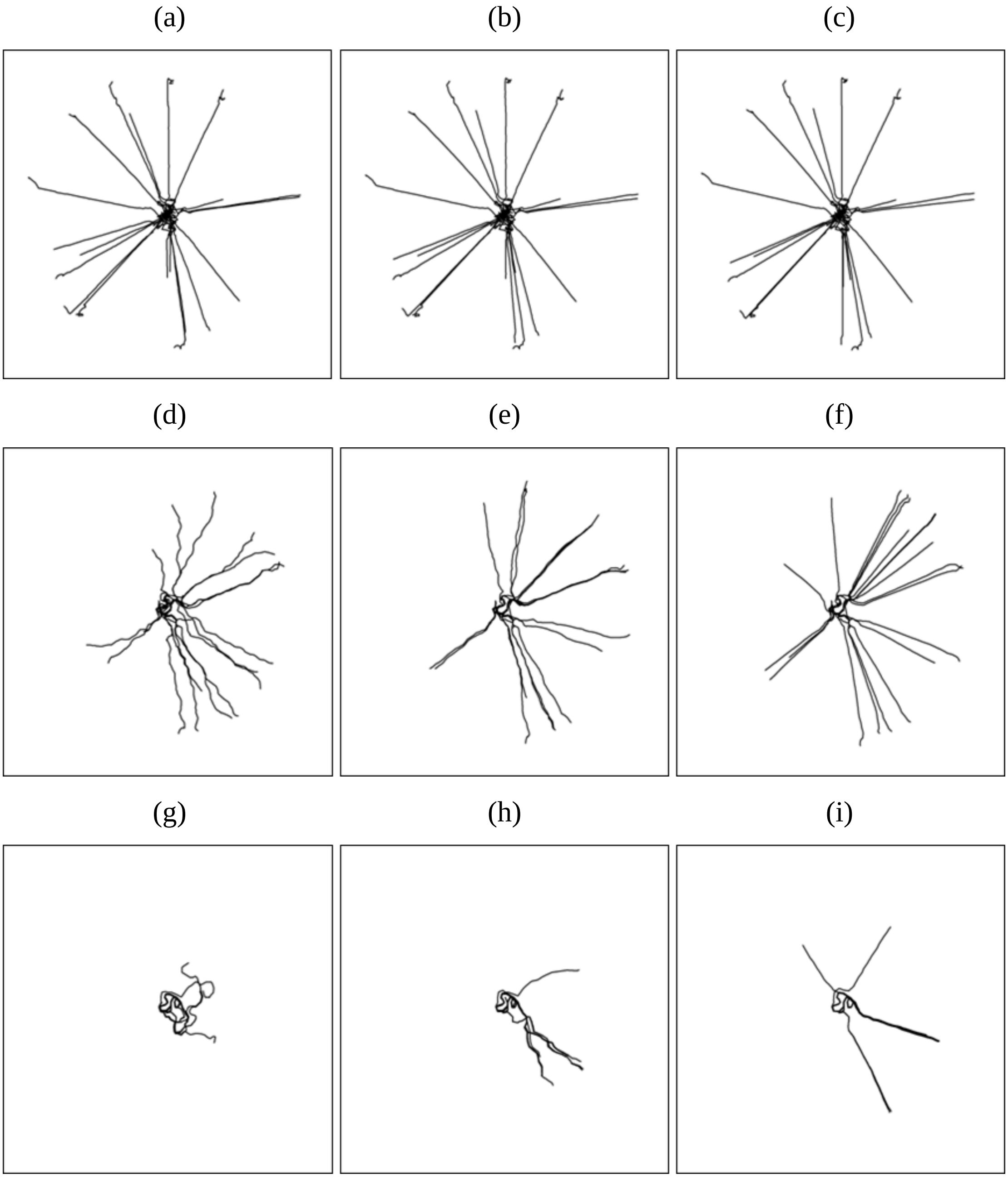

Figure 5.12: Typical cell trajectories over a 6 hour period obtained from the discrete-point cell migration model in the presence of a randomly-oriented collagen profile and an outwardly increasing chemoattractant profile. The images show results at (a-c) low, (d-f) medium and (g-i) high collagen density for a range of v_ρ values (scale of images = 960 μm x 960 μm). The contact guidance, chemotaxis, persistence and random directional cues were applied; images correspond to the v_ρ values (a, d, g) 0.1, (b, e, h) 0.5 (base case) and (c, f, i) 0.9.

realistic model of cell migration by assuming that each cell adopts an approximately spherical conformation. It should be noted that this model extension has been inspired by, and borrows from, the recent work of Macklin et al. (2012), who developed a mechanical agent-based cell model to reproduce the clinically-observed advancement of ductal carcinoma *in situ* (DCIS). As has been seen thus far, however, our cell model is not informed by mechanics; therefore, we must develop an alternative means of incorporating cell-cell interactions into the existing framework. This issue will be addressed in due course, but first we introduce some key assumptions regarding the physical characteristics of the cells.

5.5.1. Physical Characteristics of the Cell

We begin by assuming that for each cell the vectors $\boldsymbol{f}^{i}(\boldsymbol{x},t)$ and $\boldsymbol{u}^{i}(\boldsymbol{x},t)$ now represent the position and velocity, respectively, of the cell centre of mass and volume. In direct analogy to Macklin et al. (2012), we assign to each cell a volume $V^{i}(t)$ and a (fixed) nuclear volume V_N, which are characterised by equivalent cell and nuclear radii ($R^{i}(t)$ and R_N, respectively) that are related through the equations:

$$V_N = \frac{4}{3}\pi {R_N}^3, \quad V^i(t) = \frac{4}{3}\pi R^i(t)^3. \tag{5.27}$$

We have adopted the nomenclature "equivalent" radii, since the explicit cell morphology is not tracked in time; instead we additionally assume that each cell has a maximum adhesion interaction radius (or "sensing" radius) $R_S{}^{i}(t)$. This allows the model to account for two important factors: uncertainty in the extent of the cell boundary relative to its centre of mass; and the ability of cells to stretch beyond $R^{i}(t)$ for maintenance or creation of adhesive bonds (Macklin et al., 2012; see also Drasdo et al. (1995) for details of a similar approach). A schematic diagram is shown in Figure 5.13 to clarify the rationale of these assumptions, where we also demonstrate that cell deformation can be accounted for by allowing equivalent cell radii to overlap.

Before proceeding, there is one further noteworthy point to highlight. When modelling proliferation (see Section 5.5.4), cells will pass through their cell cycles asynchronously and undergo volume variations at the appropriate stage. Therefore, in the variables $V^{i}(t)$, $R^{i}(t)$ and $R_S{}^{i}(t)$, the superscripts (and time-dependence) denote that throughout a simulation each individual cell has a unique set of (inter-dependent) values characterising its physical size and shape. Therefore, we introduce a set of parameters

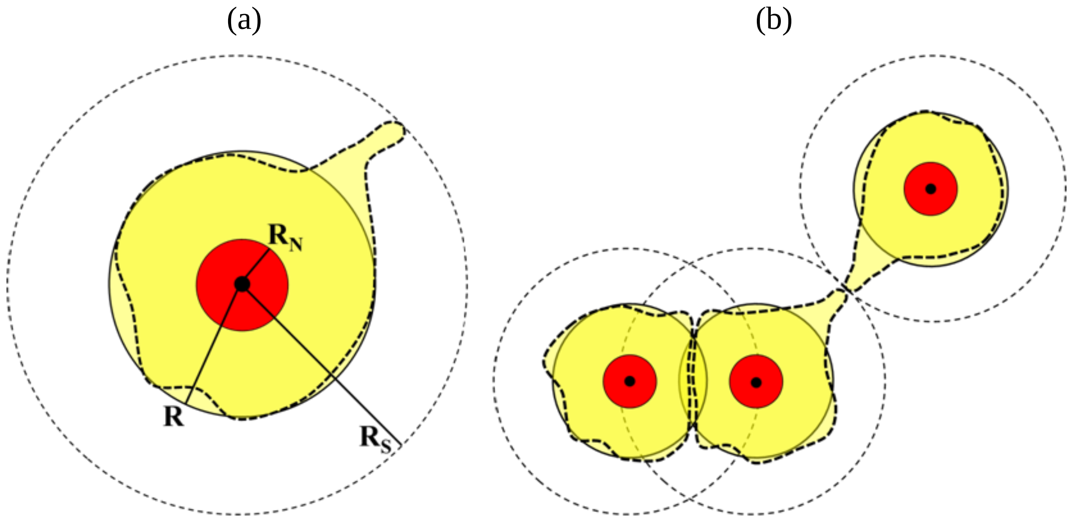

Figure 5.13: Schematic diagram illustrating the rationale of assumptions regarding cell morphology and cell-cell interactions in the spherical cell migration model. Throughout simulation, the cell volume V and nuclear volume V_N are tracked; in (a), the labels R and R_N indicate, respectively, the equivalent spherical cell and nuclear radii, while R_S indicates the maximum adhesion interaction distance, or “sensing” radius. The explicit cell morphology is not tracked in time – the thick dashed line shows one particular possibility. The configuration of cells in (b) shows that uncertainty in exact cell morphologies can be accounted for by allowing both the overlap of equivalent cell radii and adhesive contact beyond notional cell boundaries.

that constrain the maximum possible cell size throughout simulation, namely V_{max}, R_{max} and R_{Smax} (i.e. the maximum allowable cell volume, radius and sensing radius, respectively). These parameters are coupled by the following equations:

$$V_{max} = \frac{4}{3}\pi {R_{max}}^3, \quad \frac{R_{Smax}}{R_{max}} = \frac{{R_S}^i(t)}{R^i(t)}. \tag{5.28}$$

In all of the above definitions we have inherently assumed that our cells take on a spherical morphology; however, since we perform only 2D simulations, it would be possible to relax the assumption that the cell “height” is equal to $R^i(t)$ and instead assume our cells to be flatter and disc-like, as observed for certain cell types in culture. Although we neglect this possibility here, the only potential difference it would make to our simulations is a modification of the manner with which $R^i(t)$ varies during volume changes within the cell division cycle.

5.5.2. Cell-Cell Interactions

Armed with the above definitions, we now turn our attention to the concept of cell-cell interaction by introducing dynamic adhesive and repulsive effects between neighbouring cells. For this purpose, we again look to the work of Macklin et al. (2012), who generate biomechanical adhesion and repulsion forces between their *in silico* cells by appropriately defined potential functions; note that a similar approach has been proposed in a variety of publications (Drasdo et al., 1995; Drasdo and Hoehme, 2003; Ramis-Conde et al., 2008a; Ramis-Conde et al., 2008b; Byrne and Drasdo, 2009). Although we do not work explicitly with cell-cell forces, we adapt the use of these functions to inform the direction of cell-cell related movements in our model.

As with the above assumed convention for single cells, any subsequent use of the superscript *ij* shall now be assumed to refer to any variable that is uniquely defined for each *pair* of cells. The first definition of this type that we make concerns $\boldsymbol{q}^{ij}(t)$, the vector connecting the centre of mass of any two cells:

$$\boldsymbol{q}^{ij}(t) = \boldsymbol{f}^{j}(t) - \boldsymbol{f}^{i}(t), \tag{5.29}$$

This is an important definition, since any movement owing to adhesion or repulsion between neighbouring cells will be directed parallel to this vector. We can now proceed to define our potential function $h^{ij}(\|\boldsymbol{q}^{ij}\|)$, which encapsulates the manner in which two cells interact as the distance between their centres of mass varies. Adapting the respective adhesion and repulsion terms applied in Macklin et al. (2012), we define:

$$h^{ij}(\|\boldsymbol{q}^{ij}\|) = \begin{cases} \eta_{adh}\left(1 - \dfrac{\|\boldsymbol{q}^{ij}\|}{{R_S}^i + {R_S}^j}\right)^{\beta_{adh}+1} - \eta_{rep}\left\{1 + \left[\left(1 - \dfrac{2R_N}{R^i + R^j}\right)^{\beta_{rep}+1} - 1\right] \cdot \dfrac{\|\boldsymbol{q}^{ij}\|}{2R_N}\right\}, & 0 \le \|\boldsymbol{q}^{ij}\| \le 2R_N \\ \eta_{adh}\left(1 - \dfrac{\|\boldsymbol{q}^{ij}\|}{{R_S}^i + {R_S}^j}\right)^{\beta_{adh}+1} - \eta_{rep}\left(1 - \dfrac{\|\boldsymbol{q}^{ij}\|}{R^i + R^j}\right)^{\beta_{rep}+1}, & 2R_N \le \|\boldsymbol{q}^{ij}\| \le R^i + R^j \\ \eta_{adh}\left(1 - \dfrac{\|\boldsymbol{q}^{ij}\|}{{R_S}^i + {R_S}^j}\right)^{\beta_{adh}+1}, & R^i + R^j \le \|\boldsymbol{q}^{ij}\| \le {R_S}^i + {R_S}^j \\ 0, & \|\boldsymbol{q}^{ij}\| > {R_S}^i + {R_S}^j \end{cases} \tag{5.30}$$

where the exponents β_{adh} and β_{rep} characterise the form of the adhesive and repulsive responses, respectively, while the coefficients η_{adh} and η_{rep} quantify the respective adhesion and repulsion strengths. The two latter parameters are found to be of great importance in determining the overall *in silico* cell behaviour, since, for fixed β_{adh} and β_{rep}, their respective values determine the distance between any two cell centres at which the adhesion and repulsion terms are balanced (i.e. $h^{ij} = 0$). From a biological stand-point, it would seem a minimum requirement to assume that such an equilibrium distance would have its value lie in the range $(2R_N, R^i+R^j)$. Naturally, this assumption imposes a constraint on the allowable values of η_{adh} and η_{rep}, as expressed by the following:

$$\frac{\eta_{adh}}{\eta_{rep}} \in \left(0, \frac{\left(1-\frac{2R_N}{R^i+R^j}\right)^{\beta_{rep}+1}}{\left(1-\frac{2R_N}{{R_S}^i+{R_S}^j}\right)^{\beta_{adh}+1}} \right), \tag{5.31}$$

which reduces to:

$$\frac{\eta_{adh}}{\eta_{rep}} \in \left(0, \frac{\left(1-\frac{R_N}{R_{max}}\right)^{\beta_{rep}+1}}{\left(1-\frac{R_N}{R_{Smax}}\right)^{\beta_{adh}+1}} \right), \tag{5.32}$$

in the case of two fully-grown cells.

In the subsequent use of $h^{ij}(\|\boldsymbol{q}^{ij}\|)$ to inform cell movement in the model, we shall see that the *absolute* values generated by this function are actually of no great importance. Therefore, in general, we shall set $\eta_{rep} = 1$ and use the interval defined in Equation 5.32 to select an appropriate value for η_{adh}. The precise choice of this parameter uniquely defines a cell-cell equilibrium distance, and thus allows us to approximate the maximal extent of deformation between any two neighbouring cells. A typical example of the function $h^{ij}(\|\boldsymbol{q}^{ij}\|)$ is shown in Figure 5.14, where the various key features are highlighted in the corresponding caption.

Having introduced the function that we shall use to describe local interactions between cells, it is now necessary to consider the exact means by which these dynamics can be integrated into the existing model framework. This problem is necessarily

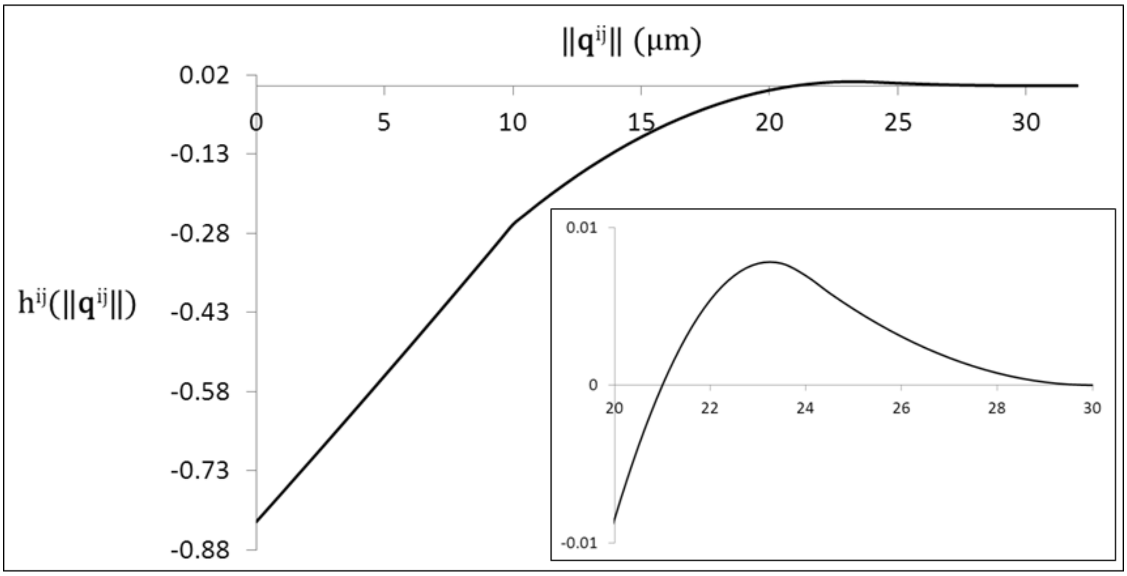

Figure 5.14: Typical plot of the function $h^{ij}(||\boldsymbol{q}^{ij}||)$, defined in Equation 5.30, which governs the behaviour of two interacting spherical cells as the distance between their centres of mass varies (i.e. $h^{ij} > 0$ indicates adhesion, $h^{ij} < 0$ indicates repulsion). The steep linear section (i.e. $||\boldsymbol{q}^{ij}|| < 10$) indicates that the cells' nuclear radii are overlapping; maximum repulsion occurs when the centres of mass share a spatial position. The inset shows the adhesive region in greater detail, where the key features include the equilibrium point (i.e. $||\boldsymbol{q}^{ij}|| = 21$) where adhesion and repulsion are balanced, and a point of maximal adhesive strength (i.e. $||\boldsymbol{q}^{ij}|| \approx 23$) close to where the equivalent radii begin to overlap (i.e. $||\boldsymbol{q}^{ij}|| = 24$). Adhesive contact is lost when the cells' sensing radii are no longer overlapping (i.e. $||\boldsymbol{q}^{ij}|| = 30$). The plot was generated for two identical cells using the parameter values $R_N = 5$ μm, $R = 12$ μm, $R_S = 15$ μm, $\eta_{adh} = 25/144$, $\eta_{rep} = 1$, $\beta_{adh} = 1$ and $\beta_{rep} = 1$.

complex, since the cell-cell effects experienced by each cell will depend crucially on the configuration of neighbouring cells in its locality (i.e. within R_S^i). In order to calculate the ultimate direction of movement for each cell experiencing cell-cell effects, we resolve that it is necessary to consider two distinct factors: the relative strength of the effect exerted by each neighbouring cell; and the relative strength of each of these effects with respect to any other migratory cues (e.g. chemotaxis). Constructing the overall cell motion in this way, we find that the key principles of the original model are maintained. We note, however, the necessary condition that any cell-cell related directional stimulus must be added *after* a direction has been calculated for *all* other required migratory cues.

Recall that even though Equation 5.1 is solved at every time step, the calculation of a new migration direction is not necessarily carried out as frequently. This vector is determined only every τ_u time units, corresponding to the assumed time between cell pseudopod attachments. Cell-cell related movements are not, however, governed by individual cell pseudopod dynamics; adhesive and repulsive effects will depend only on the instantaneous configuration of cells. Therefore, the vector characterising cell-cell interactions must be re-calculated at every time step. Adopting the terminology of Palsson and Othmer (2000), we can classify these two assumed types of cell movement as either "active" or "passive", respectively.

The first aspect that we require to address when incorporating cell-cell interactions is the competition between the effect of cell-cell adhesion or repulsion, and the other migratory cues such as persistence and chemotaxis. As an example, consider a scenario where a cell has formed adhesion bonds with a neighbouring cell on one side but also senses a chemoattractant gradient at its opposite side; the resultant cell response is likely to depend crucially on the relative strength of the "pull" experienced from each side. With this argument in mind, we firstly define, for each cell, the vector $\boldsymbol{v}_{\Sigma}^{i}$ to represent the overall directional stimulus obtained from the desired combination of migratory cues, as outlined in Section 5.3. In order to subsequently determine the overall movement direction $\boldsymbol{v}^{i}_{q,\Sigma}$ that includes the cell-cell effect imposed by each neighbour (i.e. centre of mass within $R_S^i + R_S^j$), we construct a linear combination of unit vectors with appropriate coefficients (or weightings). As a consistent point of reference we arbitrarily assign the vector $\boldsymbol{v}_{\Sigma}^{i}$ a weighting of unity, and define the equation:

$$\boldsymbol{v}_{q,\Sigma}^{i}(t) = \frac{\boldsymbol{v}_{\Sigma}^{i}(t)}{\|\boldsymbol{v}_{\Sigma}^{i}(t)\|} + \sum_{j=1}^{n^i} \begin{cases} \chi_{rep}^{ij}\left(h^{ij}(\|\boldsymbol{q}^{ij}\|)\right) \cdot \frac{\boldsymbol{q}^{ji}(t)}{\|\boldsymbol{q}^{ji}(t)\|}, & h^{ij} \le 0, \\ \chi_{adh}^{ij}\left(h^{ij}(\|\boldsymbol{q}^{ij}\|)\right) \cdot \frac{\boldsymbol{q}^{ij}(t)}{\|\boldsymbol{q}^{ij}(t)\|}, & h^{ij} > 0, \end{cases} \tag{5.33}$$

where n^i is the total number of cells interacting with cell i, and the functions $\chi^{ij}_{rep}(h^{ij})$ and $\chi^{ij}_{adh}(h^{ij})$ quantify the relative weighting of the repulsion or adhesion, respectively, from each neighbour. These two weight functions are chosen in such a manner that the qualitative features of the cell-cell interaction function $h^{ij}(\|\boldsymbol{q}^{ij}\|)$ are conserved; for repulsion we define:

$$\chi_{rep}^{ij}\left(h^{ij}\left(\|\boldsymbol{q}^{ij}\|\right)\right) = \chi_{rep} \cdot \left(\frac{h^{ij}(\|\boldsymbol{q}^{ij}\|)}{h^{ij}{}_{min}}\right)^{\beta_{\chi_{rep}}}, \tag{5.34}$$

whilst for adhesion we similarly define:

$$\chi_{adh}^{ij}\left(h^{ij}\left(\|\boldsymbol{q}^{ij}\|\right)\right) = \chi_{adh} \cdot \left(\frac{h^{ij}(\|\boldsymbol{q}^{ij}\|)}{h^{ij}{}_{max}}\right)^{\beta_{\chi_{adh}}}. \tag{5.35}$$

In these equations, the β parameters define the precise shape of the relationships, whilst the χ parameters, which are chosen to lie in the interval $[0, \infty)$, define the maximum possible strengths of cell-cell adhesion and repulsion, relative to the strength of all other appropriate directional cues (i.e. $\boldsymbol{v}_{\Sigma}{}^{i}$). The normalising parameters $h^{ij}{}_{min}$ and $h^{ij}{}_{max}$ are, respectively, the minimum and maximum values of the function $h^{ij}(\|\boldsymbol{q}^{ij}\|)$. The value of $h^{ij}{}_{min}$ can easily be calculated via the equation:

$$h^{ij}{}_{min} = h^{ij}(0) = \eta_{adh} - \eta_{rep}. \tag{5.36}$$

Calculating $h^{ij}{}_{max}$, however, is not so straightforward. Assuming that we are in the biologically realistic parameter regime stipulated by Equation 5.31, the function $h^{ij}(\|\boldsymbol{q}^{ij}\|)$ will have a unique maximum at some distance $\|\boldsymbol{q}^{ij}\| \in (2R_N, R^i+R^j)$. Denoting this distance $\|\boldsymbol{q}^{ij}\|^*$, its value can be found by solving the equation:

$$h^{ij\prime}(\|\boldsymbol{q}^{ij}\|^*) = \left[\frac{\eta_{rep}(\beta_{rep}+1)}{R^i+R^j}\right] \cdot \left(1 - \frac{\|\boldsymbol{q}^{ij}\|^*}{R^i+R^j}\right)^{\beta_{rep}} - \left[\frac{\eta_{adh}(\beta_{adh}+1)}{R_S{}^i+R_S{}^j}\right] \cdot \left(1 - \frac{\|\boldsymbol{q}^{ij}\|^*}{R_S{}^i+R_S{}^j}\right)^{\beta_{adh}} = 0. \tag{5.37}$$

For $\beta_{adh} = \beta_{rep}$, the solution can be found analytically but, in general, we may require to seek a numerical solution (e.g. by Newton's method with an appropriate initial guess). Finally, therefore, the value of $h^{ij}{}_{max}$ can be expressed as:

$$h^{ij}{}_{max} = h^{ij}(\|\boldsymbol{q}^{ij}\|^*). \tag{5.38}$$

Typical examples of the two functions defined in Equations 5.34 and 5.35 are plotted in Figure 5.15; where applicable, the parameters correspond to those used to generate Figure 5.14.

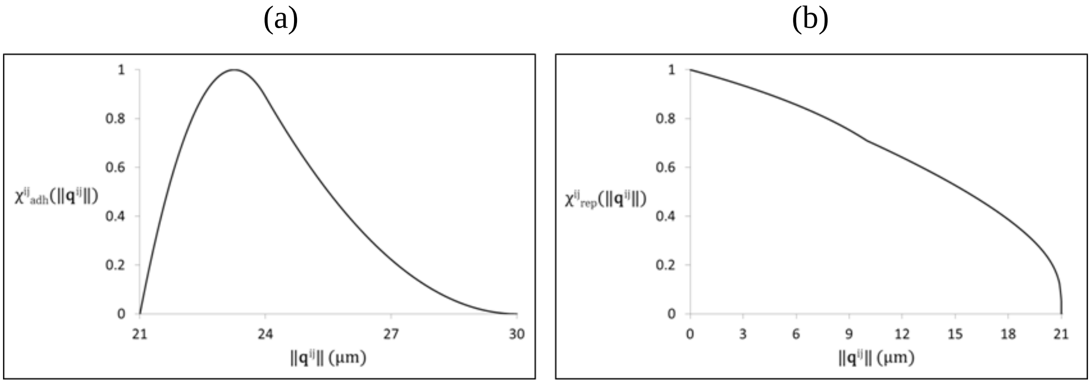

Figure 5.15: Typical plots of the cell-cell interaction directional weightings (a) $\chi^{ij}_{adh}(h^{ij}(\|\boldsymbol{q}^{ij}\|))$ and (b) $\chi^{ij}_{rep}(h^{ij}(\|\boldsymbol{q}^{ij}\|))$ between two identical spherical cells, as defined in Equations 5.34 and 5.35, respectively. Specifically, the plots show the variation with distance between the cell centres of mass in the two distinct cases of (a) adhesion and (b) repulsion. Note that both weightings are equal to zero at the equilibrium distance (i.e. $\|\boldsymbol{q}^{ij}\| = 21$). The plots were generated using the same parameter values as for Figure 5.14 with, additionally, $\chi_{rep} = 1$, $\chi_{adh} = 1$, $\beta_{\chi rep} = 0.3$ and $\beta_{\chi adh} = 1$.

Having now derived a methodology that incorporates all of our desired directional stimuli, we can express $\boldsymbol{v}^i_{q,\Sigma}$ as the final vector that describes the overall direction of movement of each individual cell. Thus, in line with our original definition governing cell movement in Equation 5.1, we finally define:

$$\boldsymbol{u}^i(t) = \boldsymbol{v}^i_{q,\Sigma}(t), \tag{5.39}$$

which now incorporates all external directional cues, as well as local cell-cell interactions.

In light of the latest model definitions, it is necessary to introduce a slight modification to one of the earlier equations. The definition of Equation 5.2, made in the case of discrete volumeless cells, stipulates that a cell will always persist in the previous direction of cell migration, or pseudopod extension, as denoted by $\boldsymbol{u}^i(t - \tau_u)$. Since we have now introduced cell-cell interactions, however, the overall cell movement direction $\boldsymbol{u}^i$ is instead constructed by a combination of pseudopod (i.e. active) and non-pseudopod (i.e. passive) driven movement. Any passive cell-cell effects should not be taken into account in the persistent random walk model, so it is clear that the definition of the persistence vector $\boldsymbol{v}_a{}^i(t)$ given by Equation 5.2 no longer holds. Therefore, we modify Equation 5.2 to become:

$$\boldsymbol{v}_a^i(t) = \boldsymbol{v}_\Sigma{}^i(t - \tau_u), \tag{5.40}$$

which insists that each cell will undergo persistence only in the direction of the previous pseudopod extension (i.e. its previous “active” movement direction).

5.5.3. Contact Inhibition

As discussed in Section 5.3, calculating the overall cell directionality is only half of the argument; cell speed must also be considered. Thus far, we have suggested simple equations to describe how cell speed may be affected in the presence of collagen, fibrin or a chemoattractant gradient. Having introduced cell-cell interactions, it becomes necessary to now incorporate a further such relationship that accounts for the presence of neighbouring cells. As such, we propose a mechanism whereby, on average, cell speeds are reduced with increasing cell density or, more specifically, increasing contact inhibition (Abercrombie, 1980). Indeed, such behaviour has previously been observed and quantified during *in vitro* fibroblast monolayer formation and wound healing (Tremel et al., 2009). Clearly, this collective phenomenon must depend crucially on the behaviour of individual cells; hence, to incorporate this into our model we consider each cell on an individual basis and calculate what shall be termed “local cell density”, $D^i(t)$. As suggested by the choice of terminology, this calculation involves making a quantitative approximation of the area surrounding a cell that is occupied by other cells. From a biological point of view, we could more readily relate this measure to the fraction of the cell surface that is in contact with other cells.

In order to perform this calculation we must first make some definitions. We begin by defining, for each cell, the following function in the x_1-x_2 plane:

$$\xi^i(\boldsymbol{x},t) = AA^i {x_1}^2 + BB^i x_1 x_2 + CC^i {x_2}^2 + DD^i x_1 + EE^i x_2 + FF^i, \tag{5.41}$$

where the coefficients are given by:

$$AA^i = \frac{1}{{R^i}^2},\;\; BB^i = 0,\;\; CC^i = \frac{1}{{R^i}^2},\;\; DD^i = -\frac{2f_1^i}{{R^i}^2},\;\; EE^i = -\frac{2f_2^i}{{R^i}^2},\;\; FF^i = \frac{{f_1^i}^2 + {f_2^i}^2}{{R^i}^2} - 1. \tag{5.42}$$

Fixed values of this function represent circular contours that are centred on the instantaneous cell centroid position $\boldsymbol{f}^{\,i} = (f_1^{\,i}, f_2^{\,i})$. We note the important property that $\xi^i \in [-1, \infty)$, and, moreover, that the set of points denoted by $\boldsymbol{x}^*$, and satisfying:

$$\xi^i(\boldsymbol{x}^*, t) = 0, \tag{5.43}$$

delineate the cell boundary. For convenience, we also define:

$$\xi_S^i(\boldsymbol{x},t) = {AA_S}^i {x_1}^2 + {BB_S}^i x_1 x_2 + {CC_S}^i {x_2}^2 + {DD_S}^i x_1 + {EE_S}^i x_2 + {FF_S}^i, \tag{5.44}$$

with coefficients:

$$\begin{gathered} {AA_S}^i = \left(\frac{R^i}{{R_S}^i}\right)^2 \cdot AA^i, \qquad {BB_S}^i = \left(\frac{R^i}{{R_S}^i}\right)^2 \cdot BB^i, \qquad {CC_S}^i = \left(\frac{R^i}{{R_S}^i}\right)^2 \cdot CC^i, \\ {DD_S}^i = \left(\frac{R^i}{{R_S}^i}\right)^2 \cdot DD^i,\;\; {EE_S}^i = \left(\frac{R^i}{{R_S}^i}\right)^2 \cdot EE^i,\;\; {FF_S}^i = \left[\left(\frac{R^i}{{R_S}^i}\right)^2 \cdot \left(FF^i + 1\right)\right] - 1, \end{gathered} \tag{5.45}$$

such that $\xi_S{}^i$ satisfies an identical property to Equation 5.43, although this time on the set of points constituting the cell sensing boundary. The key reason for defining these two functions is that they provide a simple means of testing whether or not a particular spatial co-ordinate lies within the notional boundary, or sensing boundary, of a cell.

With this in mind, we can begin to construct an algorithm designed to quantify the occupancy of space around any cell. The algorithm proceeds by first constructing a spatial grid of points within the sensing region of the target cell, where the "origin" of this grid is placed at the cell centre. Therefore, the set of grid points $\boldsymbol{X}^i_{M,N}$, for integer values $-M^* \leq M \leq M^*$ and $-N^* \leq N \leq N^*$, is defined by:

$$\boldsymbol{X}^i_{M,N} = \boldsymbol{f}^i + {\Delta_X}^i \cdot [M,N]^T, \tag{5.46}$$

where ${\Delta_X}^i \leq {R_S}^i$ - R^i is the cell-specific grid spacing, and:

$$M^* = N^* = \mathrm{Int}\left[\frac{{R_S}^i}{{\Delta_X}^i}\right]. \tag{5.47}$$

Subsequently, at each grid point we seek to satisfy the following conditions:

$$\xi^i_S\left(\boldsymbol{X}^i_{M,N}, t\right) < 0, \tag{5.48}$$

and:

$$\xi^j\left(\boldsymbol{X}^i_{M,N}, t\right) < 0, \tag{5.49}$$

for any neighbouring cell *j*. That is, we look for grid points that lie within the sensing boundary of the target cell, but also within the cell boundary of any other cell. Therefore, if we denote by ${n_X}^i$ the total number of grid points at which both of these conditions are satisfied, we can finally define the equation for the local cell density as:

$$D^i = \frac{{n_X}^i \cdot \left({\Delta_X}^i\right)^2}{\pi \cdot \left[\left({R_S}^i\right)^2 - \left(R^i\right)^2\right]}, \tag{5.50}$$

where the total area satisfying the grid conditions has been normalised by the area of the cell sensing region. An illustrative diagram is presented in Figure 5.16 to further clarify the rationale of this algorithm. As a final aside, it should be noted that under certain conditions, such as where sizeable cell overlaps occur, Equation 5.50 can predict local densities that are greater than unity. When this arises the value is simply reset to unity.

As mentioned above, the main motivation for developing this concept of local cell density was to inform the speed calculation for cells that are interacting with other cells in their locality. Therefore, in keeping with the format of Equations 5.18-5.20, we

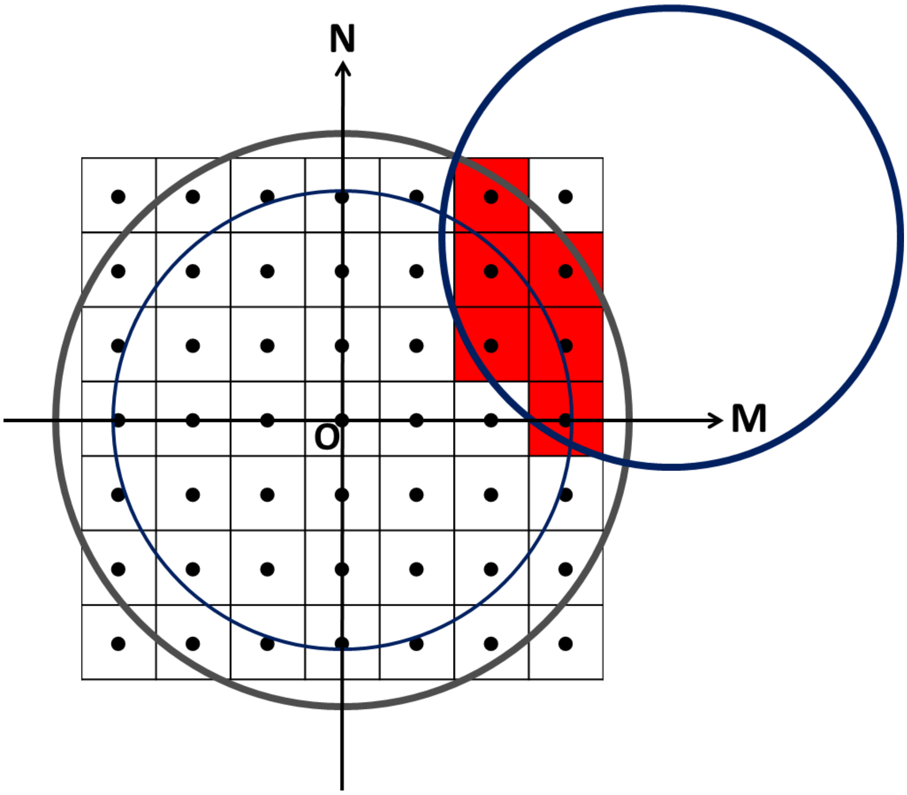

Figure 5.16: Schematic diagram illustrating the rationale of assumptions regarding the calculation of local cell density D^i in the spherical cell migration model. A regular spatial grid of integer-valued points *(M, N)* with spacing $\Delta_X{}^i$ is constructed in the vicinity of cell *i* (represented by the thin blue line). The origin *O* of this grid corresponds to the cell centre of mass, and the extent of the grid is determined by ensuring that all grid points on the respective co-ordinate axes lie within the cell sensing radius (i.e. thick grey line). The area of overlap between the sensing radius of cell *i* and cell radius of any neighbouring cell *j* (i.e. thick blue line) is approximated by summing the area of each grid block whose central point lies within this region (i.e. red squares). The final D^i value is subsequently calculated by normalising this overlap area with the area of cell *i*'s sensing region (i.e. area enclosed between the thin blue and thick grey lines).

express this relationship as:

$$\psi_D{}^i\left(D^i\right) = 1 + (\nu_D - 1) \cdot \left[D^i\right]^{\beta_{s,D}}, \tag{5.51}$$

where, in general, $\nu_D < 1$ determines the maximal extent of speed decrease at large local densities, and $\beta_{s,D}$ defines the overall shape of the relationship. Using this definition, Equation 5.17 can be modified to:

$$s^i(t) = s_0 \cdot {\psi_c}^i\left(c^*\left(\boldsymbol{f}^i, t\right)\right) \cdot {\psi_b}^i\left(b^*\left(\boldsymbol{f}^i, t\right)\right) \cdot {\psi_K}^i\left(\left\|\nabla K\left(\boldsymbol{f}^i(t)\right)\right\|\right) \cdot {\psi_D}^i\left(D^i\right). \qquad (5.52)$$

5.5.4. Proliferation

An additional advantage of having a concept of local cell density is that we can further use this value to inform the likelihood of cell proliferation, by assuming that contact inhibition also plays a role in suppressing cell cycle progression. In this vein, we can draw comparisons with other theoretical studies where it has been postulated that cellular quiescence can be induced by cell-cell mechanical stresses (Schaller and Meyer-Hermann, 2005; Shraiman, 2005). Many other paradigms for control of cell mitosis have also been considered by various groups, such as: up-regulation of proliferation in the presence of growth factors (see Chapters 3 and 4); availability of nutrients (Macklin et al., 2012); the inverse correlation between proliferation and motility known as the “Go-or-grow” hypothesis (Tektonidis et al., 2011). We shall neglect any other factors here, however, but acknowledge that the model has the potential to be extended at a later date.

We model proliferation by allowing the cells to transition between the various phases of the cell cycle: M, G1, G0, S and G2, although we do not explicitly distinguish between the latter two (denoted S/G2 hereafter). Within this cycle, progression into S/G2 for each cell is assumed to be controlled by the extent of contact inhibition. The rest of the cycle, meanwhile, is entirely deterministic; any cell that enters S/G2 is committed to completing mitosis (i.e. M phase) and its resultant daughter cells are subsequently committed to completing growth (i.e. G1 phase). These three phases of the cycle are assumed to last for times τ_{G2}, τ_M and τ_{G1}, respectively.

Upon completion of the G1 phase, every cell undergoes a check to determine whether it can progress straight to S/G2 or, alternatively, enter the quiescent G0 phase. We assume that a cell will become quiescent if it senses that space is sufficiently limited, or, more specifically, if its local cell density D^i exceeds the critical value D_{crit}. Subsequent transition out of this phase will only occur if or when D^i drops below this threshold. Essentially, incorporating the concept of cell quiescence acts to prevent the addition of cells to the domain in regions where the extent of available space is deemed to be unfavourable. It has been observed that cell division under such circumstances can occur, but reattachment to the substrate may subsequently be prevented, thus causing some daughter cells to undergo cell death by anoikis (Landman et al., 2007). In our current model formulation, however, we choose not to consider any explicit mechanisms of cell death.

Throughout the G2/S phase, where cells begin to prepare for mitosis by synthesising DNA, we assume that cell motility is gradually decreased (Cai et al., 2007). Specifically, Equation 5.52 is modulated by a further factor, decreasing in time, such that the cell speed is reduced to zero before transition into the M phase. Allowing ${t_{G2}}^i$ to parameterise the time spent by a cell in the G2 phase, the modulating factor s_{G2} is therefore given by:

$$s_{G2}\left({t_{G2}}^i\right) = \left(\frac{\tau_{G2} - {t_{G2}}^i}{\tau_{G2}}\right)^{\beta_{G2}}, \quad 0 \leq {t_{G2}}^i \leq \tau_{G2}. \tag{5.53}$$

where β_{G2} defines the manner of speed variation over time (e.g. $\beta_{G2} \ll 1$ gives a transient decrease in cell speed near the end of S/G2).

Since the cell is preparing to divide, throughout the relatively short M phase we assume that the cell loses adhesive contact with both the substrate and neighbouring cells (Cai et al., 2007). These phenomena are achieved, respectively, by maintaining the zero cell speed attained by the end of S/G2 and, without loss of generality, setting $\eta_{adh} = 0$ in Equation 5.30. Consistent with a number of existing studies (Schaller and Meyer-Hermann, 2005; Ramis-Conde et al., 2008; Macklin et al., 2012), at the end of the M phase we assume that the cell splits into two daughter cells of half volume, such that:

$$R_d = \left(2^{-\frac{1}{3}}\right) \cdot R_{max}, \tag{5.54}$$

where R_d is the radius of each of the daughter cells. By selecting a direction on the unit circle $\boldsymbol{\theta}_d$ from a uniform distribution, the two daughter cells are assigned positions $\boldsymbol{f}_{d+}$ and $\boldsymbol{f}_{d-}$ according to:

$$\boldsymbol{f}_{d\pm} = \boldsymbol{f}_p \pm (R_{max} - R_d) \cdot \boldsymbol{\theta}_d, \tag{5.55}$$

where $\boldsymbol{f}_p$ is the pre-splitting position of the parent cell. This definition ensures that the two daughter cells are initially fully contained within the volume of their parent cell and, furthermore, preserve its centre of mass.

After this instantaneous splitting process the daughter cells immediately enter the G1 phase and become subject to all of the migration equations outlined in previous sections – under appropriate parameter regimes the cells are subsequently capable of complete separation. Throughout the entirety of the G1 phase, the daughter cells are assumed to undergo a linear increase in volume. Parameterising the time spent in the G1 phase by ${t_{G1}}^i$, the growth of each daughter cell can be characterised by the equation:

$$V^i\left({t_{G1}}^i\right) = \frac{1}{2} V_{max} \cdot \left(\frac{\tau_{G1} + {t_{G1}}^i}{\tau_{G1}}\right), \quad 0 \leq {t_{G1}}^i \leq \tau_{G1}. \tag{5.56}$$

After τ_{G1} time units have elapsed and the daughter cells have regained maximum volume, the cell cycle progression in each daughter begins again.

5.5.5. Modification of the Fibrous Matrix

Before moving on, we return briefly to the component of the model that allows fibrous matrix modification. In Section 5.3.5 we presented the original weight function used by McDougall et al. (2006a), which assumed that the matrix re-orienting effect of each discrete fibroblast was manifested in a localised square region surrounding the cell centre (c.f. Equation 5.22). Since we have now implemented a significantly stronger concept of cell shape, we can modify this equation to reflect the inherent spherical morphology. Therefore, recalling Equations 5.41 and 5.42, we now define:

$$w^i(\boldsymbol{x}, t) = \max\left[\left(-\xi^i(\boldsymbol{x}, t)\right)^{\beta_w}, 0\right], \tag{5.57}$$

where β_w defines the variation in the shape of this function with increasing distance from the cell centroid position. It is also worthwhile to note that Equation 5.21, defining the concept of cell “flux” within the domain, can now be simplified by dropping the time lag τ_w. Given that we have now strengthened the concept of cell morphology in the model and, indeed, assumed that our cells are approximately spherical, it is no longer necessary to account for the fact that the head and tail of the cell may be travelling in different directions. Re-defining Equation 5.21, therefore, we have:

$$\boldsymbol{g}(\boldsymbol{x},t) = \sum_{i=1}^{N} w^i(\boldsymbol{x},t) \cdot \frac{\dot{\boldsymbol{f}}^i(t)}{\|\dot{\boldsymbol{f}}^i(t)\|}, \tag{5.58}$$

which now completes the formulation of the spherical cell migration model.

5.6. Spherical Cell Simulation Results

Much like the simulations performed in Section 5.4, here we again opt to investigate some simple sensitivities in order to explore the *in silico* cell behaviour predicted by the model. We choose to work in the absence of external directional cues such as contact guidance and chemotaxis, however, and focus strongly on the newly developed model components: cell-cell adhesion and repulsion, contact inhibition and proliferation. Where appropriate, we utilise all of the previously applied base case parameters in Table 5.1, whilst all additional base case parameters required in this section are listed in Table 5.4.

5.6.1. Cell Dispersal

The first sensitivity study that we carry out examines the ability of cells to disperse from a densely packed nodule when their persistent random walks are modulated by the above detailed biophysical cell-cell interactions (note that cell proliferation is not considered at this stage). Each simulation begins with 64 cells positioned uniformly, with boundaries just touching, at the centre of the domain (Figure 5.17a). In addition, each cell is also assigned a random initial migration direction (i.e. $\boldsymbol{v}_{\Sigma}^{i}$ in Equation 5.33). Cell movement is subsequently simulated for a 6 hour period; the result of a typical base case simulation is shown in Figure 5.17b where the original nodule has dispersed to produce a distribution of individual cells and smaller aggregates within the domain. For each simulation performed, the extent of cell dispersal was quantified by averaging the displacement of each cell from its starting position at each time step. Note that the plots

Parameter	Definition	Value
R_N	Cell nuclear radius	5 μm
R_{max}	Maximal equivalent cell radius	12 μm
R_{Smax}	Maximal cell sensing radius	15 μm
η_{adh}	Potential function cell-cell adhesion coefficient	25/784
η_{rep}	Potential function cell-cell repulsion coefficient	1
β_{adh}	Potential function cell-cell adhesion shape parameter	1
β_{rep}	Potential function cell-cell repulsion shape parameter	1
χ_{adh}	Maximal cell-cell adhesion weighting	0.8
χ_{rep}	Maximal cell-cell repulsion weighting	20
$\beta_{\chi adh}$	Cell-cell adhesion weighting shape parameter	1
$\beta_{\chi rep}$	Cell-cell repulsion weighting shape parameter	0.85
v_D	Cell speed-modulation factor (local cell density)	0.125
$\beta_{s,D}$	Cell speed-modulation shape parameter (local cell density)	1
τ_{G1}	Time spent in G1 phase of cell cycle	14/3 hr
τ_{G2}	Time spent in S/G2 phase of cell cycle	5 hr
τ_M	Time spent in M phase of cell cycle	1/3 hr
D_{crit}	Critical local cell density for quiescence	0.2
β_{G2}	Cell speed-modulation shape parameter (mitosis)	0.25

Table 5.4: Base case parameters used for all simulations in Section 5.6.

shown later represent the average of the respective cell dispersal values obtained from 5 individual simulations.

We begin by examining the impact of varying χ_{adh}, which determines the maximal adhesive strength of the cells. The predicted extent of cell dispersal upon modification of this parameter is shown quantitatively in Figure 5.18a. A reduction of the base case value by 50% is seen to produce a strong increase in the extent of cell dispersal. Although the number of individual cells that have broken away from the nodule seems comparable to that observed in the base case, the others now tend to disperse in numerous clusters of few cells rather than remaining part of extensive aggregates (Figure 5.18b vs. Figure 5.17b). We observe significantly reduced cell dispersal in the

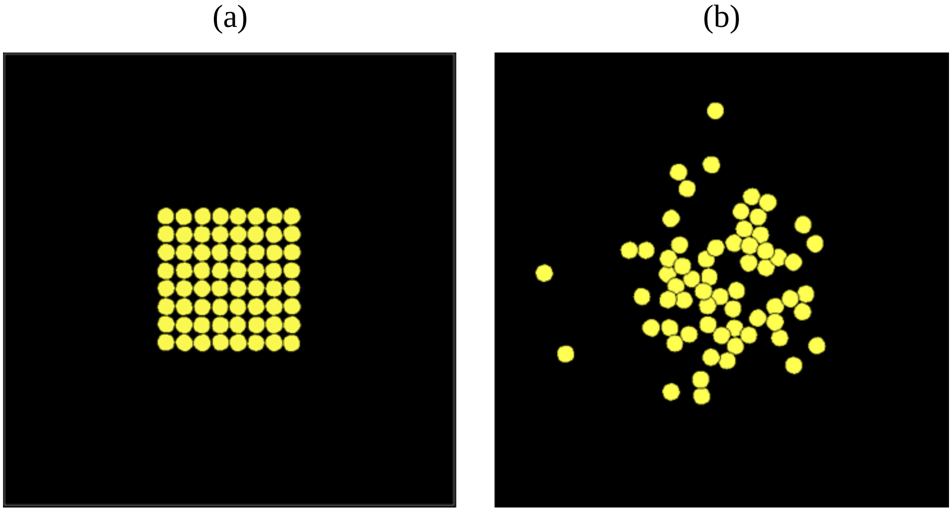

Figure 5.17: Typical base case simulation of spherical cell dispersal where individual cell movement is governed by a persistent random walk and biophysical cell-cell interactions. Images show (a) the initial uniform nodule of cells and (b) the final configuration after 6 hours of simulation. Relevant parameter values can be found in Tables 5.1 and 5.4.

case of increased adhesive strength; indeed, in contrast to the above case, absolutely no cells have managed to break free of the initial nodule (Figure 5.18c). The final configuration indicates that the cells have spent the simulation simply “jostling for position” through a combination of adhesive, repulsive and stochastic motion.

Our second sensitivity examines a different aspect of the adhesive interaction between two cells, by modifying the value of $\beta_{\chi adh}$ (c.f. Equation 5.35). This parameter quantifies the manner in which the relative strength of adhesion, with respect to existing migratory cues, varies with distance between the cell centres. That is, for $\beta_{\chi adh} > 1$, the region of strongest adhesion is concentrated about a peak, whilst for $\beta_{\chi adh} < 1$, this region is more widespread (c.f. Figure 5.15b). The results of this sensitivity are presented in Figure 5.19 where although the results are qualitatively what we would expect (i.e. larger $\beta_{\chi adh}$ gives greater dispersal), the extent of the quantitative differences are quite striking. It is clear that, even though the maximal adhesive strength remains fixed throughout, the manner with which adhesion is weakened as the *in silico* cells move apart has a strong impact on the ability of stochastic motion to ultimately drive the cells free from adhesive contact.

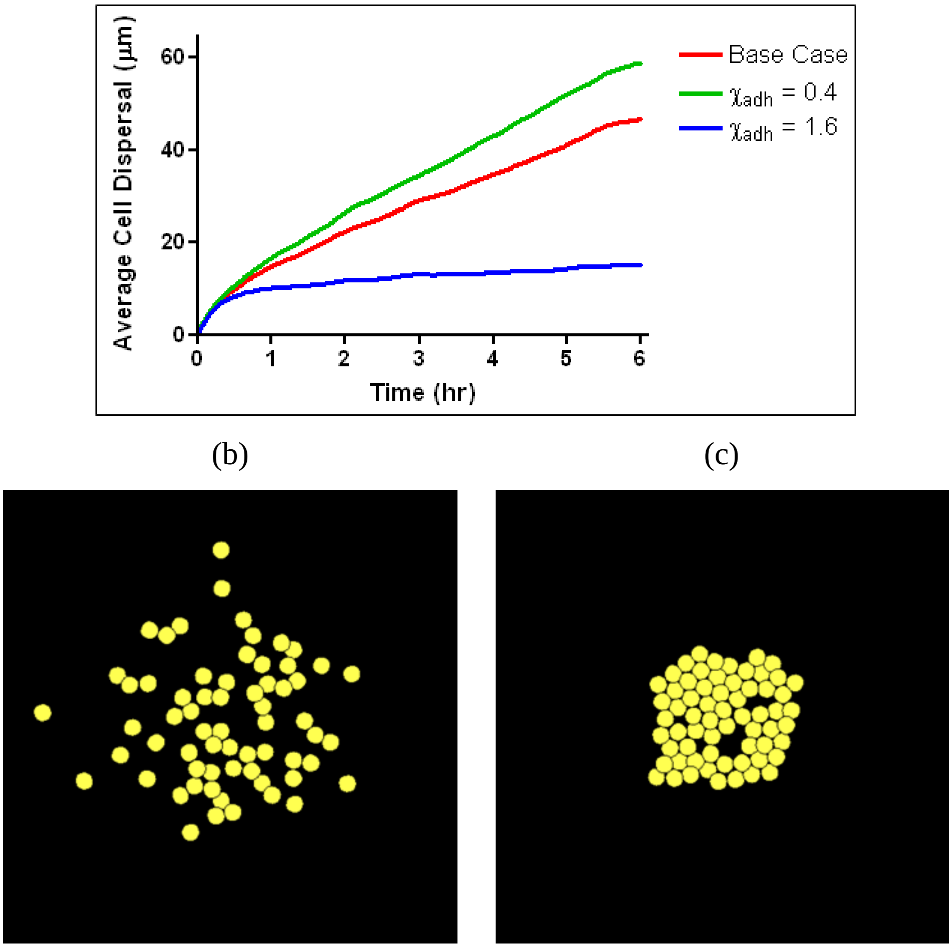
(a)

(b) (c)

Figure 5.18: Sensitivity study of spherical cell dispersal upon modification of χ_{adh}. The plot (a) quantifies the average cell dispersal of all cells from their starting position from 5 independent simulations, whilst the images show typical final cell configurations after 6 hours for parameter values (b) 0.4 and (c) 1.6; the base case parameter value was 0.8.

The final sensitivity that we consider relates to the manner in which our *in silico* cells respond to contact inhibition. Specifically, we vary the parameter $\beta_{s,D}$, defined to quantify the precise manner in which the speed of a cell is modulated by variations in the extent of available space in its locality (c.f. Equation 5.51); note that the maximum and minimum allowable cell speeds remain constant across these simulations. The quantitative impact on cell dispersal, presented in Figure 5.20a, is found to be dramatic. After 6 hours of simulation time, the sensitivity with increased $\beta_{s,D}$ (i.e. speed less easily inhibited by contact) produces an approximate two-fold increase compared to the sensitivity with $\beta_{s,D}$ reduced. Observing the final cell configurations (Figures 5.20b and

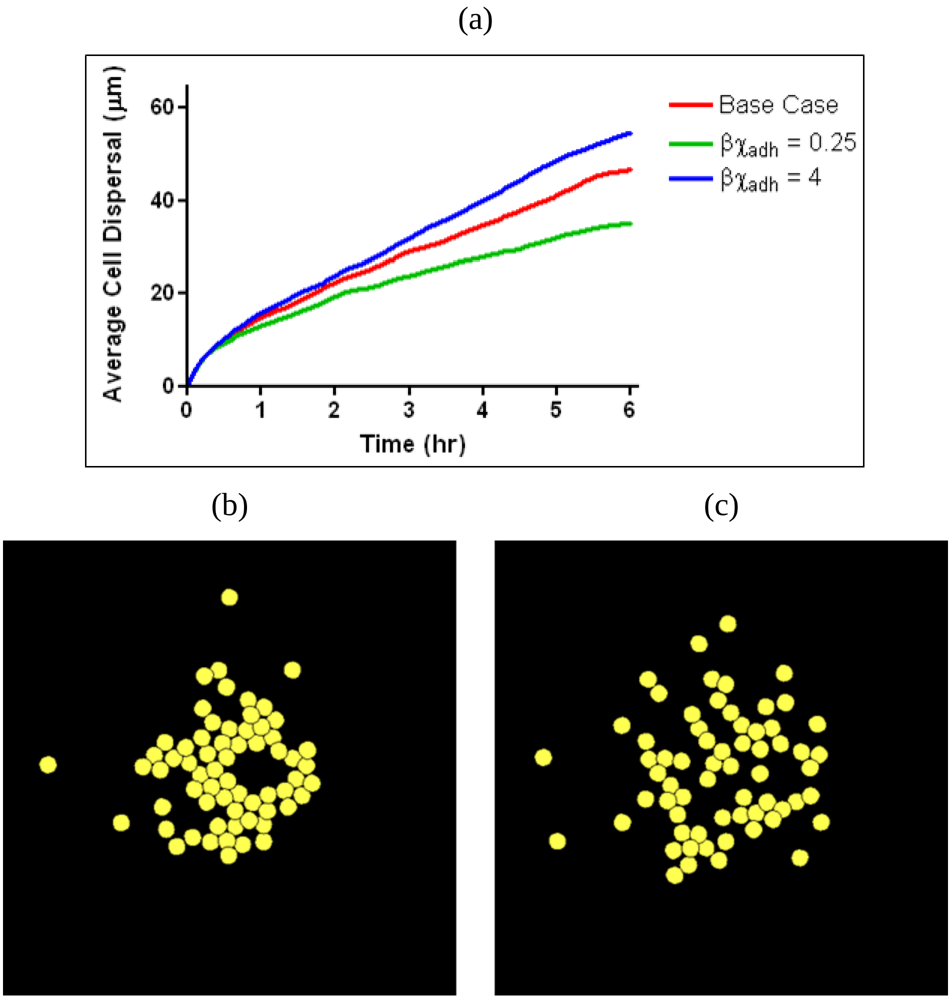

Figure 5.19: Sensitivity study of spherical cell dispersal upon modification of $\beta_{\chi adh}$. The plot (a) quantifies the average cell dispersal of all cells from their starting position from 5 independent simulations, whilst the images show typical final cell configurations after 6 hours for parameter values (b) 0.25 and (c) 4; the base case parameter value was 1.

5.20c), it is clear that this result is due to an inherently increased ability to escape adhesive contact. Indeed, when cell speeds are significantly reduced, the escape mechanism provided by persistence becomes practically useless because cells will maintain a single direction for at most a few microns. This is analogous to the situation outlined earlier (Figure 5.4b), whereby reducing the average persistence time τ_r^* resulted in cell trajectories displaying insignificant dispersal.

In summary, we find that these simulations provide insight into the manner of interaction between passive and active modes of cell migration in the model. The extent of cell dispersal is found to be greatest in the simulations where cell-cell interactions

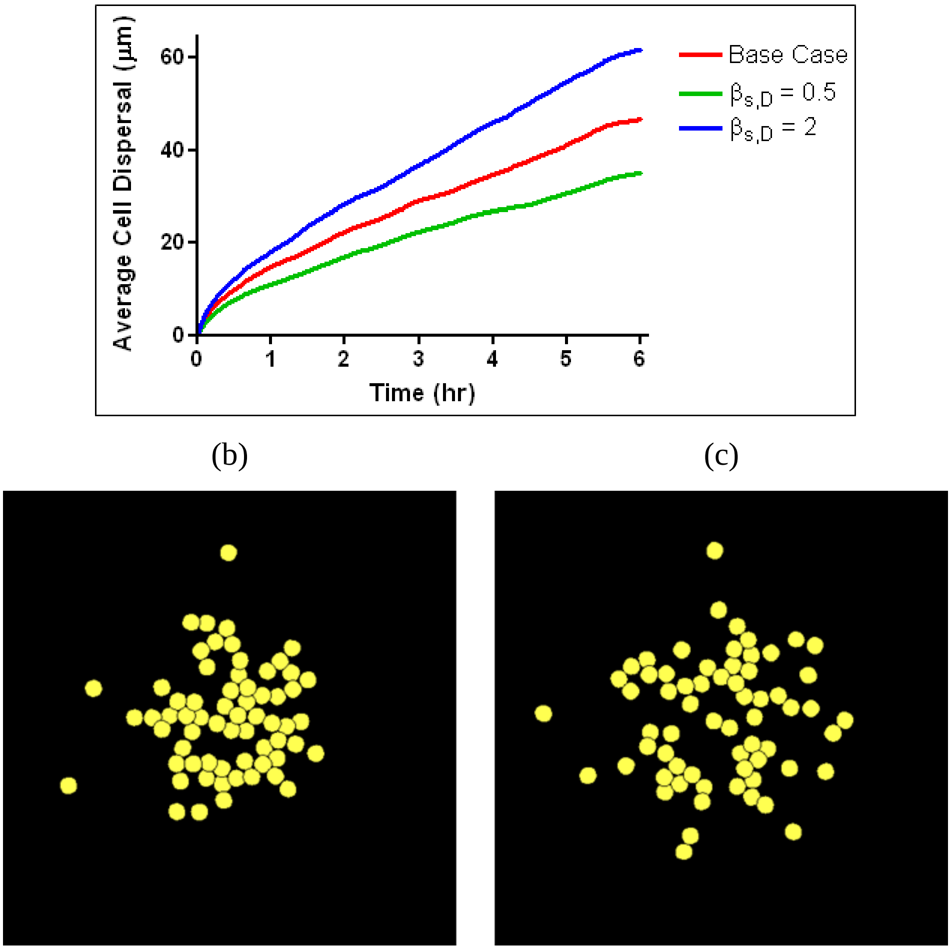

(a)

(b)

(c)

Figure 5.20: Sensitivity study of spherical cell dispersal upon modification of $\beta_{s,D}$. The plot (a) quantifies the average cell dispersal of all cells from their starting position from 5 independent simulations, whilst the images show typical final cell configurations after 6 hours for parameter values (b) 0.5 and (c) 2; the base case parameter value was 1.

have least impact on individual cell movements; that is, where the cell directionality and speed are least perturbed by the presence of neighbouring cells. Combined with data from equivalent *in vitro* experiments, simulations such as these could prove to be valuable for parameterising cell behaviour at a wide range of cell densities. Such studies could provide insight into cell migration mechanisms during wound healing, for example, where cells migrate from densely populated regions into cell-free tissue.

5.6.2. Growth to Confluence

The final simulations that we present in this chapter are used to investigate the implications of the cell proliferation algorithm detailed in Section 5.5.4. We make an analogy with the *in vitro* process of growing cells to confluence by seeding our *in silico* substrate with cells, and subsequently allowing them to undergo both contact-inhibited migration and proliferation until the domain is covered by a monolayer of cells. Specifically, we assume a domain size of 500 μm x 500 μm, and uniformly distribute 16 initial cells with randomly assigned migration directions and positions in their cell cycle (i.e. either in G1, G2/S or M with weighting dependent on the respective values of τ_{G1}, τ_{G2} and τ_M). Given the assumed value of R_{max} (c.f. Table 5.4), we terminate the simulation when the population reaches 550 cells (i.e. ~ 99.5% of available space occupied). Note that throughout a simulation we randomise the sequence in which we solve our equations for each cell at each time step – this procedure acts to prevent any particular cell gaining a proliferative advantage.

One problematic aspect of performing this type of simulation is the implementation of appropriate boundary conditions; periodic or reflective boundaries, for example, would not be particularly suitable. We assume, therefore, that the domain has solid boundaries and implement the condition that cells will migrate parallel to the boundary rather than allow any part of the cell body to leave the domain (see Appendix B for details). In addition, we assume that each cell can “sense” the boundary and, accordingly, incorporate boundary-related contact inhibition effects. Therefore, in the presence of the domain boundary, we assume that cells will not only experience a reduction in speed but also a reduced likelihood of initiating mitosis. In keeping with our earlier definitions, this involves increasing the local cell density D^i, which we achieve by incrementing n_X^i for each grid point $\boldsymbol{X}^i_{M,N}$ that lies both within the cell sensing boundary and beyond the boundary of the computational domain.

In our simulations we have considered sensitivities to three different parameters, each of which relates to separate aspects of the model. The common thread, however, is that each has implications for determining the rate of population growth under our contact inhibited proliferation assumptions. In each case, we present plots depicting how the cell population expanded over time. The first of these, Figure 5.21, shows the results of our sensitivity to the parameter D_{crit}, which defines the assumed upper threshold value of local cell density that will support successful cell cycle transition into S/G2 and, subsequently, completion of mitosis. In the case D_{crit} = 0.45, we find that very little contact inhibition of proliferation occurs and the rate of population growth comes very close to attaining the theoretical maximum in the absence of any contact

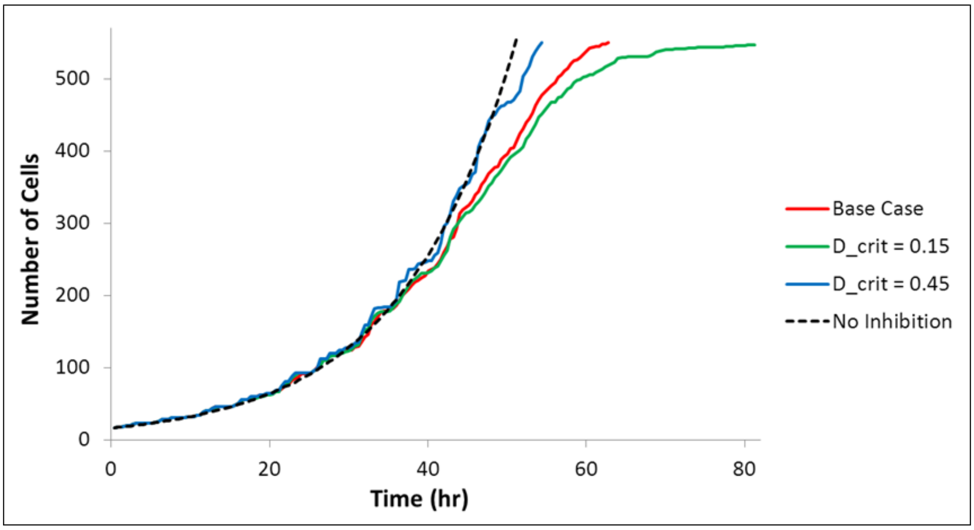

Figure 5.21: Plot showing the rate of growth of a migrating cell population undergoing contact inhibited proliferation for a range of D_{crit} values. The base case parameter was 0.2 (red line), whilst sensitivities were also performed for 0.15 (green line) and 0.45 (blue line). The black dashed line indicates the theoretical rate of growth in the absence of any contact inhibition (i.e. D_{crit} = 1).

inhibition (dashed black line). The base case simulation (D_{crit} = 0.2) is quite different, with the cell population exhibiting a roughly logistic mode of growth which takes almost 10 hours (i.e. 1 cell cycle length) longer to reach the target cell number. Decreasing D_{crit} only slightly further to 0.15 is seen to have a strong effect as the increased suppression of proliferation results in a population that experiences a significant delay in attaining the target size. It is notable that in all three of these simulations the rate of growth is essentially identical for the first three to four population doublings, before the perceived availability of space is reduced and many cells have their cell cycle progression arrested.

In view of this result, we examined the implications of modifying two further parameters that play a key role in determining the ability of cells to find space: namely, χ_{adh} and $\beta_{s,D}$. A reduction in the cell-cell adhesive strength (i.e. χ_{adh} = 0.58) is accordingly found to accelerate population growth, although the difference from the base case simulation is relatively minor (Figure 5.22). The impact of increasing χ_{adh} by an equivalent amount is found to be much more significant, with the rate of population increase noticeably slower (Figure 5.22). Choosing χ_{adh} to be 1.02 ensures that adhesive effects dominate any movement relating to the persistent random walk, and each pair of

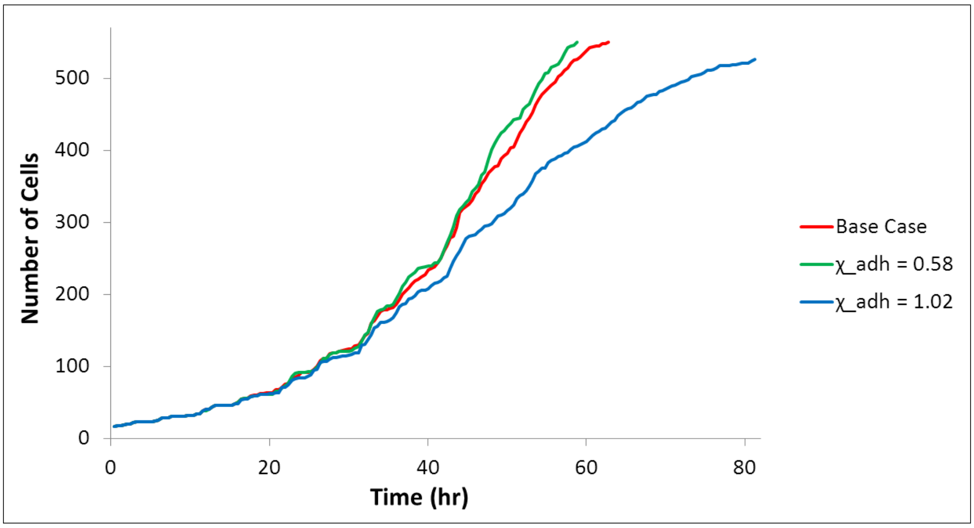

Figure 5.22: Plot showing the rate of growth of a migrating cell population undergoing contact inhibited proliferation for a range of χ_{adh} values. The base case parameter was 0.8 (red line), whilst sensitivities were also performed for 0.58 (green line) and 1.02 (blue line).

isolated daughter cells therefore remains "stuck together". This does not have any impact on the initial rate of population growth since the cells still sense sufficient available space not to inhibit proliferation of their partner. Beyond this initial phase, however, population growth is significantly slowed by the formation of large cell aggregates (c.f. Figure 5.18c), resulting in reduced capability of internal cells to progress through their proliferation cycle. It is clear that, in order to attain a rate of population growth comparable to the base case simulation, contact inhibition of proliferation in strongly adhesive cells would have to be significantly reduced.

Modifying the manner in which cell speeds are modulated by contact inhibition produces results that are qualitatively consistent with what we would expect (c.f. Figure 5.20): cells that decelerate more readily in response to contact experience a reduced ability to find space and undergo division (i.e. $\beta_{s,D}$ = 0.5), while increased cell division is observed when cell speeds are not so easily reduced (i.e. $\beta_{s,D}$ = 3). This effect is not seen to have a great impact upon the rate of population growth until the global cell density becomes relatively large, but a strong disparity is subsequently found between the times required to reach the target cell number (Figure 5.23). These results are indicative of a variation in the ability of cells at high density to transiently find sufficient space to progress through the G0 checkpoint.

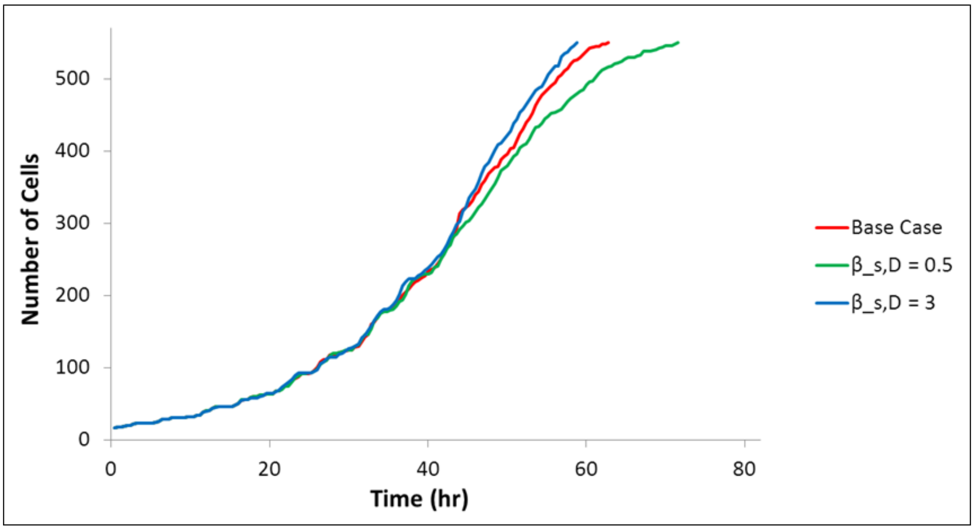

Figure 5.23: Plot showing the rate of growth of a migrating cell population undergoing contact inhibited proliferation for a range of $\beta_{s,D}$ values. The base case parameter was 1 (red line), whilst sensitivities were also performed for 0.5 (green line) and 3 (blue line).

5.7. Discussion

Lattice-based modelling approaches have been widely utilised over recent years to investigate both the migration of individual cells and the collective growth of cell populations. Whilst such models have proven to be of great value in a variety of scenarios, notably angiogenesis, many intrinsic aspects of the associated cell movements are necessarily simplified. In the study of biological systems where cell-cell and cell-environment interactions are found to be critical determinants of the precise spatial dynamics, lattice-free modelling techniques provide a much more tractable alternative.

One approach of this type, incorporating a novel dynamic feedback between migrating cells and their fibrous microenvironment, has been proposed by McDougall et al. (2006a) who sought to examine the mechanisms of wound-induced dermal scar formation. In this model each migrating fibroblast is assumed to be partially guided by the orientation of local collagen fibres, but also capable of re-orienting these fibres towards its overall migration direction. This approach, also incorporating cell movement via chemotaxis and persistence, provides the starting point for the extended model that we have presented in this chapter. As well as generalising the original discrete-point cell formulation, we have also developed the approach to incorporate physical cell-cell interactions. These modifications, coupled to the inherently adaptable nature of the underlying framework, have allowed us to broaden the future utility of the model.

In the original model formulation, performing discrete-point simulations of cell migration in the absence of contact guidance and chemotaxis would have predicted continuous motion in a straight line. Recent *in vitro* research into the behaviour of cells absent of external directional cues suggests that such results would be far from realistic (Li et al., 2008; Bosgraaf and Van Haastert, 2009). These studies, examining the movement of isolated amoebae cells, reveal a motion typically consisting of extended, relatively straight "runs" interrupted at irregular intervals by "turns" in largely random directions. Taking this work as inspiration, the most significant generalisation of the discrete-point model has been the inclusion of a stochastic migratory cue designed to capture this behaviour. Upon the subsequent addition of further migratory cues, the model design ensures that the stochastic component continues to play a part; its contribution, however, is differentially suppressed depending on the relative strength of the other assumed stimuli.

An analysis of the behaviour introduced by this random motion was examined in a series of simple sensitivities involving discrete-point cell migration in response to various combinations of directional cues. The level of cell dispersal exhibited in simulations of persistent random walks alone was shown to be widely variable, simply through variation of either the average persistence time (Figure 5.4), the straightness of "runs" (Figure 5.5) or the randomness of "turns" (Figure 5.6). Introducing a radially increasing fixed chemical profile allowed for the study of cell migration subject to variations in chemotactic receptiveness. Cells exhibiting a strong chemotactic response showed little stochastic motion, with trajectories arrowing outwards from the domain centre; weakly receptive cells, however, performed longer random walks as they struggled to locate the direction of increasing chemical concentration (Figure 5.8). Replacing the chemical gradient with a randomly-oriented undulating collagen profile, we further examined modes of cell migration within fibrous matrices of low, medium and high density. The amount of variation in these trajectories was, in general, found to be reduced with increased weighting of contact guidance since numerous cells were forced to traverse very similar pathways through the fibrous structure (Figure 5.10).

In addition to these sensitivities, we investigated the impact of assuming that the ability of cells to respond strongly to a chemotactic gradient is hampered by a tendency to undergo contact guidance, particularly within a dense ECM. Analogous to Figure

5.8, we first varied cell receptiveness to the chemical (Figure 5.11). At low collagen density, little qualitative difference was observed in comparison to the earlier matrix-free trajectories; medium collagen density, however, produced noticeably increased tortuosity in the outward trajectories. Contact guidance was again seen to largely dominate the cell paths at high density, and any chemotactic response was significantly slowed. Subsequently, we varied the maximal extent to which the fibrous matrix is capable of suppressing chemotaxis (Figure 5.12). The most interesting results from this sensitivity derived from the case where the maximum potential for chemotactic suppression was largest. At low collagen density the cells migrated directly up the chemical gradient; similar trajectories, displaying greater contact guidance-induced tortuosity, were observed at medium collagen density; whilst at high collagen density, any chemotactic response appeared largely absent.

As demonstrated by these simple sensitivities, the discrete-point cell model has the capability to predict modes of migration exhibited by isolated cells under a variety of circumstances both *in vitro* and *in vivo*. Since cells rarely migrate in isolation, however, we have proceeded to extend the applicability of the model by incorporating a biophysical concept of cell-cell interaction. Borrowing from the work of Macklin et al. (2012), we have assumed that each cell adopts an approximately spherical conformation and applied an appropriately defined potential function to describe both cell-cell adhesion and repulsion. Although neglecting to explicitly consider precise cell morphologies, this model formulation is designed to allow for both deformation of cells in close proximity and cell-cell adhesive contact beyond the notional cell boundaries.

In contrast to the work of Macklin et al. (2012), we have not determined the movement of our spherical cells on the basis of physical forces. In order to maintain the ethos of the original discrete-cell formulation, we have instead derived novel methods of determining the manner in which cell-cell interactions inform both the directionality and speed of overall cell movement. In terms of the directionality calculation, we proposed that the movement of each individual cell is based upon the solution to two distinct questions: (i) how strong are the relative effects exerted by each neighbouring cell?; and (ii) how strong are each of these effects with respect to all other directional cues?. The instantaneous cell speed calculation, based phenomenologically on the concept of contact inhibition (Abercrombie, 1980), has been introduced quite separately. Specifically, we have assumed that, in general, the speed of a cell will decrease with increasing “local cell density” – a term that we have coined to denote a normalised approximation of the amount of unoccupied space in the immediate locality of a cell.

The model behaviour upon the inclusion of these new concepts was subsequently examined by studying, in the absence of both chemotaxis and contact guidance, the dispersal of an initial nodule of cells under a series of pertinent parameter sensitivities. These simulations provided a good deal of insight into how the passive mode of cell movement integrates with the previous active migration assumptions; indeed, it was interesting to examine the mechanisms by which individual cells are capable of breaking free from adhesive cell-cell contact. As could be expected, this process was strongly inhibited by an increase in the maximal adhesive weighting (Figure 5.18). Less obvious, however, were the extensive reductions in cell dispersal upon decreasing either $\beta_{\chi adh}$, which determines the variation of adhesive strength with the distance between 2 cells (Figure 5.19), or the parameter $\beta_{s,D}$, which controls the response of cell speeds to cell-cell contact (Figure 5.20). Since the persistent random walk provides the prominent mechanism of escape from cell-cell contact, these two phenomena appear to be due, respectively, to an increased suppression of this directional cue over a longer range, and a general decrease in the distance travelled during periods of persistence.

The final aspect of the model that we introduced was a biophysical representation of proliferation, underpinned by the progression of individual cells through the appropriate phases of the cell cycle. The cycle was assumed to be largely deterministic: cells leaving S/G2 were committed to division at the end of the M phase, and newly-divided cells were committed to growth, which was completed at the end of G1. Some stochasticity was introduced, however, by assuming that cells also experience contact inhibition of proliferation; whenever a critical value of the local cell density was exceeded, cells would arrest their progression into S/G2 and instead enter the quiescent G0 phase. In cases where sufficient space was deemed to be available, each cell progressing through the S/G2 phase was decelerated to an immotile state before entering the M phase. This state was assumed to be maintained throughout M phase until each parent cell was subsequently split into two immediately motile daughter cells of half volume.

The implications of this contact-inhibited proliferation algorithm were subsequently examined by studying cell population growth within a simulation domain confined by solid boundaries. For cells with a particular set of movement properties, the first sensitivity study illustrated that, in order to achieve a logistic-type mode of population growth, the contact inhibition of proliferation was required to be relatively strong (i.e. D_{crit} small). In fact, the cell population behaviour was found to be particularly sensitive to changes in this parameter (Figure 5.21); over a relatively small range, the simulations predicted a delay of more than 2 full cell cycle lengths in the attainment of the target cell number (i.e. $D_{crit} = 0.15$), and also a rate of growth approaching the inhibition-free theoretical maximum (i.e. $D_{crit} = 0.45$). Subsequently, we also examined the sensitivity to two parameters that affect the ability of individual cells to transiently find the space required for progression through the G0 checkpoint. Accordingly, it was observed that cells reducing their speed more readily in response to contact divide more slowly (Figure 5.23), whilst significant delay in population growth is also imposed in an adhesion-dominated regime because the formation of extensive aggregates suppresses the ability of internal cells to find the space required to initiate proliferation (Figure 5.22).

A broad spectrum of results has been presented in this chapter, ranging from the migration patterns displayed by individual discrete-point cells to the population growth and dispersal of physically-sized spherical cells. In light of the work in previous chapters, it is notable that no explicit experimental data has been presented here with which to quantitatively validate the model predictions. Such validation has not, however, been the intention; given some of the novel aspects of the model implementation, performing sensitivities on each component has helped to illuminate the precise mechanisms driving the *in silico* cell behaviour. In the next chapter, however, we shall seek to demonstrate the value of the model by applying it to a widely-studied experimental system – the *in vitro* scrape wound assay. The cell type of interest in this case will once again be the fibroblast, which has been observed to be capable of exhibiting an irregular, elongated morphology. Since the model thus far caters only for cells of loosely spherical shape, we must first seek to generalise the model a little further in order to characterise the behaviour of strongly aspherical cells.

Chapter 6

A New Generalised Model of Cell Migration II: The Impact of Cell Morphology and Applications to Experimental Systems

6.1. Introduction

In the previous chapter, a new model for discrete-point cell migration was presented that included mechanisms whereby each cell assumed a loosely spherical morphology and underwent biophysical interactions with other cells in close proximity. As we stated earlier, however, our goal has been to develop a modelling framework that can reproduce a range of crawling cell movements in a variety of scenarios and, since many crawling cell types exhibit an elongated morphology (e.g. fibroblasts, *Dictyostelium*), it is clear that the current assumption of cells with fixed spherical shape is somewhat limiting. In this chapter we seek to address this important issue by extending the formulation to include non-spherical morphology.

The concept of cell shape is an important consideration: not only would we expect specific morphologies to have a strong effect on the manner in which cells interact, but the shape of particular cell types is also believed to be strongly coupled to their function (Bray, 2001). For our latest model extension, we propose that each *in silico* cell now assumes a loosely ellipsoidal shape with the capability to dynamically elongate or contract its body in response to various stimuli. Many ideas for the model are inspired by the work of Palsson and Othmer (2000); however, in order to maintain the existing model rationale, it is necessary to approach some of the inherent complexities from a very different perspective.

We begin in the next section by outlining the assumptions of our ellipsoidal cell migration model. Although some new equations are required, the majority of those presented in Chapter 5 remain largely unchanged. In some cases the validity of an equation may be subject to an additional caveat or slight redefinition of a variable, but any such required modifications will be made clear in the text. Much like the previous chapter, we shall go on to demonstrate the implications of our latest model definitions by considering a simple test case – namely, the response of an ellipsoidal cell to a moving chemoattractant source. Subsequently, the final set of simulations that we perform will be seen to provide a much more rigorous test of the modelling approach: firstly by benchmarking *in silico* cell movement and proliferation results against real experimental data, and then by applying our model to *in vitro* fibroblast scrape wound assays. Finally, we shall conclude this chapter by discussing the implications of our results and drawing appropriate conclusions, with particular consideration given to the future utility of the model.

6.2. Ellipsoidal Cell Model

6.2.1. Physical Characteristics of the Cell

Since we now wish to represent our cells as ellipsoidal, rather than spherical, it is necessary to consider three semi-axis lengths for each cell, rather than a single radius. We denote the semi-major and semi-minor axis lengths of the ellipse in the plane of simulation by $A^i(t)$ and $B^i(t)$, respectively, and assume that cell volume $V^i(t)$ is conserved during any change of shape by satisfying the equation:

$$A^i(t) \cdot B^i(t) = R^i(t)^2, \tag{6.1}$$

where $R^i(t)$ now represents the radius of a spherical cell with equivalent volume. Note from this definition that, at fixed volume, any change in cell shape is assumed to occur at fixed semi-axis length $R^i(t)$ in the plane perpendicular to the domain. In the direction of cell polarisation we assume $R^i(t) \leq A^i(t) \leq A^i_{max}(t)$, where $A^i_{max}(t)$ is the maximum allowable cell semi-major axis length at a particular volume – note that this definition also uniquely defines a set of values for $B^i(t) \leq R^i(t)$.

As in the spherical cell formulation of Macklin et al. (2012), we continue to assume that there is inherent uncertainty in the exact cell morphology and again consider each cell to have a sensing region beyond its notional boundary. Rather than assuming that each cell can sense up to a fixed distance from all points on its surface, however, we assume that the cell senses within a region equivalent to its shape such that:

$$\frac{A_S{}^i(t)}{B_S{}^i(t)} = \frac{A^i(t)}{B^i(t)}, \tag{6.2}$$

where $A_S{}^i(t)$ and $B_S{}^i(t)$ are the cell semi-major and semi-minor sensing axes, respectively. Furthermore, mirroring Equation 6.1, we assume that the area of the cell sensing region is conserved with any change in cell shape by defining:

$$A_S{}^i(t) \cdot B_S{}^i(t) = R_S{}^i(t)^2, \tag{6.3}$$

where $R_S{}^i(t)$ now represents the sensing radius of a spherical cell with equivalent volume. Importantly, it should be noted that these definitions inherently impose the condition that, compared to lateral regions, the polar extremities of an elongated cell exhibit both greater uncertainty in shape and greater ability to create and maintain adhesive bonds with neighbouring cells. As an analogue to Figure 5.13, a schematic diagram illustrating the new assumptions is presented in Figure 6.1.

We again point out that the time dependence in each of the above definitions is due to the cell volume variations that take place during the G1 phase of the cell cycle. As such, some further parameters are required to constrain the maximum possible cell size throughout simulation. As in Section 5.5.1, we have: V_{max}, the maximum cell volume; R_{max}, the radius of a spherical cell with equivalent maximum volume; and R_{Smax}, the sensing radius of a spherical cell with equivalent maximum volume. In addition to this we now also define A_{max}, the maximum attainable semi-major axis length of a fully-grown cell, subject to:

$$\frac{A^i_{max}(t)}{A_{max}} = \frac{R^i(t)}{R_{max}}, \tag{6.4}$$

where $A^i_{max}(t)$ represents the maximum possible semi-major axis length of any cell at a particular point in time. One further assumption is required with regard to the G1 phase of the cell cycle: although cell morphologies will now be allowed to vary temporally (see Section 6.2.4), at each time step where the cell volume is increased, this will be done in such a manner that the instantaneous cell eccentricity (i.e. ratio of $A^i(t)$ to $B^i(t)$) is conserved.

Finally, we point out that no further explicit assumptions are made regarding the size or shape of the nuclear component of the cell. As will be seen, it is necessary only to maintain the assumption of a fixed nuclear volume V_N, characterised by an equivalent nuclear radius R_N.

6.2.2. Cell-Cell Interactions

A major issue presented during the process of generalising the cell movement model from spherical cells to ellipsoidal cells is the construction of a consistent algorithm for simulating cell-cell interactions. For spherical cells we adopted the methodology of Macklin et al. (2012), where the behaviour of any two cells was uniquely defined by the distance between their centres of mass. This is no longer of any use for our ellipsoidal cells since, depending on the respective orientations of the two cells, any fixed distance between their centres could be associated with a range of possible behaviours: adhesion, repulsion or no interaction at all (note that this fact is intimated approximately by Figure 6.1b). The solution that we propose relies on the fact that for any two circles in the plane, their area of overlap can be expressed uniquely in terms of the distance between their centres. Therefore, by calculating the area of overlap a^{ij} between the sensing ellipses of any two cells, we can uniquely, and consistently, define an "equivalent distance" d^{ij} between the cells, had they both been identically spherical with equivalent volumes. Thus, by subsequently calculating the value of $h^{ij}(d^{ij})$ (rather than simply $h^{ij}(\|\boldsymbol{q}^{ij}\|)$), we can uniquely define the related cell-cell interaction behaviour for ellipsoidal cells without any significant modification of the equations detailed in Section 5.5.2.

Although this solution sounds quite simple and elegant, in actual fact it presents a

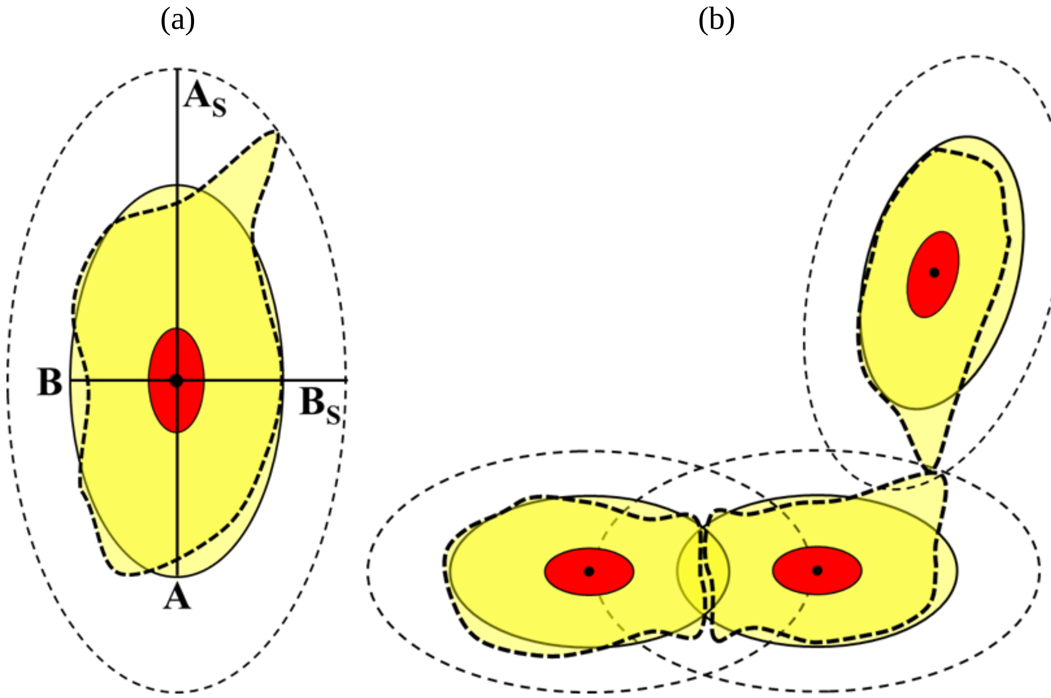

Figure 6.1: Schematic diagram illustrating the rationale of assumptions regarding cell morphology and cell-cell interactions in the ellipsoidal cell migration model. In (a), the labels A and B indicate, respectively, the equivalent semi-major and semi-minor axis lengths of the ellipsoidal cell in the plane of simulation. The maximum adhesion interaction distance varies as the cell boundary is traversed; it is characterised by a concentric ellipse of identical eccentricity, where the semi-major and semi-minor axis lengths are labeled A_S and B_S, respectively. The explicit cell morphology is not tracked in time – the thick dashed line in (a) shows one particular possibility. The configuration of cells in (b) shows that uncertainty in exact cell morphologies can be accounted for by overlapping of equivalent cell ellipses and the maintenance of adhesive contact beyond the notional cell boundaries.

variety of complex mathematical problems. Firstly, and most significantly, we require an algorithm for calculating the overlap area between two ellipses of random size at random positions in the plane. Fortunately, however, this is a problem that has recently been tackled in the development of a force-based model for studying pedestrian dynamics (Chraibi et al., 2010) and, furthermore, a detailed summary of the analysis and numerical implementation has been made freely available (Hughes and Chraibi, 2011). In general, the algorithm involves a sequential process of solving a quartic polynomial for the intersection of the respective ellipse equations; determining the number of distinct, real-valued roots; and, finally, calculating the resultant area of overlap by appropriately combining sector and segment areas demarcated by the respective ellipse boundaries and their points of intersection. For brevity we refer the reader to these references for full details and, for what follows, accept that the extent of the overlap between the sensing boundaries of any two elliptical cells can be accurately calculated.

The next problem that we require to tackle is the derivation of an expression that uniquely relates the overlap area A of two general circles in the plane of radii R_1 and R_2 to the distance between their centres d. In all that follows we shall assume $R_1 \geq R_2$, and note that $A(d \leq R_1 - R_2) = \pi R_2^2$, whilst $A(d \geq R_1 + R_2) = 0$. The key to this process is found to be splitting the derivation into two distinct cases as shown in Figure 6.2, where the transition occurs at $d_{trans} = (R_1^2 - R_2^2)^{1/2}$.

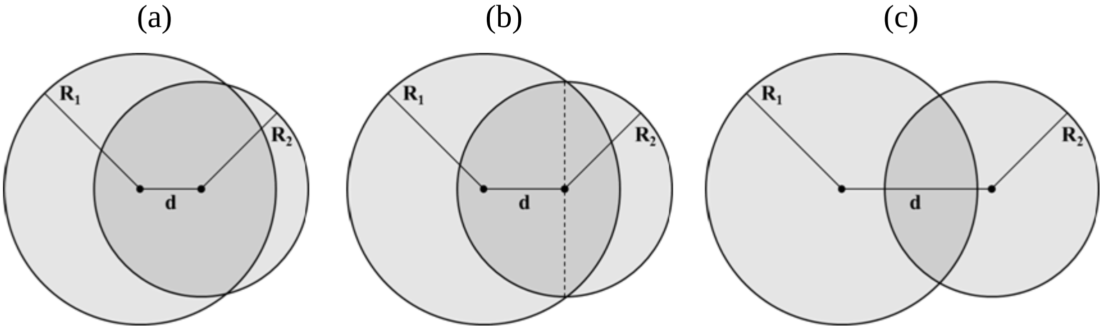

Figure 6.2: Schematic diagram illustrating (a, c) the 2 assumed cases in the calculation of the overlap area (dark shaded region) between 2 circles of radii R_1 and R_2 ($R_1 \geq R_2$) in the plane, and (b) the point of transition between these cases. The circle centres are separated by distance d, and the transition between the 2 cases occurs at $d_{trans} = (R_1^2 - R_2^2)^{1/2}$ where the points of intersection are collinear with the centre of the smaller circle (dashed vertical line).

Beginning with the case where d is larger than the transition distance, an expression for the overlap area between the circles can be constructed by appropriately combining the areas of a series of sectors and triangles. Upon elimination of any angles in the expression, the area of overlap can be defined as a function of the distance between the cell centres as follows:

$$A(d) =$$
$$R_1{}^2 \cdot \left[\cos^{-1}\left\{\frac{d^2+R_1{}^2-R_2{}^2}{2dR_1}\right\} - \left(\frac{d^2+R_1{}^2-R_2{}^2}{4d^2R_1{}^2}\right) \cdot \sqrt{4d^2R_1{}^2 - \left(d^2+R_1{}^2-R_2{}^2\right)^2}\right]$$
$$+ R_2{}^2 \cdot \left[\cos^{-1}\left\{\frac{d^2+R_2{}^2-R_1{}^2}{2dR_2}\right\} - \left(\frac{d^2+R_2{}^2-R_1{}^2}{4d^2R_2{}^2}\right) \cdot \sqrt{4d^2R_2{}^2 - \left(d^2+R_2{}^2-R_1{}^2\right)^2}\right], \tag{6.5}$$
$$\sqrt{R_1{}^2 - R_2{}^2} \leq d \leq R_1 + R_2.$$

Utilising a similar method for the case where d is smaller than the transition distance, we further derive:

$$A(d) =$$
$$R_1{}^2 \cdot \left[\cos^{-1}\left\{\frac{d^2+R_1{}^2-R_2{}^2}{2dR_1}\right\} - \left(\frac{d^2+R_1{}^2-R_2{}^2}{4d^2R_1{}^2}\right) \cdot \sqrt{4d^2R_1{}^2 - \left(d^2+R_1{}^2-R_2{}^2\right)^2}\right]$$
$$+ R_2{}^2 \cdot \left[\pi - \cos^{-1}\left\{\frac{R_1{}^2-R_2{}^2-d^2}{2dR_2}\right\} - \left(\frac{R_1{}^2-R_2{}^2-d^2}{4d^2R_2{}^2}\right) \cdot \sqrt{4d^2R_2{}^2 - \left(R_1{}^2-R_2{}^2-d^2\right)^2}\right], \tag{6.6}$$
$$R_1 - R_2 \leq d \leq \sqrt{R_1{}^2 - R_2{}^2}.$$

Given a particular overlap area A^*, our goal is to use the above expressions to calculate the corresponding distance d^* between the circle centres. Clearly, however, due to the inherent complexity of these equations, it is not possible to write an explicit expression for d in terms of A. The value of d^* must, therefore, be calculated numerically, and we choose to do so by employing Newton's Method, such that d^* is the solution of the following iterative scheme:

$$d_{n+1} = d_n - \frac{f(d_n)}{f'(d_n)}\text{, where } f(d_n) = A(d_n) - A^*. \tag{6.7}$$

Since we necessarily have two different expressions for $f(d_n)$, and $f'(d_n)$, depending on the value of d_n, the convergence to a solution depends crucially on the choice of initial value d_0. In order to demonstrate how this choice is made, we present a typical graph of $A(d)$ in Figure 6.3, where it is important to note that the maximum absolute value of

$A'(d)$ occurs at the transition distance $d_{trans} = (R_1^2 - R_2^2)^{1/2}$. This has been highlighted by plotting the tangent line at this point on the figure (i.e. dashed line).

If we consider a case where $A^* \lesssim A(d_{trans})$ and choose $d_0 \lesssim R_1 + R_2$, then $f'(d_0)$ is very small and d_1 may be less than d_{trans}, meaning that convergence cannot then be achieved. This problem is mirrored if, conversely, $A^* \gtrsim A(d_{trans})$ and we choose $d_0 \gtrsim R_1 - R_2$. Therefore, it is clear that we should always choose d_0 such that we approach the solution from the other side. As it happens, we can actually make an informed initial "guess" by utilising the linear function $A_0(d)$ (i.e. dashed tangent line) plotted on Figure 6.3. The equation of this line is given by:

$$A_0(d) = A'\left(\sqrt{{R_1}^2 - {R_2}^2}\right) \cdot \left[d - \sqrt{{R_1}^2 - {R_2}^2}\right] + A\left(\sqrt{{R_1}^2 - {R_2}^2}\right). \tag{6.8}$$

By choosing our initial value d_0 to be the solution of $A_0(d_0) = A^*$, we find that we can get "close" to the solution whilst always approaching it from the correct direction; hence, convergence will be guaranteed for $0 < A^* < \pi R_2^2$. Specifically, the value of d_0 can be calculated from the equation:

$$\begin{aligned} d_0 &= \frac{A^* - A\left(\sqrt{{R_1}^2 - {R_2}^2}\right)}{A'\left(\sqrt{{R_1}^2 - {R_2}^2}\right)} + \sqrt{{R_1}^2 - {R_2}^2} \\ &= \frac{\frac{1}{2}\pi {R_2}^2 - A^* + {R_1}^2 \cdot \cos^{-1}\left(\frac{\sqrt{{R_1}^2 - {R_2}^2}}{R_1}\right) + R_2 \cdot \sqrt{{R_1}^2 - {R_2}^2}}{2R_2}. \end{aligned} \tag{6.9}$$

Returning to our original cell model notation, we therefore see that, given an overlap area a^{ij} between two elliptical cells (c.f. A^*), and the equivalent sensing radii R_S^i and R_S^j of the cells (c.f. R_1 and R_2), the above equations can be used to numerically calculate the equivalent distance d^{ij} between the cells (c.f. d^*), had they both been spherical and of equivalent volume. By simply replacing $\|\boldsymbol{q}^{ij}\|$ with d^{ij} in Equations 5.30, 5.34 and 5.35, cell-cell interactions between non-spherical cells can thus be modelled entirely consistently without the necessity of introducing any further equations.

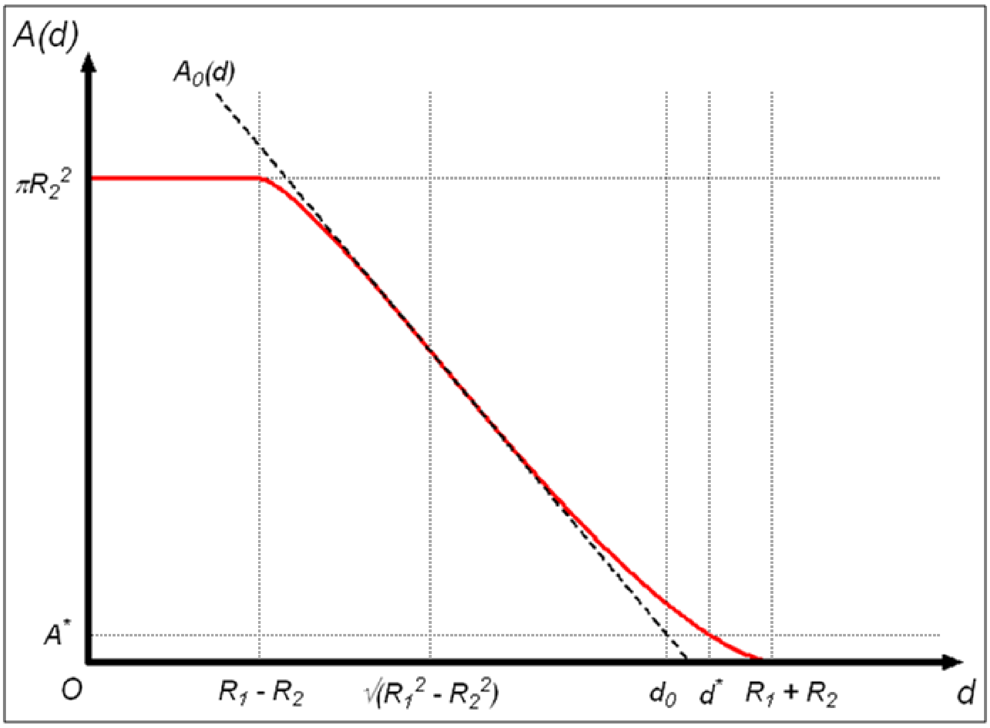

Figure 6.3: Schematic plot showing the variation of overlap area $A(d)$ between two circles of radii R_1 and R_2 ($R_1 > R_2$) with distance d between their centres (solid red line). When $d \geq R_1 + R_2$ there is no overlap, while for $d \leq R_1 - R_2$ the small circle is fully contained within the larger one (i.e. $A(d) = \pi R_2^2$). The dashed black line indicates the tangent line $A_0(d)$ at the transition point $d_{trans} = (R_1^2 - R_2^2)^{1/2}$ (c.f. Figure 6.2) where the gradient of $A(d)$ takes its maximum absolute value. If the overlap area between the circles is known to be A^*, the distance d_0 satisfying $A_0(d_0) = A^*$ provides an initial guess that guarantees convergence when using Newton's Method to solve for the exact distance d^* between the circle centres.

In essence, this technique allows us to propose that the interaction behaviour between any two cells (spheroidal or ellipsoidal) is uniquely defined in terms of the area of overlap a^{ij} between their sensing boundaries in the plane of simulation. To illustrate this point, Figure 6.4 presents a plot of the function $h_a^{ij}(a^{ij})$ that is numerically equivalent to the plot of $h^{ij}(\|\boldsymbol{q}^{ij}\|)$ given previously in Figure 5.14. Whilst the definitions used in Figure 5.14 were only capable of accounting for the cell-cell interaction between two spherical cells, the generalised plot given in Figure 6.4 can additionally be used to account for the behaviour of two interacting ellipsoidal cells

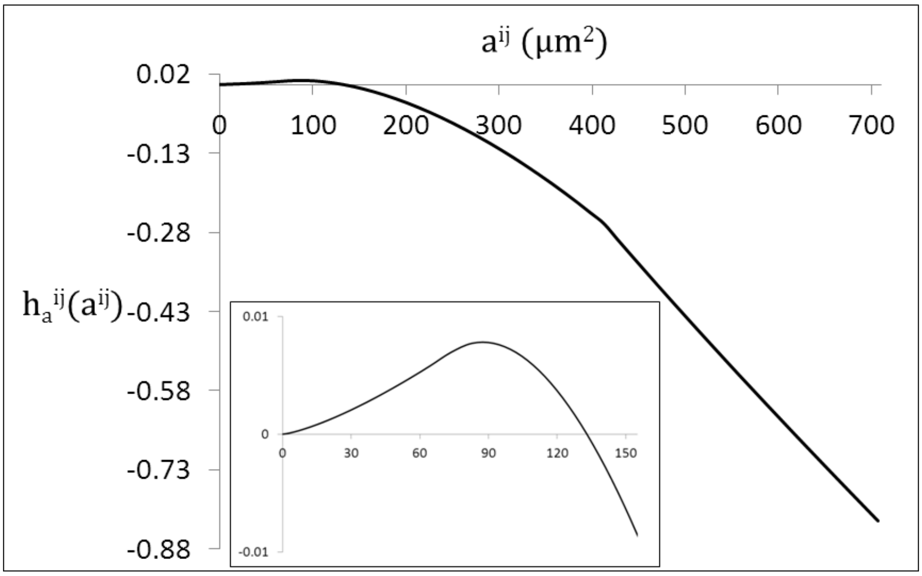

Figure 6.4: Typical plot of the function $h_a^{ij}(a^{ij})$, which is assumed to govern the behaviour of two interacting cells as the area of overlap between their sensing boundaries varies (i.e. $h_a^{ij} > 0$ indicates adhesion, $h_a^{ij} < 0$ indicates repulsion); the inset shows the features of the adhesive region in greater detail. The plot is numerically equivalent to that presented in Figure 5.14, where the function h^{ij} was expressed in terms of the distance $||\boldsymbol{q}^{ij}||$ between the centres of mass of two spherical cells. As can be seen, the key qualitative features of the function have been conserved: a steep linear section indicating a notional overlap between the cells' nuclear components (i.e. $a^{ij} > 400$); an equilibrium point where adhesion and repulsion are in balance (i.e. $a^{ij} \approx 135$); and a point of maximal adhesive strength (i.e. $a^{ij} \approx 90$). Adhesive contact is lost when the cells' sensing boundaries no longer overlap (i.e. $a^{ij} = 0$).

(with equivalent volumes). Recall that, for ellipsoidal cells, it is necessary to instead define $h^{ij}(d^{ij})$, where $d^{ij} \equiv d^{ij}(a^{ij})$ is an "equivalent distance" which accounts for the particular overlap area. Hence, although the functional form $h_a^{ij}(a^{ij})$ cannot be written explicitly, we can relate this to our earlier definitions by the implicit expression $h_a^{ij}(a^{ij}) \equiv h^{ij}(d^{ij}(a^{ij}))$.

6.2.3. Cell Movement

One of the biggest advantages of working with spherical cells is that it is not necessary to consider the concept of polarisation – each cell can be assumed to be equally polarised in all directions at all times. When we extend the model to include cells that elongate, however, we require additional rules to govern appropriate temporal dynamics when a cell changes direction. Referring back to Section 5.5.2, we recall the definition of "active" and "passive" to denote the two distinct modes of cell movement – individual cell migration and biophysical cell-cell interactions, respectively (Palsson and Othmer, 2000). These definitions are of much greater importance here since, although both modes of movement are combined to derive the overall movement direction $\boldsymbol{u}^i(t)$, cell orientations will only be modified to achieve polarisation in the direction of the overall active vector $\boldsymbol{v}_\Sigma^i(t)$ (i.e. it is assumed that adhesive and repulsive effects do not cause cell re-orientation).

The most consistent means of implementing change of cell migration direction within the existing model framework is to allow the cells to rotate around their centre of mass (although this is lacking biological realism to some extent). The maximal degree of cell rotation can, however, be reduced by assuming that each ellipsoidal cell is essentially polarised at both extremities of its semi-major axis (i.e. a cell can reverse its migration direction without performing any rotation). As detailed in the previous chapter, the vector $\boldsymbol{v}_\Sigma^i(t)$ is calculated only every τ_u time units; with this in mind, we further assume that each cell is capable of fully re-orienting its migration direction between these calculations (i.e. between pseudopod extensions). Combining these assumptions, and defining by ω the rate of cell rotation, we therefore derive the necessary condition $\omega \geq \pi / 2\tau_u$.

In order to implement these modifications we firstly define the vector $\boldsymbol{p}^i(t)$, which represents the orientation direction of any cell. Upon each new calculation of $\boldsymbol{v}_\Sigma^i(t)$, we also calculate $\theta^i_{p,\Sigma}(t)$, representing the acute angle between $\boldsymbol{v}_\Sigma^i(t)$ and $\pm\boldsymbol{p}^i(t)$. If the acute angle is made with $-\boldsymbol{p}^i(t)$, the cell polarisation is reversed before any rotation takes place. Parameterising the time since the beginning of cell rotation by t_p, the orientation of a cell is subsequently rotated in the appropriate direction, and through the appropriate angle, according to:

$$\boldsymbol{p}^i(t_p) = \begin{bmatrix} \cos(\omega t_p) & \mp\sin(\omega t_p) \\ \pm\sin(\omega t_p) & \cos(\omega t_p) \end{bmatrix} \cdot \boldsymbol{p}^i(0), \tag{6.10}$$

until $\boldsymbol{p}^i(t_p) \equiv \boldsymbol{v}_\Sigma^i(0) \equiv \boldsymbol{v}_\Sigma^i(t_p)$, where $0 \leq t_p \leq \theta^i_{p,\Sigma}(0) / \omega \leq \tau_u$. Note that in order to satisfy this final condition, we first require the $\boldsymbol{p}^i$ and $\boldsymbol{v}_\Sigma^i$ vectors to be appropriately normalised.

Due to the above stated constraint on the value of ω (i.e. $\omega \geq \pi / 2\tau_u$), upon the next calculation of $\boldsymbol{v}_\Sigma^i(t)$ the definition of persistence direction $\boldsymbol{v}_a^i(t)$ (c.f. Equation 5.40) is, by design, always equivalent to the current direction of cell orientation. That is, upon each new pseudopod extension, each cell will still have a certain tendency to maintain its current direction of migration. In this new formulation, however, there are two of the previously defined equations that we need to update. Specifically, Equations 5.33 and 5.39 are modified according to:

$$\boldsymbol{v}_{q,\mathrm{p}}^i(t) = \frac{\boldsymbol{p}^i(t)}{\|\boldsymbol{p}^i(t)\|} + \sum_{j=1}^{n^i} \begin{cases} \chi_{rep}^{ij}\left(h^{ij}\left(d^{ij}\right)\right) \cdot \frac{\boldsymbol{q}^{ji}(t)}{\|\boldsymbol{q}^{ji}(t)\|}, & h^{ij} \leq 0, \\ \chi_{adh}^{ij}\left(h^{ij}\left(d^{ij}\right)\right) \cdot \frac{\boldsymbol{q}^{ij}(t)}{\|\boldsymbol{q}^{ij}(t)\|}, & h^{ij} > 0, \end{cases} \tag{6.11}$$

and:

$$\boldsymbol{u}^i(t) = \boldsymbol{v}_{q,\mathrm{p}}^i(t), \tag{6.12}$$

respectively, to ensure that the active component of cell movement reflects the intermediate cell orientations obtained during rotation. In order to reflect this change, the appropriate vector has been re-defined to $\boldsymbol{v}^i_{q,p}(t)$. We also note, in Equation 6.11, the replacement of $\|\boldsymbol{q}^{ij}\|$ with the equivalent distance d^{ij} introduced in Section 6.2.2 above.

6.2.4. Cell Morphology

The final aspect of the model that is unique to the ellipsoidal cell concept is that of dynamic temporal variations in cell shape. The stimuli for shape change that we assume are in line with those modelled by Palsson and Othmer (2000) in their mechanical model of *Dictyostelium discoideum* movement. The overall approach to incorporating these stimuli is inherently different, however, and we do not consider viscoelastic deformations. The three factors influencing cell shape at any point in time are assumed to be: a “de-polarisation” process during cell rotation; a set-point relationship between cell speed and semi-major axis length; and stretch or compression as a result of local cell-cell interactions. We shall first provide the equation governing this process. Note that we determine the cell shape by solving an equation for $A^i(t)$, and $B^i(t)$ is then uniquely defined by Equation 6.1 at fixed cell volume. Therefore, the equation governing the evolution of the semi-major cell axis length $A^i(t)$ is:

$$\frac{dA^i(t)}{dt} = \begin{cases} -\lambda_\omega, \text{ during rotation} \\ \lambda_s \cdot \left[A^i_{speed}(t) - A^i(t)\right] + \\ \quad \lambda_q \cdot \sum_{j=1}^{n_i} \left[h^{ij}\left(d^{ij}\right) \cdot \left(\cos\left(\theta^{ij}_{q,p}(t)\right) - \sin\left(\theta^{ij}_{q,p}(t)\right)\right)\right], \text{ otherwise} \end{cases} \tag{6.13}$$

where $R^i(t) \leq A^i(t) \leq A^i_{max}(t)$.

In this equation we assume that the process of de-polarisation during cell rotation occurs independently of any other stimuli for shape change, where the parameter λ_ω characterises the associated (linear) rate of cell body contraction. We make this assumption on the basis that such an adjustment of morphology corresponds to an internal rearrangement of structure (Palsson and Othmer, 2000), which will transiently dominate any response to externally applied factors. In some sense, this term helps to compensate for the somewhat biologically unrealistic assumption of cell rotation by drawing each cell towards a decreasingly polarised morphology. Note that the larger the change in cell directionality (i.e. the longer the rotation process), the larger the potential decrease in $A^i(t)$.

When not undergoing an adjustment to migration direction we assume that, in the absence of any further stimuli for shape change, the target morphology of each cell is uniquely coupled to its speed. More precisely, we assume that the cell eccentricity increases with increasing speed. Although characterised by the rate parameter λ_s, the overall response is seen to depend crucially on the magnitude of the difference between the value of $A^i(t)$ and the set-point semi-axis length $A^i_{speed}(t)$ associated with the instantaneous cell speed. This set-point relationship between cell speed and target cell size is given by the equation:

$$A^i_{speed}(t) = R^i(t) + \left(A^i_{max(s)}(t) - R^i(t)\right) \cdot \left[\frac{s^i(t)}{s_{max}}\right]^{\beta_{A,s}}, \tag{6.14}$$

where $\beta_{A,s}$ determines the shape of this relationship, s_{max} is the maximum attainable cell speed (calculable from the parameterisation of Equation 5.52) and $A^i_{max(s)}(t)$ is the maximum possible cell semi-major axis length attributable to this stimulus alone. Note that the limiting value for this variable in fully-grown cells is $A_{max(s)} \leq A_{max}$ and, similar to Equation 6.4, we define:

$$\frac{A^{i}_{max(s)}(t)}{A_{max(s)}} = \frac{R^{i}(t)}{R_{max}}. \tag{6.15}$$

An important point to highlight here is that, under certain circumstances, Equation 6.14 can be seen to give rise to a cell "re-polarisation" process upon the cessation of any directional change (i.e. if $A^{i}(t) < A^{i}_{speed}(t)$, then $dA^{i}(t)/dt > 0$).

The final factor contributing to the elongation or contraction of cell morphology is the combined influence of other cells in close proximity. This process is characterised by the rate parameter λ_q, whilst appropriate values of $h^{ij}(d^{ij})$ are also used to capture both the relative "strength" and direction of the push (i.e. repulsion; $h^{ij}(d^{ij}) < 0$) or pull (i.e. adhesion; $h^{ij}(d^{ij}) > 0$) exerted by each neighbour. It is assumed that the contribution from each interacting cell is decomposed onto the major (i.e. *cos* term) and minor (i.e. *sin* term) cell axes (Palsson and Othmer, 2000). Therefore, whether a cell is stretched or compressed by the push or pull of a neighbouring cell depends crucially on the variable $\theta^{ij}_{p,q}(t)$, representing the acute angle between $\boldsymbol{q}^{ij}(t)$ and $\pm\boldsymbol{p}^{i}(t)$.

6.2.5. Further Model Modifications

Before we can conclude discussion of the ellipsoidal cell model, there are some further minor modifications to previous equations and methodologies that must be mentioned. The most important of these relate to the calculation of local cell density. Given the now elongated cell morphologies, it is necessary to update the function $\xi^{i}(\mathbf{x},t)$; this is done by re-defining the coefficients of Equation 5.42 such that fixed values of this function now represent elliptical – rather than spherical – contours centred on the cell centroid position. Note that Equations 5.41, 5.43, 5.44 and 5.45 are unchanged by this modification, as is Equation 5.57 describing the weight function for fibrous matrix modification. We now define:

$$\begin{aligned}
AA^i &= \frac{\cos^2\left(\theta_p{}^i\right)}{A^{i^2}} + \frac{\sin^2\left(\theta_p{}^i\right)}{B^{i^2}},\\
BB^i &= \frac{2\cos\left(\theta_p{}^i\right)\cdot\sin\left(\theta_p{}^i\right)}{A^{i^2}} - \frac{2\cos\left(\theta_p{}^i\right)\cdot\sin\left(\theta_p{}^i\right)}{B^{i^2}},\\
CC^i &= \frac{\sin^2\left(\theta_p{}^i\right)}{A^{i^2}} + \frac{\cos^2\left(\theta_p{}^i\right)}{B^{i^2}},\\
DD^i &= -\frac{2f_1^i\cdot\cos^2\left(\theta_p{}^i\right)}{A^{i^2}} - \frac{2f_2^i\cdot\cos\left(\theta_p{}^i\right)\cdot\sin\left(\theta_p{}^i\right)}{A^{i^2}} + \frac{2f_2^i\cdot\cos\left(\theta_p{}^i\right)\cdot\sin\left(\theta_p{}^i\right)}{B^{i^2}} - \frac{2f_1^i\cdot\sin^2\left(\theta_p{}^i\right)}{B^{i^2}},\\
EE^i &= -\frac{2f_2^i\cdot\cos^2\left(\theta_p{}^i\right)}{B^{i^2}} - \frac{2f_1^i\cdot\cos\left(\theta_p{}^i\right)\cdot\sin\left(\theta_p{}^i\right)}{A^{i^2}} + \frac{2f_1^i\cdot\cos\left(\theta_p{}^i\right)\cdot\sin\left(\theta_p{}^i\right)}{B^{i^2}} - \frac{2f_2^i\cdot\sin^2\left(\theta_p{}^i\right)}{A^{i^2}},\\
FF^i &= \frac{\left(f_1^i\cdot\cos\left(\theta_p{}^i\right)+f_2^i\cdot\sin\left(\theta_p{}^i\right)\right)}{A^{i^2}} + \frac{\left(f_1^i\cdot\sin\left(\theta_p{}^i\right)-f_2^i\cdot\cos\left(\theta_p{}^i\right)\right)}{B^{i^2}} - 1.
\end{aligned} \tag{6.16}$$

where $\theta_p \in (0, 2\pi)$ is the angle of the cell orientation $\boldsymbol{p}^i(t)$ measured from the positive x_1-direction. The overall algorithm for local cell density calculation remains unchanged (c.f. Equations 5.48 – 5.50), but in the interests of computational efficiency we modify the construction of the spatial grid within the sensing region of the target cell. Specifically, we now align the co-ordinate axes of our grid to coincide with the semi-major and semi-minor target cell axes; this method minimises the number of wasted grid points lying outwith the sensing region of the target cell. Therefore, modifying Equations 5.46, the set of grid points $\boldsymbol{X}^i_{M,N}$, for $-M^* \leq M \leq M^*$ and $-N^* \leq N \leq N^*$, is now defined by:

$$\boldsymbol{X}^i_{M,N} = \boldsymbol{f}^i + \Delta_X{}^i \cdot \Omega_{\theta_p^i} \cdot [M, N]^T, \text{ where } \Omega_{\theta_p^i} = \begin{bmatrix} \cos\left(\theta_p{}^i\right) & -\sin\left(\theta_p{}^i\right) \\ \sin\left(\theta_p{}^i\right) & \cos\left(\theta_p{}^i\right) \end{bmatrix}, \tag{6.17}$$

and $\Delta_X{}^i \leq B_S{}^i - B^i = R^i / A^i \cdot (R_S{}^i - R^i)$ is the grid spacing. Furthermore, the grid point extremities are now independently defined by:

$$M^* = \text{Int}\left[\frac{A_S{}^i}{\Delta_X{}^i}\right], \text{ and } N^* = \text{Int}\left[\frac{B_S{}^i}{\Delta_X{}^i}\right]. \tag{6.18}$$

A further notable feature of this calculation for ellipsoidal cells is that any two cells in close proximity may, due to their respective orientations, generate very different local cell density values. This is consistent, however, with the assumption that the cells have a greater sensing ability at the extremities of their semi-major axes.

6.3. Ellipsoidal Cell Simulation Results

Our cell migration model has now been presented in full. Given the latest model definitions for the ellipsoidal case outlined above, we begin this section by presenting results from a simple test case. Specifically, we simulate single cell chemotaxis in a series of sensitivities that examine the dynamic nature of cell shape evolution. Following this, we seek to benchmark our cell properties against real *in vitro* fibroblast data and, finally, discuss the implications of these results in the context of a healing scrape wound assay.

6.3.1. Single Cell Chemotaxis

The migratory response of cells to chemical stimuli is a widely used model system in the study of cell motility. Here, we perform simulations that are analogous to the classical experimental assay whereby *in vitro* cells are exposed to a moving chemoattractant source (see, for example, Claviez et al. (1986); Figure 6.5). The *in silico* cells in such simulations undergo a series of variations in orientation and speed, thus providing an excellent scenario in which to examine the cell shape evolution properties predicted by Equations 6.13 and 6.14.

For each simulation we choose to focus on just a single cell, which is initially positioned at the centre of a 300 μm x 300 μm square domain. A fixed concentric chemoattractant profile is initially centred in the top left of the domain, and is subsequently moved instantaneously every 3 hours to, successively, the top right, bottom left and bottom right of the domain. In each case the maximal concentration is situated 75 μm from the two nearest domain boundaries, and the domain-wide profile is described by the equation:

$$K(r) = e^{-\frac{r^3}{0.4}}, \tag{6.19}$$

where r is the normalised distance from this maximum. The appropriate parameters governing migration of the cell correspond to those of the base case simulations in the previous chapter, and can be found in Table 5.1. All additional base case parameter values required in this section are listed in Table 6.1, whilst the specific values of the modified parameters in each sensitivity study can be found in the relevant figure caption.

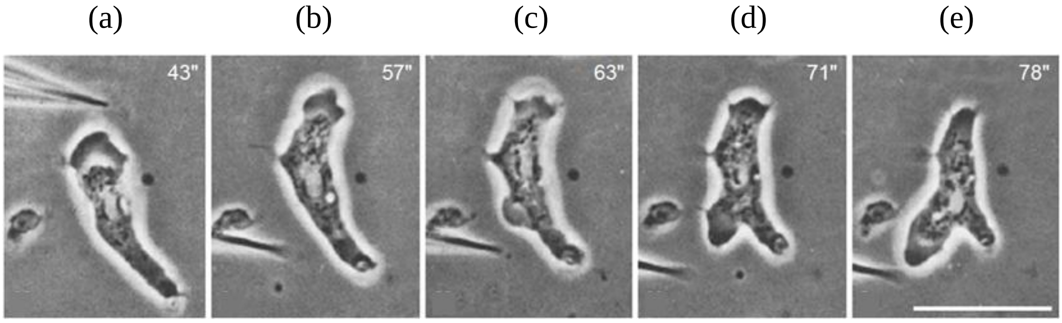

Figure 6.5: Time-series of experimental images showing the response of a *Dictyostelium* cell to a micropipette containing a source of the chemoattractant cyclic AMP. Note that the cell undergoes a process of re-orientation when the position of the micropipette is changed. Images were recorded (a) 43, (b) 57, (c) 63, (d) 71 and (e) 78 seconds after initial insertion of the micropipette (scale bar = 20 μm). Image taken from Claviez et al. (1986).

Parameter	Definition	Value
ω	Cell rotation rate	$\pi/2\tau_u$ rad · hr^{-1}
A_{max}	Maximal equivalent cell semi-major axis length	24 μm
$A_{max(s)}$	Maximal speed-related cell semi-major axis length	24 μm
λ_ω	Cell body contraction rate during rotation	400 μm · hr^{-1}
λ_s	Speed-related morphology modification rate	5 hr^{-1}
$\beta_{s,A}$	Speed-related morphology modification shape parameter	1

Table 6.1: Base case parameters used for all simulations in Section 6.3.1.

The sensitivities that we consider only involve modification of parameters that control the evolution of cell morphology. Therefore, the trajectory of the cell is not affected by any of these changes and remains consistent throughout each simulation that we perform. The cell trajectory is presented in Figure 6.6, where the red circles indicate

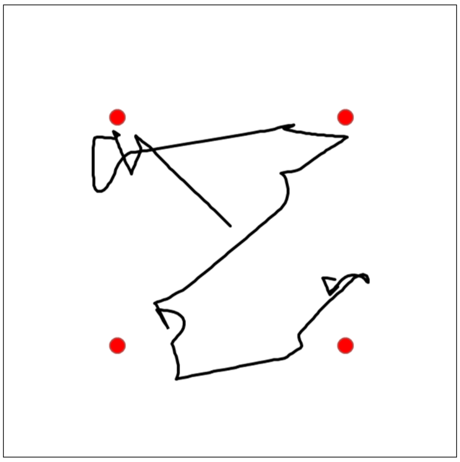

Figure 6.6: Cell trajectory exhibited during the single cell chemotaxis simulations; the red circles indicate the 4 peaks of chemoattractant concentration experienced by the cell over intervals of 3 hours. The cell begins at the centre of the domain and is sequentially attracted by the chemical peak at the top left, top right, bottom left and bottom right of the domain (scale of image = 300 μm x 300 μm).

the 4 respective positions of maximum chemical concentration. It can be seen that, much like Figure 5.8, the cells lose directionality in the vicinity of these peaks due to the relative paucity of chemical gradients. It should be noted that the cell speed does not remain fixed over the course of this trajectory, but in fact undergoes fluctuations in response to variations in the local chemical gradient. By Equation 6.14, therefore, the semi-major axis length $A^i_{speed}(t)$, which satisfies the set-point relationship between cell shape and cell speed, also fluctuates over time. The temporal evolution of $A^i_{speed}(t)$ in the base case simulation is shown in Figure 6.7, where the peaks indicate the time points at which the cell experiences maxima in the chemical gradient. Inspection of Equation 6.13 reveals that, in the absence of cell rotation (and cell-cell effects), $A^i_{speed}(t)$ is the equilibrium semi-major axis length that the cell will always tend towards; in what follows, therefore, we shall refer to this as the “target” morphology.

In Figure 6.8, we present a series of snapshots from the base case simulation, showing some typical variations in the cell morphology. Figure 6.8a shows the initial condition where the cell is already oriented towards the chemical peak, and significantly elongated due to the steepness of the gradient and associated large cell speed. This morphology is maintained for an extended period as the cell persists towards the

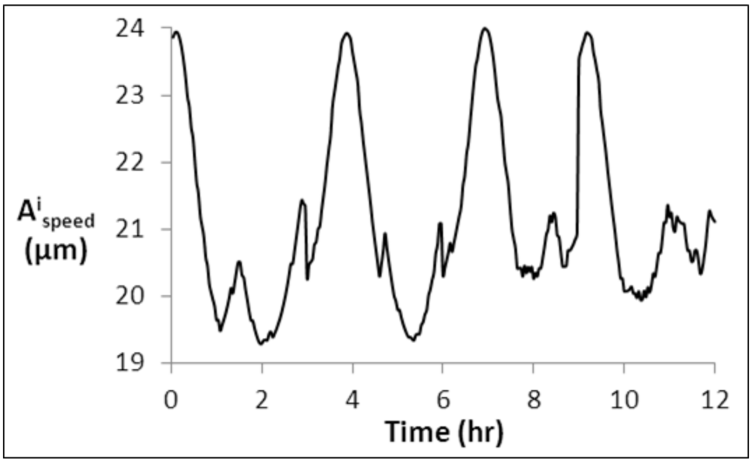

Figure 6.7: Plot showing the evolution of the "target" cell semi-major axis length $A^i_{speed}(t)$ in the base case single cell chemotaxis simulation. This value is uniquely correlated to the instantaneous cell speed $s^i(t)$ – the oscillatory behaviour reflects the temporal fluctuations in speed as the migrating cell experiences variations in the local chemical gradient.

chemical peak (Figure 6.8b). A contracted morphology is displayed in Figure 6.8c where the chemical gradient flattens out and the cell undergoes a re-orientation – Figure 6.8d indicates the subsequent "re-polarisation". Figures 6.8e and 6.8f, respectively, show cell morphologies that are contracted during the search for the new chemical source and elongated upon subsequent location of the gradient. In initial response to the final chemoattractant profile, we see that the cell has again undergone extensive elongation (Figure 6.8g), before again contracting as the ability to sense the gradient is lost and random migration replaces directed movement (Figure 6.8h).

We proceed to consider varying a series of pertinent parameters, in order that we can more rigorously assess the mechanisms by which the predicted cell morphologies evolve. In each case we plot a graph of the temporal variation of the semi-major cell axis $A^i(t)$ compared against the temporal variation in $A^i_{speed}(t)$, which represents the target semi-major axis length that is uniquely defined by the instantaneous cell speed (c.f. Equation 6.14). Note that the lower limit of $A^i(t)$ in each of these plots represents the maximal extent of cell body contraction (i.e. the cell morphology has become identically circular, $A^i(t) = R^i(t)$).

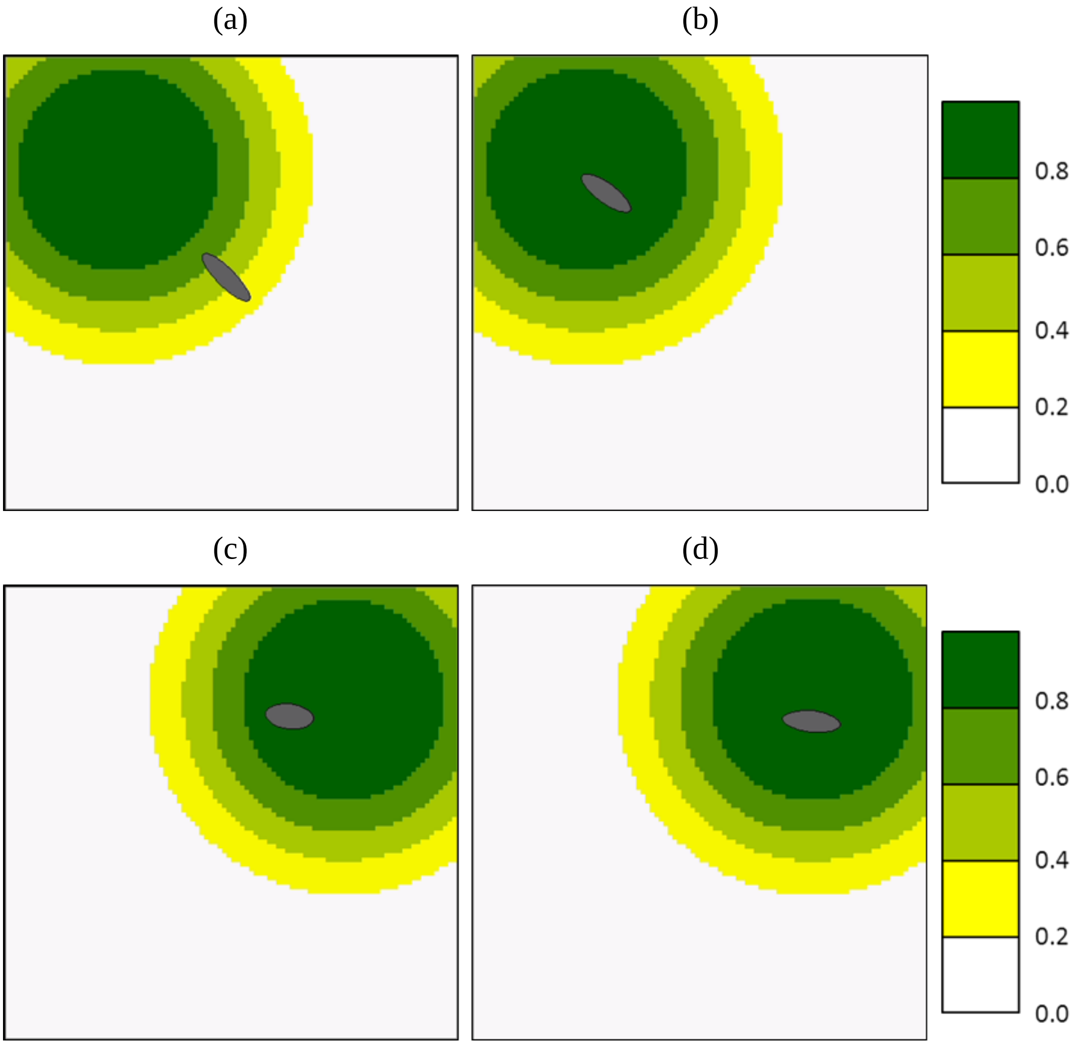

Figure 6.8: Series of snapshots from the base case simulation of single cell chemotaxis showing typical morphologies exhibited by the cell under the influence of the varying chemical profiles it experiences over time (chemical concentrations are given by the colour bars). Specifically, the images correspond to (a) 0 hr, (b) 1.1 hr, (c) 4.8 hr, (d) 5.4 hr, (e) 6.3 hr, (f) 6.6 hr, (g) 9.8 hr and (h) 10.2 hr after the beginning of the simulation.

The first sensitivity that we perform is on the parameter λ_ω, which quantifies the rate of cell body contraction during rotation. Recall that cell contraction during rotation is independent of any other stimuli for morphological change; that is, the speed-related term will not act to restore cell eccentricity until after rotation has been completed. The results from the base case simulation are presented in Figure 6.9a, where the dashed line indicates the evolution of $A^i_{speed}(t)$ (recall that the 4 pronounced peaks represent the

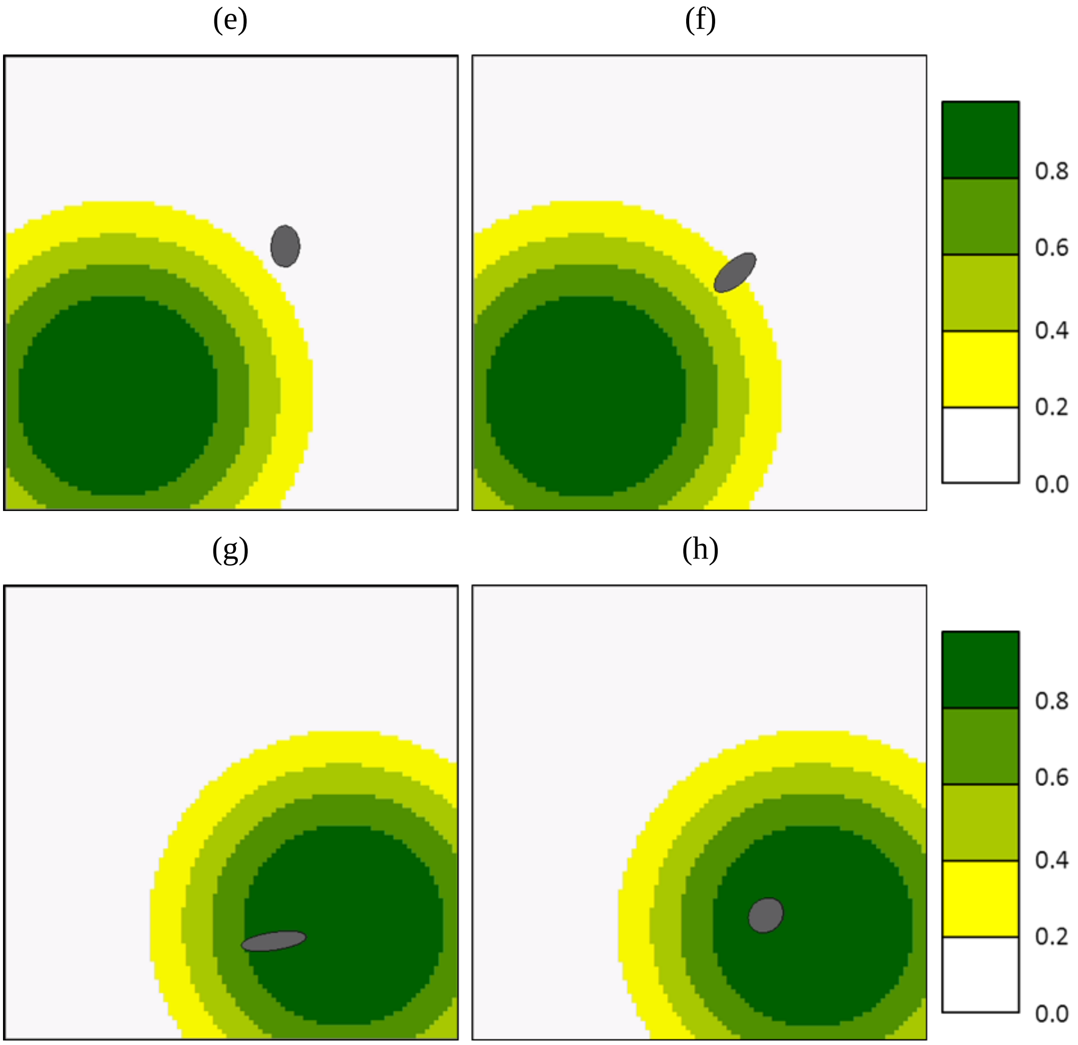

Figure 6.8 (cont'd): Series of snapshots from the base case simulation of single cell chemotaxis showing typical morphologies exhibited by the cell under the influence of the varying chemical profiles it experiences over time (chemical concentrations are given by the colour bars). Specifically, the images correspond to (a) 0 hr, (b) 1.1 hr, (c) 4.8 hr, (d) 5.4 hr, (e) 6.3 hr, (f) 6.6 hr, (g) 9.8 hr and (h) 10.2 hr after the beginning of the simulation.

maxima in the chemical gradient as experienced by the migrating cell). Although the cell comes close to attaining its target shape at each of these peaks, the shape is seen to oscillate rather extensively in regions of shallower chemical gradient as the cell undergoes a persistent random walk that is interspersed by a series of rotations. The extent to which the cell is restored towards its target shape at any point in time ultimately depends on both the amount of time spent persisting in particular directions,

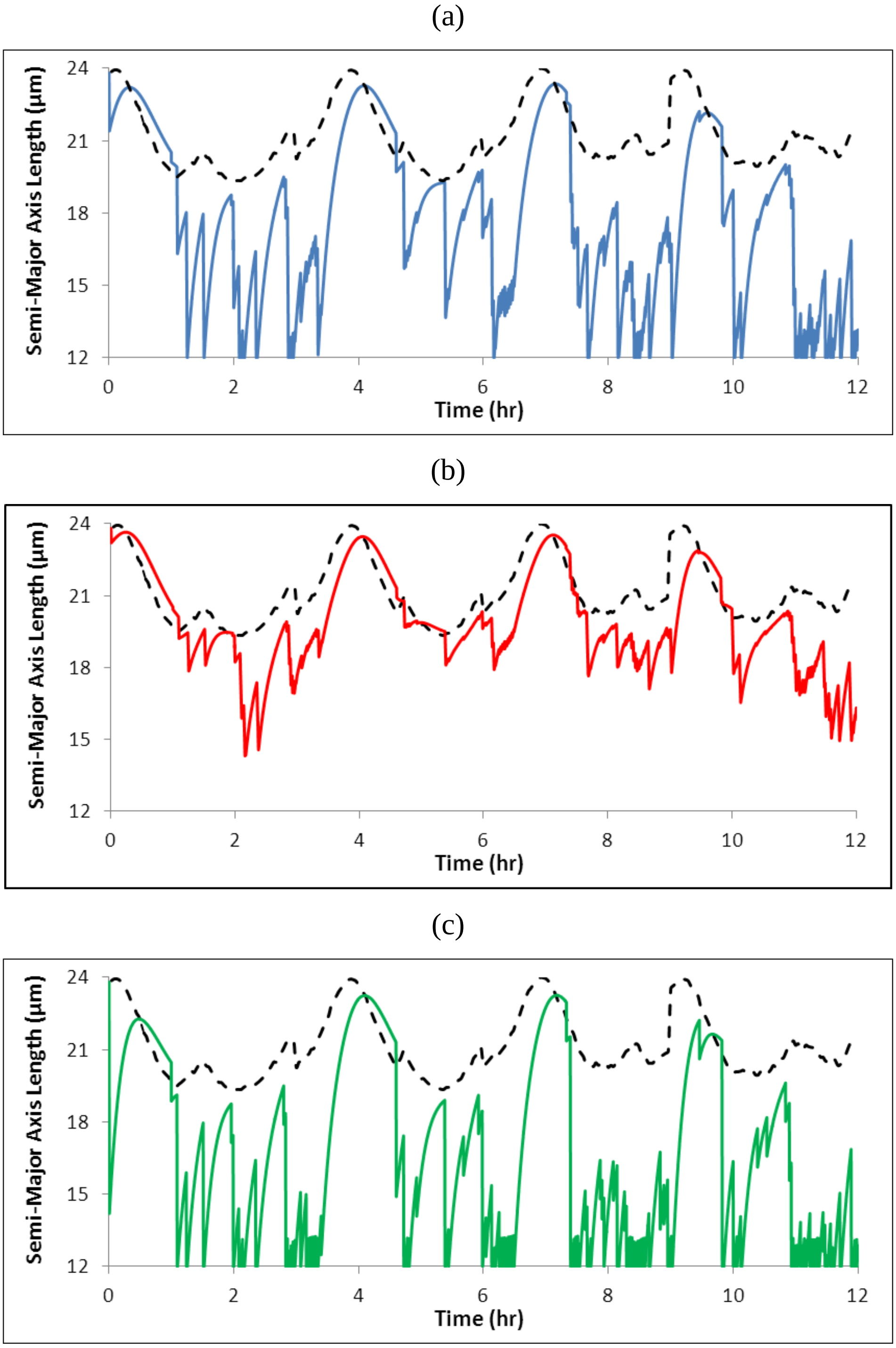

Figure 6.9: Plots showing the evolution of the cell semi-major axis length $A^i(t)$ during single cell chemotaxis simulation for a range of values of the parameter λ_ω, which quantifies the linear rate of cell body contraction during rotation. The dashed black line in each case shows the evolution of the target semi-major axis length $A^i_{speed}(t)$, which is uniquely correlated to the instantaneous cell speed $s^i(t)$ (c.f. Equation 6.14). Images correspond to the parameter values (a) 400 µm · hr^{-1} (base case), (b) 100 µm · hr^{-1} and (c) 1600 µm · hr^{-1}.

and the particular angles through which the cell rotates (i.e. time spent rotating). A 4-fold decrease in the value of λ_ω is seen to have a profound effect: throughout simulation the cell shape remains elongated and much closer to its target morphology, due to significant damping of the oscillatory behaviour (Figure 6.9b). An equivalent increase in the parameter once again results in a cell that largely achieves the target elongation at the peaks of the chemical gradient; away from this strong directional stimulus, however, the cell remains approximately spherical due to an inability to recover from the rapid body contractions undergone during de-polarisation (Figure 6.9c).

Our second sensitivity considers the implications of varying λ_s, which describes the rate of cell shape recovery upon a perturbation away from the target morphology. We firstly impose a 5-fold decrease in this value, and note that this results in an evolution of $A^i(t)$ which largely remains significantly contracted with respect to the target value (Figure 6.10b). One interesting aspect of this result is the inherent delay that is imposed in cell elongation as the cell senses the peaks of chemical gradient, with $A^i(t)$ continuing to increase even though $A^i_{speed}(t)$ has long since been decreasing. This type of delay was also weakly observable in the base case simulation (Figure 6.10a), but there is no such occurrence when λ_s is increased. In this latter case the target shape is largely attained at all times, with the exception of the various strong contractions of the cell body during changes in migration direction (Figure 6.10c).

The final sensitivity study that we perform relates to the parameter $\beta_{s,A}$, which determines the precise manner of the set-point relationship between cell speed and cell morphology. The effect of reducing this parameter is shown in Figure 6.11b where the sensitivity of cell shape to variations in cell speed is reduced, resulting in a temporal evolution of target shape that is significantly damped in comparison to the base case simulation (Figure 6.11a). Due to the tendency of the cell to lose directionality in the presence of weak chemical gradients, however, this results in a tendency to exhibit a morphology that is generally contracted with respect to the target elongation. Increasing the value of $\beta_{s,A}$ is seen to produce the exact opposite result. Oscillations in the evolution of the target shape are now strongly accentuated, such that $A^i_{speed}(t)$ has a greater tendency to reflect the temporal variations in strongly chemotactic and strongly random migration; therefore, the cell is seen to more readily attain the desired morphology (Figure 6.11c).

(a)

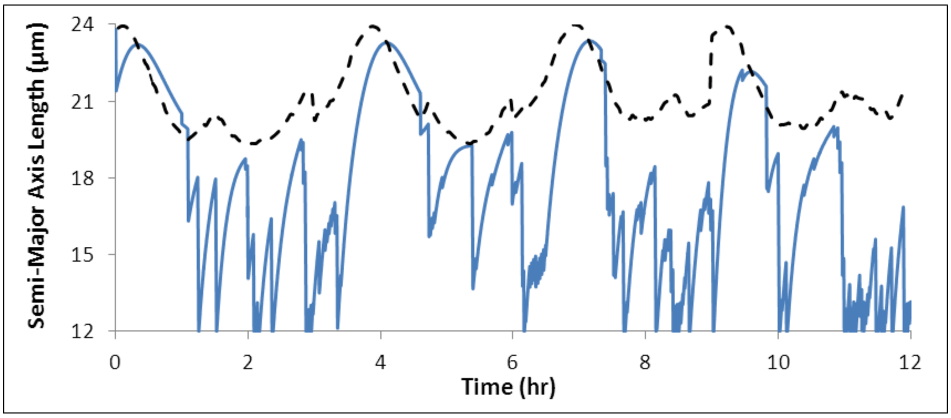

(b)

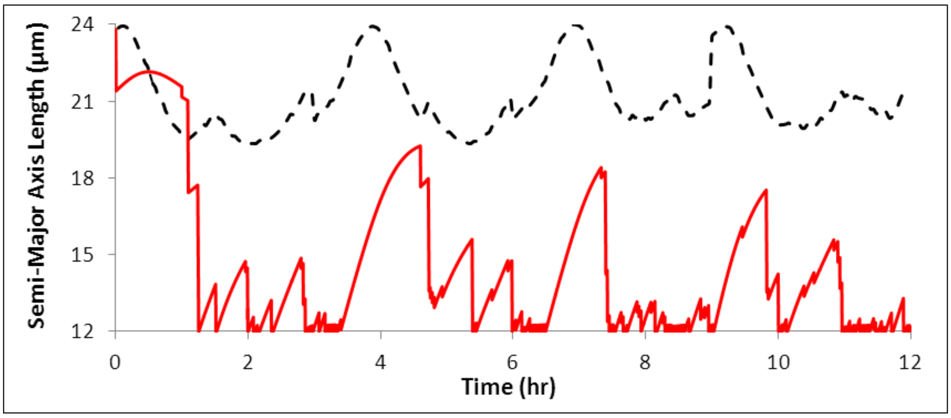

(c)

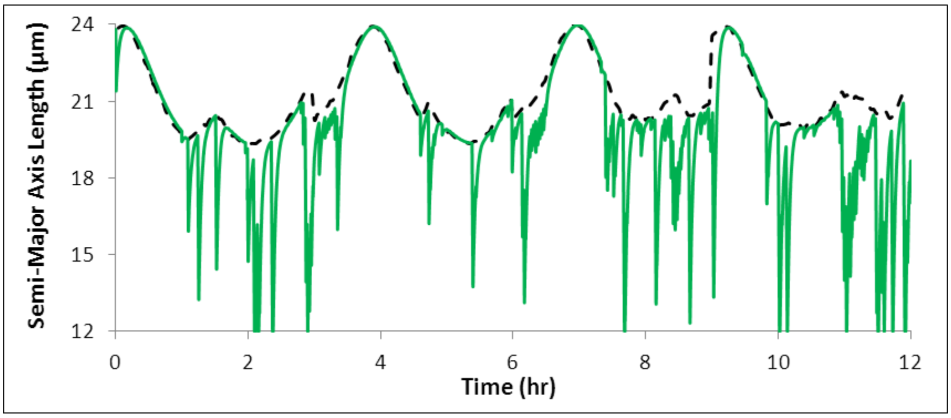

Figure 6.10: Plots showing the evolution of the cell semi-major axis length $A^i(t)$ during single cell chemotaxis simulation for a range of λ_s values; this parameter quantifies the rate at which the cell semi-major axis length recovers when perturbed away from its target value $A^i_{speed}(t)$. The dashed black line in each case shows the evolution of $A^i_{speed}(t)$, which is uniquely correlated to the instantaneous cell speed $s^i(t)$ (c.f. Equation 6.14). Images correspond to the parameter values (a) 5 hr^{-1} (base case), (b) 1 hr^{-1} and (c) 25 hr^{-1}.

(a)

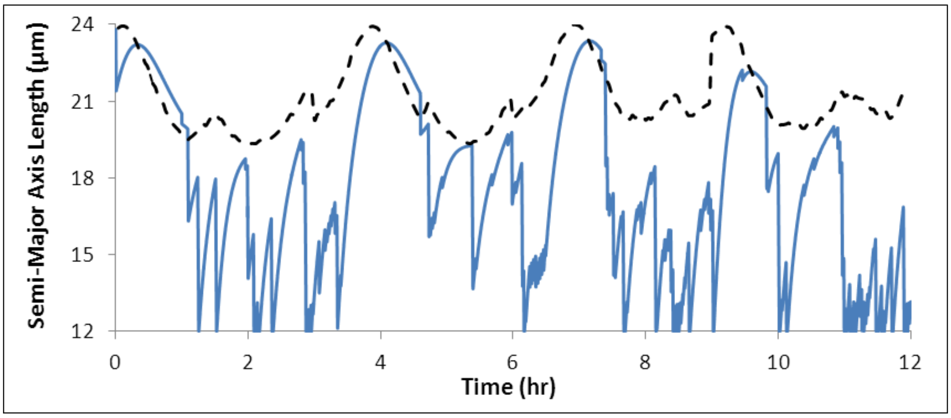

(b)

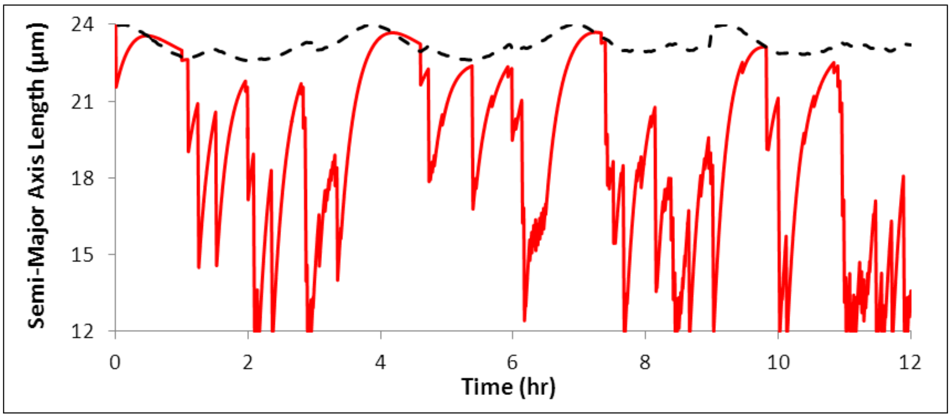

(c)

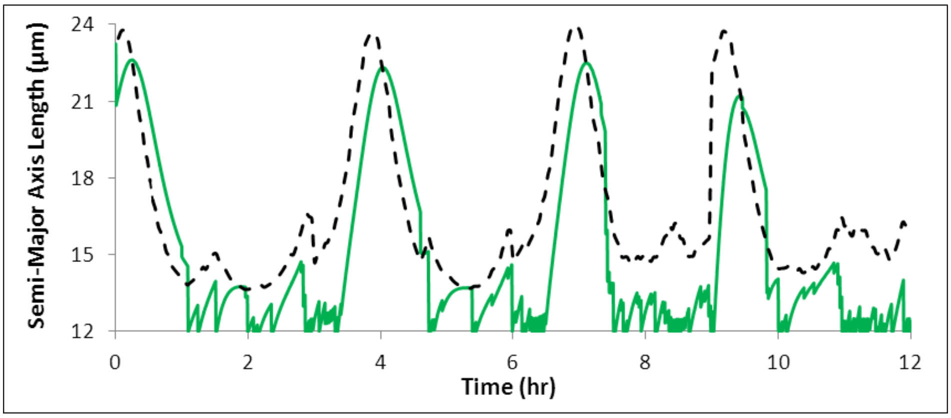

Figure 6.11: Plots showing the evolution of the cell semi-major axis length $A^i(t)$ during single cell chemotaxis simulation for a range of values of the parameter $\beta_{s,A}$, which describes the shape of the set-point relationship between instantaneous cell speed $s^i(t)$ and target cell semi-major axis length $A^i_{speed}(t)$ (c.f. Equation 6.14). The evolution of $A^i_{speed}(t)$ in each case is shown by the dashed black line. Images correspond to the parameter values (a) 1 (base case), (b) 0.25 and (c) 4.

6.3.2. Benchmarking Against *in vitro* Fibroblast Behaviour

In Section 6.3.1 above, and throughout the previous chapter, we have designed a series of simple *in silico* "assays" with which to examine the mechanisms driving the behaviour of the cells in our model. Using the knowledge gained from these studies, we now bring a more realistic focus to our results by reproducing real experimental data describing *in vitro* fibroblast migration and proliferation. For this purpose we look to the papers of Cai et al. (2007) and Tremel et al. (2009), who obtained cell trajectories at both low and high cell density during monolayer formation, as well as temporal measures of the population growth. These 3 data sets are presented in Figure 6.12, whilst in Table 6.2 we list the persistent random walk, cell-cell interaction and proliferation parameters we have used to benchmark our simulations against the experimental results. Before proceeding to present our results, however, we require some explanation as to how cell trajectory data can be processed to produce quantitative measures that allow valid comparison between simulation and experiment.

At low density the *in vitro* fibroblasts are observed to migrate in a uniform environment, whilst at high density (i.e. confluence) the cells remain motile despite almost constant contact with surrounding neighbours. Since these two scenarios suggest that the cells are essentially undergoing a process of homogeneous isotropic diffusion, Cai et al. (2007) proposed the use of statistical techniques to estimate values for the effective diffusion coefficient of a single cell in each case. Although full details can be found in the relevant publication, for clarity we proceed to summarise the key assumptions of this methodology.

Adopting the notation of Cai et al. (2007), we begin by defining the random vector $\boldsymbol{R}_t = (X_t, Y_t)$, where the Cartesian co-ordinates X_t and Y_t denote the position of a cell at time t relative to its initial position at $t = 0$. In addition, we also define a probability density function $p(x, y, t)$ such that for any planar region Ω the probability that the cell can be found there at time t is:

$$\Pr\{(X_t, Y_t) \in \Omega\} = \iint_{\Omega} p(x, y, t)\, dx\, dy. \tag{6.20}$$

Assuming that the cell movement can be approximated as undergoing homogeneous isotropic diffusion with diffusion coefficient D_0, we have:

$$\frac{\partial p}{\partial t} = D_0 \nabla^2 p. \tag{6.21}$$

The appropriate initial condition for this analysis is $p(x, y, 0) = \delta(x)\delta(y)$, and the probability density function can accordingly be expressed as:

$$p(x, y, t) = \frac{1}{4\pi D_0 t} \cdot \exp\left[-\left(\frac{x^2+y^2}{4D_0 t}\right)\right]. \tag{6.22}$$

In the Cartesian plane we can also define two further marginal probability density functions, given by:

$$p_1(x,t) = \int_{-\infty}^{\infty} p(x,y,t)dy, \ p_2(y,t) = \int_{-\infty}^{\infty} p(x,y,t)dx. \tag{6.23}$$

Using these expressions to compute appropriate moments of X_t and Y_t by the standard method:

$$\langle {X_t}^k \rangle = \int_{-\infty}^{\infty} x^k p_1(x,t)dx, \ \langle {Y_t}^k \rangle = \int_{-\infty}^{\infty} y^k p_2(y,t)dy, \tag{6.24}$$

the following relationships are obtained:

$$\langle X_t \rangle = 0, \ \langle Y_t \rangle = 0, \ \langle {X_t}^2 \rangle = 2D_0 t, \ \langle {Y_t}^2 \rangle = 2D_0 t. \tag{6.25}$$

Given a particular data set consisting of a series of discrete cell positions (X_t, Y_t) from any number of trajectories over a time interval $0 \le t \le T$, it is possible to calculate an equivalent series of averaged values $\langle X_t^2 \rangle$ and $\langle Y_t^2 \rangle$. For a sufficiently large data set, the above theory (i.e. Equation 6.25) indicates that plotting these values against t should produce a straight line relationship. Thus, the effective diffusion coefficient D_0 can be estimated by determining the gradient of a constrained linear regression through the origin. Moreover, applying the same method for $\langle X_t \rangle$ and $\langle Y_t \rangle$, where the expected value

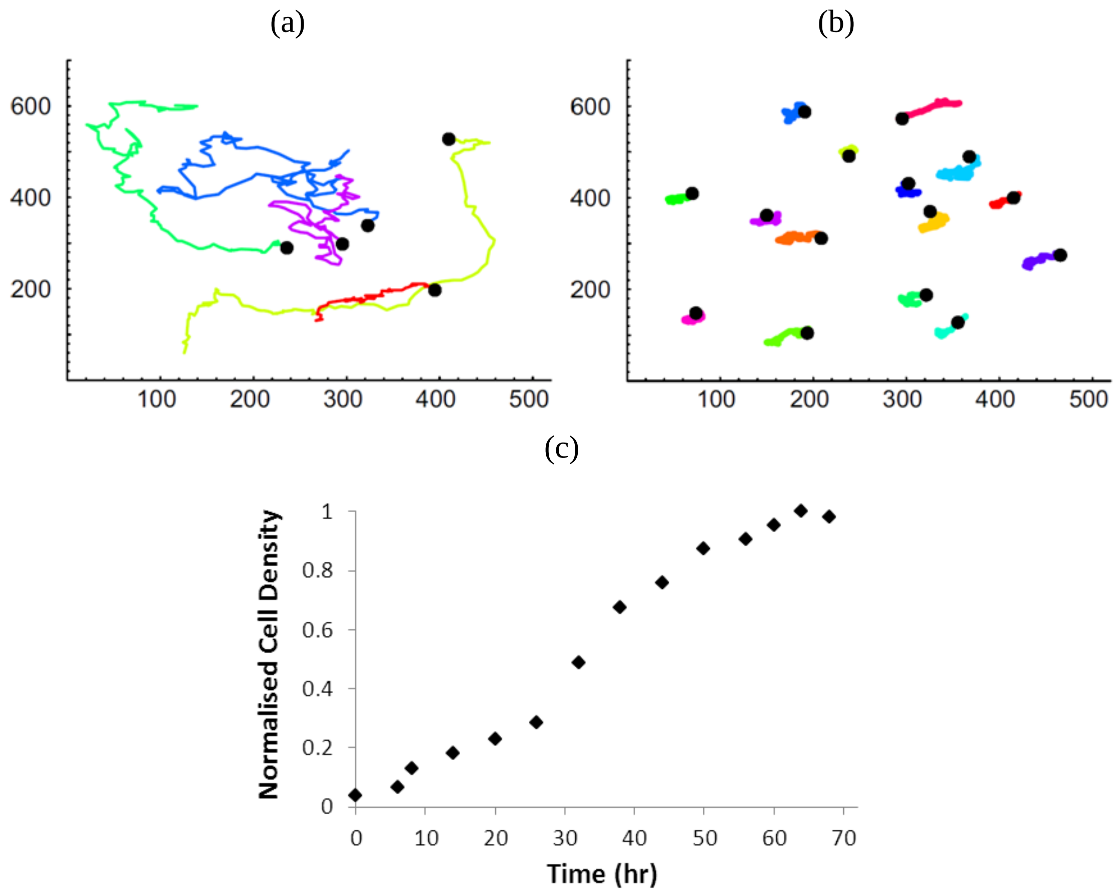

Figure 6.12: Experimental data obtained from Cai et al. (2007) and Tremel et al. (2009) showing fibroblast (a, b) migration and (c) proliferation during *in vitro* monolayer formation. Cell trajectories were recorded at both (a) low and (b) high cell density; in the plots, the black circles represent initial cell positions (axis values denote μm). At low density there are 2 trajectories obtained over 16 hours (red and purple lines) and 3 obtained over 24 hours, whilst at high density there are 15 trajectories obtained over 10 hours. All trajectories were obtained by recording cell positions at 10 minute intervals. In the population growth data, the normalising cell density is 950 cells · mm^{-2}. Plots (a) and (b) were taken directly from Cai et al. (2007), while plot (c) was generated by reading off data from Tremel et al. (2009).

of the gradient is zero, will illuminate whether there is any discernable positive or negative bias in either of the axial directions.

As can be seen, this technique gives two distinct means by which to estimate the effective cell diffusion coefficient; it is possible, however, to derive a further two equivalent equations by instead considering the probability density function $\varphi(r, t)$ for the radial displacement $||\boldsymbol{R}_t||$. This function is related to the earlier probability density function by the equation:

$$\varphi(r,t) = 2\pi r \cdot p(x,y,t), \tag{6.26}$$

and is consequently found to take the form of the Rayleigh distribution:

$$\varphi(r,t) = \frac{r}{2D_0 t} \cdot \exp\left[-\frac{r^2}{4D_0 t}\right]. \tag{6.27}$$

Hence, computing appropriate moments in the same manner as above:

$$\langle ||\boldsymbol{R}_t||^k \rangle = \int_0^\infty r^k \varphi(r,t) dr, \tag{6.28}$$

we now obtain the relationships:

$$\langle ||\boldsymbol{R}_t|| \rangle^2 = \pi D_0 t,\ \langle ||\boldsymbol{R}_t||^2 \rangle = 4D_0 t, \tag{6.29}$$

which provide two additional means of estimating the diffusion coefficient D_0 by applying a constrained linear regression to plots of $\langle ||\boldsymbol{R}_t|| \rangle^2$ and $\langle ||\boldsymbol{R}_t||^2 \rangle$ against time.

With the appropriate tools now in place, we begin by benchmarking simulated low density cell trajectories (i.e. no cell-cell interactions) against those obtained experimentally (c.f. Figure 6.12a). In general, the effective diffusion coefficient of a cell performing a random walk in a uniform environment is determined by the particular combination of its speed and tendency to persist in particular directions. An isolated measure of the diffusion coefficient does not, therefore, uniquely describe the cell behaviour: fast-moving cells with a short persistence may, for example, diffuse at a comparable rate to slow-moving cells with a long persistence time. Fortunately, however, Tremel et al. (2009) used the low density cell trajectory data from Cai et al.

Parameter	Definition	Value
s_0	External cue-free cell speed	42 μm · hr^{-1}
τ_u	Pseudopod establishment time	0.03 hr
τ_r^*	Cell persistence time	0.265 hr
γ_p	Random migration weighting	0.05
γ_r	Cell "memory" weighting	1
s_{max}	Reference maximal cell speed	63 μm · hr^{-1}
R_N	Cell nuclear radius	5 μm
R_{max}	Maximal equivalent cell radius	18.2 μm
R_{Smax}	Maximal cell sensing radius	22.8 μm
η_{adh}	Potential function cell-cell adhesion coefficient	12996/474721
η_{rep}	Potential function cell-cell repulsion coefficient	1
β_{adh}	Potential function cell-cell adhesion shape parameter	1
β_{rep}	Potential function cell-cell repulsion shape parameter	1
χ_{adh}	Maximal cell-cell adhesion weighting	0.34
χ_{rep}	Maximal cell-cell repulsion weighting	20
$\beta_{\chi adh}$	Cell-cell adhesion weighting shape parameter	1
$\beta_{\chi rep}$	Cell-cell repulsion weighting shape parameter	0.85
v_D	Cell speed-modulation factor (local cell density)	0.35
$\beta_{s,D}$	Cell speed-modulation shape parameter (local cell density)	2
τ_{G1}	Time spent in G1 phase of cell cycle	4.3 hr
τ_{G2}	Time spent in S/G2 phase of cell cycle	4.6 hr
τ_M	Time spent in M phase of cell cycle	0.3 hr
D_{crit}	Critical local cell density for quiescence	0.075
ω	Cell rotation rate	$\pi/2\tau_u$ rad · hr^{-1}
A_{max}	Maximal equivalent cell semi-major axis length	32 μm
$A_{max(s)}$	Maximal speed-related cell semi-major axis length	28.5 μm
λ_ω	Cell body contraction rate during rotation	375 μm · hr^{-1}
λ_s	Speed-related morphology modification rate	10 hr^{-1}
λ_q	Cell-cell interaction morphology modification rate	1500 μm · hr^{-1}
$\beta_{s,A}$	Speed-related morphology modification shape parameter	1.3
β_{G2}	Cell speed-modulation shape parameter (mitosis)	0.25

Table 6.2: Parameters used for all simulations in Sections 6.3.2 and 6.3.3.

(2007) to obtain an approximate value for the average cell speed. This was achieved by simply summing straight line displacements between successive data points and dividing by the accumulated migration time. An estimate of 42 μm · hr^{-1} was obtained; hence, we adopted this value for s_0 in our simulations and subsequently predicted an average persistence time τ_r^* of approximately 16 minutes (c.f. Table 6.2).

Since the experimental data set comprised only 5 long (i.e. 16 – 24 hours) trajectories, the number of realisations was increased by splitting each into many shorter (i.e. 40 minutes) paths under the assumption that each step was independent of its predecessor (Cai et al., 2007). The simulation data consists of 240 trajectories over 10 hours. Summaries of the bias and diffusivity estimates for both the experimental and *in silico* cells are presented in Tables 6.3 and 6.4, respectively. Both data sets are found to predict negligible bias in the cell migration, and the simulated diffusivity estimates match up well to the averaged experimental values (i.e. 3.6 μm^2 · min^{-1} *in vitro* vs. 3.61 μm^2 · min^{-1} *in silico*). Some typical simulated cell trajectories are given in Figure 6.13, while Figure 6.14 presents the plots that were used to obtain the various *in silico* estimates of bias and diffusivity (c.f. Equations 6.25 and 6.29).

	Paths	Time Points	Time Interval (min)	$\langle X_t \rangle$	$\langle Y_t \rangle$
Cai et al. (2007)	125	5	10	-0.080	0.010
Simulation	240	501	1.2	0.008	-0.009

Table 6.3: Comparison of the simulated low density bias estimates with those obtained *in vitro* by Cai et al (2007). All values are given in units of μm · min^{-1}.

	Paths	Time Points	Time Interval (min)	$\langle X_t^2 \rangle$	$\langle Y_t^2 \rangle$	$\langle \|\|\boldsymbol{R}_t\|\| \rangle^2$	$\langle \|\|\boldsymbol{R}_t\|\|^2 \rangle$	Avg.
Cai et al. (2007)	125	5	10	3.3	4.2	3.2	3.7	3.6
Simulation	240	501	1.2	3.63	3.56	3.66	3.59	3.61

Table 6.4: Comparison of the simulated low density diffusivity estimates with those obtained *in vitro* by Cai et al (2007). All values are given in units of μm^2 · min^{-1}.

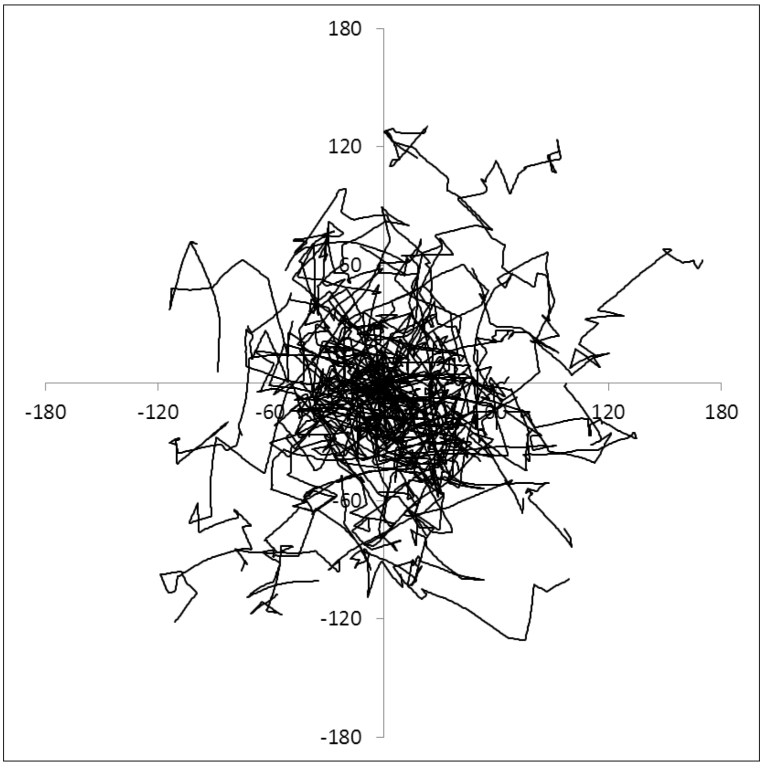

Figure 6.13: Selection of 40 *in silico* fibroblast trajectories obtained over a period of 10 hours at low cell density (axis values denote μm). Statistical analysis of the full data set of 240 trajectories revealed the effective cell diffusion coefficient to be approximately 3.6 $\mu m^2 \cdot min^{-1}$, in line with the *in vitro* estimates of Cai et al. (2007).

Having benchmarked the movement properties of fibroblasts migrating in isolation, we now proceed to consider the two other experimental data sets obtained by Cai et al. (2007) and Tremel et al. (2009). These measures, namely the rate of growth of a confluent cell population and the resultant high density cell diffusivity, are strongly interlinked; Section 5.6.2, for example, clearly illustrated that the manner in which the cells interact can have significant implications for the rate of population growth. Thus, although the two sets of simulation results shall be presented entirely separately, it is important to bear in mind that many of the underlying cell-cell interaction parameters contribute to both outcomes.

In both experiment and simulation, growth to confluence of the cell population was performed prior to extracting cell trajectory data at sufficiently high density. Therefore, in the interest of chronology, we shall firstly present the results obtained from our simulation of cell population growth. In the experimental data presented in Figure

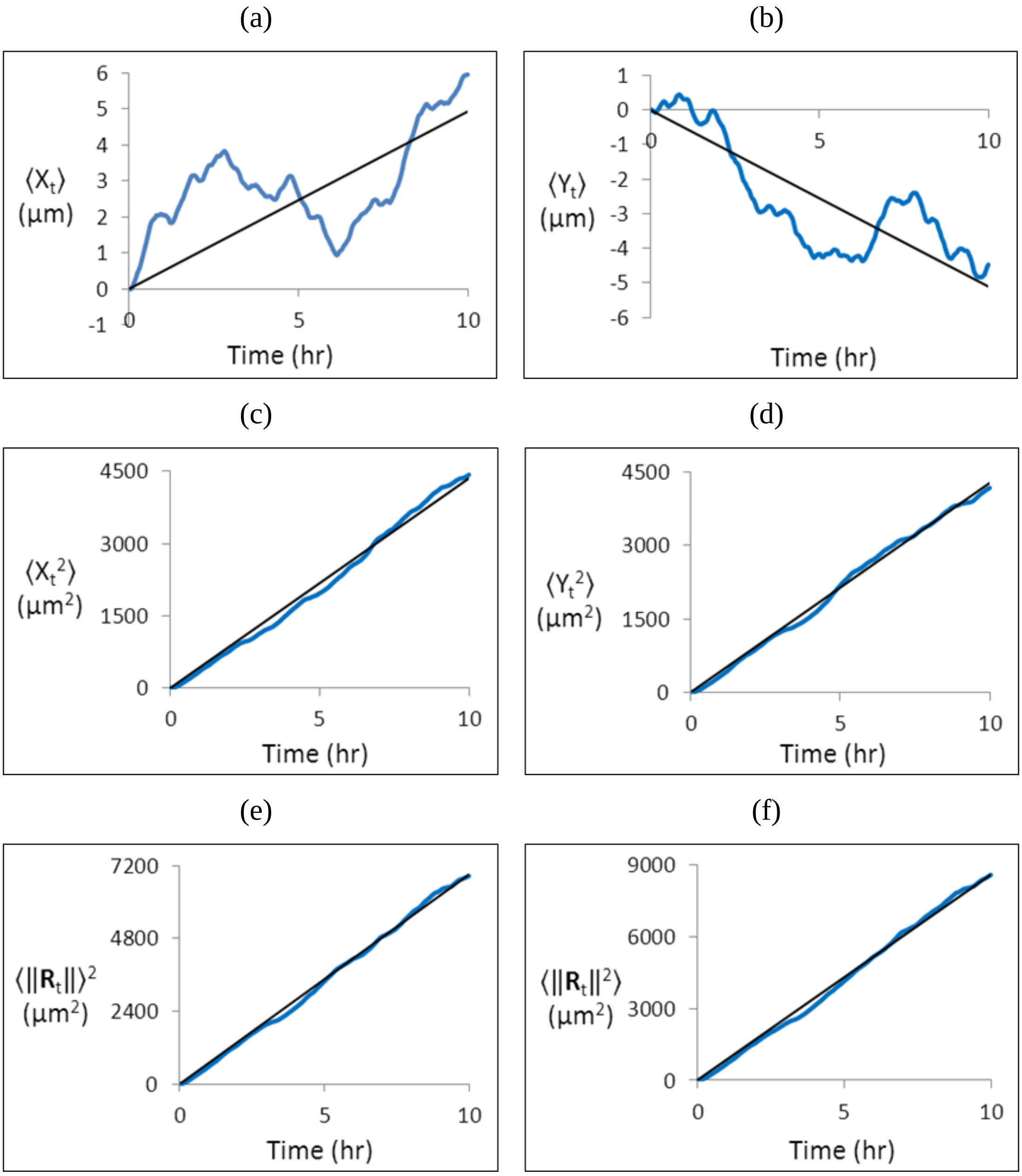

Figure 6.14: Series of plots depicting the constrained linear regression technique used to obtain estimates of the (a, b) bias and (c-f) diffusivity of 240 *in silico* cell trajectories obtained at low cell density over a period of 10 hours. Each individual trajectory consists of 501 discrete cell positions $\boldsymbol{R}_t = (X_t, Y_t)$, obtained at 1.2 minute intervals, where the Cartesian co-ordinates X_t and Y_t denote the position of a cell at time t relative to its initial position at $t = 0$. The blue lines on each plot depict the variation of the averaged values (a) $\langle X_t \rangle$, (b) $\langle Y_t \rangle$, (c) $\langle X_t^2 \rangle$, (d) $\langle Y_t^2 \rangle$, (e) $\langle \|\boldsymbol{R}_t\| \rangle^2$, and (f) $\langle \|\boldsymbol{R}_t\|^2 \rangle$ with time, while the black lines represent a constrained linear regression in each case. The estimated bias or diffusivity is given by the gradient of these lines; see Equations 6.20 – 6.29 for the full rationale of this technique.

6.12c the normalising cell density was 950 cells · mm^{-2}; on this basis we approximated the cell size by setting the maximum equivalent cell radius R_{max} to be 18.2 μm (i.e. 2D cell surface area ≈ 0.00104 mm^2). In addition, we also set R_{Smax} = 22.8 μm and A_{max} = 32 μm, which, by Equations 6.1 – 6.3, constrains the maximum semi-major sensing axis of each cell $A_S^i(t)$ to be roughly 40 μm. Given the lack of explicit information regarding physical cell sizes, these values were approximated from the experimental images presented in Cai et al. (2007) and Tremel et al. (2009). It should also be noted that s_{max} in Equation 6.14 was chosen to be larger than the external cue-free maximum speed s_0 in order to account for the fact that we would expect the cells to elongate more readily in the presence of a chemoattractant gradient, for example.

For our simulation we chose to use a domain size of 1.28 mm x 1.28 mm; the appropriate initial condition was accordingly achieved by placing 64 cells uniformly within the domain (i.e. normalised cell density ≈ 0.04), whilst it was assumed that confluence was achieved upon reaching a population size of 1536 cells (i.e. normalised cell density ≈ 0.985). As in the simulations performed in Section 5.6.2, the initial cells are assigned both random migration directions and positions in their cell cycle. Furthermore, we once again randomise the order of solution of our equations at each time step, and also implement the same assumption of solid domain boundaries (see Appendix B for details) that can be "sensed" by the cells. The only difference in this case is that, in order to achieve migration along the solid wall, an elongated cell may be incrementally re-oriented towards the direction of the boundary.

In this benchmarking exercise, the best fit to the experimental data was found to be achieved by designating an overall cell cycle length (i.e. $\tau_{G1} + \tau_{G2} + \tau_M$) of 9.2 hours. Also pertinent was the choice of value for D_{crit}, which directly governs progression into the S phase of the cycle; the selection of 0.075 suggests a strong contact inhibition of proliferation, but the concurrently weak cell-cell adhesion (i.e. χ_{adh} = 0.34) means that sufficient space is found with relative ease. A series of snapshots from the simulation are presented in Figure 6.15; note that the colour-coding of individual cells represents the different stages of the cell cycle (i.e. red = G1; blue = S/G2; green = M; yellow = G0). In the early stages the majority of cells are seen to migrate largely in isolation, so cellular quiescence is rare and morphologies tend to be elongated (Figure 6.15a, b). As confluence is approached, however, the dominance of contact inhibition means that many more cells exhibit spherical shapes and remain arrested in the G0 phase of their

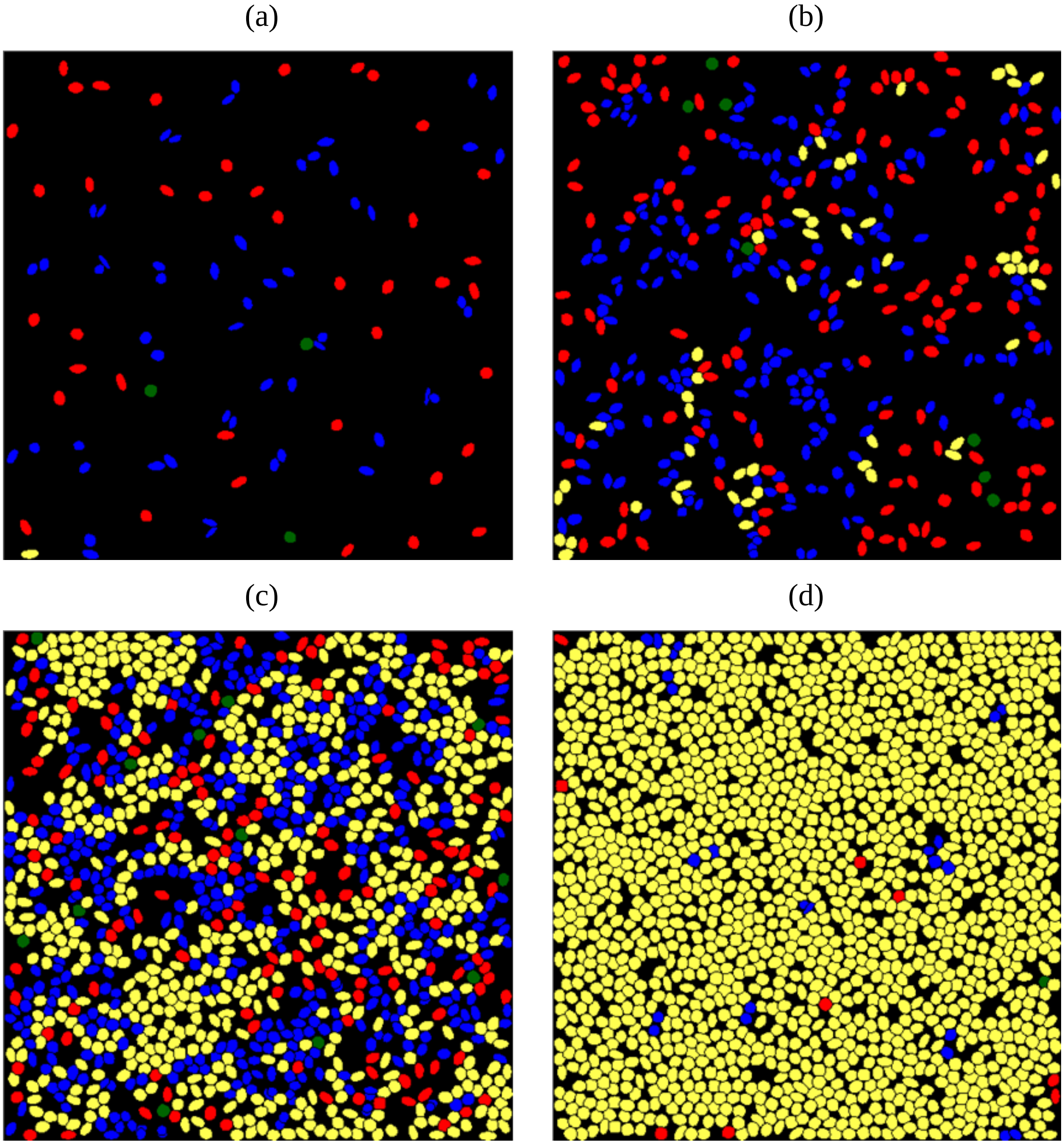

Figure 6.15: Series of snapshots from a simulation in which a fibroblast population undergoes contact inhibited migration and proliferation until reaching confluence (note that the domain is assumed to have solid boundaries). The domain was initialised with 64 uniformly positioned cells; the images depict the subsequent cell configurations after (a) 5, (b) 25, (c) 45 and (d) 65 hours. The colour-coding of cells represents position in the cell cycle, namely: G1 (red), S/G2 (blue), M (green) and G0 (yellow). The rate of population growth in this simulation was benchmarked against *in vitro* growth to confluence data obtained by Tremel et al. (2009).

cell cycle (Figure 6.15c, d). A comparison between the population growth data from simulation and experiment is given in Figure 6.16, where it is clear that an excellent match has been achieved.

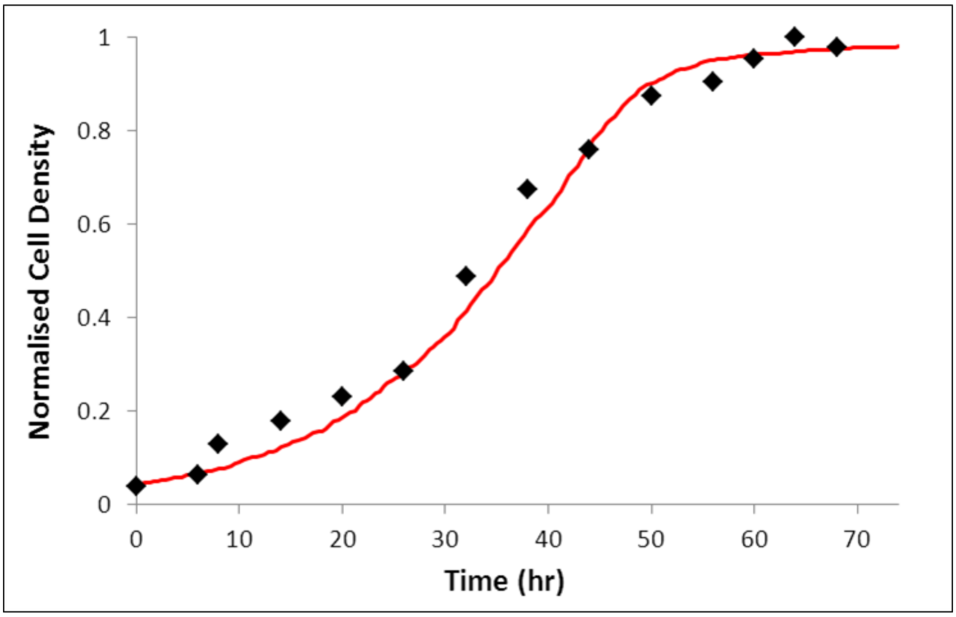

Figure 6.16: Plot comparing the rate of fibroblast population growth obtained during growth to confluence both experimentally (black diamonds) and by simulation (red line; c.f. Figure 6.14). The normalising cell density in each case was 950 cells · mm^{-2}; note that the experimental data, taken from Tremel et al. (2009), corresponds to that presented earlier in Figure 6.11c.

Upon reaching the target cell population size, all *in silico* cells were given sufficient time to attain their maximal volume before high density trajectories were subsequently recorded over a period of 10 hours. In order to minimise any potential boundary effects, for the analysis that follows we considered only cells that did not come within 250 µm of any boundary during this timeframe. As in the case of low density trajectories discussed above, Tremel et al. (2009) used an identical technique of summing straight line displacements between recorded cell positions in order to estimate the average individual cell speed at high cell density. A value of 15 µm · hr^{-1} was obtained and subsequently informed our choice of v_D to be 0.35, giving a minimum cell speed of 14.7 µm · hr^{-1} when the entire cell boundary is deemed to be in contact with neighbouring cells (i.e. $D^i(t)$ = 1; c.f. Equations 5.51 and 5.52).

Summaries of the bias and diffusivity estimates at high cell density for both the experimental and *in silico* cells are presented in Tables 6.5 and 6.6, respectively; the simulation data is again based on 240 trajectories, and the *in vitro* data set has once again been extended by splitting up each of the 15 original cell paths into shorter sections (c.f. Figure 6.12b). As in the low density case, neither data set is found to predict any appreciable bias in the axial directions. In addition, the simulated diffusivity estimates are seen to lie within the range predicted *in vitro*, and the averaged values in each case match up relatively well (i.e. 0.303 μm^{2} · min^{-1} *in vitro* vs. 0.295 μm^{2} · min^{-1} *in silico*). Some randomly selected *in silico* cell trajectories are presented in Figure 6.17, where they are shown both in their relative positions within the domain during simulation (Figure 6.17a) and upon normalisation from a fixed origin (Figure 6.17b).

	Paths	Time Points	Time Interval (min)	$\langle X_t \rangle$	$\langle Y_t \rangle$
Cai et al. (2007)	180	5	10	-0.011	-0.015
Simulation	240	501	1.2	-0.002	0.006

Table 6.5: Comparison of the simulated high density bias estimates with those obtained *in vitro* by Cai et al (2007). All values are given in units of μm · min^{-1}.

	Paths	Time Points	Time Interval (min)	$\langle X_t^2 \rangle$	$\langle Y_t^2 \rangle$	$\langle \lVert \boldsymbol{R}_t \rVert \rangle^2$	$\langle \lVert \boldsymbol{R}_t \rVert^2 \rangle$	Avg.
Cai et al. (2007)	180	5	10	0.32	0.32	0.25	0.32	0.303
Simulation	240	501	1.2	0.323	0.269	0.290	0.296	0.295

Table 6.6: Comparison of the simulated high density diffusivity estimates with those obtained *in vitro* by Cai et al (2007). All values are given in units of μm^{2} · min^{-1}.

6.3.3. Fibroblast Scrape Wound Healing

The *in vitro* cell trajectory analysis performed by Cai et al. (2007) has revealed an

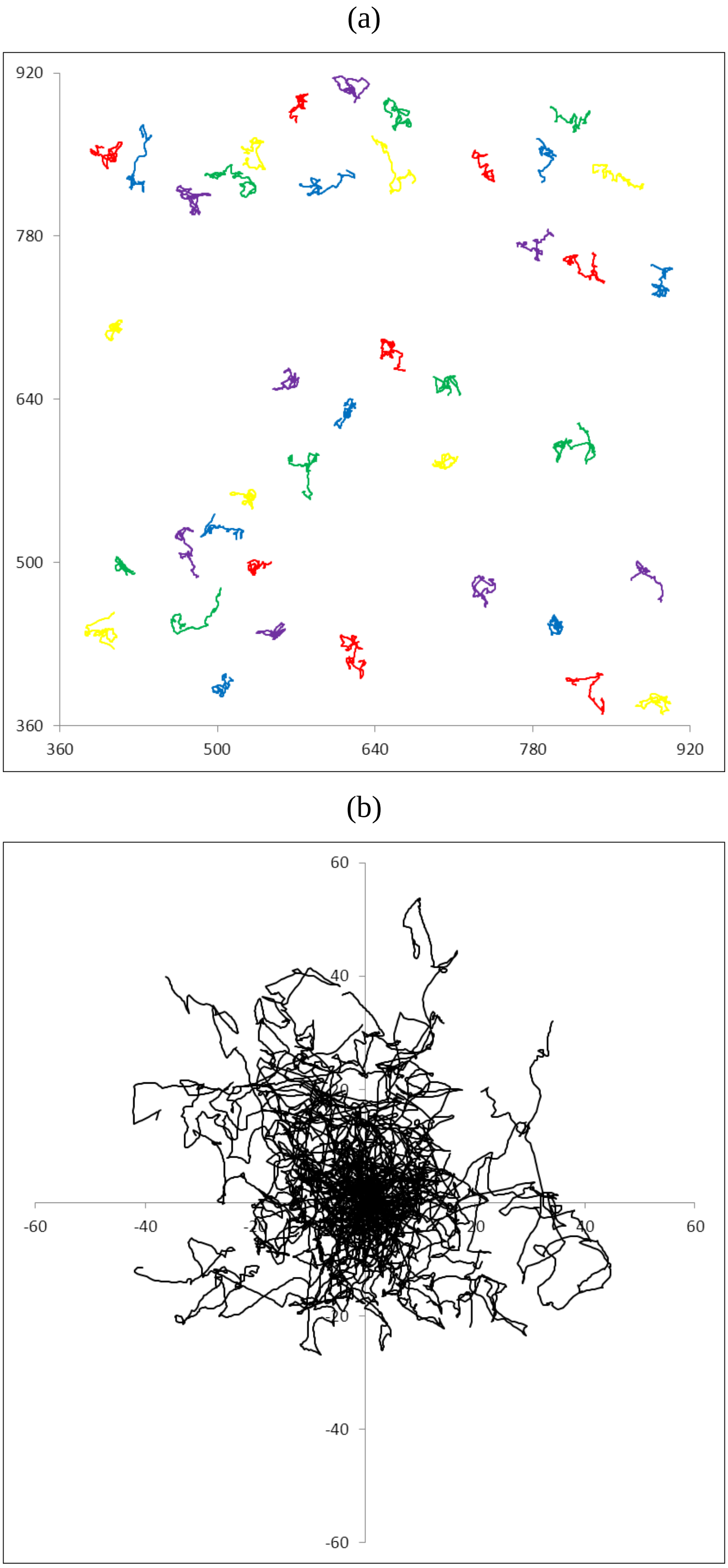

Figure 6.17: Caption overleaf.

Figure 6.17: Selection of 40 *in silico* fibroblast trajectories obtained over a period of 10 hours at high cell density (i.e. confluence). The trajectories are shown both (a) in their relative positions within the domain, and (b) normalised to a common origin (axis values denote μm in both cases). Statistical analysis of the full data set, consisting of 240 trajectories isolated from the domain boundaries, revealed the effective cell diffusion coefficient to be approximately 0.3 $\mu m^2 \cdot min^{-1}$, in line with the *in vitro* estimates of Cai et al. (2007).

approximately ten-fold decrease in the effective cell diffusion coefficient between uniform low density and high density environments (c.f. Tables 6.4 and 6.6). Thus far our mathematical model has successfully replicated these results, as well as the rate of cell population growth, under the assumption of cell-cell interactions and related contact inhibition effects. Given these results, it seems pertinent to consider the resultant cell behaviour in a scenario that allows cells to smoothly transition between distinct regions of both low and high cell density. Indeed, this is precisely the route followed by Cai et al. (2007) who proceeded to introduce just such an interface in their confluent cell population by removing a region of cells to create an *in vitro* scrape wound (Figure 6.18). Naturally, our next goal is to investigate the implications of reproducing this assay *in silico* with our experimentally benchmarked cell migration model.

Experimental data, including further cell trajectories and cell density measurements, were collected by Cai et al. (2007) over a 48 hour period after inflicting the scrape wound. In order to be able to perform our simulation over the same time range, we elect to create a wound of width 680 μm. Using the final cell configuration from the high density trajectory simulation as our starting point, we impose our scrape wound initial condition by removing all cells with centroid position more than 600 μm from the left domain boundary (Figure 6.19). This setup preserves sufficient depth in the initial cell population such that the overall results of our simulation are not adversely affected.

A series of snapshots showing the healing progression of the *in silico* scrape wound are presented in Figure 6.20. Although cell-cell adhesion could be expected play a role in holding back migration at the leading edge, the sharp interface is readily disrupted in the early stages with a number of cells breaking free and, accordingly, sensing sufficient space to re-enter their cell cycle (Figure 6.20a). Consequently, as time progresses, a

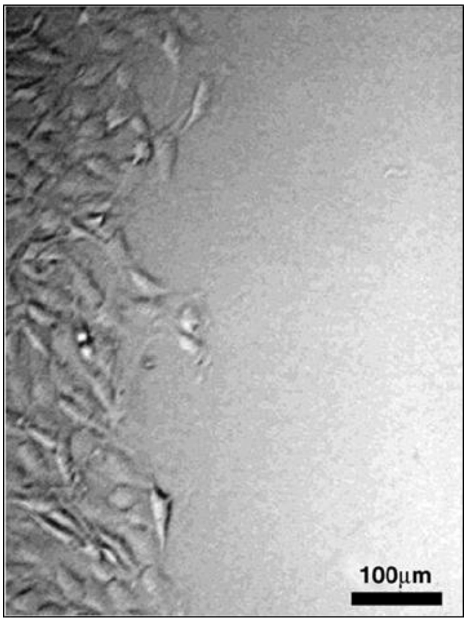

Figure 6.18: Experimental image, taken from Cai et al. (2007), showing an *in vitro* fibroblast scrape wound that has been created by removing a region of cells from an initially confluent population.

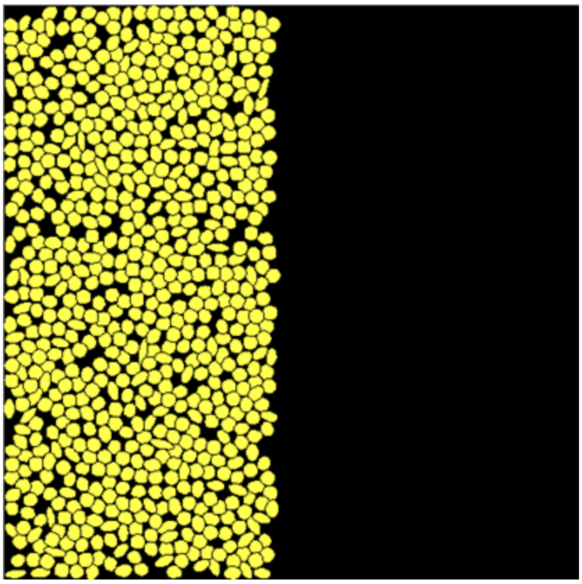

Figure 6.19: Initial condition used for the *in silico* fibroblast scrape wound simulation. After collecting trajectory data for 10 hours at high density, this cell configuration was obtained by removing all cells with centroid position more than 600 μm from the left domain boundary. Note that all cells are initially in the quiescent G0 phase of their cell cycle.

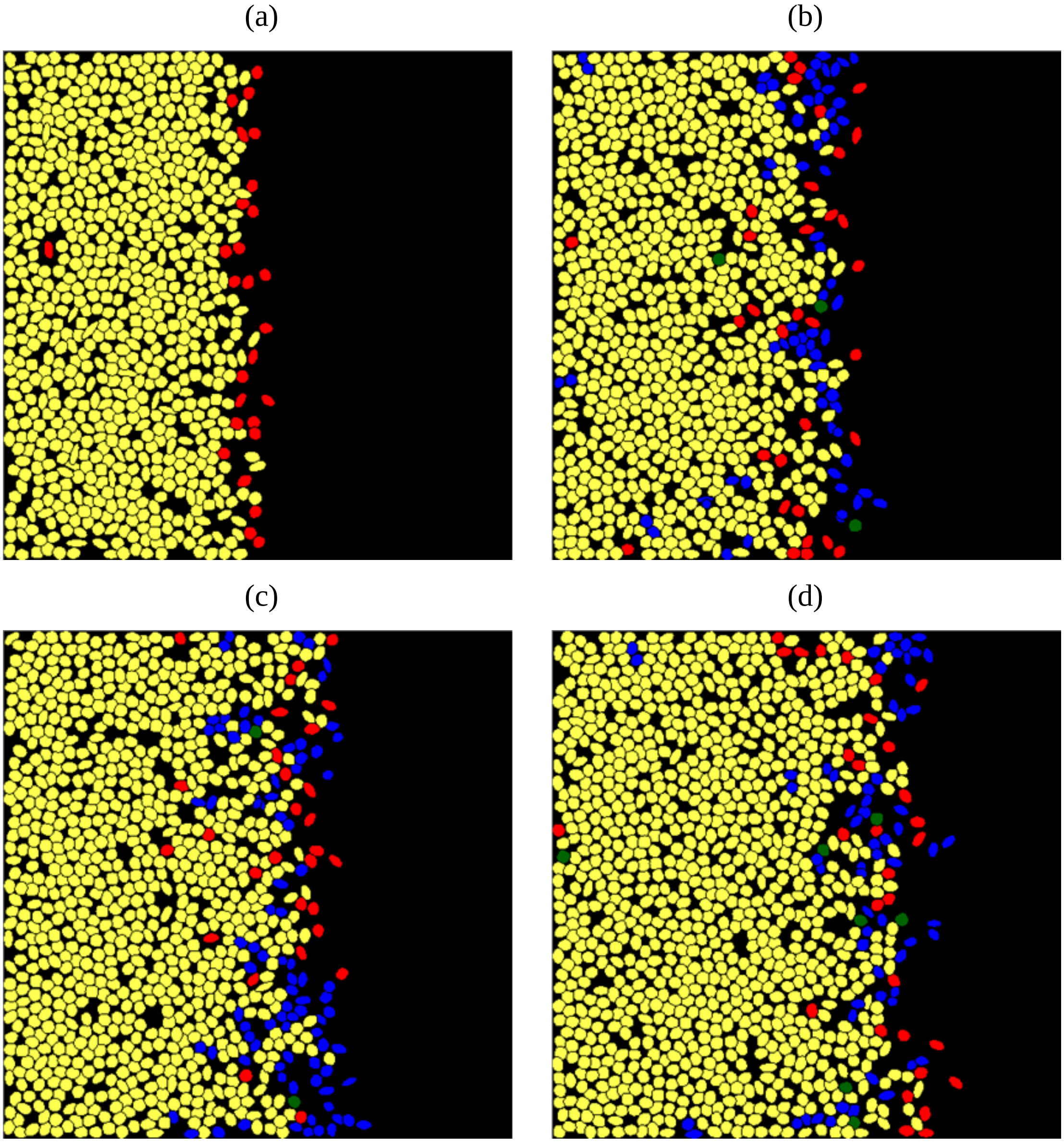

Figure 6.20: Series of snapshots from the *in silico* fibroblast scrape wound simulation, where the cells undergo contact inhibited migration and proliferation. The images show the evolving cell configuration at (a) 4, (b) 20, (c) 32 and (d) 48 hours post-scraping. The colour-coding of cells again represents the position in the cell cycle: G1 (red), S/G2 (blue), M (green) and G0 (yellow).

significant amount of proliferation is seen to have occurred at the cell front; however, it is also notable that some cells, although relatively few, have undergone mitosis in positions further back from the leading edge where pockets of space transiently develop (Figure 6.20b). The cell behaviour seen at early times subsequently persists for the rest of the simulation, and it becomes clear that the population is invading the scrape at a roughly constant rate in a manner driven largely by proliferation rather than migration (Figure 6.20c, d).

In order to obtain a quantitative measure of the predicted rate of healing progression, we split the domain into a number of 50 μm wide vertical sub-domains, sum the number of cells in each and, finally, calculate a series of appropriately normalised cell densities. In Figure 6.21, we compare these calculated values at selected time points with an equivalent set of measures made experimentally by Cai et al. (2007). The two data sets are seen to produce an excellent match after 24 hours of healing time (Figure 6.21a), but the advancement of the *in vitro* cell population is subsequently seen to undergo a marked increase that is not reproduced in the simulation results (Figure 6.21b-d).

In Cai et al. (2007), it was shown that healing at these later times occurs at an approximately fixed rate, and the evolution of cell density can accordingly be described as a travelling wave solution of the Fisher equation. As such, the earlier stage of slow healing was simply interpreted as a period of evolution required to transition from a cell population exhibiting a sharp wound edge into this co-ordinated wave-like motion. One significant assertion, however, is that this early healing phase is “dominated by cell proliferation” (Tremel et al., 2009) – recall that we noted a similar feature in our simulation results (Figure 6.20). Thus, given this observation and the excellent match produced in Figure 6.21a (as well as the earlier benchmarking results), our simulation results suggest that the cell behaviour displayed over this initial period is “normal”. Perhaps more significantly, however, this also suggests that a distinct behavioural change may be required to induce the observed increase in the rate of healing.

There are a number of potential modifications to the fibroblast behaviour that could be proposed as an explanation of the increase in the rate of wound closure, including increased cell speed, decreased cell-cell adhesion, reduced contact inhibition of proliferation or a combination of these and other factors. A more complex but equally viable explanation could be, for example, the response of the cell population to a diffusible chemoattractant produced by cells in the wound edge region. Directed movement of this type, co-ordinated by so-called “pacemaker” cells, has been both experimentally observed (Gross et al., 1976) and mathematically modelled (Palsson and Othmer, 2000) during *Dictyostelium discoideum* aggregate formation.

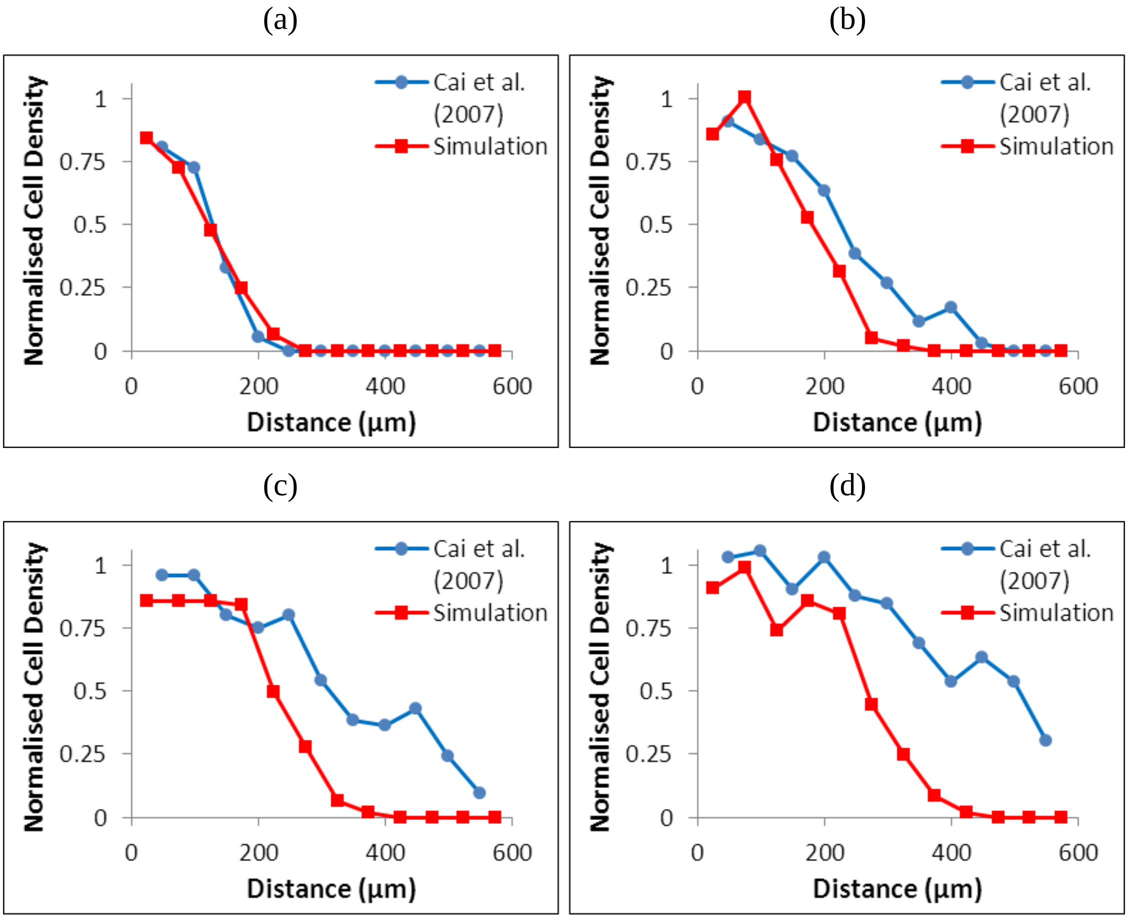
(a) (b) (c) (d)

Figure 6.21: Series of plots comparing the spatial distribution of cell density obtained by both experiment (blue circles) and simulation (red squares) in the healing fibroblast scrape wound; the normalising cell density in each case was 950 cells · mm^{-2}. The plots correspond to (a) 24, (b) 32, (c) 40 and (d) 48 hours post-scraping.

Further cell trajectories were obtained by Cai et al. (2007) and Tremel et al. (2009) during the *in vitro* scrape wound assay, and examining these results provides a simple means to investigate potential mechanisms that may be at play. Figure 6.22 shows two typical sets of trajectories that were obtained either near the leading edge (Figure 6.22a, right) or behind the wavefront (Figure 6.22a, left) between 36 and 48 hours post-scraping, while Figure 6.22b plots calculated estimates of cell speed at different distances behind the leading edge between 30 and 36 hours post-scraping. It is immediately clear that the results are consistent with the previous assumptions of contact inhibited migration: cells at the leading edge have more freedom to move and, accordingly, migrate more quickly (Figure 6.22b) and cover a longer distance than those

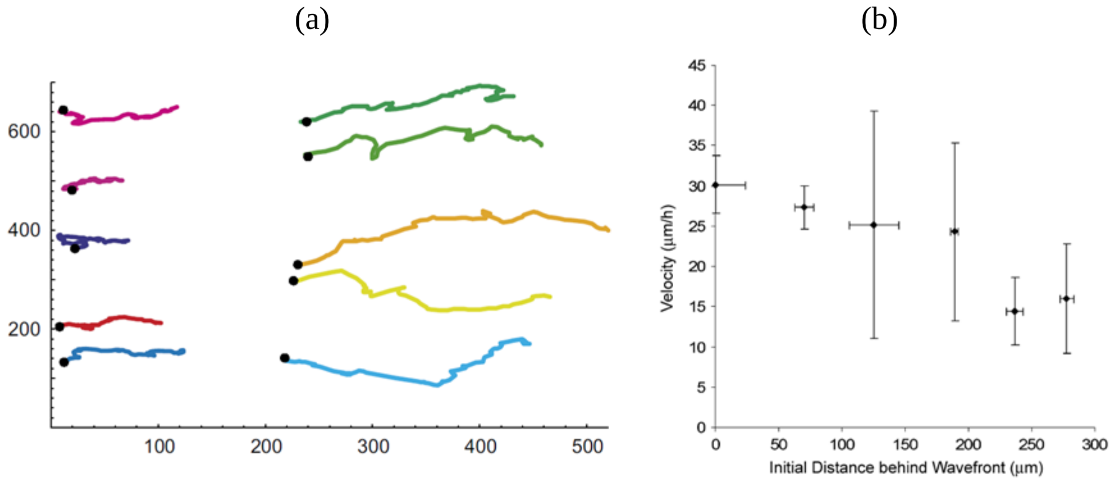

Figure 6.22: Experimental data showing (a) cell trajectories (image taken from Cai et al. (2007)) and (b) estimated cell speeds (image taken from Tremel et al. (2009)) at various distances behind the wavefront during *in vitro* fibroblast scrape wound healing. The given cell trajectories were recorded at 10 minute intervals between 36 and 48 hours post-scraping; black circles represent initial cell positions (axis values denote μm). Cell speed estimates were obtained from trajectories recorded at 10 minute intervals between 30 and 36 hours post-scraping: straight line displacements between successive data points were summed, and the speed calculated via division by the accumulated migration time.

further back from the wounded region (Figure 6.22a). The range of estimated cell speeds (i.e. ~ 10 – 40 μm · hr^{-1}) is also notable because this is entirely consistent with the previously benchmarked “normal” cell behaviour; hence, it seems highly unlikely that an increase in cell speed could account for the increased rate of healing. Overall, therefore, the observed bias in the cells’ movement direction seems to suggest that the travelling wave in fact evolves as a result of a tendency of cells to reduce random migration and instead maintain polarisation towards the wound gap. Although other factors such as increased cell proliferation may also be involved, we are led to conclude that our present simulation model seems to currently lack an important directional cue that is required to inform the fibroblast migration.

The evidence detailed above strongly suggests that an additional directional cue is required in order to adequately explain the experimental results; it remains unclear, however, as to how such a stimulus may be initiated, co-ordinated and sustained. These precise details may not be readily uncovered, but recent experimental findings at least provide a suggestion as to the mechanism that may be underlying the observed phase of directed cell migration. Connexins, a family of transmembrane proteins involved in the assembly of intercellular communication channels known as gap junctions (Figure 6.23), have been shown to modify their expression during both *in vitro* and *in vivo* wound repair processes (Goliger and Paul, 1995; Wright et al., 2009). Although both connexins and gap junctions have been linked to a wide variety of roles in a wide variety of cell types (Evans et al., 2012), our findings suggest that co-ordinated perturbation of cell-cell communication patterns could be a critical regulator of the scrape wound healing process.

Connexin 43 (Cx43), the most commonly expressed connexin in skin cells, has been found to elicit a naturally reduced expression in migrating keratinocytes at the margins of *in vivo* wounds (Goliger and Paul, 1995), and in both keratinocytes and fibroblasts near the leading edge of *in vitro* scrape wounds (Wright et al., 2009). Furthermore, upregulation of Cx43 expression at the wound edge has been observed in a diabetic rat model, with an associated delay in cell migration and healing (Wang et al., 2007). Consistent with these findings is also the intriguing observation that inhibiting either Cx43 expression (Mori et al., 2006) or, more directly, Cx43 function (Wright et al., 2009) accelerates wound closure rates (Figure 6.24). In the latter case, inhibition of Cx43 function was achieved through the use of specifically designed gap junction blockers known as connexin mimetic peptides (CMPs). These peptides are believed to have great potential as a novel therapeutic tool for improving wound closure; however, their precise mechanisms of action at the molecular and cellular scales are yet to be fully elucidated.

Mathematical modelling may well provide a powerful tool in this respect, and such an investigation provides a challenging future target for our cell migration model. Coupling appropriate models of intracellular and intercellular molecular dynamics to the existing framework, and benchmarking cell movement against real experimental data in the manner performed above, may help to provide key insights into the individual and collective behaviour displayed by cells both in the presence and absence of CMPs. Specifically, the model has the potential to investigate the relative impact on key aspects of the wound healing process such as cell directionality, speed and proliferation.

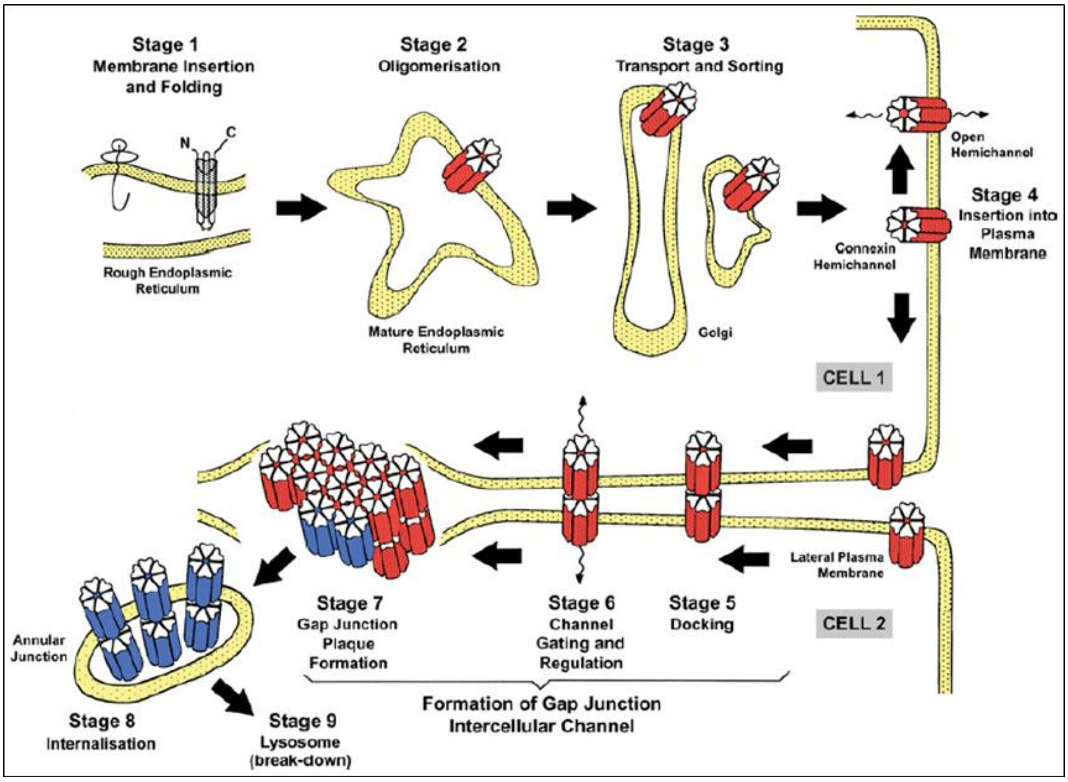

Figure 6.23: Schematic diagram showing the life cycle of connexins and gap junction intercellular channels. Connexins are initially synthesised within the rough endoplasmic reticulum, a membrane-bound internal cell compartment (Stage 1). Sets of six connexins come together to form hemichannels known as connexons (Stage 2), and these are subsequently transported along the secretory pathway (Stage 3) before insertion into the plasma membrane (Stage 4). These hemichannels, which can translocate around the membrane, then proceed to dock with partners from adhesively attached neighbouring cells to form gap junctions (Stage 5). In an open configuration, cell-cell communication can occur by the passage of small molecules through the channel (Stage 6); this may occur simultaneously with the aggregation of many channels to form aggregates known as gap junction plaques (Stage 7). The individual components of these plaques are rapidly turned over: new gap junctions can be added, while others are lost due to internalisation (Stage 8) and breakdown (Stage 9) by one of the host cells. Image adapted from Evans et al. (2006).

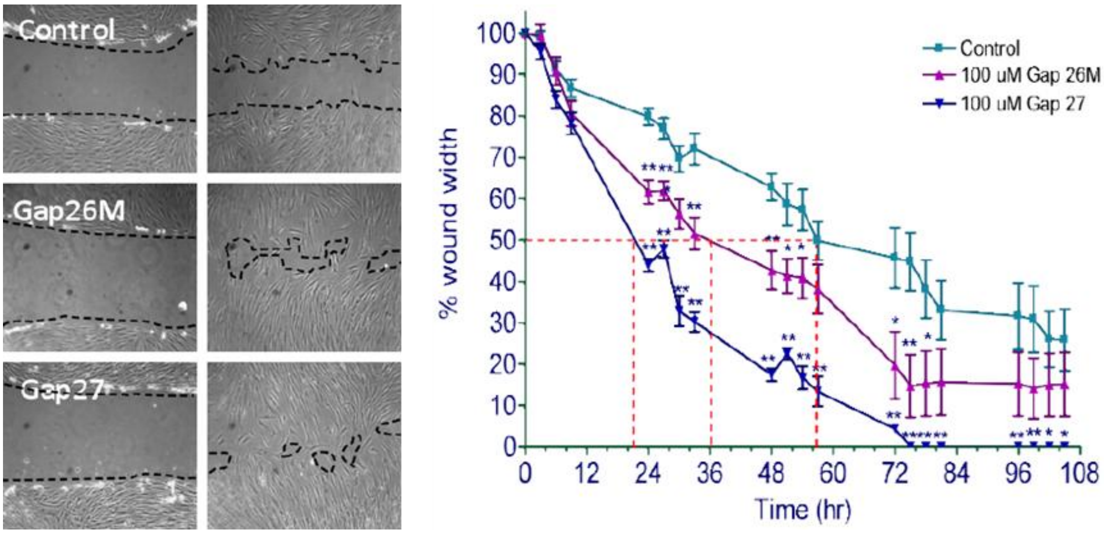

Figure 6.24: Experimental data from an *in vitro* fibroblast scrape wound assay examining the implications of connexin mimetic peptide (CMP) application; CMPs are believed to operate by blocking gap junction intercellular channels and preventing cell-cell communication. The images show (a) photomicrographs of cell configurations at 0 hours (wound width ≈ 600 μm) and 24 hours post-scraping, and (b) a plot quantifying the rate of wound closure both in the absence (control) or presence (Gap26M and Gap27) of CMPs. The dashed lines in (b) indicate the time taken to reach 50% wound closure; note that the peptide treated cells exhibit a significantly increased rate of healing. Images taken from Wright et al. (2009).

6.4. Discussion

Tissue development and maintenance procedures require the large-scale co-ordination of a wide variety of cell types with typically diverse morphologies – each of which is regarded to be function-specific (Bray, 2001). The crawling dermal fibroblast, for example, is well-known for its elongated form and concurrent polarisation towards the direction of migration. Such features undoubtedly have a strong impact on the manner in which cells of this type behave both individually within a prescribed environment and, furthermore, in the presence of other cells. Therefore, in this chapter we have generalised our spherical cell migration model in order to capture the movement properties of cells with elongated morphologies.

A consistent generalisation from identically spherical cells to those of an elongated nature has been achieved by stipulating that each cell now assumes an ellipsoidal form, characterised by three semi-axis lengths rather than a single radius. The concept of cell polarisation has been achieved, in addition, by assuming that the cell body undergoes rotation in order to maintain alignment with the instantaneous migration direction. Rotation *per se*, however, inadequately describes the mechanisms of directional change in real cells; instead, the process is more likely achieved by an internal re-organisation of structure. Thus, by endowing each cell with the ability to dynamically adapt its shape, an assumed contraction of the cell body throughout rotation more readily captures this phenomenon. Consistent with a previous mechanical cell migration model (Palsson and Othmer, 2000), the cells have also been allowed to modify their morphology in response to evolving environmental factors: adhesive and repulsive interactions with local cells cause the cell body to either stretch or compress, whilst cells also act to maintain a target morphology that is uniquely correlated to their instantaneous speed.

The dynamic interaction between cell migration and cell shape was subsequently examined in a simple sensitivity study that considered the response of an isolated cell to a moving source of chemoattractant. By the nature of the assumed migratory response, the cell experienced significant variations in both cell speed and frequency of directional changes throughout the simulation. Accordingly, this was reflected by a simultaneously oscillatory evolution of the cell morphology in all cases. The relative values of the parameters λ_ω and λ_s, which quantify, respectively, the rate of cell body contraction during rotation and the rate of recovery of the target morphology, were found to strongly impact upon the manner of this evolution (Figures 6.9 and 6.10). The greatest competition between these two stimuli for morphological change was seen to occur in regions of shallow chemical gradient where the incidence of pronounced directional changes experiences a significant increase. In these regions, the ability of the cell to attain the speed-associated target morphology was seen to depend crucially on the intensity of the repeated cell body contractions, and the tendency to intermittently recover the required elongation (i.e. “re-polarise”). The final sensitivity examined the impact of the parameter $\beta_{s,A}$ (Figure 6.11), which defines the precise shape of the assumed set-point relationship between cell speed and cell morphology. The evolution of cell shape most consistently resembled this target morphology in the case of large $\beta_{s,A}$, where the target cell length underwent large temporal oscillations that reflected the concurrently strong variations between directed and random modes of movement (Figure 6.11c).

As summarised above, reproducing the movement properties of single elongated cells requires the introduction of several new definitions and equations. Incorporating cell-cell interactions in the new model formulation, on the other hand, has been achieved by conserving all of the assumptions from the earlier spherical cell formulation. Each cell is still endowed with a sensing region beyond its boundary, accounting for uncertainty in the precise morphology and the ability to maintain adhesive contact at distance, and each cell still interacts with neighbours in a manner governed by the potential function h^{ij}. The key advancement that allows simple transition between spherical and ellipsoidal model formulations, however, relies on a consistent transformation of this potential. Since the area of overlap between two circles can be uniquely expressed in terms of the distance between their centres, it follows that h^{ij} can also be uniquely expressed as a function of overlap area between cell sensing regions rather than a distance between (spherical) cell centres. Thus, in the ellipsoidal case, where the distance between two cell centres alone cannot precisely describe their relative configuration, calculating the extent of sensing region overlap provides a superior measure to feed into the potential function and appropriately determine their manner of interaction. It is worth noting here that, although extension to 3D is a desirable future target for the model, it is highly unlikely that this precise mechanism for ellipsoidal cell-cell interactions could be conserved. The current calculation of overlap area requires solution of a quartic equation; solving polynomials of degree six for overlap *volumes* would prove more difficult and so some other approach may be necessary.

Having completed the full model formulation for ellipsoidal cells, the potential of the model was subsequently demonstrated by using *in vitro* experimental data from Cai et al. (2007) and Tremel et al. (2009) to benchmark the behaviour of migrating and proliferating fibroblasts. Appropriate quantification of cell-cell interactions and contact inhibition effects allowed us to successfully predict the experimentally observed rate of cell population growth (Figure 6.16). Furthermore, statistical analysis of *in silico* cell trajectories obtained over a 10 hour period at both low and high cell density revealed a strong synergy with the estimated *in vitro* cell diffusion coefficients.

Accepting the parameterisation underlying these results to therefore represent "normal" cell behaviour, we proceeded to examine the response of our cells to the creation of an *in silico* scrape wound (Figure 6.19). Invasion of the wounded region was subsequently seen to be relatively slow; random cell movement near the leading edge provided insignificant penetration and closure of the gap was instead driven largely by proliferation at the cell front (Figure 6.20). Comparing quantitative cell density results with those obtained from an analogous experiment, the two data sets were found to match up well – but only over a 24 hour period (Figure 6.21). Beyond this time point, the *in vitro* cell population was found to undergo a striking change in behaviour and invade the wound gap at a significantly increased rate.

With no apparent increase in cell speeds, the *in vitro* results are suggestive of an additional stimulus that co-ordinates collective outward cell movement (Figure 6.22). Given the current model formulation, only the inclusion of a chemoattractant gradient could possibly allow reproduction of this type of behaviour. Recent experimental evidence, however, suggests that cell-cell communication may provide a more viable explanation: expression patterns of connexins, the building blocks required to form gap junction intercellular channels, have been shown to be perturbed at the leading edge of both *in vitro* and *in vivo* wounds (Goliger and Paul, 1995; Mori et al., 2006; Wang et al., 2007; Wright et al., 2009).

Although the molecular biology of connexins and gap junction communication is undoubtedly complex and remains poorly understood, the apparent impact on collective cell behaviour provides an intriguing prospect for mathematical modelling. *In vitro* scrape wound healing, in particular, provides a relatively simple assay with which study the mechanisms by which cell-cell signalling could impact upon both individual and population level cell migratory properties. The experimental benchmarking presented in this chapter has indicated that the current modelling approach can successfully predict “normal” *in vitro* cell behaviour; incorporating the additional effects of cell-cell communication provides an intriguing challenge for future studies.

Chapter 7

Discussion

The development of multi-cellular organisms, and subsequent maintenance of their tissues, requires the co-ordination of a cascade of events at both the cellular and molecular scales. The multi-scale nature of such phenomena signals the potential of mathematical modelling as an investigative tool. In this thesis, we have presented a variety of new models of discrete cell migration to study the mechanisms by which cells respond to their temporally-evolving environments and have applied our methods to two specific physiological processes: *viz*, wound healing and retinal vascular plexus (RVP) development. Using two distinct mathematical approaches – one lattice-based, the other lattice-free – we have reproduced a range of experimental data and provided a number of novel insights into the dynamics of the underlying biology.

Our extensive review of the modelling literature in Chapter 1 revealed that, outwith the context of tumour-induced angiogenesis, relatively few studies of discrete vessel growth have been performed. As such, we believe that the models of wound healing angiogenesis (Chapter 3) and RVP development (Chapter 4) presented here are the first of their kind in this field. In addition to successfully reproducing the capillary plexus data observed experimentally, these models have also been used to predict the subsequent evolution of the emergent vascular architectures themselves.

In Chapter 2, we presented an extended model of blood perfusion that included empirically-derived equations describing both phase separation at capillary junctions and shunt-preventing angioadaptation stimuli. Although these aspects of the microcirculatory dynamics have been largely neglected in previous angiogenesis models, our results intimated that their inclusion would prove to be significant. Using a series of simple, idealised vessel networks, we highlighted the strong impact on the resultant distributions of both haematocrit and capillary radii. This was demonstrated more profoundly in the later simulations of RVP development: phase separation was seen to result in strongly heterogeneous distributions of haematocrit with corresponding implications for oxygen delivery, while shunt prevention was seen to be largely responsible for the evolution of realistic capillary architectures. Even though the precise biology of these two phenomena may not yet be fully understood, our results suggest that their inclusion in future angiogenesis models will be crucial in order to faithfully reproduce vascular architectures resembling those observed *in vivo*.

A novel approach to studying wound-induced angiogenesis was presented in Chapter 3, where our *in silico* results were benchmarked against longitudinal *in vivo* experimental data obtained from a dorsal skinfold window chamber (DSWC) assay. In both the presence and absence of an anti-angiogenic treatment, the model was found to be capable of reproducing spatial and temporal measures of *in vivo* capillary density and branch point density, as well as the experimentally-observed reduction in wound area. Although the model provides predictions regarding the distribution of intra-wound haematocrit in the evolving neo-vasculature, a future goal would involve a more detailed investigation into how this impacts upon oxygen delivery to the wounded region. Using the model of retinal oxygenation presented in Chapter 4, such a study would now be eminently possible, and could provide valuable predictions regarding the spatio-temporal evolution of wound oxygen concentration.

The inclusion of oxygen delivery and associated capillary pruning are two of the extensions to the wound healing angiogenesis model that needed to be developed in order to successfully reproduce *in vivo* observations of RVP development. Although growth of the RVP was driven by identical mechanisms – diffusion, chemotaxis and haptotaxis – the system was seen to be much more dynamic than that assumed for the earlier wound model. Incorporating the migration of VEGF-producing astrocytes allowed the EC plexus to expand outwards across the retinal surface in response to an evolving, rather than fixed, chemoattractant profile. The manner of this VEGF evolution, namely an outwardly moving wave-like profile, is one of the valuable insights derived from our model; others include the demonstration that both phase separation and capillary pruning play prominent roles in promoting oxygen delivery to distal regions of the retina.

The series of parameter sensitivities presented towards the end of Chapter 4 provide a brief glimpse as to the future potential of the model. Having benchmarked the model against normal RVP development, a variety of pathological scenarios – such as diabetic retinopathy or retinopathy of prematurity (ROP) – could be investigated in significantly greater detail. Such a study, however, may require further expansion of the model to include the development of the two deeper layers of the retinal vasculature. The molecular mechanisms controlling downward sprouting and migration from the superficial layer are as yet poorly understood – a modelling study may prove valuable in helping to test experimental hypotheses.

During our studies of angiogenesis in both wound healing and retinal development, the *in silico* modelling approach has been rigorously tested. Through various extensions, the model has been shown to be capable of successfully predicting both the topology and architecture of *in vivo* capillary networks. As it stands, however, our simulations largely assume angiogenesis to be a stand-alone process and, in truth, this may limit future applications of the model. *In vivo* angiogenesis generally occurs as part of a wider response to hypoxia, and may involve an abundance of cellular activity; dermal wound healing, for example, requires the co-ordinated response of a variety of cell types including macrophages, fibroblasts and neutrophils. Naturally, therefore, future iterations of the angiogenesis model may wish to incorporate more complex feedbacks with other cells in the surrounding milieu.

It is clear that the generalised cell migration model presented in Chapters 5 and 6 could provide a first step towards realising such a goal. Our simulations have demonstrated, however, that this off-lattice model also has the potential to be applied, in its own right, to a wide range of scenarios. Much of this is down to its inherent adaptability: we have developed discrete-point, spherical and ellipsoidal cell formulations capable of simulating cell movement in response to a variety of environmental stimuli. The current 2D nature of this model immediately marks it out as an appropriate tool for investigating *in vitro* cell behaviour and it is clear that such studies could be used in future to minimise parameter searches in experimental programmes.

The experimental benchmarking performed in Chapter 6 indicates the predictive power of such an approach. Utilising an experimental dataset gathered during *in vitro* fibroblast migration and proliferation, we reproduced the observed rate of growth to a confluent population, as well as measures of cell diffusivity at both low and high cell density. Introducing a scrape wound into the confluent *in silico* fibroblast population, and comparing the predicted behaviour with that observed *in vitro*, suggested that an interesting biphasic response was taking place in the experimental setting: the cells spend an initial period behaving in a “normal” manner, before largely reducing random movement and increasing polarisation towards the wounded region. In its present form, the model was unable to capture the behavioural change at later times, and future work will examine whether cell-cell communication or a chemotactic mechanism could explain the source of this discrepancy.

As mentioned above, an important consideration for future investigations is the possibility that our two modelling approaches (angiogenesis in the presence of discrete fibroblast migration, for example) could be applied in combination. Given that it represents one of our key focuses in this thesis, wound healing would be an attractive system with which to commence such a study. *In vivo* wound healing angiogenesis could, for example, be simulated alongside migration of pertinent cell types such as macrophages or fibroblasts. There are a number of feedbacks that could be introduced between the two models, including: EC chemotaxis in response to macrophage-derived cytokines; EC haptotaxis, or contact guidance, in response to fibroblast-produced collagen fibres; and capillary dilatation in response to cell-produced nitric oxide. In light of earlier work by Cobbold and Sherratt (2000), such a model could provide a more detailed 2D investigation into the role played by angiogenesis in pathological scar formation. More generally, however, combining different model components in this manner broadens the scope for investigating the dynamics of impaired healing, as observed in chronic or diabetic wounds.

Another potential application of the combined modelling approach concerns another type of healing – that of the bone fracture. Similarly to wound healing, it has been found that successful bone generation (osteogenesis) can only be achieved with blood vessels in close attendance; hence, angiogenesis is a critical factor in this healing process. As well as providing oxygen and nutrients, blood vessels also deliver osteoprogenitor cells, which can differentiate into bone-forming osteoblasts under favourable mechanical and metabolic conditions (Cenni, 2005). Models of bone formation have previously been developed to study normal fracture healing (Geris et al., 2008), but also to investigate the viability of tissue engineered implants (Checa and

Prendergast, 2008). The latter case, involving simultaneous bone cell migration and vascularisation within a porous scaffold, provides an intriguing future application for our models.

In conclusion, we re-iterate that we have taken two existing discrete approaches to modelling cell migration and extended them by incorporating various aspects of the underlying biology that had previously been neglected. In so doing, we have shown our models to be capable of reproducing a range of pertinent experimental data, and also providing a number of novel insights into the progression of both retinal development and wound healing. In these studies, we have largely focussed on benchmarking our models against observations from normal healing and development; this work paves the way for important future studies that examine the mechanisms controlling aberrant and pathological cases.

Appendix A

Numerical Implementation of the Angiogenesis Model

Here we provide some additional information regarding the numerical implementation and solution of the different aspects of the angiogenesis model. All solution techniques utilised throughout this work have been coded in the C++ programming language.

A.1. Basic Network Model

The starting point for the simulation of angiogenesis is a network model, which consists of a three-dimensional regular cubic lattice of bonds that meet at n_x x n_y x n_z nodes. The total number of bonds is given by the expression: $3n_xn_yn_z + n_yn_z$; this indicates that each node has three bonds associated with it (one in each space direction), whilst one additional x-bond is appended to each node on the right-hand y-z plane (Figure A.1). This set-up allows the entrance and exit of fluid across the y-z boundaries when a pressure gradient is maintained in the x-direction.

All of the simulations performed in this thesis, however, were achieved using a distorted network. It has been found that flow simulations performed on regular networks exhibit a flow bias parallel to the pressure gradient with a concurrent reduction in transverse flow. To remedy this, each of the $n_xn_yn_z$ nodes are displaced from their original positions (i, j, k) to new positions $(i + \varepsilon_i, j + \varepsilon_j, k + \varepsilon_k)$ (Figure A.2). The ε are random numbers chosen uniformly from the range $[-\alpha, \alpha]$ where, in general, α

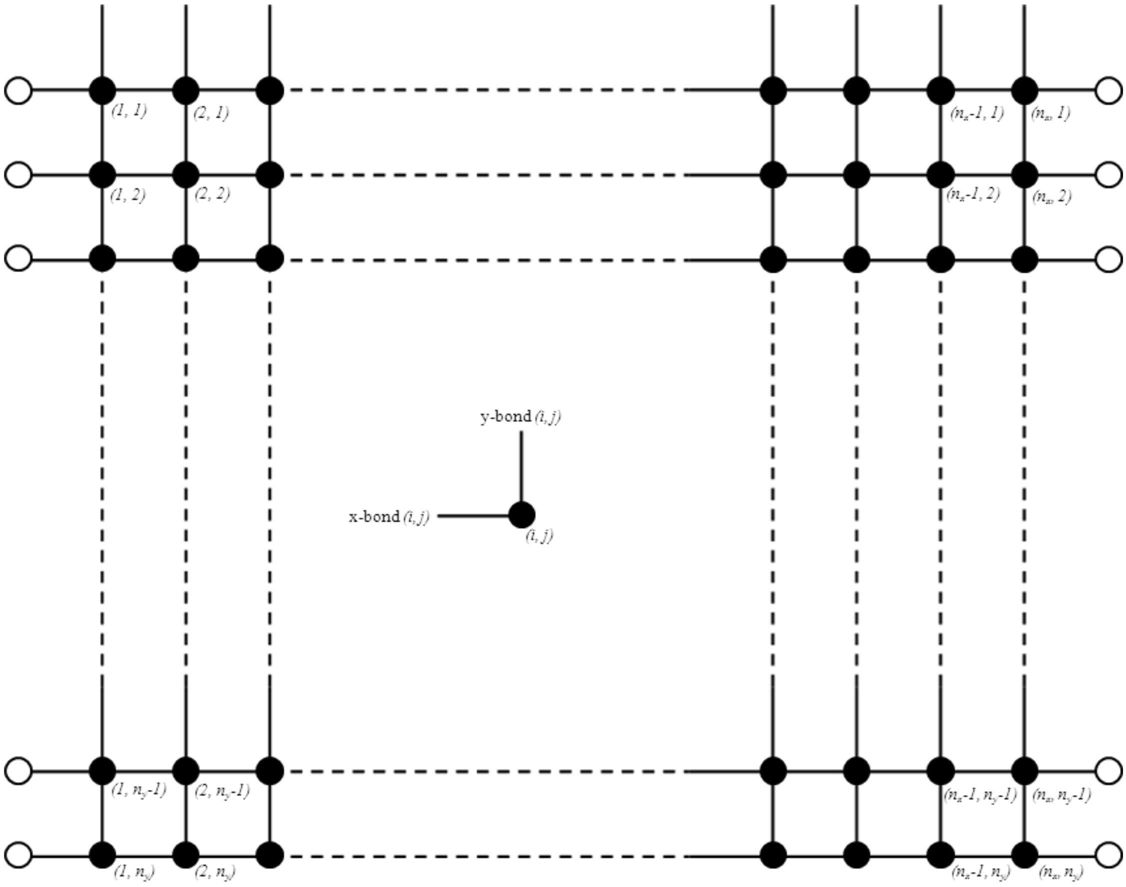

Figure A.1: Two-dimensional schematic showing the basic network model structure, and rationale of the bond and node labelling. The nodal dimensions of the network are n_x x n_y (i.e. $n_z = 1$, and z-bonds neglected for clarity).

≤ 0.5 to prevent bonds crossing; for all simulations in this work we chose $\alpha = 0.35$. Thus, whilst the global structure of the network remains intact, the bonds of the network now exhibit a variety of lengths.

A.2. Flow Calculation

The calculation of flow in the simulated vessel networks proceeds on the basis of mass conservation, by assuming that all of the individual flows in and out of each node at each time step must sum up to zero. Allowing the subscript *a,b* to denote a bond connecting adjacent nodes *a* and *b*, then the flows at each nodal point *a* must satisfy:

$$\sum_{b=1}^{6} Q_{a,b} = 0,\ \left(a = 1, 2, \dots, n_x n_y n_z\right). \tag{A.1}$$

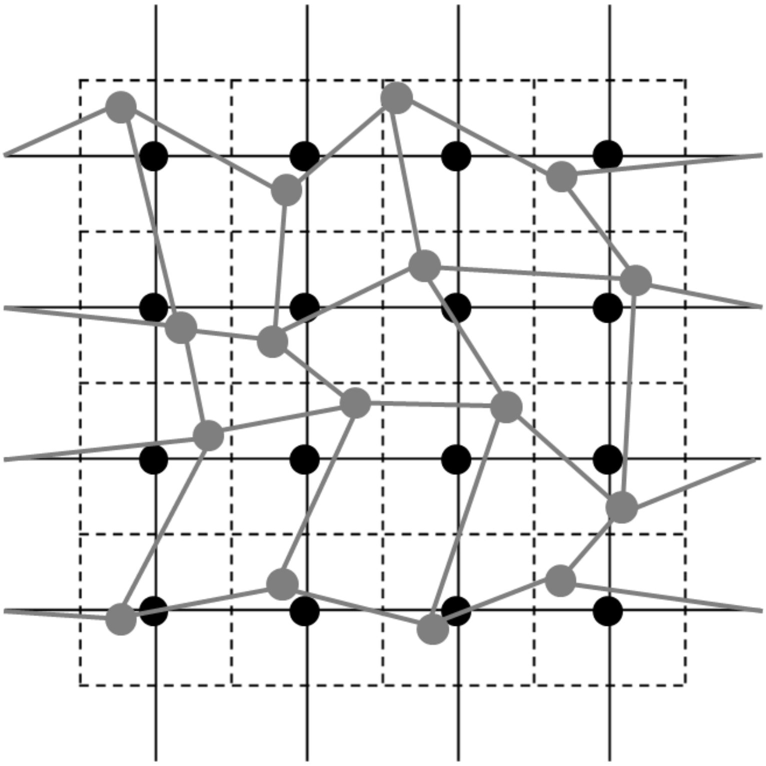

Figure A.2: Two-dimensional schematic of a distorted network structure. Each node has been displaced from its original position *(i, j)* to a new position $(i + \varepsilon_i, j + \varepsilon_j)$ where the ε are random numbers selected uniformly from the interval *[-0.5, 0.5]*. Note that the positions of the inlet and outlet "nodes" remain fixed.

Assuming that Poiseuille's law holds in each individual bond, we also have:

$$Q_{a,b} = \frac{\pi \cdot {R_{a,b}}^4 \cdot \Delta P_{a,b}}{8 \cdot \eta_{a,b} \cdot L_{a,b}}, \tag{A.2}$$

where $\Delta P_{a,b} = P_a - P_b$ is the pressure difference across the bond, $R_{a,b}$ the radius of the bond, $L_{a,b}$ the length of the bond and $\eta_{a,b}$ the apparent viscosity of the blood in the bond. Given that $R_{a,b}$, $L_{a,b}$ and $\eta_{a,b}$ have known values at any one time, the expressions in Equation A.2 can be appropriately substituted into Equation A.1 to produce a linear system of $n_x n_y n_z$ equations relating the pressures at each node of the network. Throughout this work, the sparse linear system of pressure equations has been solved iteratively using successive over-relaxation (SOR).

It is clear from this explanation that solution of the pressure equations requires consideration of all nodes and bonds in the network model. For a given vessel network, however, not all bonds will correspond to capillary vessels. Therefore, we assign to each of these non-capillary bonds a negligible conductance (i.e. assume it is filled with a fluid of arbitrarily large viscosity), and the overall pressure solution can be calculated as detailed.

In addition, unique solution of the pressure equations also requires the assignment of appropriate boundary conditions. Fixed pressures (P_{in} and P_{out}) are set at each respective inlet and outlet bond of the network. Furthermore, periodic boundary conditions are imposed on the x-y and x-z boundaries. This assumption has no appreciable impact on any of our results, since the bonds at these boundaries never become capillaries and maintain negligible conductance throughout.

Finally, in order to ensure that mass conservation continues to be observed throughout simulation, we must impose a restriction on the flow time step. The volume of fluid leaving a bond at any time step (i.e. $Q\Delta t$) cannot be allowed to exceed the volume of fluid contained instantaneously within that bond (i.e. $\pi R^2 L$). Therefore, the (adaptive) time step size is calculated to be:

$$\Delta t = \min\left(\frac{\pi R^2 L}{Q}\right), \tag{A.3}$$

where we consider all bonds in the network.

A.3. Discrete Cell Migration

In our simulations, both individual ECs and astrocytes are assumed to occupy individual bonds of the network model; subsets of these cells are the so-called tip-cells that constitute the growing front of the cellular structures. The unconnected end of such a bond thus lies at a particular node of the network, and migration occurs by subsequent movement to an adjacent node. The hybrid PDE-discrete approach to this migration involves the discretisation of a PDE describing the cell behaviour at a macroscopic level, and derivation of a set of movement weightings that determine the likelihood of an individual cell to remain stationary (P_0) or move left (P_1), right (P_2), up (P_3) or down (P_4) on a two-dimensional network lattice (Figure A.3).

The relevant PDEs were discretised using the following representative finite

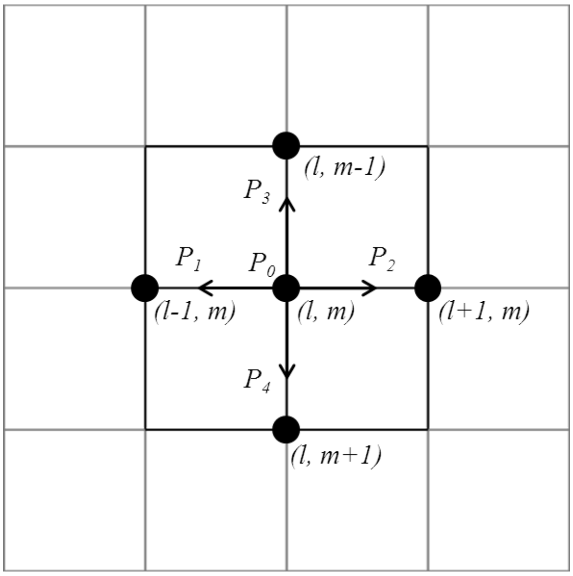

Figure A.3: Schematic diagram showing the rationale of cell movement in the angiogenesis model. A cell located at position *(l, m)* can either move to one of the four orthogonal neighbouring nodes (characterised by the respective weightings P_1, P_2, P_3 and P_4) or remain stationary (characterised by P_0). Note that, in practice, it is in fact the cell tip that lies at *(l, m)*, and the cell itself occupies one of the four connected bonds; the appropriate weighting is therefore set to zero so the cell cannot grow back on itself.

difference formulae (A is an arbitrary variable):

$$\frac{\partial A}{\partial t} = \frac{A_{l,m}^{q+1} - A_{l,m}^{q}}{\Delta t}, \tag{A.4}$$

$$\frac{\partial A}{\partial x} = \frac{A_{l+1,m}^{q} - A_{l-1,m}^{q}}{2\Delta x}, \tag{A.5}$$

$$\frac{\partial A}{\partial y} = \frac{A_{l,m+1}^{q} - A_{l,m-1}^{q}}{2\Delta y}, \tag{A.6}$$

$$\frac{\partial^2 A}{\partial x^2} = \frac{A_{l+1,m}^{q} - 2A_{l,m}^{q} + A_{l-1,m}^{q}}{(\Delta x)^2}, \tag{A.7}$$

$$\frac{\partial^2 A}{\partial y^2} = \frac{A_{l,m+1}^{q} - 2A_{l,m}^{q} + A_{l,m-1}^{q}}{(\Delta y)^2}, \tag{A.8}$$

where l and m characterise the spatial discretisations in the x- and y-directions, respectively, and q denotes the discretisation of time. Note, in addition, that $\Delta x = 1/n_x$

and $\Delta y = 1/n_y$. Upon rearrangement of the appropriately discretised expression, we have an equation of the form:

$$A_{l,m}^{q+1} = P_0 A_{l,m}^{q} + P_1 A_{l-1,m}^{q} + P_2 A_{l+1,m}^{q} + P_3 A_{l,m-1}^{q} + P_4 A_{l,m+1}^{q}, \quad \text{(A.9)}$$

The movement direction of an individual tip-cell is then determined by the following procedure:

1. The coefficient characterising growth of a sprout back on itself is set to zero.
2. Any negative coefficients are set to zero and the absolute value is added to the directly opposing coefficient.
3. Calculate the sum of all coefficient values, $P_{tot} = P_0 + P_1 + P_2 + P_3 + P_4$.
4. Normalise the coefficients such that they sum to unity (i.e. $P_0^* = P_0/P_{tot}$ etc.).
5. Define the five ranges $[R_0, S_0]$, $[R_1, S_1]$, $[R_2, S_2]$, $[R_3, S_3]$ and $[R_4, S_4]$ by the equations:

$$\begin{aligned} &R_0 = 0,\ S_0 = P_0^*, \\ &R_j = S_{j-1},\ S_j = S_{j-1} + P_j^*,\ j = 1,2,3,4. \end{aligned} \quad \text{(A.10)}$$

6. Generate a random number between 0 and 1, then move the cell tip according to the range in which the number falls.

A.4. Growth Factors, ECM Components and MMPs

Taking advantage of the basic network model structure, the various continuum representations of growth factor concentration, matrix density and MMP concentration are spatially discretised such that their values are updated at the nodes of the network (Figure A.4). The equations absent of diffusive terms were solved at each time step by using a time derivative discretisation equivalent to that given in Equation A.4. The more involved solution of those equations containing diffusive terms was instead performed using the Alternate Direction Implicit (ADI) method. For an n-dimensional domain (n = 2 or 3), this method proceeds by splitting each time step Δt into n distinct intervals of equal length (i.e. $\Delta t/n$). Over the first interval, each node is visited and the

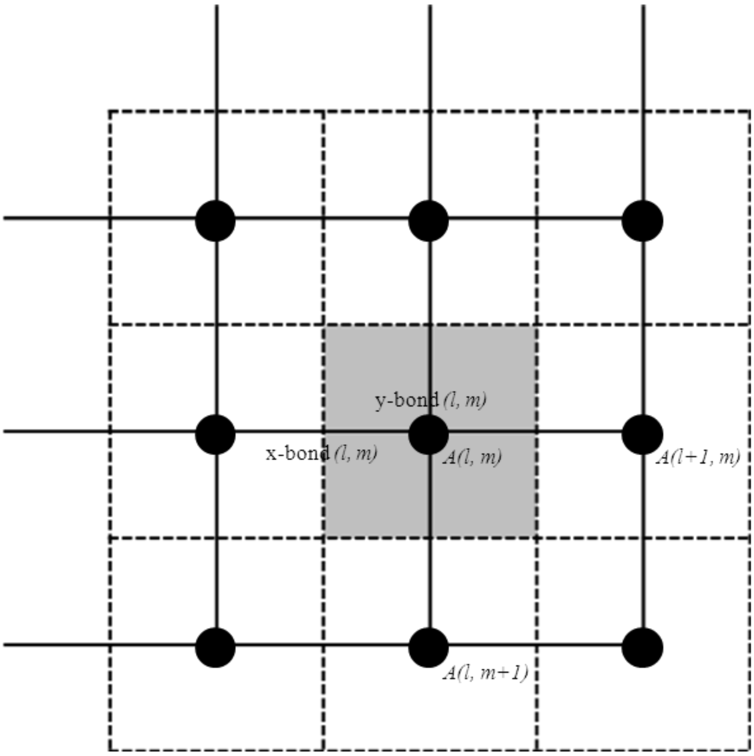

Figure A.4: Two-dimensional schematic of the spatial discretisation applied for calculating the growth factor concentrations, ECM densities and MMP concentrations (arbitrarily represented by *A* here) in the angiogenesis model. Note that the grid values of these variables lie in identical positions to the nodes of the basic network structure.

PDE is discretised implicitly in one direction (i.e. x-direction) and explicitly in the remaining *n-1* directions (i.e. y-direction or y- and z-directions). The explicit discretisation is performed using expressions equivalent to Equations A.7 and A.8, while the implicit discretisation corresponds to the Crank-Nicolson method (given for the x-direction in a two-dimensional domain):

$$\frac{\partial^2 A}{\partial x^2} = \frac{\left(A_{l+1,m}^{q+1} - 2A_{l,m}^{q+1} + A_{l-1,m}^{q+1}\right) + \left(A_{l+1,m}^{q} - 2A_{l,m}^{q} + A_{l-1,m}^{q}\right)}{2(\Delta x)^2}. \tag{A.9}$$

These assumptions ultimately lead to a tri-diagonal system of linear equations, which are solved by the Thomas Algorithm and the variable updated at each node. This process is then repeated a further *n-1* times, where a new space direction is subject to the implicit discretisation on each occasion, until a full time step *Δt* has elapsed.

A.5. Oxygen Transport

Here we highlight that the scheme of spatial discretisation for obtaining the oxygen solution is different to that used for the other continuous variables. Given that oxygen is delivered from the vessels (i.e. bonds) to the extracellular tissue (i.e. voids in between), it is somewhat simpler to define grid points for the tissue oxygen solution in the manner shown in Figure A.5.

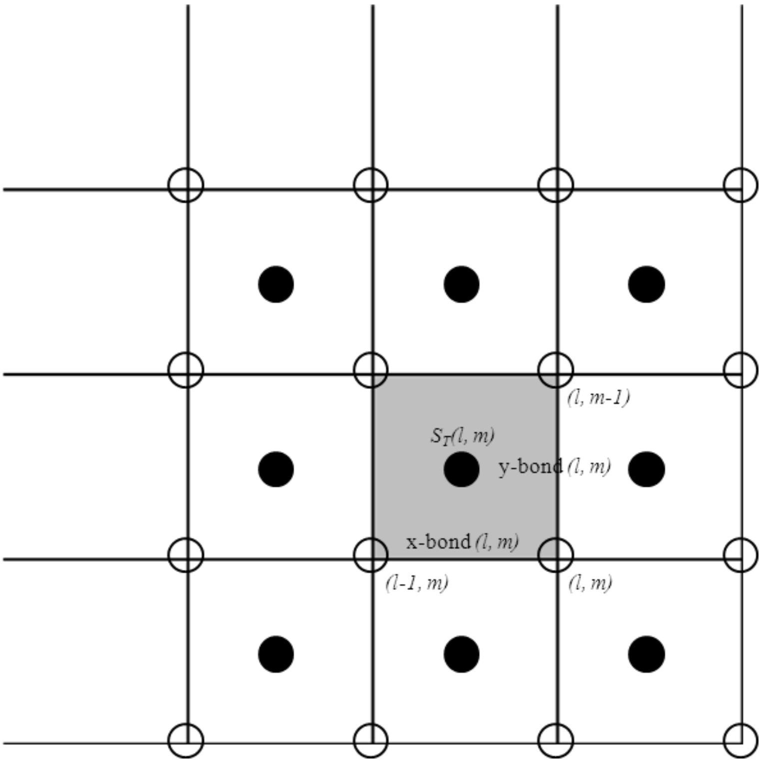

Figure A.5: Two-dimensional schematic of the spatial discretisation applied for calculating the tissue oxygen concentration S_T in the angiogenesis model. The black circles represent the discretised grid value positions of S_T, whilst the clear circles represent the nodes of the basic network structure. Note that each tissue block is bounded by four potential vessel sources (becoming twelve in the three-dimensional analogue), and the surface of each vessel source shares an interface with two tissue blocks (becoming four in the three-dimensional analogue).

Once again, the reaction-diffusion system describing the evolution of oxygen concentration is solved using a combination of the ADI method and the Thomas Algorithm. A fixed time step for solution of these coupled equations is chosen in order to ensure that, throughout simulation, mass is conserved in all tissue blocks and all capillary vessels.

Appendix B

Numerical Implementation of the Cell Migration Model

Here we provide some additional details regarding the numerical implementation and solution of the cell migration model. In particular, we focus only on aspects of the model that were borne out in the simulations performed (e.g. we provide no further details regarding modification of the fibrous matrix). Once again, all solution techniques utilised throughout this work have been coded in the C++ programming language.

B.1. Model Set-Up and Discrete-Continuum Interpolation

The two-dimensional simulation domain for the cell migration model is designed in a manner that allows simple interpolation between the movement of the discrete off-lattice cells and the continuum representations of collagen matrix and chemoattractant concentration. The continuum variables are discretised spatially on a n_x x n_y grid, and the values of the Cartesian co-ordinate system (x, y) describing the cell positions coincide identically with the integer labelling system (l, m) at the grid block centres (Figure B.1). Although the dimensional domain size was varied throughout, all simulations in this thesis were performed on a square domain with $n_x = n_y = 100$.

At each grid point (l, m) we assign appropriate values defining the collagen

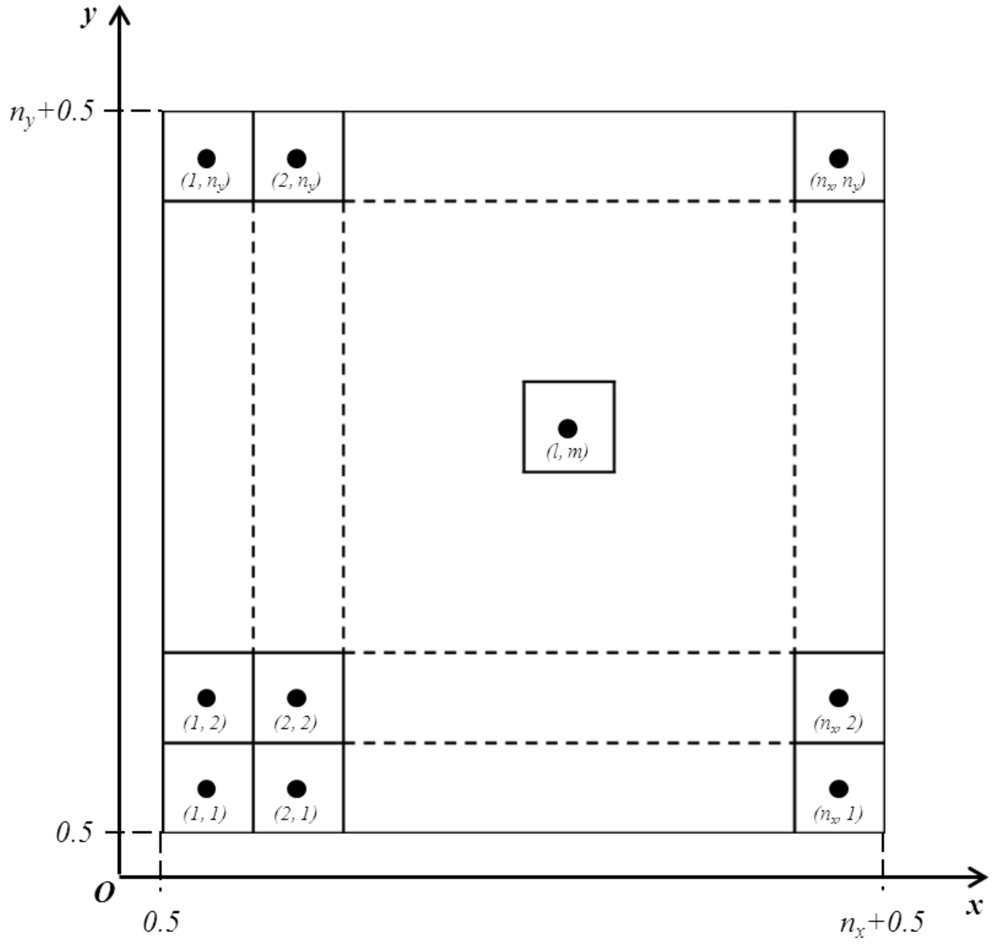

Figure B.1: Schematic diagram showing the set-up of the simulation domain for the cell migration model. Note that the values of the Cartesian co-ordinate system *(x, y)*, describing the cell positions, coincide numerically with the discretised grid block values *(l, m)* representing the continuum variables.

orientation, the collagen density, the chemoattractant concentration and the chemoattractant gradient. In order to solve the equations governing cell speed and migration direction, however, we must quantify these variables in the Cartesian co-ordinate system *(x, y)*. Therefore, for each integer-valued grid point *(l, m)* we define the following interpolation function:

$$X(x,y) = X^*(l,m), \text{ where } x \in (l-0.5, l+0.5] \text{ and } y \in (m-0.5, m+0.5]. \qquad \text{(B.1)}$$

Here, X arbitrarily represents any one of the above variables in the Cartesian system, and X^* is its discrete analogue defined only at grid points. Importantly, this function asserts that, at each time step, each cell will only be influenced by the properties of the collagen matrix and chemoattractant profile within the grid block containing its centroid $\boldsymbol{f}^{i}(t)$.

One further clarification must also be made regarding the implementation of contact guidance (c.f. Equation 5.11). When the persistent-random walk component of cell directionality $\boldsymbol{v}^{i}_{a,r}(t)$ is weighted against the matrix-associated component $\boldsymbol{v}^{i}_{c,b}(t)$, it should be noted that $\boldsymbol{v}^{i}_{c,b}(t)$ is assumed to be bi-directional. This stipulates that the resultant vector $\boldsymbol{v}^{i}_{(a,r),(c,b)}$ is always directed towards the acute angle between these two components. Hence, the cell migration direction can never be "reversed" by the fibrous matrix.

B.2. Finite Difference Approximations

Calculating the evolving cell positions and morphologies during simulations requires the approximation of a number of spatial and temporal derivatives. All temporal derivatives (e.g. update of cell positions) were represented by the following finite difference approximation:

$$\frac{\partial X}{\partial t} = \frac{X^{q+1} - X^{q}}{\Delta t}, \tag{B.2}$$

where X again represents an arbitrary variable, Δt is the time step, and q denotes the discretisation of time. Furthermore, all spatial derivatives (e.g. calculation of the chemoattractant gradient) were approximated by the following equations:

$$\frac{\partial X}{\partial x} = \frac{X_{l+1,m} - X_{l,m}}{\Delta x}, \tag{B.3}$$

$$\frac{\partial X}{\partial y} = \frac{X_{l,m+1} - X_{l,m}}{\Delta y}, \tag{B.4}$$

where Δx and Δy represent the spatial step sizes of the grid discretisation.

B.3. Solid Domain Boundaries

The simulations presented in Sections 5.6.2, 6.3.2 and 6.3.3 were performed under the assumption that the domain boundaries were solid walls that the cells were not permitted to cross. Here, we provide some further details regarding the implementation of these boundary conditions for both spherical and ellipsoidal cells.

B.3.1. Spherical Cells

Although these boundary conditions are implemented for both spherical and ellipsoidal cells using the same algorithm, the spherical case is much simpler and, as such, can be summarised more briefly. The procedure (illustrated graphically in Figure B.2) is as follows:

4. Calculate the cell migration direction $\boldsymbol{u}^i(t)$ and the cell speed $s^i(t)$.
5. Update the cell centroid position $\boldsymbol{f}^i(t)$.
6. Determine whether $\boldsymbol{f}^i(t)$ is less than the cell radius $R^i(t)$ from any of the domain boundaries (N.B. a cell near one of the domain corners may have crossed two boundaries).
7. If so, shift the cell centroid perpendicularly to the appropriate boundary (or boundaries) until the whole cell body is just within the domain.

These assumptions ensure that, rather than exit the domain, cells will generally be forced to migrate along the boundary.

B.3.2. Ellipsoidal Cells

The ellipsoidal cell case becomes rather more complicated due to the elongated nature of the cell body; in this case we assume that any cell which crosses the domain boundary must be repositioned and/or reoriented in order to force migration along, rather than across, the wall. Determining whether or not any part of a particular cell has crossed a domain boundary in the first place, however, requires a non-trivial calculation. In order to make this possible, we must determine the left-, right-, lower- or upper-most extreme of the cell boundary. For this purpose, we parameterise the cell boundary $\boldsymbol{x}^i(r) = (x^i(r), y^i(r))$ using the following equations:

$$x^i(r) = f_x^i + A^i \cos(\varphi^i)\cos(r) - B^i \sin(\varphi^i)\sin(r), \tag{B.5}$$

$$y^i(r) = f_y^i + A^i \sin(\varphi^i)\cos(r) - B^i \cos(\varphi^i)\sin(r), \tag{B.6}$$

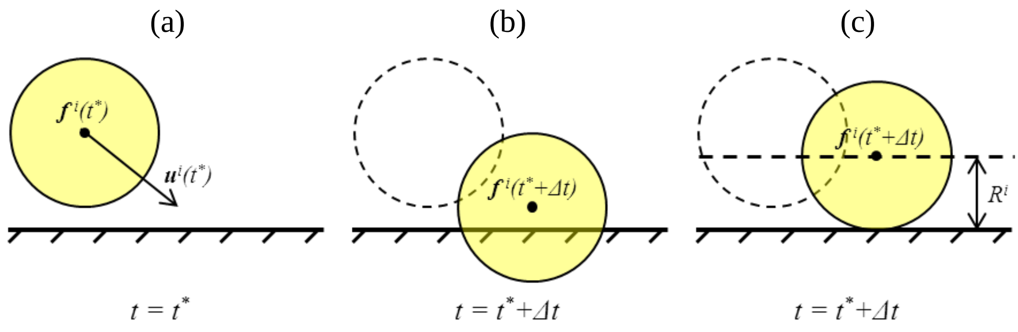

Figure B.2: Schematic diagram illustrating the implementation of solid domain boundaries in the case of spherical cells: (a) at $t = t^*$, the cell is inside the domain but is migrating towards the boundary; (b) after a time step Δt, some of the cell body has crossed the domain boundary; (c) hence, before the next time step, the cell is shifted in a direction perpendicular to the boundary until its body is just touching the wall.

where $r \in (0, 2\pi]$ is the parameter, $\boldsymbol{f}^i = (f_x^i, f_y^i)$ is the position of the cell centroid, and $\varphi^i \in (-\pi/2, \pi/2)$ is the angle of orientation of the cell's major axis with respect to the horizontal. The desired quantities (x^i_{min}, x^i_{max}, y^i_{min} and y^i_{max}) are then found by identifying the stationary points of these expressions and eliminating r to give:

$$x^i_{min/max} = f^i_x \pm \frac{{A^i}^2\cos(\varphi^i)+{B^i}^2\sin(\varphi^i)\tan(\varphi^i)}{\sqrt{{A^i}^2+{B^i}^2\tan^2(\varphi^i)}}, \tag{B.7}$$

$$y^i_{min/max} = f^i_y \pm \frac{{B^i}^2\cos(\varphi^i)+{A^i}^2\sin(\varphi^i)\tan(\varphi^i)}{\sqrt{{B^i}^2+{A^i}^2\tan^2(\varphi^i)}}. \tag{B.8}$$

If any of these four cell extremities lie beyond the domain boundary, it is then clear that the cell position $\boldsymbol{f}^i(t)$ and/or the cell orientation $\boldsymbol{p}^i(t)$ must be modified. Unlike the spherical case, however, it is necessary to implement this modification by an iterative process. The procedure is as follows:

1. Calculate the cell migration direction $\boldsymbol{u}^i(t)$ and the cell speed $s^i(t)$.
2. Update the cell centroid position $\boldsymbol{f}^i(t)$.
3. Use Equations B.5 – B.8 to determine whether any part of the cell body has crossed a domain boundary.
4. If two boundaries have been crossed, shift the cell centroid perpendicularly to the appropriate boundaries until the whole cell body is just within the domain.

Alternatively, if only one boundary has been crossed and the cell centroid is less than the cell semi-minor radius $B^i(t)$ from this boundary, shift the cell centroid perpendicularly inwards until it is no closer than $B^i(t)$.

5. If the cell remains outside the domain, there are two alternatives:
   i. If the cell is oriented towards the boundary, increment the cell orientation $\boldsymbol{p}^i(t)$ a small amount away from the boundary. A cell initially oriented perpendicular to the boundary is randomly rotated in one of the two directions.
   ii. If the cell is oriented away from the boundary, the cell centroid is shifted perpendicular to the boundary until the whole cell body lies within the domain.
6. Iterate steps 3-5 until the whole cell body lies within the domain (i.e. a cell may not yet have been rotated sufficiently, or the rotation may have caused crossing of a second boundary).
7. If the number of iterations exceeds the maximum number n_{max}, reverse the cell orientation (i.e. the cell must be "stuck" in a corner of the domain).

A simple example illustrating the rationale of this process is shown in Figure B.3.

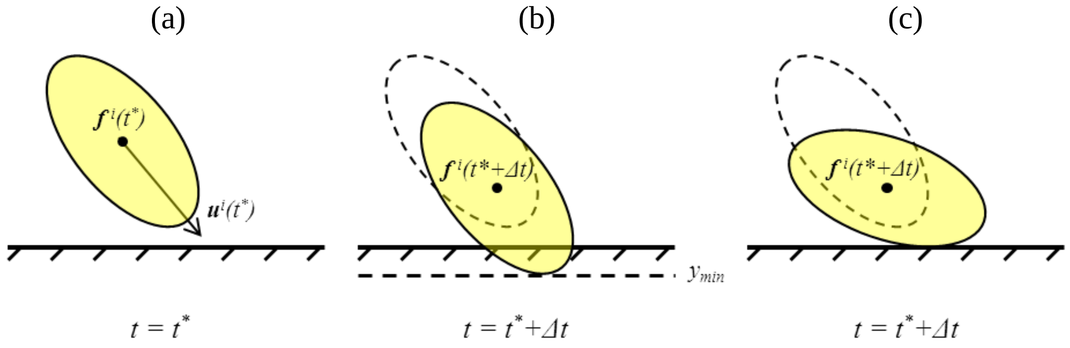

Figure B.3: Schematic diagram illustrating a typical example of the implementation of solid domain boundaries in the case of ellipsoidal cells: (a) at $t = t^*$, the cell is inside the domain but is migrating towards the boundary; (b) after a time step Δt, the lower-most extremity of the cell y_{min} lies beneath the boundary; (c) hence, before the next time step, the cell is incrementally rotated until y_{min} is coincident with the wall.

References

Abercrombie M., 1980, The crawling movement of metazoan cells, *Proc. R. Soc. London B*, **207**, 129-147.

Alarcon T., Byrne H.M. & Maini P.K., 2003, A cellular automaton model for tumour growth in inhomogeneous environment, *J. Theor. Biol.*, **225**, 257-274.

Alarcon T., Byrne H.M. & Maini P.K., 2005a, A multiple scale model for tumor growth, *Multiscale Model. Simul.*, **3**, 440-475.

Alarcon T., Byrne H.M. & Maini P.K., 2005b, A design principle of vascular beds: the effects of complex blood rheology, *Microvasc. Res.*, **69**, 156-172.

Alarcon T., Owen M.R., Byrne H.M. & Maini P.K., 2006, Multiscale modelling of tumour growth and therapy: the influence of vessel normalisation on chemotherapy, *Comput. Math. Methods Med.*, **7**, 85-119.

Alberts B., Bray D., Lewis J., Raff M., Roberts K. & Watson J.D., 2002, Molecular Biology of the Cell 4th Edition, Garland, New York.

Albrecht K.H., Gaehtgens P., Pries A.R. & Heuser M., 1979, The Fahraeus effect in narrow capillaries (i.d. 3.3 to 11.0 μm), *Microvasc. Res.*, **18**, 33-47.

Alon T., Hemo I., Itin A., Pe'er J., Stone J. & Keshet E., 1995, Vascular endothelial growth factor acts as a survival factor for newly formed retinal vessels and has implications for retinopathy of prematurity, *Nat. Med.*, **1**, 1024–1028.

Anderson A.R.A. & Chaplain M.A.J., 1998a, A mathematical model for capillary network formation in the absence of endothelial cell proliferation, *Appl. Math. Lett.*, **3**, 109-114.

Anderson A.R.A. & Chaplain M.A.J., 1998b, Continuous and discrete mathematical models of tumor-induced angiogenesis, *Bull. Math. Biol.*, **60**, 857-899.

Anderson A.R.A., Chaplain M.A.J., Newman E.L., Steele R.J.C. & Thompson A.M., 2000, Mathematical modelling of tumour invasion and metastasis, *J. Theor. Med.*, **2**, 129-154.

Anderson A.R.A., 2005, A hybrid mathematical model of solid tumour invasion: the importance of cell adhesion, *Math. Med. Biol.*, **22**, 163-186.

Armstrong N.J., Painter K.J. & Sherratt J.A., 2006, A continuum approach to modelling cell-cell adhesion, *J. Theor. Biol.*, **243**, 98-113.

Arnold F. & West D.C., 1991, Angiogenesis in wound healing, *Pharmacol. Ther.*, **52**, 407-422.

Ash J.D. & Overbeek P.A., 2000, Lens-specific VEGF-A expression induces angioblast migration and proliferation and stimulates angiogenic remodelling, *Dev. Biol.*, **223**, 383-398.

Aubert M., Chaplain M.A.J., McDougall S.R., Devlin A. & Mitchell C.A., 2011, A continuous mathematical model of the developing murine retinal vasculature, *Bull. Math. Biol.*, **73**, 2430-2451.

Balding D. & McElwain D.L.S., 1985, A mathematical model of tumour-induced capillary growth, *J. Theor. Biol.*, **114**, 53-73.

Barbee J.H. & Cokelet G.R., 1971, The Fahraeus effect, *Microvasc. Res.*, **3**, 6-16.

Bauer A., Jackson T.L. & Jiang Y., 2007, A cell-based model exhibiting branching and anastomosis during tumour-induced angiogenesis, *Biophys. J.*, **92**, 3105-3121.

Bayliss L.E., 1959, The axial drift of the red cells when blood flows in a narrow tube, *J. Physiol. (Lond.)*, **149**, 593-613.

Bentley K., Gerhardt H. & Bates P.A., 2008, Agent-based simulation of notch-mediated tip cell selection in angiogenic sprout initialisation, *J. Theor. Biol.*, **250**, 25-36.

Bentley K., Mariggi G., Gerhardt H. & Bates P.A., 2009, Tipping the balance: robustness of tip cell selection, migration and fusion in angiogenesis, *PLoS Comput. Biol.*, **5**(10), e1000549.

Beyer T., Meyer-Hermann M. & Soff G., 2002, A possible role of chemotaxis in germinal center formation, *Int. Immunol.*, **14**, 1369-1381.

Block M., Scholl E. & Drasdo D., 2007, Classifying the expansion kinetics and critical surface dynamics of growing cell populations, *Phys. Rev. Lett.*, **99**, 248101.

Bluff J.E., O'Ceallaigh S., O'Kane S., Ferguson M.W. & Ireland G., 2006, The microcirculation in acute murine cutaneous incisional wounds shows a spatial and temporal variation in the functionality of vessels, *Wound Rep. Reg.*, **14**, 434-442.

Bosgraaf L. & Van Haastert P.J.M., 2009, The ordered extension of pseudopodia by amoeboid cells in the absence of external cues, *PLoS One*, **4**, e5253.

Bozukova D., Pagnoulle C., Jerome R. & Jerome C., 2010, Polymers in modern ophthalmic implants – historical background and recent advances, *Mater. Sci. Eng. R*, **69**, 63-83.

Bray D., 2001, Cell Movements: From Molecules to Motility 2nd Edition, Garland, New York.

Brodland G.W. & Veldhuis J.H., 2002, Computer simulations of mitosis and interdependencies between mitosis orientation, cell shape and epithelia reshaping, *J. Biomech.*, **35**, 673-681.

Byrne H.M. & Chaplain M.A.J., 1995, Explicit solutions of a simplified model of capillary sprout growth during angiogenesis, *Appl. Math. Lett.*, **9**, 69-74.

Byrne H. & Drasdo D., 2009, Individual-based and continuum models of growing cell populations: a comparison, *J. Math. Biol.*, **58**, 657-687.

Cai A.Q., Landman K.A. & Hughes B.D., 2007, Multi-scale modelling of a wound-healing cell migration assay, *J. Theor. Biol.*, **245**, 576-594.

Cai Y., Xu S., Wu J. & Long Q., 2011, Coupled modelling of tumour angiogenesis, tumour growth and blood perfusion, *J. Theor. Biol.*, **279**, 90-101.

Cardinal M., Eisenbud D.E., Phillips T. & Harding K., 2008, Early healing rates and wound area measurements are reliable predictors of later complete wound closure, *Wound Rep. Reg.*, **16**, 19-22.

Carmeliet P. & Jain R.K., 2000, Angiogenesis in cancer and other diseases, *Nature*, **407**, 249-257.

Carr R.T. & Wickham L.L., 1991, Influence of vessel diameter on red cell distribution at microvascular bifurcations, *Microvasc. Res.*, **41**, 184-196.

Cenni E., 2005, Angiogenesis and bone regeneration, *J. Bone Joint Surg.*, **87B**, 58.

Chaplain M.A.J. & Stuart A.M., 1993, A model mechanism for the chemotactic response of endothelial cells to tumour angiogenesis factor, *IMA J. Math. App. Med. Biol.*, **10**, 149-168.

Chaplain M.A.J. & Byrne H.M., 1996, Mathematical modelling of wound healing and tumor growth: two sides of the same coin, *Wounds: Compend. Clin. Res. Pract.*, **8**, 42-48.

Chaudhry H.R., Bukiet B., Siegel M., Findley T., Ritter A.B. & Guzelsu N., 1998, Optimal patterns for suturing wounds, *J. Biomech.*, **31**, 653-662.

Checa S. & Prendergast P.J., 2008, A mechanobiological model for tissue differentiation that includes angiogenesis: a lattice-based modelling approach, *Ann. Biomed. Eng.*, **37**, 129-145.

Chraibi M., Seyfried A. & Schadschneider A., 2010, Generalized centrifugal-force model for pedestrian dynamics, *Phys. Rev. E*, 046111.

Clark R.A.F., 1996, Wound repair: overview and general consideration. In: Clark R.A.F., ed., The Molecular and Cellular Biology of Wound Repair 2nd Edition, New York, Plenum Press, 3-35.

Claviez M., Brink M. & Gerisch G., 1986, Cytoskeletons from a mutant of *Dictyostelium discoideum* with flattened cells, *J. Cell Sci.*, **86**, 69-82.

Claxton S. & Fruttiger M., 2003, Role of arteries in oxygen induced vaso-obliteration, *Exp. Eye Res.*, **77**, 305-311.

Cobbold C.A. & Sherratt J.A., 2000, Mathematical modelling of nitric oxide activity in wound healing can explain keloid and hypertrophic scarring, *J. Theor. Biol.*, **204**, 257-288.

Cringle S.J., Yu D., Yu P.K. & Su E., 2002, Intraretinal oxygen consumption in the rat in vivo, *Invest. Ophtalmol. Vis. Sci.*, **43**, 1922-1927.

Cringle S.J., Yu P.K., Su E. & Yu D., 2006, Oxygen distribution and consumption in the developing rat retina, *Invest. Ophtalmol. Vis. Sci.*, **47**, 4072-4076.

Cumming B.D., McElwain D.L.S. & Upton Z., 2010, A mathematical model of wound healing and subsequent scarring, *J. R. Soc. Interface*, **7**, 19-34.

Dale P.D., Maini P.K. & Sherratt J.A., 1994, Mathematical modelling of corneal epithelial wound healing, *Math. Biosci.*, **124**, 127-147.

Dale P.D., Sherratt J.A. & Maini P.K., 1996, A mathematical model for collagen fibre formation during foetal and adult dermal wound healing, *Proc. R. Soc. Lond. B*, **263**, 653-660.

Dale P.D., Sherratt J.A. & Maini P.K., 1997, Role of fibroblast migration in collagen fiber formation during fetal and adult dermal wound healing, *Bull. Math. Biol.*, **59**, 1077-1100.

Dallon J.C., Sherratt J.A. & Maini P.K., 1999, Mathematical modelling of extracellular matrix dynamics using discrete cells: fiber orientation and tissue regeneration, *J. Theor. Biol.*, **199**, 449-471.

Dallon J., Sherratt J., Maini P. & Ferguson M., 2000, Biological implications of a mathematical model for collagen deposition and alignment in dermal wound repair, *IMA J. Math. Med. Biol.*, **17**, 379-393.

Dallon J.C., Sherratt J.A. & Maini P.K., 2001, Modeling the effects of transforming growth factor-β on extracellular matrix alignment in dermal wound repair, *Wound Rep. Reg.*, **9**, 278-286.

Dallon J.C. & Othmer H.G., 2004, How cellular movement determines the collective force generated by the Dictyostelium discoideum slug, *J. Theor. Biol.*, **231**, 203-222.

Davies M.H., Stempel A.J., Hubert K.E. & Powers M.R., 2010, Altered vascular expression of EphrinB2 and EphB4 in a model of oxygen-induced retinopathy, *Dev. Dyn.*, **239**, 1695-1707.

Davis G.E., Pintar Allen K.A., Salazar R. & Maxwell S.A., 2000, Matrix metalloproteinase-1 and -9 activation by plasmin regulates a novel endothelial cell-mediated mechanism of collagen gel contraction and capillary tube regression in three-dimensional collagen matrices, *J. Cell Sci.*, **114**, 917-930.

Davis J.M. & Pozrikidis C., 2011, Numerical simulation of unsteady blood flow through capillary networks, *Bull. Math. Biol.*, **73**, 1857-1880.

Dor Y., Porat R. & Keshet E., 2001, Vascular endothelial growth factor and vascular adjustments to perturbations in oxygen homeostasis, *Am. J. Physiol. Cell Physiol.*, **280**, 1367-1374.

Dorrell M.I., Aguilar E. & Friedlander M., 2002, Retinal vascular development is mediated by endothelial filopodia, a preexisting astrocytic template and specific R-cadherin adhesion, *Invest. Ophtalmol. Vis. Sci.*, **43**, 3500-3510.

Dorrell M.I., Aguilar E., Jacobson R., Trauger S.A., Friedlander J., Siuzdak G. & Friedlander M., 2010, Maintaining retinal astrocytes normalizes revascularization and prevents vascular pathology associated with oxygen-induced retinopathy, *Glia*, **58**, 43-54.

Drasdo D., Kree R. & McCaskill J.S., 1995, Monte Carlo approach to tissue-cell populations, *Phys. Rev. E*, **52**, 6635-6657.

Drasdo D. & Forgacs G., 2000, Modeling the interplay of generic and genetic mechanisms in cleavage, blastulation, and gastrulation, *Dev. Dyn.*, **219**, 182-191.

Drasdo D. & Hoehme S., 2003, Individual-based approaches to birth and death in avascular tumors, *Math. Comput. Model.*, **37**, 1163-1175.

Dullien F.A.L., 1992, Porous Media, Fluid Transport and Pore Structure 2nd Edition, New York, Academic Press Inc.

Ehrlich P.H. & Krummel T.M., 1996, Regulation of wound healing from a connective tissue perspective, *Wound Rep. Reg.*, **4**, 203-210.

Enden G. & Popel A.S., 1994, A numerical study of plasma skimming in small vascular bifurcations, *J. Biomech. Eng.*, **119**, 79-88.

Erber R., Eichelsbacher U., Powajbo V., Korn T., Djonov V., Lin J., Hammes H.P., Grobholz R., Ullrich A. & Vajkoczy P., 2006, EphB4 controls blood vascular morphogenesis during postnatal angiogenesis, *Embo. J.*, **25**, 628-641.

Evans W.H., de Vuyst E. & Leybaert L., 2006, The gap junction cellular internet: connexin hemichannels enter the signalling limelight, *Biochem. J.*, **397**, 1-14.

Evans W.H., Bultynck G. & Leybaert L., 2012, Manipulating connexin communication channels: use of peptidomimetics and the translational outputs, *J. Membrane Biol.*, **245**, 437-449.

Fahraeus R., 1929, The suspension stability of the blood, *Physiol. Rev.*, **9**, 241-274.

Fahraeus R. & Lindqvist T., 1931, The viscosity of the blood in narrow capillary tubes, *Am. J. Physiol.*, **96**, 562-568.

Fatt I., 1956, The network model of porous media, *Trans. AIME*, **207**, 144.

Fenton B.M., Carr R.T. & Cokelet G.R., 1985, Nonuniform red cell distribution in 20-100 micron bifurcations, *Microvasc. Res.*, **29**, 103-126.

Ferrara N., Houck K., Jakeman L. & Leung D.W., 1992, Molecular and biological properties of the vascular endothelial growth factor family of proteins, *Endocr. Rev.*, **13**, 18-32.

Flegg J.A., McElwain D.L.S., Byrne H.M. & Turner I.W., 2009, A three species model to simulate application of hyperbaric oxygen therapy to chronic wounds, *PLoS Comput. Biol.*, **5**(7), e1000451.

Flegg J.A., Byrne H.M. & McElwain D.L.S., 2010, Mathematical model of hyperbaric oxygen therapy applied to chronic diabetic wounds, *Bull. Math. Biol.*, **72**, 1867-1891.

Flegg J.A., Byrne H.M., Flegg M.B. & McElwain D.L.S., 2012, Wound healing angiogenesis: the clinical implications of a simple mathematical model, *J. Theor. Biol.*, **300**, 309-316.

Folkman J. & Shing Y., 1992, Angiogenesis, *J. Biol. Chem.*, **267**, 10931-10934.

Fomovsky G.M., Rouillard A.D. & Holmes J.W., 2012, Regional mechanics determine collagen fiber structure in healing myocardial infarcts, *J. Mol. Cell. Cardiol.*, **52**, 1083-1090.

Friedman A., Hu B. & Xue C., 2010, Analysis of a mathematical model of ischemic cutaneous wounds, *SIAM J. Math. Anal.*, **42**, 2013-2040.

Friedman A. & Xue C., 2011, A mathematical model for chronic wounds, *Math. Biosci. Eng.*, **8**, 253-261.

Fruttiger M., Calver A.R., Kruger W.H., Mudhar H.S., Michalovich D., Takakura N., Nishikawa S. & Richardson W.D., 1996, PDGF mediates a neuron-astrocyte interaction in the developing retina, *Neuron.*, **17**, 1117-1131.

Fruttiger M., 2002, Development of the mouse retinal vasculature: angiogenesis versus vasculogenesis, *Invest. Ophtalmol. Vis. Sci.*, **43**, 522-527.

Fruttiger M., 2007, Development of the retinal vasculature, *Angiogenesis*, **10**, 77-88.

Fusi L., 2009, Macroscopic models for fibroproliferative disorders: a review, *Math. Comput. Model.*, **50**, 1474-1494.

Gaffney E.A., Maini P.K., Sherratt J.A. & Dale P.D., 1997, Wound healing in the corneal epithelium: biological mechanisms and mathematical models, *J. Theor. Med.*, **1**, 13-23.

Gaffney E.A., Maini P.K., Sherratt J.A. & Tuft S., 1999, The mathematical modelling of cell kinetics in corneal epithelial wound healing, *J. Theor. Biol.*, **197**, 15-40.

Gaffney E.A., Pugh K., Maini P.K. & Arnold F., 2002, Investigating a simple model of cutaneous wound healing angiogenesis, *J. Math. Biol.*, **45**, 337-374.

Galle J., Loeffler M. & Drasdo D., 2005, Modeling the effect of deregulated proliferation and apoptosis on the growth dynamics of epithelial cell populations in vitro, *Biophys. J.*, **88**, 62-75.

Ganesan P., He S. & Xu H., 2010a, Analysis of retinal circulation using an image-based network model of retinal vasculature, *Microvasc. Res.*, **80**, 99-109.

Ganesan P., He S. & Xu H., 2010b, Development of an image-based network model of retinal vasculature, *Ann. Biomed. Eng.*, **38**, 1566-1585.

Ganesan P., He S. & Xu H., 2011, Modelling of pulsatile blood flow in arterial trees of retinal vasculature, *Med. Eng. Phy.*, **33**, 810-823.

Gariano R.F., 2003, Cellular mechanisms in retinal vascular development, *Prog. Retin. Eye Res.*, **22**, 295-306.

Gerhardt H., Golding M., Fruttiger M., Ruhrberg C., Lundkvist A., Abramsson A., Jeltsch M., Mitchell C., Alitalo K., Shima D. & Betsholtz C., 2003, VEGF guides angiogenic sprouting utilizing endothelial tip cell filopodia, *J. Cell Biol.*, **161**, 1163-1177.

Geris L., Gerisch A., Vander Sloten J., Weiner R. & Van Oosterwyck H., 2008, Angiogenesis in bone fracture healing: a bioregulatory model, *J. Theor. Biol.*, **251**, 137-158.

Geris L., Schugart R. & Van Oosterwyck H., 2010, In silico design of treatment strategies in wound healing and bone fracture healing, *Phil. Trans. R. Soc. A*, **368**, 2683-2706.

Gerlee P. & Anderson A.R.A., 2007, Stability analysis of a hybrid cellular automaton model of cell colony growth, *Phys. Rev. E*, **75**, 051911.

Godde R. & Kurz H., 2001, Structural and biophysical simulation of angiogenesis and vascular remodeling, *Dev. Dyn.*, **220**, 387-401.

Goldsmith H.G. & Mason S.G., 1961, Axial migration of particles in Poiseuille flow, *Nature*, **190**, 1095-1096.

Goliger J.A. & Paul D.L., 1995, Wounding alters epidermal connexin expression and gap junction-mediated intercellular communication, *Mol. Biol. Cell*, **6**, 1491-1501.

Gracheva M.E. & Othmer H.G., 2004, A continuum model of motility in ameboid cells, *Bull. Math. Biol.*, **66**, 167-193.

Graner F. & Glazier J.A., 1992, Simulation of biological cell sorting using a two-dimensional Extended Potts model, *Phys. Rev. Lett.*, **69**, 2013-2016.

Griffith E.C., Su Z., Turk B.E., Chen S., Chang Y.H., Wu Z., Biemann K. & Liu J.O., 1997, Methionine aminopeptidase (type 2) is the common target for angiogenesis inhibitors AGM-1470 and ovalicin, *Chem. Biol.*, **4**, 461-471.

Grinnell F., Fibroblasts, myofibroblasts and wound contraction, *J. Cell Biol.*, **124**, 401-404.

Groh A. & Louis A.K., 2010, Stochastic modelling of biased cell migration and collagen matrix modification, *J. Math. Biol.*, **61**, 617-647.

Groh A. & Wagner M., 2011, Biased three-dimensional cell migration and collagen matrix modification, *Math. Biosci.*, **231**, 105-119.

Gross J.D., Peacey M.J. & Trevan D.J., 1976, Signal emission and signal propagation during early aggregation in *Dictyostelium discoideum, J. Cell Sci.*, **22**, 645-656.

Gruionu G., Hoying J.B., Pries A.R. & Secomb T.W., 2005, Structural remodelling of mouse gracilis artery after chronic alteration in blood supply, *Am. J. Physiol. Heart Circ. Physiol.*, **288**, H2047-H2054.

Guerreiro-Lucas L.A., Pop S.R., Machado M.J.C., Ma Y.L., Waters S.L., Richardson G., Saetzler K., Jensen O.E. & Mitchell C.A., 2008, Experimental and theoretical modelling of blind-ended vessels within a developing angiogenic plexus, *Microvasc. Res.*, **76**, 161-168.

Guido S. & Tranquillo R. T., 1993, A methodology for the systematic and quantitative study of cell contact guidance in oriented collagen gels, *J. Cell Sci.*, **105**, 317–331.

Gurtner G.C., Werner S., Barrandon Y. & Longaker M.T., 2008, Wound repair and regeneration, *Nature*, **453**, 314-321.

Hanahan D. & Weinberg R.A., 2000, The hallmarks of cancer, *Cell*, **100**, 57-70.

Hashimoto H. & Prewitt R.L., 1987, Microvascular density changes during wound healing, *Int. J. Microcirc. Clin. Exp.*, **5**, 303-310.

Haugh J.M., 2006, Deterministic model of dermal wound invasion incorporating receptor-mediated signal transduction and spatial gradient sensing, *Biophys. J.*, **90**, 2297-2308.

He S., Prasanna G. & Yorio T., 2007, Endothelin-1-mediated signaling in the expression of matrix metalloproteinases and tissue inhibitors of metalloproteinases in astrocytes, *Invest. Ophthalmol. Vis. Sci.*, **48**, 3737-3745.

Hidalgo M. & Eckhardt S.G., 2001, Development of matrix metalloproteinase inhibitors in cancer therapy, *J. Natl. Cancer Inst.*, **93**, 178-193.

Hogeweg P., 2000, Evolving mechanisms of morphogenesis: on the interplay between differential adhesion and cell differentiation, *J. Theor. Biol.*, **203**, 317-333.

Honda H. & Yoshizato K., 1997, Formation of the branching pattern of blood vessels in the wall of the avian yolk sac studied by a computer simulation, *Dev. Growth Differ.*, **39**, 581-589.

Howard C.V. & Reed M.G., 2005, Unbiased Stereology, BIOS Scientific Publishers, New York.

Hughes G.B. & Chraibi M., 2011, Calculating ellipse overlap areas, arXiv:1106.3787v1 [physics.comp-ph].

Ichioka S., Shibata M., Kosaki K., Sato Y., Harii K. & Kamiya A., 1997, Effects of shear stress on wound-healing angiogenesis in the rabbit ear chamber, *J. Surg. Res.*, **72**, 29-35.

Ingber D., Fujita T., Kishimoto S., Sudo K., Kanamaru T., Brem H., & Folkman J., 1990, Synthetic analogues of fumagillin that inhibit angiogenesis and suppress tumour growth, *Nature*, **348**, 555-557.

Jackson T. & Zheng X., 2010, A cell-based model of endothelial cell migration, proliferation and maturation during corneal angiogenesis, *Bull. Math. Biol.*, **72**, 830-868.

Javierre E., Vermolen F.J., Vuik C. & van der Zwaag S., 2009, A mathematical analysis of physiological and morphological aspects of wound closure, *J. Math. Biol.*, **59**, 605-630.

Jennings R.W. & Hunt T.K., 1991, Overview of postnatal wound healing. In: Adzick N.S. & Longaker M.T., eds., Fetal Wound Healing, New York, Elsevier, 165-178.

Ji J.W., Tsoukias N.M., Goldman D. & Popel A.S., 2006, A computational model of oxygen transport in skeletal muscle for sprouting and splitting modes of angiogenesis, *J. Theor. Biol.*, **241**, 94-108.

Jones M.A., Song B. & Thomas D.M., 2004, Controlling wound healing through debridement, *Math. Comput. Model.*, **40**, 1057-1064.

Karagiannis E.D. & Popel A.S., 2006, Distinct modes of collagen type I proteolysis by matrix metalloproteinase (MMP) 2 and membrane type I MMP during the migration of a tip endothelial cell: insights from a computational model, *J. Theor. Biol.*, **238**, 124-145.

Keyt B.A., Berleau L.T., Nguyen H.V., Chen H., Heinsohn H., Vandlen R. & Ferrara N., 1996, The carboxyl-terminal domain (111-165) of vascular endothelial growth factor is critical for its mitogenic potency, *J. Biol. Chem.*, **271**, 7788-7795.

Klein S.A., Bond S.J., Gupta S.C., Yacoub O.A. & Anderson, G.L., 1999, Angiogenesis inhibitor TNP-470 inhibits murine cutaneous wound healing, *J. Surg. Res.*, **82**, 268-274.

Klitzman B. & Johnson P.C., 1982, Capillary network geometry and red cell distribution in hamster cremaster muscle, *Am. J. Physiol.*, **242**, 211-219.

Lackie J.M., 1986, Cell Movement and Cell Behaviour, Allen & Unwin, London.

Landman K.A., Cai A.Q. & Hughes B.D., 2007, Travelling waves of attached and detached cells in a wound-healing cell migration assay, *Bull. Math. Biol.*, **69**, 2119-2138.

Lapidus I.R. & Schiller R., 1976, Model for the chemotactic response of a bacterial population, *Biophys. J.*, **16**, 779-789.

Lehr H.A., Leunig M., Menger M.D., Nolte D. & Messmer K., 1993, Dorsal skinfold chamber technique for intravital microscopy in nude mice, *Am. J. Pathol.*, **143**, 1055-1062.

Levick J.R., 2000, An Introduction to Cardiovascular Physiology 3rd Edition, Arnold, London.

Levin M., Dawant B. & Popel A.S., 1986, Effect of dispersion on vessel diameters and lengths in stochastic networks. I. Modelling of microvascular haematocrit distribution, *Microvasc. Res.*, **31**, 223-234.

Levine H.A., Sleeman B.D. & Nilsen-Hamilton M., 2000, A mathematical model for the roles of pericytes and macrophages in the initiation of angiogenesis: I. The role of protease inhibitors in preventing angiogenesis, *Math. Biosci.*, **168**, 77-115.

Levine H.A., Sleeman B.D. & Nilsen-Hamilton M., 2001a, Mathematical modelling of the onset of capillary formation initiating angiogenesis, *J. Math. Biol.*, **42**, 195-238.

Levine H.A., Pamuk S., Sleeman B.D. & Nilsen-Hamilton M., 2001b, Mathematical modelling of capillary formation and development in tumour angiogenesis: penetration into the stroma, *Bull. Math. Biol.*, **63**, 801-863.

Li L., Norrelykke S.F. & Cox E.C., 2008, Persistent cell motion in the absence of external signals: a search strategy for eukaryotic cells, *PLoS One*, **3**, e2093.

Lipowsky H.H., Kovalcheck S. & Zweifach B.W., 1978, The distribution of blood rheological parameters in the microcirculation of cat mesentery, *Circ. Res.*, **43**, 738-749.

Lipowsky H.H., Usami S. & Chien S., 1980, In vivo measurements of "apparent viscosity" and microvessel hematocrit in the mesentery of the cat, *Microvasc. Res.*, **19**, 297-319.

Liu D., Wood N.B., Witt N., Hughes A.D., Thom S.A. & Xu X.Y., 2009, Computational analysis of oxygen transport in the retinal arterial network, *Curr. Eye Res.*, **34**, 945-956.

Lott-Crumpler D.A. & Chaudhry H.R., 2001, Optimal patterns for suturing wounds of complex shapes to foster healing, *J. Biomech.*, **34**, 51-58.

Maggelakis S.A. & Savakis A.E., 1996, A mathematical model of growth factor induced capillary growth in the retina, *Math. Comput. Model.*, **24**, 33-41.

Maggelakis S.A. & Savakis A.E., 1999, A mathematical model of retinal neovascularization, *Math. Comput. Model.*, **29**, 91-97.

Macklin P., McDougall S., Anderson A.R.A., Chaplain M.A.J., Cristini V. & Lowengrub J., 2009, Multiscale modelling and nonlinear simulation of vascular tumour growth, *J. Math. Biol.*, **58**, 765-798.

Macklin P., Edgerton M.E., Thompson A.M. & Cristini V., 2012, Patient-calibrated agent-based modelling of ductal carcinoma in situ (DCIS): from microscopic measurements to macroscopic predictions of clinical progression, *J. Theor. Biol.*, **301**, 122-140.

Maini P.K., Alarcon T., H.M. Byrne, Owen M.R. & Murphy J., 2007, Structural adaptation in normal and cancerous vasculature. In: Aletti G., Burger M., Michelette A. & Morale D., eds., Math Everywhere. Deterministic and Stochastic Modelling in Biomedicine, Economics and Industry. Dedicated to the 60th Birthday of Vincenzo Capasso, New York, Springer, 165-178.

Mansury Y. & Deisboeck T.S., 2003, The impact of “search precision” in an agent-based tumor model, *J. Theor. Biol.*, **224**, 325-337.

Mantzaris N.V., Webb S. & Othmer H.G., 2004, Mathematical modelling of tumour-induced angiogenesis, *J. Math. Biol.*, **49**, 111-187.

Martini P., Pierach A. & Schreyer E., 1930, Die stroemung des blutes in engen gefaessen. Eine abweichung vom Poiseuille'schen gesetz, *Dtsch. Arch. Klin. Med.*, **169**, 212-222.

McDougall S.R. & Sorbie K.S., 1997, The application of network modeling techniques to multiphase flow in porous media, *Petroleum Geosci.*, **3**, 161-169.

McDougall S.R., Anderson A.R.A., Chaplain M.A.J. & Sherratt J.A., 2002, Mathematical modelling of flow through vascular networks: implications for tumour-induced angiogenesis and chemotherapy strategies, *Bull. Math. Biol.*, **64**, 673-702.

McDougall S., Dallon J., Sherratt J. & Maini P., 2006a, Fibroblast migration and collagen deposition during dermal wound healing: mathematical modelling and clinical implications, *Phil. Trans. R. Soc. A*, **364**, 1385-1405.

McDougall S.R., Anderson A.R.A. & Chaplain M.A.J., 2006b, Mathematical modelling of dynamic adaptive tumour-induced angiogenesis: clinical implications and therapeutic targeting strategies, *J. Theor. Biol.*, **241**, 564-589.

McDougall S.R., Chaplain M.A.J., Stephanou A. & Anderson A.R.A., 2010, Modelling the impact of pericyte migration and coverage of vessels on the efficacy of vascular disrupting agents, *Math. Model. Nat. Phenom.*, **5**, 163-202.

Metcalfe A.D. & Ferguson M.W.J., 2007, Bioengineering skin using mechanisms of regeneration and repair, *Biomaterials*, **28**, 5100-5113.

Mitchell A.R. & Griffiths D.F., 1980, The Finite Difference Method in Partial Differential Equations, Wiley, Chichester.

Mitchell C.A., Rutland C.S., Walker M., Nasir M., Foss A.J., Stewart C., Gerhardt H., Konerding M.A., Risau W. & Drexler H.C., 2006, Unique vascular phenotypes following over-expression of individual VEGFA isoforms from the developing lens, *Angiogenesis*, **9**, 209-24.

Mori R., Power K.T., Wang C.M., Martin P. & Becker D.L., 2006, Acute downregulation of connexin43 at wound sites leads to a reduced inflammatory response, enhanced keratinocyte proliferation and wound fibroblast migration, *J. Cell Sci.*, **119**, 5193-5203.

Mudhar H.S., Pollock R.A., Wang C., Stiles C.D. & Richardson W.D., 1993, PDGF and its receptors in the developing rodent retina and optic nerve, *Development*, **118**, 539-552.

Murphy K.E., Hall C.L., McCue S.W. & D.L.S. McElwain, 2011, A two-compartment mechanochemical model of the roles of transforming growth factor β and tissue tension in dermal wound healing, *J. Theor. Biol.*, **272**, 145-159.

Murphy K.E., Hall C.L., Maini P.K., McCue S.W. & D.L.S. McElwain, 2012, A fibrocontractive mechanochemical model of dermal wound closure incorporating realistic growth factor kinetics, *Bull. Math. Biol.*, **74**, 1143-1170.

Neilson M.P., Mackenzie J.A., Webb S.D. & Insall R.H., 2011, Modeling cell movement and chemotaxis using pseudopod-based feedback, *SIAM J. Sci. Comput.*, **33**, 1035-1057.

Ng Y.S., Rohan R., Sunday M.E., Demello D.E. & D'Amore P.A., 2001, Differential expression of VEGF isoforms in mouse during development and in the adult, *Dev. Dyn.*, **220**, 112-121.

Norton K., Wininger M., Bhanot G., Ganesan S., Barnard N. & Shinbrot T., 2010, A 2D mechanistic model of breast ductal carcinoma in situ (DCIS) morphology and progression, *J. Theor. Biol.*, **263**, 393-406.

Olsen L., Sherratt J.A. & Maini P.K., 1995, A mechanochemical model for adult dermal wound contraction and the permanence of the contracted tissue displacement profile, *J. Theor. Biol.*, **177**, 113-128.

Olsen L., Sherratt J.A., Maini P.K. & Arnold F., 1997, A mathematical model for the capillary endothelial cell-extracellular matrix interactions in wound-healing angiogenesis, *IMA J. Math. Appl. Med. Biol.*, **14**, 261-281.

Olsen L., Maini P.K., Sherratt J.A. & Dallon J., 1999, Mathematical modelling of anisotropy in fibrous connective tissue, *Math. Biosci.*, **158**, 145-170.

Orme M.E. & Chaplain M.A.J., 1996a, A mathematical model of vascular tumour growth and invasion, *Math. Comput. Model.*, **23**, 43-60.

Orme M.E. & Chaplain M.A.J., 1996b, A mathematical model of the first steps of tumour-related angiogenesis: capillary sprout formation and secondary branching, *IMA J. Math. Appl. Med. Biol.*, **13**, 73-98.

Othmer H.G., Dunbar S.R. & Alt W., 1988, Models of dispersal in biological systems, *J. Math. Biol.*, **26**, 263-298.

Othmer H.G. & Stevens A., 1997, Aggregation, blowup and collapse: the ABC’s of taxis and reinforced random walks, *SIAM J. Appl. Math.*, **57**, 1044-1081.

Owen M.R., Alarcon T., Maini P.K. & Byrne H.M., 2009, Angiogenesis and vascular remodelling in normal and cancerous tissues, *J. Math. Biol.*, **58**, 689-721.

Painter K.J. & Sherratt J.A., 2003, Modelling the movement of interacting cell populations, *J. Theor. Biol.*, **225**, 327-339.

Palsson E. & Othmer H.G., 2000, A model for individual and collective cell movement in *Dictyostelium discoideum*, *PNAS*, **97**, 10448-10453.

Palsson E., 2001, A three-dimensional model of cell movement in multicellular systems, *Future Gener. Comp. Sy.*, **17**, 835-852.

Paques M., Tadayoni R., Sercombe R., Laurent P., Genevois O., Gaudric A. & Vicaut E., 2003, Structural and hemodynamic analysis of the mouse retinal circulation, *Invest. Ophtalmol. Vis. Sci.*, **44**, 4960-4967.

Park J.E., Keller G.A. & Ferrara N., 1993, The vascular endothelial growth factor (VEGF) isoforms: differential deposition into the subepithelial extracellular matrix and bioactivity of extracellular matrix-bound VEGF, *Mol. Biol. Cell.*, **4**, 1317-1326.

Patel A.A., Gawlinski E.T., Lemieux S.K. & Gatenby R.A., 2001, A cellular automaton model of early tumour growth and invasion: the effects of native tissue vascularity and increased anaerobic tumor metabolism, *J. Theor. Biol.*, **213**, 315-331.

Patlak C.S., 1953, Random walk with persistence and external bias, *Bull. Math. Biophys.*, **15**, 311-338.

Peirce S.M., 2008, Computational and mathematical modelling of angiogenesis, *Microcirculation*, **15**, 739-751.

Perfahl H., Byrne H.M., Chen T., Estrella V., Lapin A., Gatenby R.A., Gillies R.J., Lloyd M.C., Maini P.K., Reuss M. & Owen M.R., 2011, Multiscale modelling of vascular tumour growth in 3D: the roles of domain size and boundary conditions, *PLoS ONE*, **6**(4), e14790.

Pettet G.J., Byrne H.M., McElwain D.L.S. & Norbury J., 1996a, A model of wound-healing angiogenesis in soft tissue, *Math. Biosci.*, **136**, 35-63.

Pettet G.J., Chaplain M.A.J., McElwain D.L.S. & Byrne H.M., 1996b, On the role of angiogenesis in wound healing, *Proc. R. Soc. Lond. B*, **263**, 1487-1493.

Pettet G.J. & McElwain D.L.S., 2000, Lotka-Volterra equations with chemotaxis: walls, barriers and travelling waves, *IMA J. Math. Appl. Med. Biol.*, **17**, 395-413.

Plank M.J., Sleeman B.D. & Jones P.F., 2004a, A mathematical model of tumour angiogenesis, regulated by vascular endothelial growth factor and the angiopoietins, *J. Theor. Biol.*, **229**, 435-454.

Plank M.J. & Sleeman B.D., 2004b, Lattice and non-lattice models of tumour angiogenesis, *Bull. Math. Biol.*, **66**, 1785-1819.

Pons-Salort M., van der Sanden B., Juhem A., Popov A. & Stephanou A., 2012, A computational framework to assess the efficacy of cytotoxic molecules and vascular disrupting agents against solid tumours, *Math. Model. Nat. Phenom.*, **7**, 49-77.

Powathil G.G., Gordon K.E., Hill L.A. & Chaplain M.A.J., 2012, Modelling the effects of cell-cycle heterogeneity on the response of a solid tumour to chemotherapy: biological insights from a hybrid multiscale cellular automaton model, *J. Theor. Biol.*, **308**, 1-19.

Pozrikidis C., 2009, Numerical simulation of blood flow through microvascular capillary networks, *Bull. Math. Biol.*, **71**, 1520-1541.

Price R.J. & Skalak T.C., 1995, A circumferential stress-growth rule predicts arcade arteriole formation in a network model, *Microcirculation*, **2**, 41-51.

Pries A.R., Ley K. & Gaehtgens P., 1986, Generalization of the Fahraeus principle for microvessel networks, *Am. J. Physiol.*, **251**, 1324-1332.

Pries A.R. & Gaehtgens P., 1989a, Dispersion of blood cell flow in microvascular networks. In: Lee J.S. & Skalak T.C., eds., Microvascular Mechanics. Hemodynamics of Systemic & Pulmonary Microcirculation, New York, Springer, 50-64.

Pries A.R., Ley K., Claassen M. & Gaehtgens P., 1989b, Red cell distribution at microvascular bifurcations, *Microvasc. Res.*, **38**, 81-101.

Pries A.R., Secomb T.W., Gaehtgens P. & Gross J.F., 1990, Blood flow in microvascular networks – experiments and simulation, *Circ. Res.*, **67**, 826-834.

Pries A.R., Fritzsche A, Ley K. & Gaehtgens P., 1992, Redistribution of red blood cell flow in microcirculatory networks by hemodilution, *Circ. Res.*, **70**, 1113-1121.

Pries A.R., Secomb T.W., Gessner T., Sperandio M.B., Gross J.F. & Gaehtgens P., 1994, Resistance to blood flow in microvessels in vivo, *Circ. Res.*, **75**, 904-915.

Pries A.R., Secomb T.W. & Gaehtgens P., 1996, Biophysical aspects of blood flow in the microvasculature, *Cardiovasc. Res.*, **32**, 654-667.

Pries A.R., Secomb T.W. & Gaehtgens P., 1998, Structural adaptation and stability of microvascular networks: theory and simulations, *Am. J. Physiol.*, **275**, 349-360.

Pries A.R., Reglin B. & Secomb T.W., 2001, Structural adaptation of microvascular networks: functional roles of adaptive responses, *Am. J. Physiol. Heart Circ. Physiol.*, **281**, 1015-1025.

Pries A.R., Reglin B. & Secomb T.W., 2005, Remodeling of blood vessels: responses of diameter and wall thickness to hemodynamic and metabolic stimuli, *Hypertension*, **46**, 725-731.

Pries A.R., Cornelissen A.J.M., Sloot A.A., Hinkeldey M., Dreher M.R., Hopfner M., Dewhirst M.W. & Secomb T.W., 2009, Structural adaptation and heterogeneity of normal and tumor microvascular networks, *PLoS Comput. Biol.*, **5**(5), e1000394.

Pries A.R., Hopfner M., le Noble F., Dewhirst M.W. & Secomb T.W., 2010, The shunt problem: control of functional shunting in normal and tumour vasculature, *Nat. Rev. Cancer*, **10**, 587-593.

Qutub A.A., MacGabhann F., Karagiannis E.D., Vempati P. & Popel A.S., 2009, Multiscale models of angiogenesis: integration of molecular mechanisms with cell- and organ-level models, *IEEE Eng. Med. Biol. Mag.*, **28**, 14-31.

Ramis-Conde I., Drasdo D., Anderson A.R.A. & Chaplain M.A.J., 2008a, Modeling the influence of the E-cadherin-β-catenin pathway in cancer cell invasion: a multiscale approach, *Biophys. J.*, **95**, 155-165.

Ramis-Conde I., Chaplain M.A.J. & Anderson A.R.A., 2008b, Mathematical modelling of cancer cell invasion of tissue, *Math. Comput. Model.*, **47**, 533-545.

Ramis-Conde I., Chaplain M.A.J., Anderson A.R.A. & Drasdo D., 2009, Multi-scale modelling of cancer cell intravasation: the role of cadherins in metastasis, *Phys. Biol.*, **6**, 016008.

Reglin B., Secomb T.W. & Pries A.R., 2009, Structural adaptation of microvessel diameters in response to metabolic stimuli: where are the oxygen sensors?, *Am. J. Physiol. Heart Circ. Physiol.*, **297**, H2206-H2219.

Rejniak K.A., Kliman H.J. & Fauci L.J., 2004, A computational model of the mechanics of growth of the villous trophoblast bilayer, *Bull. Math. Biol.*, **66**, 199-232.

Rejniak K.A., 2007, An immersed boundary framework for modelling the growth of individual cells: an application to the early tumour development, *J. Theor. Biol.*, **247**, 186-204.

Rejniak K.A. & Dillon R.H., 2007, A single cell-based model of the ductal tumour microarchitecture, *Comp. Math. Meth. Med.*, **8**, 51-69.

Rejniak K.A. & Anderson A.R.A., 2008a, A computational study of the development of epithelial acini: I. Sufficient conditions for the formation of a hollow structure, *Bull. Math. Biol.*, **70**, 677-712.

Rejniak K.A. & Anderson A.R.A., 2008b, A computational study of the development of epithelial acini: II. Necessary conditions for structure and lumen stability, *Bull. Math. Biol.*, **70**, 1450-1479.

Riches D.W.H., 1996, Macrophage involvement in wound repair, modelling and fibrosis. In: Clark R.A.F., ed., The Molecular and Cellular Biology of Wound Repair 2nd Edition, New York, Plenum Press, 95-142.

Risau W., 1997, Mechanisms of angiogenesis, *Nature*, **386**, 671-674.

Robson M.C., Steed D.L. & Franz M.G., 2001, Wound healing: biologic features and approaches to maximize healing trajectories, *Curr. Probl. Surg.*, **38**, 65-140.

Rubinstein B., Jacobson K. & Mogilner A., 2005, Multiscale two-dimensional modelling of a motile simple-shaped cell, *Multiscale Model. Simul.*, **3**, 413-439.

Rutland C.S., Mukhopadhyay M., Underwood S., Clyde N., Mayhew T.M. & Mitchell C.A., 2005, Induction of intrauterine growth restriction by reducing placental vascular growth with the angioinhibin TNP-470, *Biol. Reprod.*, **73**, 1164-1173.

Rutland C.S., Mitchell C.A., Nasir M., Konerding M.A. & Drexler H.C., 2007, Microphthalmia, persistent hyperplastic hyaloid vasculature and lens anomalies following overexpression of VEGF-A188 from the alphaA-crystallin promoter, *Mol. Vis.*, **13**, 47-56.

Savill N.J. & Hogeweg P., 1997, Modeling morphogenesis: from single cells to crawling slugs, *J. Theor. Biol.*, **184**, 229-235.

Savill N.J. & Sherratt J.A., 2003, Control of epidermal stem cell clusters by Notch-mediated lateral induction, *Dev. Biol.*, **258**, 141-153.

Schaller G. & Meyer-Hermann M., 2005, Multicellular tumor spheroid in an off-lattice Voronoi-Delaunay cell model, *Phys. Rev. E*, **71**, 051910.

Schmid-Schoenbein G.W., Skalak R., Usami S. & Chien S., 1980, Cell distribution in capillary networks, *Microvasc. Res.*, **19**, 18-44.

Schmid-Schoenbein G.W., 1999, Biomechanics of microcirculatory blood perfusion, *Ann. Rev. Biomed. Eng.*, **1**, 73-102.

Schugart R.C., Friedman A., Zhao R. & Sen C.K., 2008, Wound angiogenesis as a function of tissue oxygen tension: a mathematical model, *PNAS*, **105**, 2628-2633.

Schwacha M.G., 2009, γδ T-cells: potential regulators of the post-burn inflammatory response, *Burns*, **35**, 318-326.

Scott A., Powner M.B., Gandhi P., Clarkin C., Gutmann D.H., Johnson R.S., Ferrara N. & Fruttiger M., 2010, Astrocyte-derived vascular endothelial growth factor stabilizes vessels in the developing retinal vasculature, *PLoS One*, **5**, e11863.

Secomb T.W. & Hsu R., 1996, Motion of red blood cells in capillaries with variable cross-sections, *J. Biomech. Eng.*, **118**, 538-544.

Secomb T.W., Hsu R. & Pries A.R., 2001, Motion of red blood cells in a capillary with an endothelial surface layer: effect of flow velocity, *Am. J. Physiol. Heart Circ. Physiol.*, **281**, H629-H636.

Secomb T.W., Alberding J.P., Hsu R. & Pries A.R., 2007, Simulation of angiogenesis, remodeling and pruning in microvascular networks, *FASEB Journal*, **21**, 897.10.

Sen C.K., 2009, Wound healing essentials: let there be oxygen, *Wound Rep. Reg.*, **17**, 1-18.

Sen C.K., Gordillo G.M., Roy S., Kirsner L., Lambert L., Hunt T.K., Gottrup F., Gurtner G.G. & Longaker M.T., 2009, Human skin wounds: a major and snowballing threat to public health and the economy, *Wound Rep. Reg.*, **17**, 763-771.

Shafer I., Nancollas R., Boes M., Sieminski A.L. & Geddes J.B., 2011, Stability of a microvessel subject to structural adaptation of diameter and wall thickness, *Math. Med. Biol.*, **28**, 271-286.

Sherratt J.A. & Murray J.D., 1990, Models of epidermal wound healing, *Proc. R. Soc. Lond. B*, **241**, 29-36.

Sherratt J.A. & Murray J.D., 1991, Mathematical analysis of a basic model for epidermal wound healing, *J. Math. Biol.*, **29**, 389-404.

Sherratt J.A. & Murray J.D., 1992, Epidermal wound healing: a theoretical approach, *Comm. Theor. Biol.*, **2**, 315-333.

Sherratt J.A., Martin P., Murray J.D. & Lewis J., 1992, Mathematical models of wound healing in embryonic and adult epidermis, *IMA J. Math. Appl. Med. Biol.*, **9**, 177-196.

Sherratt J.A., 1993, Actin aggregation and embryonic epidermal wound healing, *J. Math. Biol.*, **31**, 703-716.

Sherratt J.A. & Dallon J.C., 2002, Theoretical models of wound healing: past successes and future challenges, *C. R. Biologies*, **325**, 557-564.

Shima D.T., Kuroki M., Deutsch U., Ng Y.S., Adamis A.P. & D'Amore P.A., 1996, The mouse gene for vascular endothelial growth factor. Genomic structure, definition of the transcriptional unit, and characterization of transcriptional and post-transcriptional regulatory sequences, *J. Biol. Chem.*, **271**, 3877-3883.

Shirinifard A., Gens J.S., Zaitlen B.L., Poplawski N.J., Swat M. & Glazier J.A., 2009, 3D multi-cell simulation of tumor growth and angiogenesis, *PLoS ONE*, **4**(10), e7190.

Shraiman B.I., 2005, Mechanical feedback as a possible regulator of tissue growth, *PNAS*, **102**, 3318-3323.

Sin N., Meng L.H., Wang M.Q.W., Wen J.J., Bornmann W.G. & Crews C.M., 1997, The anti-angiogenic agent fumagillin covalently binds and inhibits the methionine aminopeptidase, MetAP-2, *Proc. Natl. Acad. Sci. USA*, **94**, 6099-6103.

Singer A.J. & Clark R.A.F., 1999, Cutaneous wound healing, *N. Engl. J. Med.*, **341**, 738-746.

Stalmans I., Ng Y.S., Rohan R., Fruttiger M., Bouche A., Yuce A., Fujisawa H., Hermans B., Shani M., Jansen S., Hicklin D., Anderson D.J., Gardiner T., Hammes H.P., Moons L., Dewerchin M., Collen D., Carmeliet P. & D'Amore P.A., 2002, Arteriolar and venular patterning in retinas of mice selectively expressing VEGF isoforms, *J. Clin. Invest.*, **109**, 327-36.

Stephanou A., Chaplain M.A.J. & Tracqui P., 2004, A mathematical model for the dynamics of large membrane deformations of isolated fibroblasts, *Bull. Math. Biol.*, **66**, 1119-1154.

Stephanou A., McDougall S.R., Anderson A.R.A. & Chaplain M.A.J., 2005, Mathematical modelling of flow in 2D and 3D vascular networks: applications to anti-angiogenic and chemotherapeutic drug strategies, *Math. Comput. Model.*, **41**, 1137-1156.

Stephanou A., McDougall S.R., Anderson A.R.A. & Chaplain M.A.J., 2006, Mathematical modelling of the influence of blood rheological properties upon adaptative tumour-induced angiogenesis, *Math. Comput. Model.*, **44**, 96-123.

Stephanou A., Mylona E., Chaplain M. & Tracqui P., 2008, A computational model of cell migration coupling the growth of focal adhesions with oscillatory cell protrusions, *J. Theor. Biol.*, **253**, 701-716.

Sternlicht M.D. & Werb Z., 2001, How matrix metalloproteinases regulate cell behaviour, *Annu. Rev. Cell Dev. Biol.*, **17**, 463-516.

Stokes C.L. & Lauffenburger D.A., 1991, Analysis of the roles of microvessel endothelial cell random motility and chemotaxis in angiogenesis, *J. Theor. Biol.*, **152**, 377-403.

Stone J., Chan-Ling T., Pe'er J., Itin A., Gnessin H. & Keshet E., 1996, Roles of vascular endothelial growth factor and astrocyte degeneration in the genesis of retinopathy of prematurity, *Invest. Ophthalmol. Vis. Sci.*, **37**, 290-299.

Stott E.L., Britton N.F., Glazier J.A. & Zajac M., 1999, Stochastic simulation of benign avascular tumour growth using the Potts model, *Math. Comput. Model.*, **30**, 183-198.

Stout A.U. & Stout J.T., 2003, Retinopathy of prematurity, *Pediatr. Clin. North Am.*, **50**, 77-87.

Sutton D.W. & Schmid-Schoenbein G.W., 1994, The influence of pure erythrocyte suspensions on the pressure-flow relation in rat skeletal muscle, *Biorheology*, **32**, 107-120.

Szczerba D. & Szekely G., 2005, Computational model of flow-tissue interactions in intussuceptive angiogenesis, *J. Theor. Biol.*, **234**, 87-97.

Szczerba D., Kurz H. & Szekely G., 2009, A computational model of intussusceptive microvascular growth and remodelling, *J. Theor. Biol.*, **261**, 570-583.

Tektonidis M., Hatzikirou H., Chauviere A., Simon M., Schaller K. & Deutsch A., 2011, Identification of intrinsic in vitro cellular mechanisms for glioma invasion, *J. Theor. Biol.*, **287**, 131-147.

Thackham J., McElwain D. & Long R., 2008, The use of hyperbaric oxygen therapy to treat chronic wounds: a review, *Wound Rep. Reg.*, **16**, 321-330.

Tong S. & Yuan F., 2001, Numerical simulations of angiogenesis in the cornea, *Microvasc. Res.*, **61**, 14-27.

Tremel A., Cai A., Tirtaatmadja N, Hughes B.D., Stevens G.W., Landman K.A. & O’Connor A.J., 2009, Cell migration and proliferation during monolayer formation and wound healing, *Chem. Eng. Sci.*, **64**, 247-253.

Turner S. & Sherratt J.A., 2002, Intercellular adhesion and cancer invasion: a discrete simulation using the Extended Potts model, *J. Theor. Biol.*, **216**, 85-100.

Uemura A., Kusuhara S., Wiegand S.J., Yu R.T. & Nishikawa S., 2006, Tlx acts as a proangiogenic switch by regulating extracellular assembly of fibronectin matrices in retinal astrocytes, *J. Clin. Invest.*, **116**, 369-377.

Vader G. & Lens S.M.A., 2008, The Aurora kinase family in cell division and cancer, *Biochim. Biophys. Acta*, **1786**, 60-72.

Vermolen F.J., van Baaren E. & Adam J.A., 2006, A simplified model for growth factor induced healing of wounds, *Math. Comput. Model.*, **44**, 887-898.

Wang C.M., Lincoln J., Cook J.E. & Becker D.L., 2007, Abnormal connexin expression underlies delayed wound healing in diabetic skin, *Diabetes*, **56**, 2809-2817.

Waugh H.V. & Sherratt J.A., 2006, Macrophage dynamics in diabetic wound healing, *Bull. Math. Biol.*, **68**, 197-207.

Waugh H.V. & Sherratt J.A., 2007, Modelling the effects of treating diabetic wounds with engineered skin substitutes, *Wound Rep. Reg.*, **15**, 556-565.

Weidemann A., Krohne T.U., Aguilar E., Kurihara T., Takeda N., Dorrell M.I., Simon M.C., Haase V.H., Friedlander M. & Johnson R.S., 2010, Astrocyte hypoxic response is essential for pathological but not developmental angiogenesis of the retina, *Glia*, **58**, 1177-1185.

Wearing H.J. & Sherratt J.A., 2000, Keratinocyte growth factor signalling: a mathematical model of dermal-epidermal interaction in epidermal wound healing, *Math. Biosci.*, **165**, 41-62.

Welter M., Bartha K. & Rieger H., 2008, Emergent vascular network inhomogeneities and resulting blood flow patterns in a growing tumor, *J. Theor. Biol.*, **250**, 257-280.

Welter M., Bartha K. & Rieger H., 2009, Vascular remodelling of an arterio-venous blood vessel network during solid tumour growth, *J. Theor. Biol.*, **259**, 405-422.

West H., Richardson W.D. & Fruttiger M., 2005, Stabilization of the retinal vascular network by reciprocal feedback between blood vessels and astrocytes, *Development*, **132**, 1855-1862.

Wipf P.-J. & Hinz B., 2008, Integrins and the activation of latent transforming growth factor β1 – an intimate relationship, *J. Cell Biol.*, **87**, 601-615.

Wipf P.-J. & Hinz B., 2009, Myofibroblasts work best under stress, *J. Bodyw. Mov. Ther.*, **13**, 121-127.

Witte M.B. & Barbul A., 2002, Role of nitric oxide in wound repair, *Am. J. Surg.*, **183**, 406-412.

Wright C.S., van Steensel M.A.M., Hodgins M.B. & Martin P.E.M., 2009, Connexin mimetic peptides improve cell migration rates of human epidermal keratinocytes and dermal fibroblasts *in vitro, Wound Rep. Reg.*, **17**, 240-249.

Wu D. & Lin F., 2011, Modeling cell gradient sensing and migration in competing chemoattractant fields, *PLoS ONE*, **6**(4), e18805.

Wu J., Xu S., Long Q., Collins M.W., Koenig C.S., Zhao G., Jiang Y. & Padhani A.R., 2008, Coupled modelling of blood perfusion in intravascular, interstitial spaces in tumor microvasculature, *J. Biomech.*, **41**, 996-1004.

Xue C., Friedman A. & Sen C.K., 2009, A mathematical model of ischemic cutaneous wounds, *PNAS*, **106**, 16782-16787.

Yan L., Moses M.A., Huang S. & Ingber D., 2000, Adhesion-dependent control of matrix metalloproteinase-2 activation in human capillary endothelial cells, *J. Cell Sci.*, **113**, 3979-3987.

Yana I., Sagara H., Takaki S., Takatsu K., Nakamura K., Nakao K., Katsuki M., Taniguchi S., Aoki T., Sato H., Weiss S.J. & Seiki M., 2007, Crosstalk between neovessels and mural cells directs the site-specific expression of MT1-MMP to endothelial tip cells, *J. Cell Sci.*, **120**, 1607-1614.

Yen R.T. & Fung Y.C., 1978, Effect of velocity distribution on red cell distribution in capillary blood vessels, *Am. J. Physiol.*, **235**, 251-257.

Yu D. & Cringle S.J., 2001, Oxygen distribution and consumption within the retina in vascularised and avascular retinas and in animal models of retinal disease, *Prog. Retin. Eye Res.*, **20**, 175-208.

Zhang X., Cheng M. & Chintala S.K., 2004, Optic nerve ligation leads to astrocyte-associated matrix metalloproteinase-9 induction in the mouse retina, *Neurosci. Lett.*, **356**, 140-144.

Zheng X., Wise S.M. & Cristini V., 2005, Nonlinear simulation of tumour necrosis, neo-vascularization and tissue invasion via an adaptive finite-element/level-set method, *Bull. Math. Biol.*, **67**, 211-259.